UNIVERSITÀ DEGLI STUDI DI TRIESTE

e

UNIVERSITÀ CA' FOSCARI DI VENEZIA

XXXIII CICLO DEL DOTTORATO DI RICERCA IN

CHIMICA

PO FRIULI VENEZIA GIULIA - FONDO SOCIALE EUROPEO 2014/2020

DEVELOPMENT OF NOVEL CATALYTIC TRANSFORMATIONS TOWARDS VALUABLE ORGANIC INTERMEDIATES

Settore scientifico-disciplinare: **CHIM/06**

DOTTORANDO
CRISTIAN ROSSO

COORDINATORE
PROF. ENZO ALESSIO

SUPERVISORE DI TESI
PROF. MAURIZIO PRATO

CO-SUPERVISORE DI TESI
DR. GIACOMO FILIPPINI

ANNO ACCADEMICO 2019/2020

Acknowledgments

First, I would like to thank my supervisor *Prof. Maurizio Prato* for giving me the opportunity to join his research group. His passion, expertise and humanity represented for me a source of inspiration during these doctoral studies. Thanks for his precious suggestions and guidance in all the research projects I participated. Moreover, working within his laboratories, I had a great chance to improve my scientific and human skills. I am grateful to him for allowing me to have this stimulating experience with such a high-level mentor.

I would like to thank my co-supervisor, *Dr. Giacomo Filippini* for the friendly and fruitful collaboration over these three years. I especially thank him for his brilliant ideas in all the scientific projects we developed, for bringing me into the fascinating world of photocatalysis and for his valuable support at all stages of this PhD course. Most of these results would not have been possible without his active assistance.

Additionally, I would like to thank all the former and current members of the Prato group I had the opportunity to work with. In particular, I would like to mention *Dr. Zois Syrgiannis* for encouraging me to undertake this scientific path. Thanks to all the colleagues and friends of the Chemistry Department of University of Trieste for all the significant time spent together inside and outside the lab.

I would like to expressly thank *Prof. C. Oliver Kappe* for hosting me in his group at University of Graz (Austria) and for giving me the opportunity to learn the tremendous potentialities that flow chemistry offers for both academia and industry. A special thank goes to *Dr. Jason Williams* for friendly guiding me though all the aspects of this research field with his very useful teachings and support. I would like to thank all the members of the Kappe group for their help and for the nice time spent together. It was a delightful experience that will surely be beneficial for the forthcoming future.

I must thank my previous scientific mentors, *Prof. Marco Lombardo* and *Prof. Claudio Trombini* for all they taught me in the field of organic chemistry.

I would also like to personally acknowledge the European Social Fund, Operational Program 2014/2020 - Friuli-Venezia Giulia for a doctoral fellowship (Regional Code FP1799043001).

I would like to express my gratitude to my family and all my friends for the support they have constantly provided me along these years.

Table of Contents

Abbreviations

0D	Zero-Dimensional
1D	One-Dimensional
2D	Two-Dimensional
3D	Tri-Dimensional
A	Acceptor
AFM	Atomic Force Microscopy
API	Active Pharmaceutical Ingredient
Arg	*L*-Arginine
Asc	Ascorbate
ATRA	Atom Transfer Radical Addition
BET	Back-Electron Transfer
BPR	Back-Pressure Regulator
CB	Conduction Band
CDs	Carbon Dots
CNDs	Carbon NanoDots
CNMs	Carbon NanoMaterials
CNs	Carbon Nitrides
CQDs	Carbon Quantum Dots
CSTR	Continuous Stirred-Tank Reactor
D	Donor
DCM	Dichloromethane
DLS	Dynamic Light Scattering
DMAc	Dimethylacetamide
DMF	*N,N*-dimethylformamide
DMSO	Dimethylsulfoxide
E	Electrophile
E^0	Redox Potential
E_{00}	Excitation Energy
EA	Electron Acceptor
ED	Electron Donor
EDA	Electron Donor-Acceptor
EdA	Ethylenediamine
EDG	Electron-Donating Group
EDTA	Ethylenediaminetetraacetic acid
EDX	Energy-Dispersive X-ray
EWG	Electron-Withdrawing Group
FT-IR	Fourier Transform Infrared spectroscopy
g	Graphitic
GQDs	Graphene Quantum Dots
HA	Protic Acid
HAS	Homolytic Aromatic Substitution
HAT	Hydrogen Atom Transfer
HOMO	Highest Occupied Molecular Orbital
HPLC	High Performance Liquid Chromatography
KT	Kaiser Test
LEDs	Light Emitting Diodes

LUMO	Lowest Unoccupied Molecular Orbital
m	Molten salts
mpg	Mesoporous
NMR	Nuclear Magnetic Resonance
Nu	Nucleophile
PC	Photocatalyst
PDIs	Perylene Dimmides
PDs	Polymer Dots
PET	Photoinduced Electron Transfer
PL	Photoluminescence
QDs	Quantum Dots
R_F	Perfluoroalkyl moiety
R_FI	Perfluoroalkyl iodide
RTD	Residence Time Distribution
SCE	Saturated Calomel Electrode
SET	Single Electron Transfer
TCA	Trichloroacetic Acid
TEEDA	*N,N,N',N'*-tetraethylethylenediamine
TEM	Transmission Electron Microscopy
TEMPO	2,2,6,6-tetramethylpiperidine 1-oxyl
TFA	Trifluoroacetic Acid
TGA	Thermogravimetric Analysis
THF	Tetrahydrofuran
TLC	Thin Layer Chromatography
TMG	1,1,3,3-tetramethylguanidine
UV	Ultraviolet
UV/Vis	Ultraviolet-Visible
VB	Valence Band
XPS	X-ray Photoelectron Spectroscopy

Abstract

The main scientific objective of this doctoral research was to develop powerful metal-free organic (photo)catalytic systems to efficiently realize new carbon-carbon and carbon-heteroatom bond forming transformations of practical importance. These approaches had to meet the sustainability requirements for green chemical productions by using effective, non-toxic, safe, readily available from economic precursors and potentially recyclable catalysts. In doing so, the preparation of synthetically relevant organic intermediates could be promptly achieved in mild conditions, thus envisaging the potential application of the studied methodologies at preparative scale.

Chapter I introduces the general concepts of organic catalysis, including both polar and radical chemistry. Moreover, it aims to illustrate the physicochemical principles underlying the operative mechanisms of the abovementioned catalytic systems.

Chapter II focuses on the development of a photochemical strategy for the iodoperfluoroalkylation of alkenes triggered by a simple perylene diimide photocatalyst. Successively, this Chapter describes the translation of the established procedure into continuous flow with the aim of up-scaling the preparation of the relevant perfluorinated compounds.

Chapter III discusses the use of photoactive nitrogen-doped carbon dots as catalysts for the light-driven perfluoroalkylation of electron-rich organic substrates. This approach allows the extension of the reactivity to more inert arenes and heteroarenes.

Chapter IV describes the development of green polar organocatalytic methodologies in aqueous media by exploiting the surface amino functionalities of the very same nitrogen-doped carbon nanoparticles. Remarkably, this original approach has been made possible by a fine characterization of the nanomaterial at unprecedent level of detail.

Chapter V shows how another carbon-based nanomaterial, namely carbon nitride, can trigger photochemical aryl amination reactions of high synthetic importance. Interestingly, this transformation is carried out under flow conditions by means of an innovative oscillatory microstructured reactor to overcome the challenges associated with handling solids in flow.

Riassunto

L'obiettivo scientifico primario di questo dottorato di ricerca è stato sviluppare efficaci sistemi (foto)catalitici organici senza metalli per reazioni di formazione di legami carbonio-carbonio e carbonio-eteroatomo di grande rilevanza. Questi approcci dovettero soddisfare i requisiti di sostenibilità per la produzione "verde" di sostanze chimiche attraverso l'uso di catalizzatori efficienti, non tossici, sicuri, economici e potenzialmente riciclabili. In tal modo, la preparazione di intermedi organici di rilevanza sintetica può essere facilmente ottenuta in condizioni blande, prevedendo così la potenziale applicazione delle metodologie studiate su scala preparativa.

Il Capitolo I presenta i concetti generali di catalisi organica, includendo la chimica polare e radicalica. In aggiunta, mira ad illustrare i principi chimico-fisici che sottintendono ai meccanismi operativi dei sistemi catalitici menzionati.

Il capitolo II si focalizza sullo sviluppo di una strategia fotochimica per la iodoperfluoroalchilazione di alcheni innescata da un semplice perilene diimmide come fotocatalizzatore. Successivamente, descrive la traduzione in flusso continuo della procedura sviluppata al fine di scalare la preparazione dei rilevanti composti perfluorurati.

Il capitolo III discute dell'uso di dots di carbonio dopati all'azoto foto-attivi come catalizzatori per la perfluoroalchilazione di substrati organici elettron-ricchi stimolata dalla luce. Questo approccio permette l'estensione della reattività ai più inerti areni ed etero-areni.

Il capitolo IV descrive lo sviluppo di metodologie organocatalitiche polari "verdi" in ambiente acquoso sfruttando le funzionalità amminiche sulla superficie degli stessi dots di carbonio dopati all'azoto. Questo originale approccio è reso possibile da una caratterizzazione del nanomateriale ad un livello di dettaglio senza precedenti.

Il capitolo V mostra come un altro nanomateriale carbonioso, il nitruro di carbonio, possa indurre reazioni fotochimiche di amminazione arilica di grande rilevanza sintetica. In particolare, questa trasformazione è condotta in flusso grazie all'uso di un innovativo reattore oscillativo per superare i problemi relativi al maneggiare solidi in flusso.

Chapter I

General Introduction

"Chemistry without catalysis, would be a sword without a handle, a light without brilliance, a bell without sound."

Alwin Mittasch

A catalyst is a substance that increases the rate of a reaction without modifying the overall standard Gibbs energy change in the reaction.[1] In particular, a catalyst operates by lowering the activation energy of the rate-determining step(s) with respect to the uncatalyzed pathway.[2] The whole process is known as catalysis (Figure 1). Catalysis has a fundamental role to solve arduous tasks in synthetic chemistry and is thus involved in the global economy in many industrial fields.[3] In fact, in the last 50 year, catalysis has seen enormous progress in the development of optimized large-scale productions within the area of pharmaceutical, agrochemical and petrochemical industry.[4,5] Moreover, a catalytic approach presents multiple benefits for business and sustainability compared to stoichiometric processes. These include cost reduction, time and energy saving, waste reduction, carbon-footprint minimization, etc.[3] For these reasons, it is estimated that more than 90% of all chemical productions have at least one catalytic step in their manufacture.[6] Not surprisingly, an ever-growing interest in developing novel catalytic transformations has been exhibited both from academia and industry in order to resolve the related present-day challenges in organic synthesis.[7]

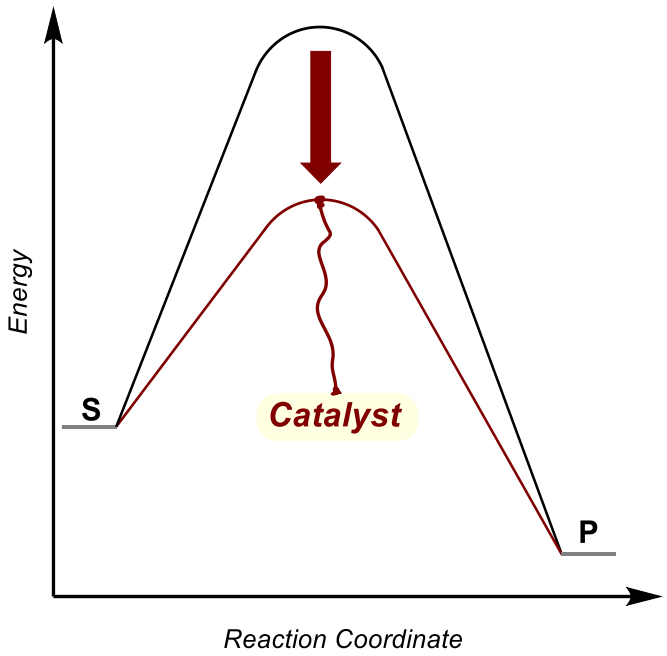

Figure 1. Simplified energy profiles of an uncatalyzed reaction (black line) *versus* a catalyzed counterpart (red line). The actual profiles may be more sophisticated with different minima and maxima. S = substrate, P = product.

1.1 Organocatalysis

Organocatalysis is a prominent area of catalysis that has emerged in the last decades. This field is based on the use of small organic molecules as catalysts to drive relevant transformations.[8] Thanks to its robust nature and high chemical compatibility, organocatalysis turned out to be a versatile tool in modern synthesis.[9] Indeed, its use is particularly suitable to access previously unachievable reactivities. For instance, highly valuable compounds can be prepared towards multistep organocatalytic processes or by combining organocatalysis with different bio-, metal- or photoredox systems.[10–14] Remarkably, the abovementioned reactions can be carried out in a enantioselective fashion by means of chiral organocatalysts.[15–17] This is of fundamental importance because enantiomers have different behavior in chiral environments, such as those present in biological systems. As a result, organocatalysis is widely recognized as one of the main branches of asymmetric synthesis, beyond enzymatic catalysis and organometallic catalysis.[8]

One of the key points for the success of organocatalysis has been the identification of generic modes of catalyst activation. These provide reactive species that can participate in many reaction types. Such reactive species arises from the interaction of the catalyst with a defined functional group of the substrate, in a highly organized and predictable manner.[8] Based on the nature of this interaction, the generic activation modes can be identified as *covalent* and *non-covalent* activations.[18] In the former case, the catalyst covalently binds the substrate within the catalytic cycle. In the latter case only non-covalent interactions activate the molecule towards the catalytic transformation.

Among the various organocatalytic methodologies belonging to the covalent activation category, aminocatalysis is undeniably the most widespread and known.[19] It relies on the use of primary, secondary or tertiary amines to activate a carbonyl substrate by the reversible formation of an enamine, an iminium ion, an ammonium enolate or a 3π-electrons system as the reactive species (SOMO catalysis).[15,16,20,21] These approach can be also extended to vinylogous substrates.[22] A different kind of covalent activation is represented by *N*-heterocyclic carbene (NHC) catalysis, which has being proposed as a catalytic alternative to the acyl anion equivalents.[23] Generally, the covalent activation modes are built on strong and directional interactions between substrate and catalyst. These interactions provided a reliable synthetic platform for the functionalization of carbonyl compounds at α- or β-position.

Conversely, non-covalent activation modes involve weaker and less-directional interactions between substrate and catalyst than their covalent counterparts. Nevertheless, those methodologies found broad application in organic synthesis. For instance, hydrogen-bond catalysis operates through the formation of a network between the hydrogen-bond donor (catalyst) and the acceptor (substrate).[24] Another non-covalent activation mode consists of the interaction of an ionic substrate with the organocatalyst through the formation of ion pairs, including phase-transfer catalysis and acid-base catalysis.[25]

1.1.1 Aminocatalysis

The use of simple chiral amines as organocatalysts to promote the functionalization of carbonyl compounds has been originally proposed in the early 1970s by Hajos and Wiechert.[26,27] Almost thirty years later, in 2000, two seminal works conceptualized the concept of asymmetric aminocatalysis. Barbas, Lerner and List reported the proline-catalyzed intermolecular aldol reaction whereas MacMillan described the first stereoselective aminocatalyzed Diels-Alder reaction.[28,29] These publications are nowadays recognized as milestones in aminocatalysis, since they caused a tremendous increase in number and quality of the researches within this field. Therefore, aminocatalysis quickly became an established branch of asymmetric synthesis.[15]

In particular, the mentioned pivotal studies laid the foundations for two novel activation modes for carbon-carbon bond forming reactions. These modes involve reactive covalent intermediates, transiently generated upon condensation of chiral amines with carbonyl compounds. In the case of α,β-unsaturated aldehydes or ketones, the condensation leads to reversible formation of a positively charged iminium ion derivatives. This species lowers the energy of the lowest unoccupied molecular orbital (LUMO) of the parent carbonyl compound, thus facilitating conjugated additions of suitable nucleophiles and pericyclic reactions.[30] As a consequence, the described iminium ion activation mode enables the β-functionalization of carbonyl compounds (Figure 2a).[31]

Conversely, by reacting an enolizable aldehydes or ketones with the aminocatalyst, the so-obtained iminium ion can undergo fast α-deprotonation, leading to the generation of an enamine derivative. This species is a nucleophilic enolate equivalent thanks to the highest occupied molecular orbital (HOMO) raising effect. For this reason, the enamine can trap a variety of electrophiles providing, upon catalyst release, α-functionalized carbonyl compounds (Figure 2b).[32] Typically, aldehydes readily react with secondary amines, whereas ketones are more prone to interact with primary amines.[33]

In most of the cases reported in literature, the abovementioned reactivities are efficiently carried out by means of the so-called “privileged aminocatalysts”. They are represented by natural compounds like aminoacids (e.g. proline) or cinchona alkaloids, as well as their derivatives such as diaryl prolinols, imidazolidinones, ureas, etc. (Figure 2c).[9,34]

In this thesis work, the iminium ion and enamine activation modes have been utilized in order to trigger synthetically relevant C-C and C-heteroatom bond forming reactions. In particular, these key intermediates were formed on the surface of amine-rich nanomaterials, namely carbon dots. Moreover, the concept has been translated to intrinsically chiral carbon nanoparticles to carry out the mentioned transformations in an enantioselective fashion. These results are discussed in Chapter IV.

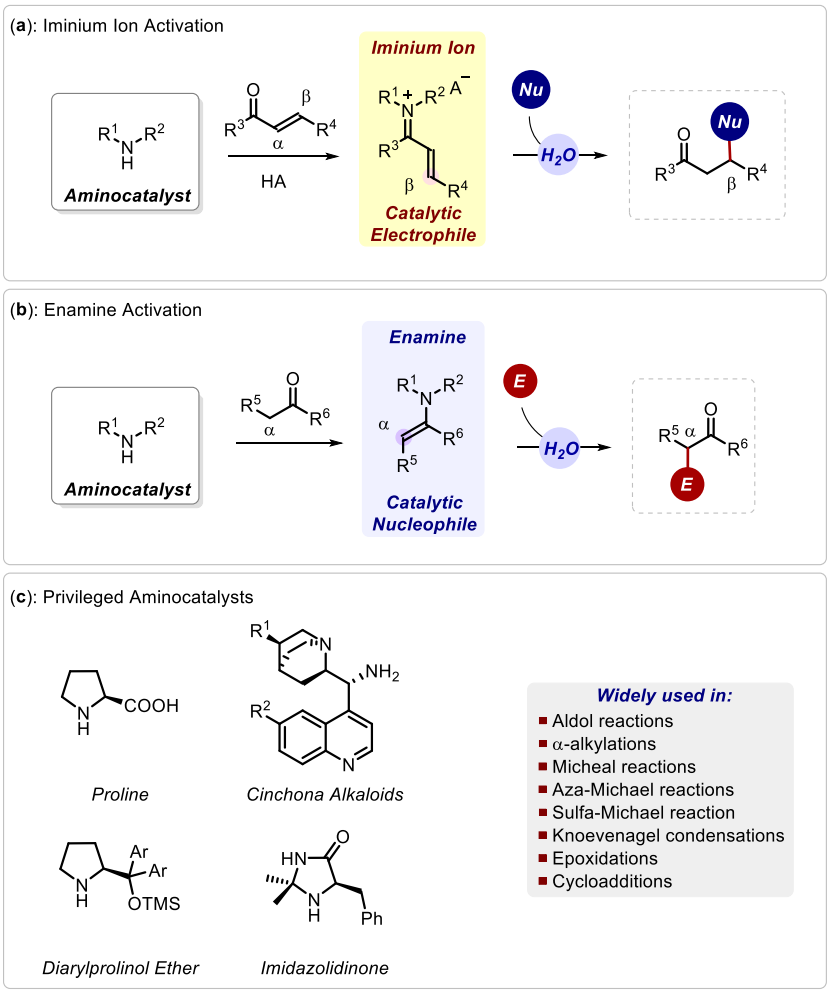

Figure 2. (**a**) Iminium ion activation of α,β-unsaturated carbonyl compounds. HA = protic acid. Nu = nucleophile (**b**) Enamine activation of enolizable carbonyl compounds. E = electrophile (**c**) Some of the most used "privileged aminocatalysts".

Remarkably, in recent times organocatalysis and in particular aminocatalysis, showed great applicability in the total synthesis of chiral drugs that are currently available on the market in an enantiopure fashion.[35] This intrinsic potential can be explained considering some of the great advantages of organocatalysis compared to traditional organometallic chemistry. In fact, the most used organocatalysts are usually inexpensive, readily available from the natural chiral pool, non-toxic, moisture and air tolerant and environmentally friendly. Moreover, thanks to the absence of transition metal contaminants, organocatalytic methodologies are particularly attractive for the preparation of pharmaceutical compounds at industrial scale (Figure 3).[35,36] Notwithstanding, a few limitation of these catalytic methods could in some cases hamper their complete applicability. For instance, relatively high catalytic loadings (between 5 and 30 mol%) and long reaction times (often more than 24 hours) are generally required. Furthermore, the substrate tolerance might be low in some procedures.[36] Despite this, organocatalysis has become a trend topic in research and a widely employed approach in synthetic chemistry over the last twenty years.

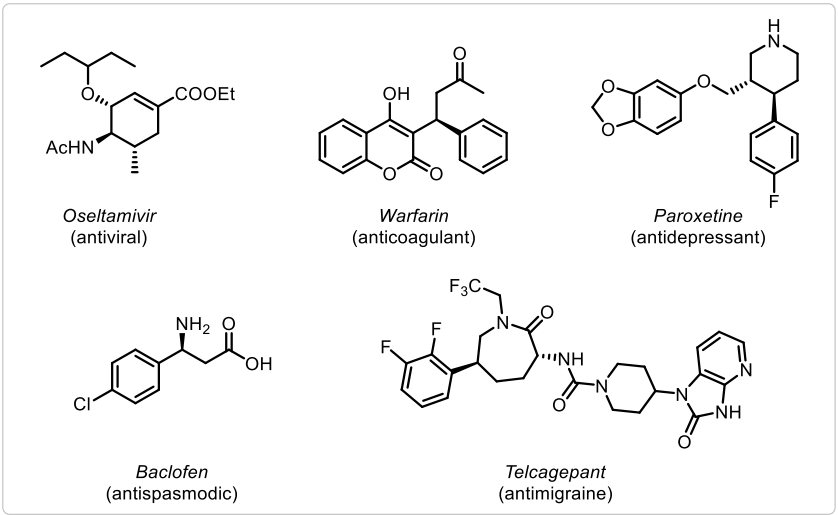

Figure 3. Representative examples of pharmaceutical compounds prepared at industrial scale by means of organocatalysis.

1.2 Photocatalysis

1.2.1 From Photochemistry to Photoredox Catalysis

The branch of chemistry that deals with chemical changes promoted by the absorption of light is known as photochemistry.[1] In these chemical transformations, the energy required to convert the starting materials into the final products is provided by photons. In response to the first pioneering studies of Giacomo Ciamician in the early 1910s,[37] photochemistry has attract an ever-growing attention from the scientific community. However, a critical impediment has limited the growth of photochemistry on global scale for decades. This relies to the inability of most organic molecules to absorb visible light, making necessary the use of dangerous high-energy UV radiation to carry out the photo-induce reactivities.[38,39] In the past decade, the independent efforts of MacMillan, Yoon, Stephenson, and other contributors allowed to circumnavigate this problem, thus opening the way to a new field of research, namely visible-light photocatalysis.[12,40–43] This approach is founded on the ability of light-absorbing metal-based complexes to generate reactive radicals from suitable precursors under visible light irradiation. In particular, when the light-excited photocatalysts can act as photo-oxidants or photo-reductants towards a reaction component, the described approach is known as photoredox catalysis.[14] In fact, it made possible the renaissance of radical chemistry for synthetic purposes by accessing the generation of highly reactive open-shell species in very mild conditions.[14] Furthermore, photoredox catalysis has introduced novel reactivities that are otherwise difficult or impossible to achieve by means of polar catalysis.[12,44–47] Therefore, this research field attracted the interest of many chemists from academia and industry dealing with organic synthesis, materials science, energy production and biomedicine.[48–53]

One of the reasons for the success of photoredox catalysis resides in the effectiveness and versatility of transition metal chromophores (mainly Ru, Ir and Cu) for a wide range of photochemical transformations under visible light irradiation.[39,45,54,55] In addition, this type of catalysis provides new opportunities for both fundamental and applied investigations, through improved energy

efficiency, atom economy, and sustainability.[56] However, a series of drawbacks could hamper the applicability of transition metal-based photocatalysts. In particular, their relatively high cost, limited abundance and toxicity have prompted the research towards more cost-efficient and sustainable photocatalytic systems.[12] Metal-free organic chromophores can fulfill these requirements thanks to their tunable optical and redox properties and thus have emerged as promising photocatalytic platforms for innovative green synthetic methodologies.[12,57]

Specifically, this thesis deals with the utilization of molecular organic dyes, namely perylene diimides (PDIs), or optically active metal-free nanomaterials to trigger synthetically relevant transformations under visible light irradiation. These results are depicted in the following chapters (Chapter II-III, V).

The chemistry developed during these doctoral studies has largely capitalized upon the ability of fully organic photocatalytic systems to drive photoredox reactions. For this reason, it is important to discuss the general mechanistic aspects that lead to the formation of key radical species that trigger the mentioned reactivities. This is the main aim of the following sections.

1.2.2 Light Absorption and Excited-state Deactivation Pathways

Light absorption is the peculiarity that characterizes all the photochemical transformations. This event prompts the formation of electronically excited-state species starting from ground-state compounds and it is one of the crucial steps in the light-matter interaction. The phenomenon of the absorption of a monochromatic photon by an absorber species in solution governed by the Beer-Lambert law (*eq*. 1):

$$A = log\left(\frac{I_0}{I}\right) = \varepsilon lc \qquad (eq.\ 1)$$

where *A* is the absorbance, *I* the intensity of the transmitted light, I_0 the intensity of the incident light, ε the molar absorption coefficient, *l* the optical path length and *c* the concentration of the absorber solution.

Absorbing molecules contain antennae groups, known as chromophores, which are responsible for light absorption. The energy of the absorbed photon triggers the transition of one electron from the HOMO to the LUMO. This implies that the molecule passes from the ground electronic state to an electronically excited state, respectively described by the wave functions $\Psi_{initial}$ and Ψ_{final}. The feasibility of the electronic transition is determined by the correspondence between the energy of the photons ($h\nu$) and the energy of a pair of electronic energy levels Ψ in the absorber (*eq*. 2):

$$h\nu = E_f - E_i \qquad (eq.\ 2)$$

where E_f and E_i are the energies of the excited-state Ψ_f and the ground-state Ψ_i. Moreover, the magnitude of the electronic transition relies on the selection rules, that indicate which transitions are allowed or forbidden, taking into account the symmetry of the orbitals involved and their spin multiplicity.[58]

After the electronic transition, the excited-state species may release its energy content or undergo chemical reactions. The energy-releasing pathways can be classified as radiative (transitions to lower states involving light emission, i.e. fluorescence and phosphorescence) and non-radiative (transitions involving the release of heat, i.e. internal conversion and vibrational relaxation). While ground-state compounds are indefinitely stable, excited states are short-lived species and with a temporary character. Their lifetime (τ) depends on the rate of the abovementioned deactivation processes (10^{-12} – 10^{-3} s). In addition, the excited state intermediate can participate in numerous inter- and intramolecular processes that lead to a change in the chemical composition of the species involved (Figure 4).[59]

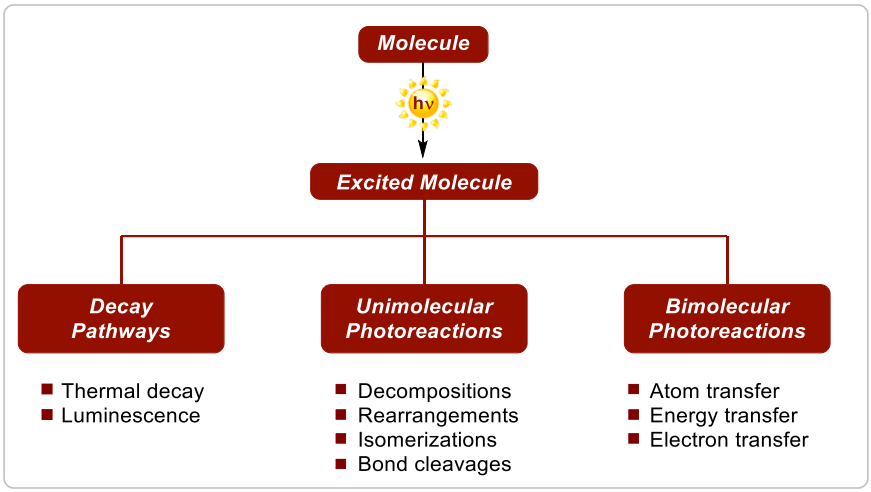

Figure 4. Light-absorption produces an excited-state molecule that can undergo various deactivation pathways.

1.2.3 Photoinduced Electron Transfer

One of the most relevant excited-state deactivation pathways in synthetic photochemistry is indisputably electron transfer. Specifically, it occurs when a light-excited molecule can donate or accept an electron by interacting with suitable redox-active compounds. This process is named photoinduced electron transfer (PET). Remarkably, the high energy content of the excited-state species influences its electron transfer ability, making it both a better oxidant and reductant than the corresponding ground-state compound.[59] To explain this phenomenon, is necessary to consider the whole photochemical process from a thermodynamic point of view. In fact, upon excitation of the absorbing molecule, one electron populates the antibonding orbital, which is positioned at a greater separation distance from the nucleus. For this reason, the energy required for a single-electron ejection process (also called ionization potential) is lower with respect to the ground-state species. On the other hand, the presence of a half-filled orbital near the nucleus increases the amount of energy released during a single-electron addition process (known as electron affinity), compared to the ground-state species (Figure 5).[60] The concomitant enhanced oxidation and reduction ability of the light-excited compounds, compared with their ground-states, is crucial for the for the work described in this thesis work.

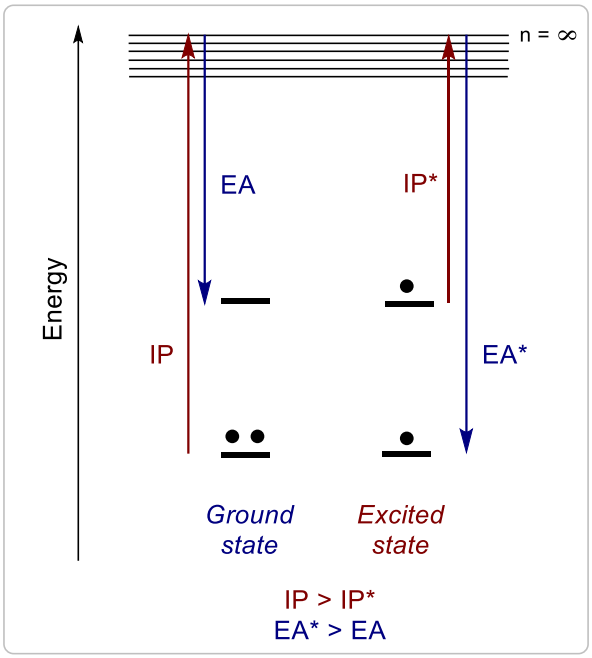

Figure 5. The ionization potential (IP) and electron affinity (EA) of an excited-state species that explains why it is a better oxidant and reductant than its corresponding ground-state.

In the ground state, a single-electron transfer (SET) from a donor (D) to an acceptor (A) is thermodynamically favored when the reduction potential of the donor ($E^0_{D^+/D}$) is lower than the reduction potential of the acceptor (E^0_{A/A^-}). Indeed, the Gibbs free energy variation of the process (ΔG^0_{et}) depends on the difference between these two values and the term C which describes the interaction between the charged species formed and the solvation effects (*eq*. 3-4).[61]

$$D + A \rightarrow D^+ + A^- \qquad (eq.\ 3)$$

$$\Delta G^0_{et} = \left(E^0_{D^+/D} - E^0_{A/A^-}\right) + C \qquad (eq.\ 4)$$

On the other hand, a PET event that involves an excited-state species and a ground-state molecule can occur in two different circumstances (*eq*. 5-6):

$$D^* + A \rightarrow D^+ + A^- \qquad (eq.\ 5)$$

$$D + A^* \rightarrow D^+ + A^- \qquad (eq.\ 6)$$

where D* and A* are respectively the excited-state donor and acceptor. In this case, the ΔG^0_{et} associated to the PET must include the excitation energy (E_{00}) and can be calculated through the Rehm-Weller equation.[62,63] For the case of an excited donor (D*) that reacts with a ground-state acceptor (A, *eq*. 7-9):

$$\Delta G^0_{et} = \left(E^0_{D^+/D^*} - E^0_{A/A^-}\right) + C \qquad (eq.\ 7)$$

$$E^0_{D^+/D^*} = E^0_{D^+/D} - E_{00} \qquad (eq.\ 8)$$

$$\Delta G^0_{et} = \left(E^0_{D^+/D} - E^0_{A/A^-} - E_{00}\right) + C \qquad (eq.\ 9)$$

where $E^0_{D^+/D^*}$ is the reduction potential of the donor in the excited state (D*). This value is expected to be smaller than $E^0_{D^+/D}$, since D* is a better reducing agent than D. While the redox potential of the ground-state species can be easily assessed through cyclic voltammetry measurements, the excitation energy (E_{00}) may be spectroscopically estimated. Specifically, it can be derived from the position of the long wavelength tail of the absorption spectrum of the electron donor (D) or, alternatively, from the position of the short wavelength tail of the emission spectrum of D.[58] An analogous discussion may be done to evaluate the magnitude of ΔG^0_{et} for a PET between an excited acceptor (A*) and a ground-state donor (D). It is evident that the use of the Rehm-Weller equation is fundamental to evaluate the excited-state potential of light-absorbing species. In this way it is possible to predict the feasibility of a productive PET for synthetic purposes.[64]

1.2.4 Photocatalytic Transformations

PET represents a straightforward strategy to easily access reactive open-shell species. This is the fundament of photoredox catalysis, where a light-absorbing photocatalyst (PC), present in sub-stoichiometric amount, can harvest the energy of the incident photons reaching its excited state (PC*).[12,14] This high energetic species thus drives the photochemical reaction by interacting with the ground-state substrate through a bimolecular process. Depending on the nature of both the PC and the substrate, three mechanistic paths are generally possible: (*i*) electron transfer; (*ii*) energy transfer; (*iii*) atom transfer. Let it consider first the electron transfer event. PC* may interact through an oxidative or reductive quenching cycle. In the oxidative quenching cycle, PC* acts as a reductant, giving an electron to a suitable electron acceptor (A) via PET. This step produces the radical anion of the acceptor ($A^{\bullet-}$) and the oxidized photocatalyst ($PC^{\bullet+}$). $PC^{\bullet+}$ can act as an oxidant, taking an electron from a donor (D) via SET, thus affording the corresponding radical cation ($D^{\bullet+}$) and restoring the ground-state PC. The catalytic cycle is hence closed. Alternatively, in the reductive quenching cycle, PC* can act as an oxidant, gaining an electron from a suitable donor (D) with a PET mechanism. This provides the radical cation of the donor ($D^{\bullet+}$) and the reduced photocatalyst ($PC^{\bullet-}$). $PC^{\bullet-}$ can donate an electron to an acceptor (A) via SET, yielding the corresponding radical anion ($A^{\bullet-}$) and restoring the PC cycle (Figure 6a). The described open-shell species produced in the photoredox mechanism may undergo subsequent transformations, until they form stable products. This approach can be employed to build new synthetically useful chemical bonds.[39,65,66]

In literature, the most common metal-based visible light-absorbing PCs are made of Ru and Ir. The corresponding polypyridyl complexes can act as strong oxidant or reducing agent in the excited state towards suitable donors or acceptors (Figure 6b). Indeed, ligands play an important role in the redox activity of these PCs, therefore they can be finely tuned to transmit the desired properties to the photoactive catalysts. When the electron density of the metal center increases, the oxidative-power of the complex decreases while, its reductive-power simultaneously increases.[13] This is important for a rational choice of the reaction partners. Parallelly, the most employed metal-free organic PCs possess a highly functionalized aromatic core that confers them the desired features, such as a strong absorption in the visible region and prominent redox character. From a structural point of

view, these organic dyes consist of acridinium salts, cyanoarenes, xanthenes, thiazines and so on (Figure 6b). This demonstrates the large diversification possible within this field for the preparation of highly photo-oxidant or photo-reducing dyes, depending on their tailorable electronic properties. Due to the ability of the organic chromophores to participate in productive PET in many transformations, along with the abovementioned sustainability advantages that they present with respect to the transition metal-based PCs, the field of organic photoredox catalysis plays an increasingly important role in the development of novel photochemical transformations.[12,57]

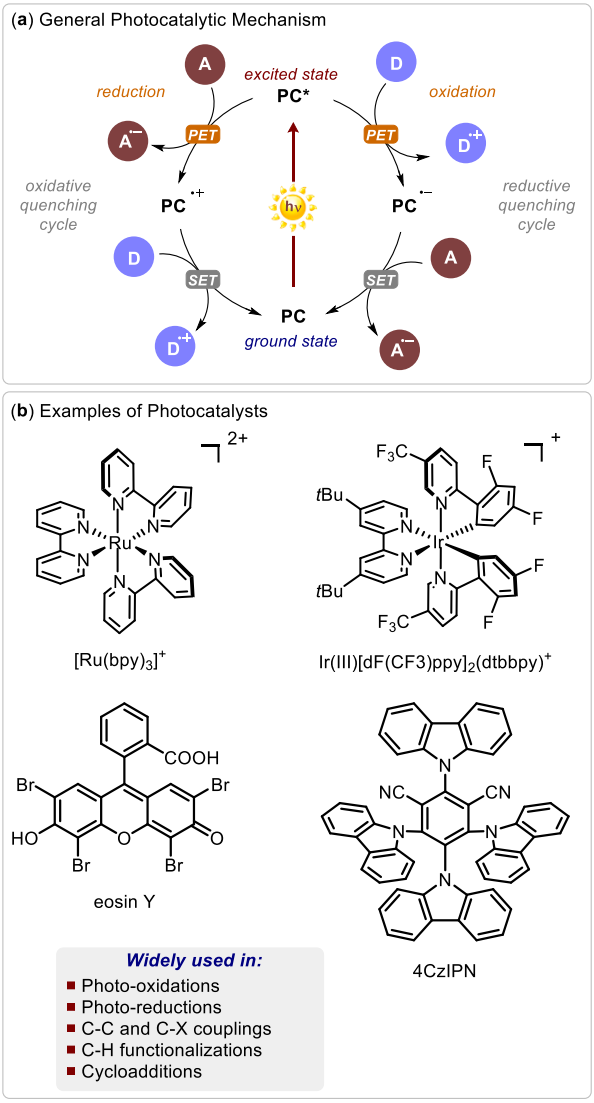

Figure 6. (**a**) General oxidative and reduction quenching cycles for a photocatalytic reaction. (**b**) Some examples of the most employed metal-based and metal-free photocatalysts.

Apart from electron transfer, the photocatalyst (PC) can undergo other two possible bimolecular pathways, namely energy transfer and atom transfer. The energy transfer process consists of the deactivation of the excited-state photocatalyst (PC*) through the excitation of the ground-state substrate. This event is commonly known as *photosensitization* and allows the indirect excitation of a molecule that can not absorb the incident photons.[67] The energy transfer mechanism is frequent in Nature, since has a key role in photosynthesis.[68] The other possible bimolecular PC* deactivation involves the generation of open-shell species through hydrogen atom transfer (HAT) from ground-

state compounds. HAT is defined as the concerted movement of a proton and an electron between two substrates in a single kinetic step. This is a typical mode of catalysis for some families of aromatic ketones, polyoxometalates and uranyl cations as PC.[69]

1.2.5 Other Light-harvesting Scenarios: Direct Substrate Photoexcitation and Electron Donor-Acceptor (EDA) Complexes

In the field of synthetic photochemistry, not only the PC can harvest the energy of the incident photons to drive photochemical transformations. Indeed, other two different scenarios can be at play.[38] In the simplest case, as anticipated in Section 1.2.1, a reaction substrate (S) directly absorbs the light and prompts the formation of the product (P). For instance, this happens in the Paternò-Büchi reaction, where an aldehyde absorbs UV light before reacting with an olefin to provide the corresponding oxetane (Figure 7a).[70] A similar approach is followed in [2+2] photocycloadditions, that represent a common way to access carbocyclic products,[71] or in the alkylation of photoenols through unconventional Michael-type addition manifolds.[72] Alternatively, the light radiation can be absorbed by a colored molecular association of two or more species, transiently generated in the ground-state. This new chemical entity is called electron donor-acceptor (EDA) complex and it is held together by non-covalent interactions between an electron-rich donor (D) and an electron-poor acceptor (A).[73,74] The EDA complex is characterized by a new absorption band, typically in the visible region. Importantly, taken individually, D and A usually are not colored, and this new band appears only when is present their associated form. Therefore, the EDA complex can be excited with a light of appropriate wavelength. When this occurs, a PET from the HOMO of D to the LUMO of the A leads to the formation of radicals or radical ions. Lastly, these highly reactive species can evolve through the formation of the desired products. Conversely, in some cases, these radical ion pairs may also return to the initial state through a rapid back-electron transfer (BET) process. This happens when BETs are faster with respect to all other processes ($k_{BET} > k_P$). In fact, the synthetic utility of EDA complexes has been limited until the last decade.[75] Indeed, in 2013, Melchiorre's group paved the way for their utilization in synthetic photochemistry through a seminal work which described the α-alkylation of aldehydes by means of the photochemical activity of an EDA complex.[76] This key intermediate was generated upon aggregation of an electron-rich enamine, formed by condensation of the aldehydes with an aminocatalyst, and an electron-poor benzyl bromide (Figure 7b). Thereafter, a variety of examples on the utilization of colored EDA complexes in synthetic photochemistry has been reported, providing new opportunity within this field.[77] Among them, in the most relevant case-studies the donors are usually electron-rich arenes, amines, enamines or enolates, whereas the acceptors are typically electron-poor arenes, alkyl halides, boronic acids, iminium ions and so on.[73,75,77,78]

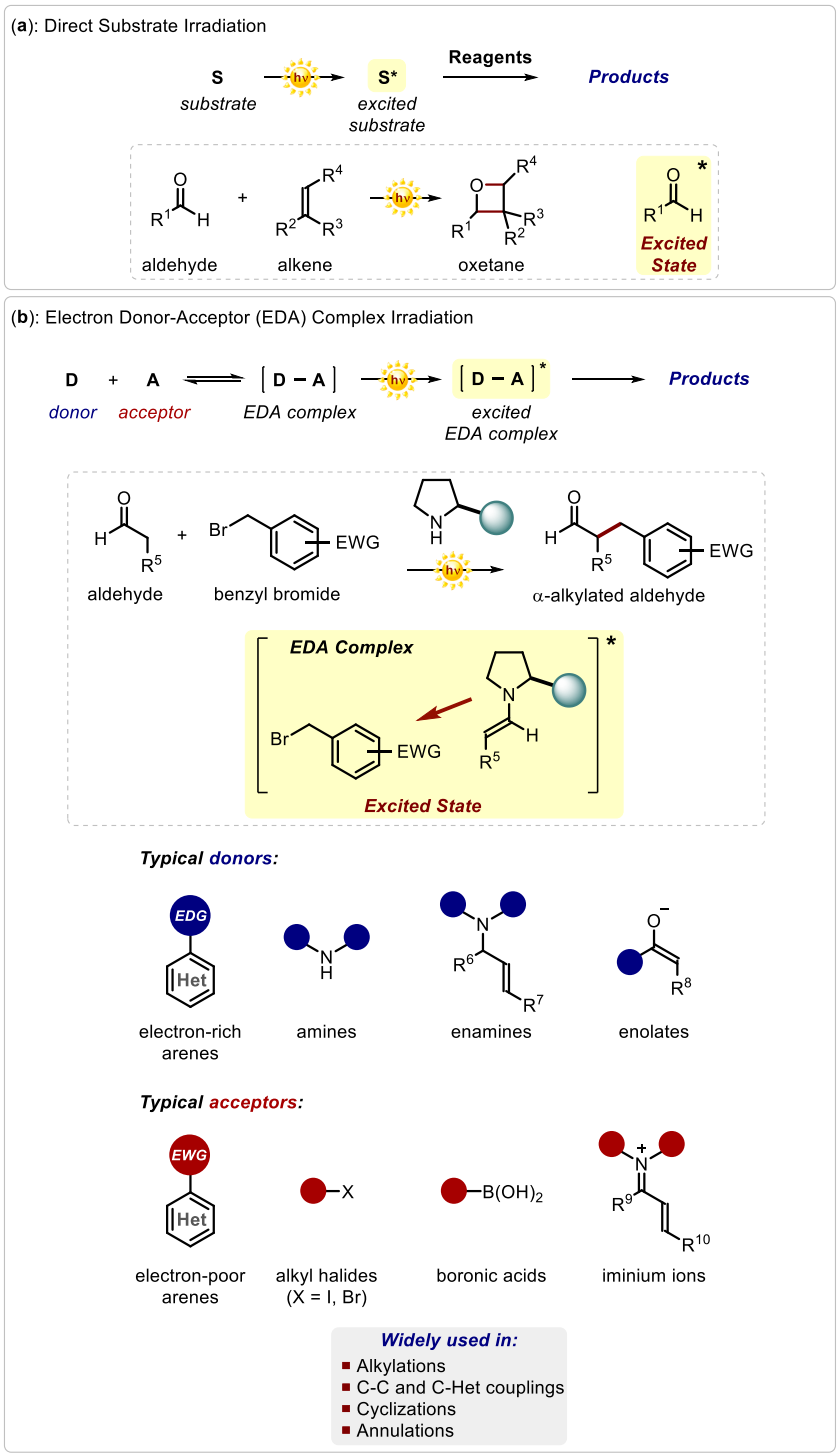

Figure 7. Ground-state species that can harvest the energy of incident photons. (**a**) Direct irradiation of the reaction substrate with the Paternò-Büchi example. (**b**) Irradiation of an electron donor-acceptor complex with the photo-organocatalytic α-alkylation of aldehydes example and the typical donor and acceptors employed in this approach. EDG = electron-donating group. EWG = electron-withdrawing group.

In this thesis work, the photochemical activity of EDA complexes has been extensively exploited in different catalytic systems in order to prompt synthetically relevant C-C bond forming reactions. These results are depicted in the following chapters (Chapter II-III).

1.2.6 Mechanistic Investigation of Photochemical Transformations

Mechanistic studies are instrumental in guiding the development of synthetically useful photochemical transformations.[64] In this section are briefly presented the main mechanistic experiments that are commonly carried out during the study of a light-driven reaction, with particular attention towards those related with this thesis.

In every photochemical transformation, the first event that occurs is the absorption of light from a ground-state molecule to give an electronically excited state. Indeed, the initial studies are usually focused on the ground-state features of the light absorbers by using ultraviolet-visible (UV/Vis) spectroscopy. In this way, the chromophore can be identified, and the corresponding irradiation wavelength can be carefully chosen to selectively excite the photoactive target. Besides its optical properties, the electrochemical features of the chromophore may be determined through cyclic voltammetry measurements. Thereby, knowing its redox potential value, is possible to appropriately select the reaction partners needed to design the whole photochemical process.

As anticipated, the analysis of the radiative deactivation of the excited state *via* fluorescence or phosphoresce can provide significant mechanistic information. Specifically, the excitation energy (E_{00}) can be spectroscopically estimated according to the Rehm-Weller theory (*vide supra*, *eq*. 9). Furthermore, a powerful tool to clarify the interaction of excited-state species with other reaction components is undeniably Stern-Volmer quenching analysis, which can be performed with a simple spectrofluorometer. In particular, a decrease in intensity of emission (quenching) occurs when an excited-state molecule is deactivated by collision with another species (quencher). Although this approach cannot discriminate between energy-transfer and electron-transfer processes, it can nevertheless give helpful clues for elucidating the mechanism of a photochemical reaction.[64]

A central point in this thesis work is related to the identification and characterization of ground-state aggregates, namely EDA complexes. Indeed, even if transiently generated under the experimental conditions, they are relatively stable to be studied by common analytical techniques, such as UV/Vis spectroscopy, nuclear magnetic resonance (NMR) titration experiments or computational calculations. Occasionally, it is even possible to isolate the bench-stable EDA complexes and determining their exact structure by X-ray diffraction.[73] By exploiting the mentioned characterization methods, the stoichiometry and the association constant (K_{EDA}) of these complexes can be evaluated *via* a Job's plot analysis.[79]

1.2.7 Continuous Flow Photochemistry

One of the notable benefits of synthetic photochemistry is its broad applicability in the preparation of valuable organic compounds of great industrial interest.[52] In particular, the typical efficient, mild and sustainable methodologies developed within the field of photocatalysis turned out to be very attractive for large-scale chemical productions, primarily for the pharmaceutical industry.[56] However, photochemical transformations frequently have limited scale-up potential from laboratory to preparative scale (from milligrams to multi-grams or even kilograms). This is because they can be hampered by significant light attenuation, as the size of a reaction vessel increases (as

described by the Beer–Lambert law).[80] Indeed, light penetration within the reaction mixture is limited by the absorption of the components and diminishes rapidly with distance from the lamp.[81,82] Continuous flow photochemistry can overcome this limitation by using a short irradiated path length, which, when combined with the correct light source, can improve photochemical efficiency, leading to shorter reaction times and higher productivity (Figure 8a).[82–86] Therefore, the abovementioned pharmaceutical industry is increasingly adopting flow chemistry, and in particular photocatalysis, to achieve the preparation of large amounts of relevant compounds in a safe, effective and viable manner (Figure 8b).[87,88]

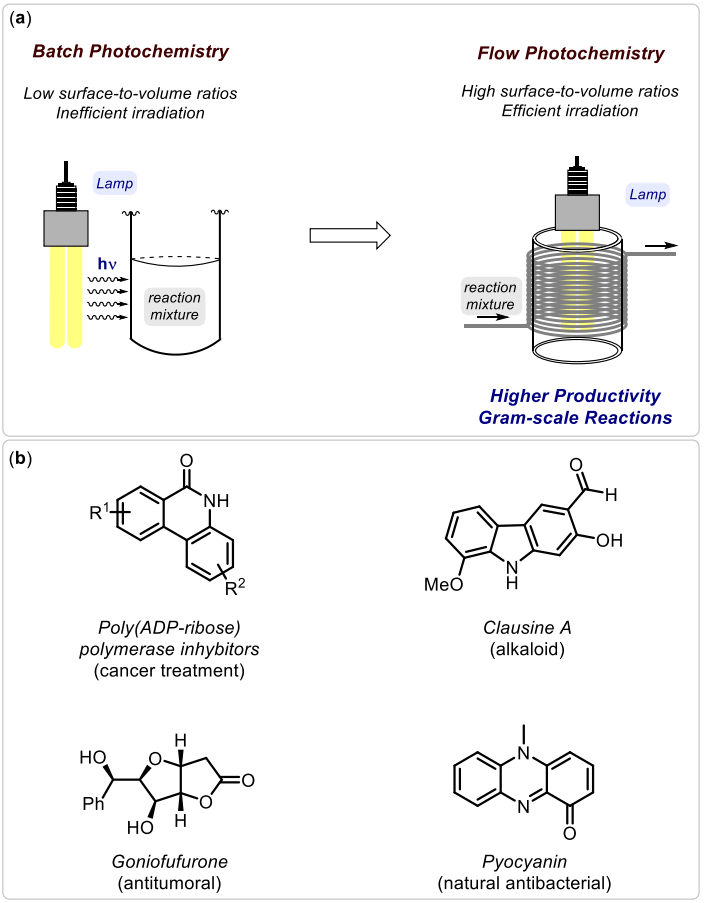

Figure 8. (**a**) Batch photochemistry *vs* flow photochemistry. (**b**) Representative examples of pharmaceutical compounds obtained at preparative scale by means of flow photochemistry.

To this aim, two distinct sections of this thesis are dedicated to translating the previously developed batch photochemical methodologies into continuous flow. Thus, the facile production of benchmark pharmaceutical intermediates in multi-gram scale is herein showed. These results are depicted in the Chapters II, V.

1.3 Nanocatalysis

1.3.1 Carbon-based Nanomaterials as Nanocatalysts

Carbon-based nanomaterials (CNMs) play a key role in the field of nanotechnology. In fact, the discovery of fullerenes in 1985 represented a breakthrough in the study of nanomaterials.[89] Fullerene C_{60} is the first molecular CNM made only of a discrete number of carbon atoms. After the identification of fullerenes, new carbon-based nanoforms have been identified in the CNMs family: carbon nanotubes,[90,91] graphene,[92] and more recently, carbon dots (CDs).[93] Successively, a number of more exotic nanoforms have been discovered.[94] All these materials can be classified through the dimensional class which they belong, namely 0D (e.g., fullerenes and carbon dots), 1D (e.g., carbon nanotubes), 2D (e.g., graphene) or 3D (e.g., graphite, Figure 9).[95,96] In recent times, CNMs have attracted the attention of the scientific community due to their physicochemical features and diversity in structure and morphology. However, a main drawback of CNMs in their pristine form is their difficult manipulation and strong tendency to aggregate in most common solvents.[97] Importantly, the features of these carbon-based nanostructures can be readily fine-tuned through the chemical functionalization of their surfaces, improving their valuable properties and allowing their employment in different technological applications, ranging from catalysis to optoelectronics and nanomedicine.[97–100]

In particular, within the field of catalysis, the term *nanocatalysis* refers to the use of nanosized catalysts (in the range of 1-100 nm) to carry out chemical transformations.[101] Originally, most of the reported nanocatalytic processes were driven by metal nanoparticles,[101,102] while CNMs were merely employed as supports for heterogeneous catalysis.[95,96] Nowadays, functionalized CNMs can actively take part to the catalytic cycle through various chemical interactions between their surface functionalities and the reaction components.[96] As a result, functionalized CNMs are no longer acting just as classical inert supports, but may also determine the reaction outcome. Moreover, the growing attention towards the implementation of green and sustainable methodologies further prompted the development of metal-free nanocatalytic systems.[103–105] Modified CNMs can therefore represent a promising platform that fulfill these requirements of nontoxic, readily available, and potentially recyclable catalysts for green chemical production.[106] To this aim, rational design and careful surface derivatizations of CNMs is pivotal to ensure the effectiveness of the catalytic transformations. Thus, both polar and light-driven radical processes of synthetical importance can currently be carried out by means of carbon-based nanocatalysts.[96,100,107–109]

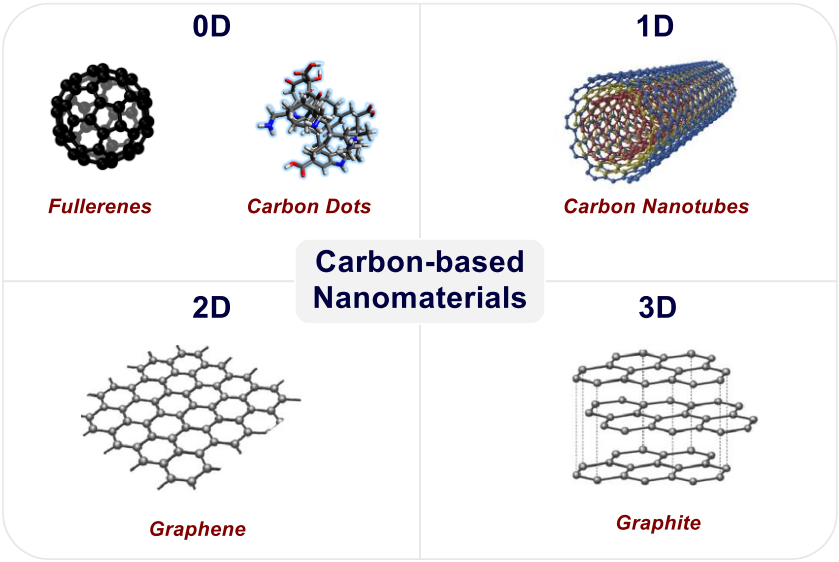

Figure 9. Classification of the most common carbon nanoforms based on their dimensionality.

1.3.2 Nano-organocatalysis

Among all the metal-free carbon-based nanostructured catalysts described in literature so far, some representative examples for organocatalysis are depicted in Figure 10. For instance, functionalized CNMs have been used in organocatalytic aldol, Michael and Knoevenagel reactions, even in enantioselective fashion, by following the general activation modes described in Section 1.1.[110–112]

Specifically, carbon dots (CDs) represent a potential platform in the field of nano-organocatalysis.[100] They consist of carbon cores that can be surrounded by shells containing numerous polar groups. The nature of these heteroatom functionalities arises from the precursors and the operative conditions employed in the CD synthesis. These surface groups play a pivotal role in determining the overall chemical behavior of the nanoparticles. The ever-growing popularity of these nanoparticles is substantiated by their fast and facile preparation from economic raw materials (including natural renewable sources or waste), their scalability for large-scale productions, and their tailorable surfaces. Explicitly, the presence of reactive surface groups on CDs have paved the way to new catalytic possibilities, enabling the preparation of valuable organic compounds under mild and green operating conditions by means of classical polar reactivities.[100,113,114] However, despite their high potential, only exploratory applications of CDs as nano-organocatalysts have been reported in the important branch of aminocatalysis.[100]

To this aim, in the present thesis work, nitrogen-doped CDs have been exploited to trigger synthetically relevant C-C and C-heteroatom bond forming reactions, *via* enamine and iminium ion activation. As anticipated in the previous sections, the key catalytic intermediates were generated on the surface of these amine-rich nanomaterials. Moreover, this concept has been extended to chiral carbon nanoparticles to carry out enantioselective aminocatalytic transformations. These results are depicted in the following chapters (Chapter IV).

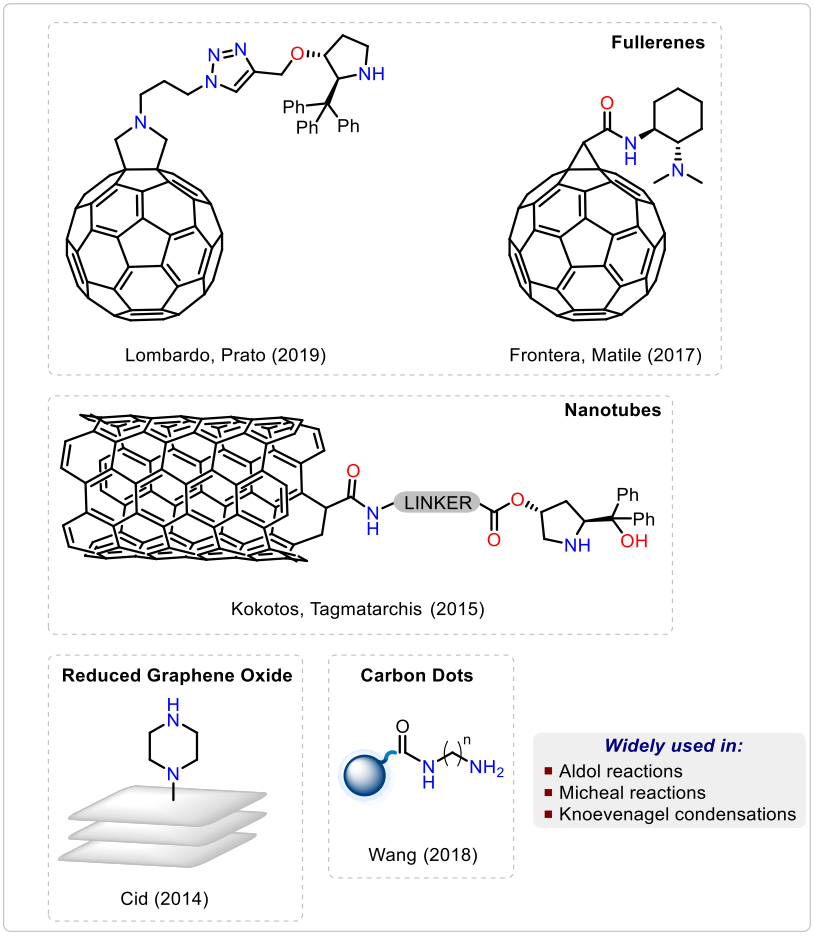

Figure 10. Selected examples of carbon-based nano-organocatalysts for the most common organocatalytic transformations.

1.3.3 Nano-photocatalysis

Besides, light-driven transformations triggered by nano-sized photocatalysts, particularly functionalized CNMs, are becoming ever more important in synthetic chemistry. In fact, several classes of modified CNMs show excellent optoelectronic properties, along with low toxicity, facile preparation and potential recyclability. Therefore, they are emerging as promising nano-photocatalytic platforms for a wide range of radical reactions.

Specifically, efficient nanosized carbon-based photocatalysts that behave as semiconductor-like materials, typically show strong light absorption. This event causes the excitation of electrons from the valence band (VB) to the conduction band (CB), with consequent charge separation (electrons and holes). Depending on the specific energy positions of the VB and CB, the considered photocatalysts may provide sufficiently high redox potential and abundant surface sites to induce the desired transformations.[115,116] It is worth notice that solid-phase semiconductor-like photocatalysts are capable of generating both oxidizing and reducing species on the same single particle and at the same time. These materials are therefore suitable for the application in organic synthesis through oxidative or reductive pathways (Figure 11a).[117]

Among all the photoactive CNM derivatives, two families are undeniably the most popular in synthetic photochemistry. These are represented by carbon dots (CDs) and carbon nitrides (CNs, Figure 11b).[100,107,108] In addition to the abovementioned properties, CDs are optically active CNMs capable of absorbing UV/Vis light and releasing such energetic surplus through a bright fluorescence or by prompting radical processes. Additionally, the tailorable surface of CDs has a key role in determining the overall photochemical reactivity of the nanoparticles.[118] In fact, various heteroatom-doped CDs may found, in principle, application in different photoredox transformations.[100] However, despite their unique physical and chemical features, not so many of these applications involve synthetic photochemistry at present.[100] In this regard, in the present thesis, photoactive nitrogen-doped CDs have been utilized to trigger important C-C bond forming reactions under light irradiation. These results are described in the following chapters (Chapter III).

Carbon nitrides (CNs) are a relevant class of visible light-absorbing metal-free polymeric semiconductors that mostly consists of carbon and nitrogen.[119] Concerning their redox features, the position of VB and CB can be modulated on the basis of C/N ratio, polymerization degree (for example adding inorganic salts during the preparation), crystallinity and through the use of suitable of doping agents.[107,120–122] Moreover, CNs can be straightforwardly prepared from economic molecular precursors (e.g. melamine, urea, cyanamide) and, primarily, they are robust and easy to recover and reuse multiple time without any deterioration.[121] Therefore, CNs have found widespread application in many relevant photocatalytic radical reactions.[107,108] Considering the potential industrial relevance of some of these transformations, a continuous flow scale-up would be highly desirable, as explained in Section 1.2.7. However, the use of solid compounds, such as CN photocatalysts, in a flow setup remains one of the central challenges in continuous processing.[123] Therefore, in this thesis we investigated a way to tackle this issue by means of an innovative pulsation-based flow system design that allows the formation of a stable suspension of the photocatalyst, circumventing clogging of the photoreactor. These results are described in the following chapters (Chapter V).

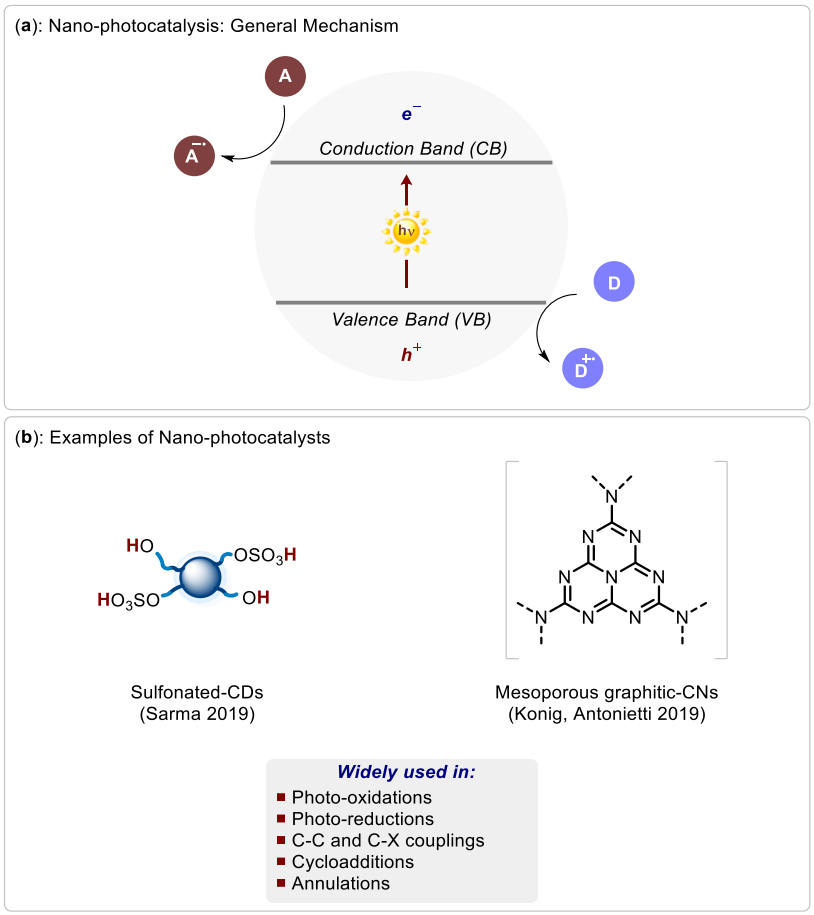

Figure 11. (**a**) General photocatalytic mechanism of heterogeneous nano-photocatalysts. (**b**) Examples of CDs and CNs as nano-photocatalysts.

1.4 References Chapter I

(1) McNaught, A. D.; Wilkinson, A. *IUPAC. Compendium of Chemical Terminology, 2nd Ed. (the "Gold Book")*; Blackwell Scientific Publications, Oxford, 1997.

(2) Jencks, W. P. *Catalysis in Chemistry and Enzymology*; Dover, 1987.

(3) Busacca, C. A.; Fandrick, D. R.; Song, J. J.; Senanayake, C. H. The Growing Impact of Catalysis in the Pharmaceutical Industry. *Adv. Synth. Catal.* **2011**, *353*, 1825–1864.

(4) Schlögl, R. Catalysis 4.0. *ChemCatChem* **2017**, *9*, 533–541.

(5) Armor, J. N. A History of Industrial Catalysis. *Catal. Today* **2011**, *163*, 3–9.

(6) De Vries, J. G.; Jackson, S. D. Homogeneous and Heterogeneous Catalysis in Industry. *Catal. Sci. Technol.* **2012**, *2*, 2009.

(7) Michaudel, Q.; Ishihara, Y.; Baran, P. S. Academia-Industry Symbiosis in Organic Chemistry. *Acc. Chem. Res.* **2015**, *48*, 712–721.

(8) MacMillan, D. W. C. The Advent and Development of Organocatalysis. *Nature* **2008**, *455*, 304–308.

(9) Dalko, P. I.; Moisan, L. In the Golden Age of Organocatalysis. *Angew. Chem. Int. Ed.* **2004**, *43*, 5138–5175.

(10) Wende, R. C.; Schreiner, P. R. Evolution of Asymmetric Organocatalysis: Multi- and Retrocatalysis. *Green Chem.* **2012**, *14*, 1821–1849.

(11) Du, Z.; Shao, Z. Combining Transition Metal Catalysis and Organocatalysis – an Update. *Chem. Soc. Rev.* **2013**, *42*, 1337–1378.

(12) Romero, N. A.; Nicewicz, D. A. Organic Photoredox Catalysis. *Chem. Rev.* **2016**, *116*, 10075–10166.

(13) Twilton, J.; Le, C. C.; Zhang, P.; Shaw, M. H.; Evans, R. W.; MacMillan, D. W. C. The Merger of Transition Metal and Photocatalysis. *Nat. Rev. Chem.* **2017**, *1*, 0052.

(14) Shaw, M. H.; Twilton, J.; MacMillan, D. W. C. Photoredox Catalysis in Organic Chemistry. *J. Org. Chem.* **2016**, *81*, 6898–6926.

(15) Melchiorre, P.; Marigo, M.; Carlone, A.; Bartoli, G. Asymmetric Aminocatalysis - Gold Rush in Organic Chemistry. *Angew. Chem. Int. Ed.* **2008**, *47*, 6138–6171.

(16) Bertelsen, S.; Jørgensen, K. A. Organocatalysis—after the Gold Rush. *Chem. Soc. Rev.* **2009**, *38*, 2178–2189.

(17) Seayad, J.; List, B. Asymmetric Organocatalysis. *Org. Biomol. Chem.* **2005**, *3*, 719–724.

(18) Berkessel, A.; Gröger, H. *Asymmetric Organocatalysis: From Biomimetic Concepts to Applications in Asymmetric Synthesis*; Wiley-VCH, 2005.

(19) List, B. The Ying and Yang of Asymmetric Aminocatalysis. *Chem. Commun.* **2006**, 819–824.

(20) Beeson, D. T.; Mastracchio, A.; Hong, J.-B.; Ashton, K.; MacMillan, D. W. C. Enantioselective Organocatalysis Using SOMO Activation. *Science* **2007**, *316*, 582–586.

(21) Gaunt, M. J.; Johansson, C. C. C. Recent Developments in the Use of Catalytic Asymmetric Ammonium Enolates in Chemical Synthesis. *Chem. Rev.* **2007**, *107*, 5596–5605.

(22) Hepburn, H. B.; Dell'Amico, L.; Melchiorre, P. Enantioselective Vinylogous Organocascade Reactions. *Chem. Rec.* **2016**, 1787–1806.

(23) Bugaut, X.; Glorius, F. Organocatalytic Umpolung: N-Heterocyclic Carbenes and Beyond. *Chem. Soc. Rev.* **2012**, *41*, 3511–3522.

(24) Taylor, M. S.; Jacobsen, E. N. Asymmetric Catalysis by Chiral Hydrogen-Bond Donors. *Angew.*

Chem. Int. Ed. **2006**, *45*, 1520–1543.

(25) Brak, K.; Jacobsen, E. N. Asymmetric Ion-Pairing Catalysis. *Angew. Chem. Int. Ed.* **2013**, *52*, 534–561.

(26) Eder, U.; Sauer, G.; Wiechert, R. New Type of Asymmetric Cyclization to Optically Active Steroid CD Partial Structures. *Angew. Chem. Int. Ed.* **1971**, *10*, 496–497.

(27) Hajos, Z. G.; Parrish, D. R. Asymmetric Synthesis of Bicyclic Intermediates of Natural Product Chemistry. *J. Org. Chem.* **1974**, *39*, 1615–1621.

(28) List, B.; Lerner, R. a; Barbas III, C. F. Proline-Catalyzed Direct Asymmetric Aldol Reactions. *J. Am. Chem. Soc.* **2000**, *122*, 2395–2396.

(29) Ahrendt, K. A.; Borths, C. J.; Macmillan, D. W. C. New Strategies for Organic Catalysis: The First Highly Enantioselective Organocatalytic Diels-Alder Reaction. *J. Am. Chem. Soc.* **2000**, *122*, 4243–4244.

(30) Lelais, G.; MacMillan, D. W. C. Modern Strategies in Organic Catalysis: The Advent and Development of Iminium Activation. *Aldrichimica Acta* **2006**, *39*, 79–87.

(31) Erkkilä, A.; Majander, I.; Pihko, P. M. Iminium Catalysis. *Chem. Rev.* **2007**, *107*, 5416–5470.

(32) Mukherjee, S.; Yang, J. W.; Hoffmann, S.; List, B. Asymmetric Enamine Catalysis. *Chem. Rev.* **2007**, *107*, 5471–5569.

(33) Melchiorre, P. Cinchona-Based Primary Amine Catalysis in the Asymmetric Functionalization of Carbonyl Compounds. *Angew. Chem. Int. Ed.* **2012**, *51*, 9748–9770.

(34) Yoon, T. P.; Jacobsen, E. N. Privileged Chiral Catalysts. *Science* **2003**, *299*, 1691–1693.

(35) Alemán, J.; Cabrera, S. Applications of Asymmetric Organocatalysis in Medicinal Chemistry. *Chem. Soc. Rev.* **2013**, *42*, 774–793.

(36) Sahoo, B. M.; Banik, B. K. Organocatalysis: Trends of Drug Synthesis in Medicinal Chemistry. *Curr. Organocatalysis* **2019**, *6*, 92–105.

(37) Ciamician, G. The Photochemistry of the Future. *Science* **1912**, *36*, 385.

(38) Albini, A.; Fagnoni, M. *Handbook of Synthetic Photochemistry*; 2010.

(39) Fagnoni, M.; Dondi, D.; Ravelli, D.; Albini, A. Photocatalysis for the Formation of the C−C Bond. *Chem. Rev.* **2007**, *107*, 2725–2756.

(40) Ravelli, D.; Fagnoni, M.; Albini, A. Photoorganocatalysis. What For? *Chem. Soc. Rev.* **2013**, *42*, 97–113.

(41) Nicewicz, D. A.; Macmillan, D. W. C. Merging Photoredox Catalysis with Organocatalysis: The Direct Asymmetric Alkylation of Aldehydes. *Science* **2008**, *322*, 77–80.

(42) Ischay, M. A.; Anzovino, M. E.; Du, J.; Yoon, T. P. Efficient Visible Light Photocatalysis of [2+2] Enone Cycloadditions. *J. Am. Chem. Soc.* **2008**, *130*, 12886–12887.

(43) Narayanam, J. M. R.; Tucker, J. W.; Stephenson, C. R. J. Electron-Transfer Photoredox Catalysis: Development of a Tin-Free Reductive Dehalogenation Reaction. *J. Am. Chem. Soc.* **2009**, *131*, 8756–8757.

(44) Narayanam, J. M. R.; Stephenson, C. R. J. Visible Light Photoredox Catalysis: Applications in Organic Synthesis. *Chem. Soc. Rev.* **2011**, *40*, 102–113.

(45) Prier, C. K.; Rankic, D. A.; MacMillan, D. W. C. Visible Light Photoredox Catalysis with Transition Metal Complexes: Applications in Organic Synthesis. *Chem. Rev.* **2013**, *113*, 5322–5363.

(46) Reckenthäler, M.; Griesbeck, A. G. Photoredox Catalysis for Organic Syntheses. *Adv. Synth. Catal.* **2013**, *355*, 2727–2744.

(47) Wang, C. S.; Dixneuf, P. H.; Soulé, J. F. Photoredox Catalysis for Building C-C Bonds from C(Sp2)-H Bonds. *Chem. Rev.* **2018**, *118*, 7532–7585.

(48) Silvi, M.; Melchiorre, P. Enhancing the Potential of Enantioselective Organocatalysis with Light. *Nature* **2018**, *554*, 41–49.

(49) König, B. Photocatalysis in Organic Synthesis – Past, Present, and Future. *Eur. J. Org. Chem.* **2017**, 1979–1981.

(50) Petzold, D.; Giedyk, M.; Chatterjee, A.; König, B. A Retrosynthetic Approach for Photocatalysis. *Eur. J. Org. Chem.* **2020**, No. 10, 1193–1244.

(51) Douglas, J. J.; Sevrin, M. J.; Stephenson, C. R. J. Visible Light Photocatalysis: Applications and New Disconnections in the Synthesis of Pharmaceutical Agents. *Org. Process Res. Dev.* **2016**, *20*, 1134–1147.

(52) Blakemore, D. C.; Castro, L.; Churcher, I.; Rees, D. C.; Thomas, A. W.; Wilson, D. M.; Wood, A. Organic Synthesis Provides Opportunities to Transform Drug Discovery. *Nat. Chem.* **2018**, *10*, 383–394.

(53) Gust, D.; Moore, T. A.; Moore, A. L. Solar Fuels via Artificial Photosynthesis. *Acc. Chem. Res.* **2009**, *42*, 1890–1898.

(54) Konig, B. *Chemical Photocatalysis*; 2013.

(55) Marzo, L.; Pagire, S. K.; Reiser, O.; König, B. Visible-Light Photocatalysis: Does It Make a Difference in Organic Synthesis? *Angew. Chem. Int. Ed.* **2018**, *57*, 10034–10072.

(56) Crisenza, G. E. M.; Melchiorre, P. Chemistry Glows Green with Photoredox Catalysis. *Nat. Commun.* **2020**, *11*, 8–11.

(57) Amos, S. G. E.; Garreau, M.; Buzzetti, L.; Waser, J. Photocatalysis with Organic Dyes: Facile Access to Reactive Intermediates for Synthesis. *Beilstein J. Org. Chem.* **2020**, *16*, 1163–1187.

(58) Balzani, V.; Ceroni, P.; Juris, A. *Photochemistry and Photophysics: Concepts, Research, Applications*; Wiley & Sons, 2014.

(59) Kavarnos, G. J. *Fundamentals of Photoinduced Electron Transfer*; VCH, Weinheim, New York, 1993.

(60) Pitre, S. P.; McTiernan, C. D.; Scaiano, J. C. Understanding the Kinetics and Spectroscopy of Photoredox Catalysis and Transition-Metal-Free Alternatives. *Acc. Chem. Res.* **2016**, *49*, 1320–1330.

(61) Marcus, R. A. Electron Transfer Reactions in Chemistry: Theory and Experiment. *Rev. Mod. Phys.* **1993**, *65*, 599.

(62) Rehm, D.; Weller, A. Kinetics of Fluorescence Quenching by Electron and H-Atom Transfer. *Isr. J. Chem.* **1970**, *8*, 259–271.

(63) Farid, S.; Dinnocenzo, J. P.; Merkel, P. B.; Young, R. H.; Shukla, D.; Guirado, G. Reexamination of the Rehm-Weller Data Set Reveals Electron Transfer Quenching That Follows a Sandros-Boltzmann Dependence on Free Energy. *J. Am. Chem. Soc.* **2011**, *133*, 11580–11587.

(64) Buzzetti, L.; Crisenza, G. E. M.; Melchiorre, P. Mechanistic Studies in Photocatalysis. *Angew. Chem. Int. Ed.* **2019**, *58*, 3730–3747.

(65) Yoon, T. P.; Ischay, M. A.; Du, J. Visible Light Photocatalysis as a Greener Approach to Photochemical Synthesis. *Nat. Chem.* **2010**, *2*, 527–532.

(66) Stephenson, C. R. J.; Yoon, T. P.; MacMillan, D. W. C. *Visible Light Photocatalysis in Organic Chemistry*; 2018.

(67) Strieth-Kalthoff, F.; James, M. J.; Teders, M.; Pitzer, L.; Glorius, F. Energy Transfer Catalysis

Mediated by Visible Light: Principles, Applications, Directions. *Chem. Soc. Rev.* **2018**, *47*, 7190–7202.

(68) Govindjee; Shevela, D.; Björn, L. O. Evolution of the Z-Scheme of Photosynthesis: A Perspective. *Photosynth. Res.* **2017**, *133*, 5–15.

(69) Capaldo, L.; Ravelli, D. Hydrogen Atom Transfer (HAT): A Versatile Strategy for Substrate Activation in Photocatalyzed Organic Synthesis. *Eur. J. Org. Chem.* **2017**, *2017*, 2056–2071.

(70) Büchi, G.; Inman, C. G.; Lipinsky, E. S. Light-Catalyzed Organic Reactions. I. The Reaction of Carbonyl Compounds with 2-Methyl-2-Butene in the Presence of Ultraviolet Light. *J. Am. Chem. Soc.* **1954**, *76*, 4327–4331.

(71) Poplata, S.; Tröster, A.; Zou, Y. Q.; Bach, T. Recent Advances in the Synthesis of Cyclobutanes by Olefin [2+2] Photocycloaddition Reactions. *Chem. Rev.* **2016**, *116*, 9748–9815.

(72) Dell'Amico, L.; Fernández-Alvarez, V. M.; Maseras, F.; Melchiorre, P. Light-Driven Enantioselective Organocatalytic β-Benzylation of Enals. *Angew. Chem. Int. Ed.* **2017**, *56*, 3304–3308.

(73) Yuan, Y.; Majumder, S.; Yang, M.; Guo, S. Recent Advances in Catalyst-Free Photochemical Reactions via Electron-Donor-Acceptor (EDA) Complex Process. *Tetrahedron Lett.* **2020**, *61*, 151506.

(74) Mulliken, R. S. Structures of Complexes Formed by Halogen Molecules with Aromatic and with Oxygenated Solvents. *J. Am. Chem. Soc.* **1950**, *72*, 600–608.

(75) Lima, C. G. S.; Lima, T. D. M.; Duarte, M.; Jurberg, I. D.; Paixão, M. W. Organic Synthesis Enabled by Light-Irradiation of EDA Complexes: Theoretical Background and Synthetic Applications. *ACS Catal.* **2016**, *6*, 1389–1407.

(76) Arceo, E.; Jurberg, I. D.; Álvarez-Fernández, A.; Melchiorre, P. Photochemical Activity of a Key Donor-Acceptor Complex Can Drive Stereoselective Catalytic α-Alkylation of Aldehydes. *Nat. Chem.* **2013**, *5*, 750–756.

(77) Crisenza, G. E. M.; Mazzarella, D.; Melchiorre, P. Synthetic Methods Driven by the Photoactivity of Electron Donor-Acceptor Complexes. *J. Am. Chem. Soc.* **2020**, *142*, 5461–5476.

(78) Cao, Z.; Ghosh, T.; Melchiorre, P. Enantioselective Radical Conjugate Additions Driven by a Photoactive Intramolecular Iminium-Ion-Based EDA Complex. *Nat. Commun.* **2018**.

(79) Job, P. Formation and Stability of Inorganic Complexes in Solution. *Ann. Chim. Appl.* **1928**, *9*, 113–203.

(80) Cambié, D.; Bottecchia, C.; Straathof, N. J. W.; Hessel, V.; Noël, T. Applications of Continuous-Flow Photochemistry in Organic Synthesis, Material Science, and Water Treatment. *Chem. Rev.* **2016**, *116*, 10276–10341.

(81) Knowles, J. P.; Elliott, L. D.; Booker-Milburn, K. I. Flow Photochemistry: Old Light through New Windows. *Beilstein J. Org. Chem.* **2012**, *8*, 2025–2052.

(82) Plutschack, M. B.; Pieber, B.; Gilmore, K.; Seeberger, P. H. The Hitchhiker's Guide to Flow Chemistry. *Chem. Rev.* **2017**, *117*, 11796–11893.

(83) Politano, F.; Oksdath-Mansilla, G. Light on the Horizon: Current Research and Future Perspectives in Flow Photochemistry. *Org. Process Res. Dev.* **2018**, *22*, 1045–1062.

(84) Noël, T. A Personal Perspective on the Future of Flow Photochemistry. *J. Flow Chem.* **2017**, *7*, 87–93.

(85) Su, Y.; Straathof, N. J. W.; Hessel, V.; Noël, T. Photochemical Transformations Accelerated in Continuous-Flow Reactors: Basic Concepts and Applications. *Chem. Eur. J.* **2014**, *20*, 10562–

10589.

(86) Elliott, L. D.; Knowles, J. P.; Koovits, P. J.; Maskill, K. G.; Ralph, M. J.; Lejeune, G.; Edwards, L. J.; Robinson, R. I.; Clemens, I. R.; Cox, B.; Pascoe, D. D.; Koch, G.; Eberle, M.; Berry, M. B.; Booker-Milburn, K. I. Batch versus Flow Photochemistry: A Revealing Comparison of Yield and Productivity. *Chem. Eur. J.* **2014**, *20*, 15226–15232.

(87) Porta, R.; Benaglia, M.; Puglisi, A. Flow Chemistry: Recent Developments in the Synthesis of Pharmaceutical Products. *Org. Process Res. Dev.* **2016**, *20*, 2–25.

(88) Di Filippo, M.; Bracken, C.; Baumann, M. Continuous Flow Photochemistry for the Preparation of Bioactive Molecules. *Molecules* **2020**, *25*, 356.

(89) Kroto, H. W.; Heath, J. R.; O'Brien, S. C.; Curl, R. F.; Smalley, R. E. C60: Buckminsterfullerene. *Nature* **1985**, *318*, 162–163.

(90) Iijima, S. Helical Microtubules of Graphitic Carbon. *Nature* **1991**, *354*, 56–58.

(91) Iijima, S.; Ichihashi, T. Single-Shell Carbon Nanotubes of 1-Nm Diameter. *Nature* **1993**, *363*, 603–605.

(92) Novoselov, K. S.; Geim, A. K.; Morozov, S. V.; Jiang, D.; Zhang, Y.; Dubonos, S. V.; Grigorieva, I. V.; Firsov, A. A. Electric Field Effect in Atomically Thin Carbon Films. *Science* **2004**, *306*, 666–669.

(93) Xu, X.; Ray, R.; Gu, Y.; Ploehn, H. J.; Gearheart, L.; Raker, K.; Scrivens, W. A. Electrophoretic Analysis and Purification of Fluorescent Single-Walled Carbon Nanotube Fragments. *J. Am. Chem. Soc.* **2004**, *126*, 12736–12737.

(94) Georgakilas, V.; Perman, J. A.; Tucek, J.; Zboril, R. Broad Family of Carbon Nanoallotropes: Classification, Chemistry, and Applications of Fullerenes, Carbon Dots, Nanotubes, Graphene, Nanodiamonds, and Combined Superstructures. *Chem. Rev.* **2015**, *115*, 4744–4822.

(95) Campisciano, V.; Gruttadauria, M.; Giacalone, F. Modified Nanocarbons for Catalysis. *ChemCatChem* **2019**, *11*, 90–133.

(96) Campisciano, V.; Gruttadauria, M.; Giacalone, F. Modified Nanocarbons as Catalysts in Organic Processes. In *Catalyst Immobilization*; Wiley-VCH, 2020; pp 77–113.

(97) Vázquez, E.; Giacalone, F.; Prato, M. Non-Conventional Methods and Media for the Activation and Manipulation of Carbon Nanoforms. *Chem. Soc. Rev.* **2014**, *43*, 58–69.

(98) Martín, N. Carbon Nanoforms for Photovoltaics: Myth or Reality? *Adv. Energy Mater.* **2017**, *7*, 1–8.

(99) Reina, G.; González-Domínguez, J. M.; Criado, A.; Vázquez, E.; Bianco, A.; Prato, M. Promises, Facts and Challenges for Graphene in Biomedical Applications. *Chem. Soc. Rev.* **2017**, *46*, 4400–4416.

(100) Rosso, C.; Filippini, G.; Prato, M. Carbon Dots as Nano-Organocatalysts for Synthetic Applications. *ACS Catal.* **2020**, *10*, 8090–8105.

(101) Serp, P.; Philippot, K. *Nanomaterials in Catalysis*; Wiley-VCH, 2012.

(102) Chng, L. L.; Erathodiyil, N.; Ying, J. Y. Nanostructured Catalysts for Organic Transformations. *Acc. Chem. Res.* **2013**, *46*, 1825–1837.

(103) Simon, M. O.; Li, C. J. Green Chemistry Oriented Organic Synthesis in Water. *Chem. Soc. Rev.* **2012**, *41*, 1415–1427.

(104) Egorova, K. S.; Ananikov, V. P. Which Metals Are Green for Catalysis? Comparison of the Toxicities of Ni, Cu, Fe, Pd, Pt, Rh, and Au Salts. *Angew. Chem. Int. Ed.* **2016**, *55*, 12150–12162.

(105) Monai, M.; Melchionna, M.; Fornasiero, P. From Metal to Metal-Free Catalysts: Routes to

Sustainable Chemistry. In *Advances in Catalysis*; Academic Press, 2018; pp 1–73.

(106) Burgman, M.; Tennant, M.; Voulvoulis, N.; Makuch, K.; Madani, K. Facilitating the Transition to Sustainable Green Chemistry. *Curr. Opin. Green Sustain. Chem.* **2018**, *13*, 130–136.

(107) Mazzanti, S.; Savateev, A. Emerging Concepts in Carbon Nitride Organic Photocatalysis. *Chempluschem* **2020**, *85*, 2499–2517.

(108) Gisbertz, S.; Pieber, B. Heterogeneous Photocatalysis in Organic Synthesis. *ChemPhotoChem* **2020**, *4*, 1–21.

(109) Antonietti, M.; Lopez-Salas, N.; Primo, A. Adjusting the Structure and Electronic Properties of Carbons for Metal-Free Carbocatalysis of Organic Transformations. *Adv. Mater.* **2018**, *31*, 1805719.

(110) Chronopoulos, D. D.; Tsakos, M.; Karousis, N.; Kokotos, C. G.; Tagmatarchis, N. Fullerene-Proline Hybrids: Synthesis, Characterization and Organocatalytic Properties in Aldol Reactions. *Mater. Lett.* **2014**, *137*, 343–346.

(111) Rosso, C.; Emma, M. G.; Martinelli, A.; Lombardo, M.; Quintavalla, A.; Trombini, C.; Syrgiannis, Z.; Prato, M. A Recyclable Chiral 2-(Triphenylmethyl)Pyrrolidine Organocatalyst Anchored to [60]Fullerene. *Adv. Synth. Catal.* **2019**, *361*, 2936–2944.

(112) López-Andarias, J.; Frontera, A.; Matile, S. Anion-π Catalysis on Fullerenes. *J. Am. Chem. Soc.* **2017**, *139*, 13296–13299.

(113) Kang, Z.; Lee, S. T. Carbon Dots: Advances in Nanocarbon Applications. *Nanoscale* **2019**, *11*, 19214–19224.

(114) Gao, J.; Zhu, M.; Huang, H.; Liu, Y.; Kang, Z. Advances, Challenges and Promises of Carbon Dots. *Inorg. Chem. Front.* **2017**, *4*, 1963–1986.

(115) Liu, G.; Zhen, C.; Kang, Y.; Wang, L.; Cheng, H. M. Unique Physicochemical Properties of Two-Dimensional Light Absorbers Facilitating Photocatalysis. *Chem. Soc. Rev.* **2018**, *47*, 6410–6444.

(116) Hutton, G. A. M.; Martindale, B. C. M.; Reisner, E. Carbon Dots as Photosensitisers for Solar-Driven Catalysis. *Chem. Soc. Rev.* **2017**, *46*, 6111–6123.

(117) Friedmann, D.; Hakki, A.; Kim, H.; Choi, W.; Bahnemann, D. Heterogeneous Photocatalytic Organic Synthesis: State-of-the-Art and Future Perspectives. *Green Chem.* **2016**, *18*, 5391–5411.

(118) Ragazzon, G.; Cadranel, A.; Ushakova, E. V.; Wang, Y.; Guldi, D. M.; Rogach, A. L.; Kotov, N. A.; Prato, M. Optical Processes in Carbon Nanocolloids. *Chem* **2020**, DOI: 10.1016/j.chempr2020.11.012.

(119) Wang, Y.; Wang, X.; Antonietti, M. Polymeric Graphitic Carbon Nitride as a Heterogeneous Organocatalyst: From Photochemistry to Multipurpose Catalysis to Sustainable Chemistry. *Angew. Chem. Int. Ed.* **2012**, *51*, 68–89.

(120) Savateev, A.; Antonietti, M. Heterogeneous Organocatalysis for Photoredox Chemistry. *ACS Catal.* **2018**, *8*, 9790–9808.

(121) Savateev, A.; Ghosh, I.; König, B.; Antonietti, M. Photoredox Catalytic Organic Transformations Using Heterogeneous Carbon Nitrides. *Angew. Chem. Int. Ed.* **2018**, *57*, 15936–15947.

(122) Markushyna, Y.; Smith, C. A.; Savateev, A. Organic Photocatalysis: Carbon Nitride Semiconductors vs. Molecular Catalysts. *Eur. J. Org. Chem.* **2019**, 1294–1309.

(123) Hartman, R. L. Managing Solids in Microreactors for the Upstream Continuous Processing of Fine Chemicals. *Org. Process Res. Dev.* **2012**, *16*, 870–887.

Chapter II

Novel Photochemical Methodologies for the Radical Iodoperfluoroalkylation of Alkenes

Abstract

In Chapter II is discussed the development of novel metal-free photochemical strategies for the synthesis of valuable iodoperfluoroalkyl compounds **3** under mild conditions in batch and flow.

Initially, the batch methodology is examined, where the use of a simple perylene diimide derivative **A**, in an extremely low catalytic loading, facilitated the formation of the iodoperfluorinated compounds **3** under blue light irradiation (450 nm). This project was conducted within the Prato group. In particular, the work was carried out together with *Prof. Maurizio Prato* and *Dr. Giacomo Filippini*, who conceived and supervised the project. Moreover, *Prof. Pier Giorgio Cozzi* and *Dr. Andrea Gualandi* (University of Bologna) participated to the initial discussions. A significant part of this work has been published in 2019.[1]

Thereafter, the batch procedure has been translated into continuous flow in order to increase the productivity of the photochemical process. The aim was pursued in collaboration with the group of Prof. Oliver Kappe (University of Graz, Austria). In his laboratories, we first successfully converted in a flow regime the photochemical methodology in the presence of **A** under blue light irradiation (450 nm). Moreover, a complementary mechanistic pathway was found to be operative under purple light irradiation (405 nm), through a different photochemical initiation step. The latter methodology was envisaged for the preparation of a relevant pharmaceutical intermediate in gram-scale. This project was conducted within the Prato and Kappe groups together with *Prof. Maurizio Prato*, *Prof. Oliver Kappe*, *Dr. Jason D. Williams*, who supervised the project and *Dr. Giacomo Filippini*, who conceived the idea. A significant part of this work has been published in 2019.[2] Adapted with permission from *Org. Lett*. **2019**, *21*, 5341–5345. Copyright 2019 American Chemical Society.

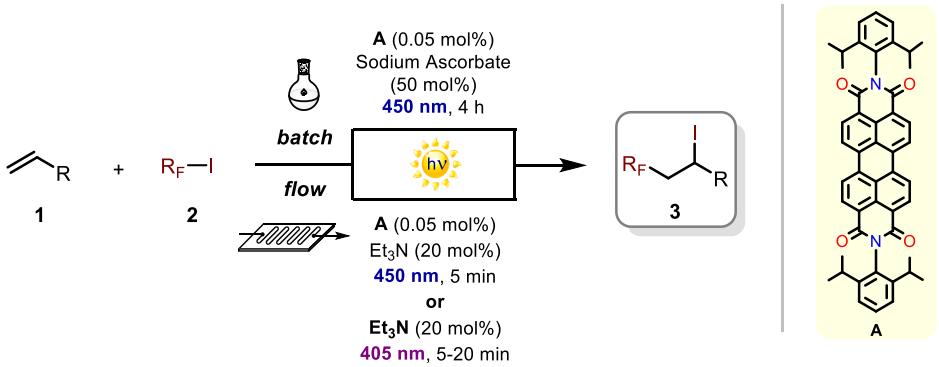

2.1 Introduction

Atom transfer radical addition (ATRA) reaction between alkenes (**1**) and perfluoroalkyl iodides (R_FI, **2**) is a simple and atom economical strategy to prepare iodoperfluoroalkyl compounds (**3**) in a single synthetic step (Figure 1a).[3]

This transformation is of practical importance, since the introduction of fluorine-containing functional groups can profoundly alter the physical and chemical features of organic molecules such as acidity, lipophilicity, bioavailability, along with their thermal, redox and metabolic stability.[4–6] Therefore, fluorinated compounds have been widely used in numerous fields of application, including medicinal chemistry, agrochemistry and materials science.[7–9] Moreover, iodoperfluoroalkyl derivatives (**3**) could be easily transformed into more complex and valuable products by exploiting the ability of iodide as an excellent leaving group. In fact, a variety of industrially relevant compounds containing fluorinated moieties can in principle arise from **3** (Figure 1c).[10,11]

For these reasons, several methodologies for the direct radical iodofluoroalkylation of olefins (**1**) have been developed over the last 70 years.[7] Since 1950,[12] the formation of perfluoroalkyl radicals ($R_F^{\bullet}$, **I**), involved in the ATRA mechanism, has been achieved through two general activation modes, starting from R_FI (**2**): (*i*) thermal activation or (*ii*) photochemical activation (Figure 1a). Those electron-poor radicals (**I**) can react with alkenes (**1**) to generate the corresponding open-shell adducts (**II**). The latter species can abstract an iodine atom from another molecule of R_FI (**2**) through a classic radical chain propagation mechanism, thus affording the iodoperfluoroalkyled products **3** and restoring the key radicals **I**. The ATRA cycle is therefore closed (Figure 1b).[13]

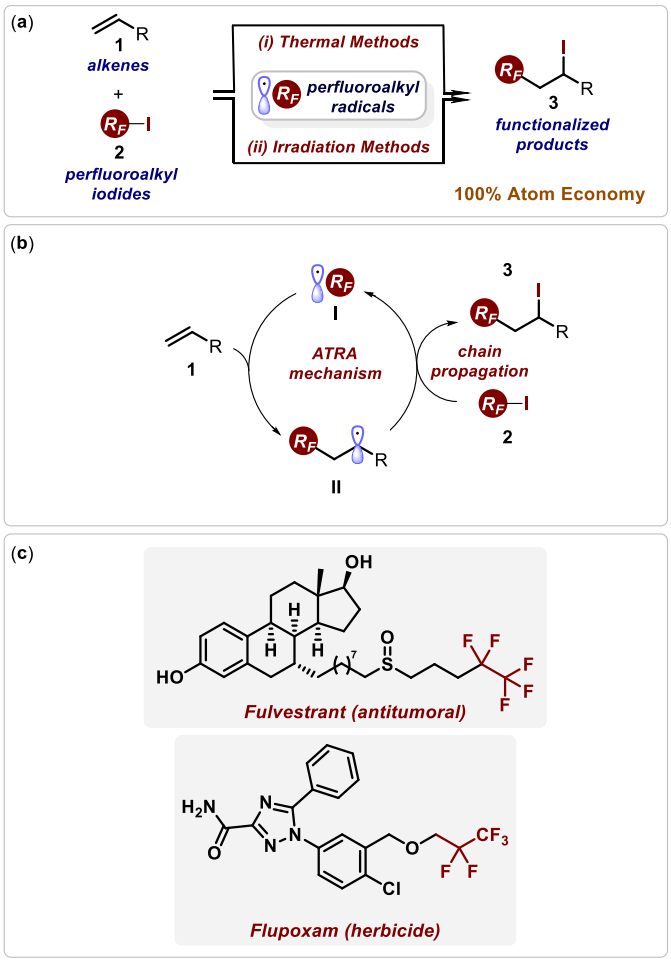

Figure 1. (**a**) General ATRA reactions between alkenes **1** and perfluoroalkyl iodides **2**. (**b**) Classical radical chain mechanism of ATRA reactions. (**c**) Industrially relevant compounds containing fluorinated moieties.

Originally, the homolytic cleavage of the C–I bond in **2**, as responsible for the $R_F^{\bullet}$ generation, required harsh conditions such as high temperatures (> 220°C) or high-energy UV-light irradiation (Hg lamp, λ < 300 nm, Figure 2).[14]

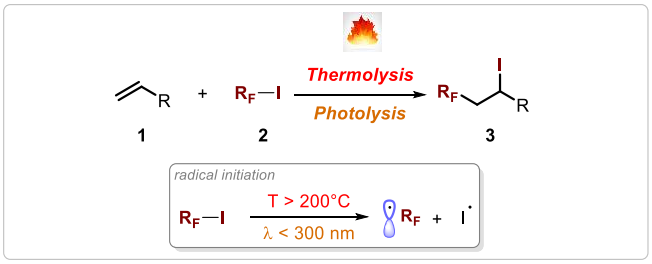

Figure 2. Direct thermolysis or photolysis for the formation of fluorinated radicals **I**.

Thereafter potentially dangerous radical initiators, including peroxides and azo-nitriles, have been successfully employed for this purpose in stoichiometric or sub-stoichiometric amount (Figure 3).[15] Generally, these initiators operate at relatively high temperature and lead to the formation of non-negligible amount of gases (e.g., N_2, O_2, SO_2), particularly at industrial scale, which might cause explosions.

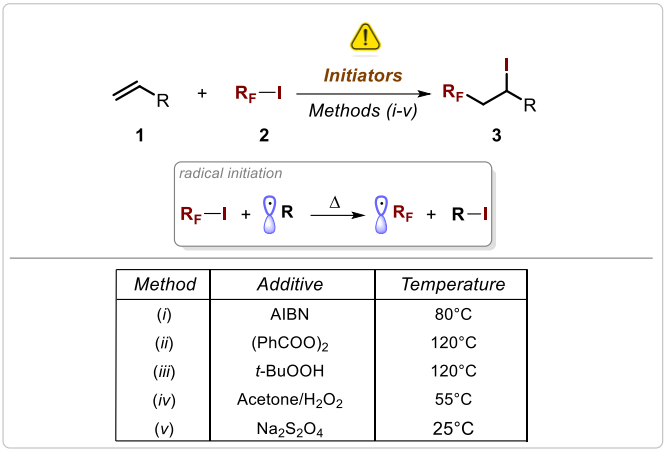

Method	Additive	Temperature
(*i*)	AIBN	80°C
(*ii*)	$(PhCOO)_2$	120°C
(*iii*)	*t*-BuOOH	120°C
(*iv*)	Acetone/H_2O_2	55°C
(*v*)	$Na_2S_2O_4$	25°C

Figure 3. Representative examples of the use of thermal radical initiators. AIBN = azobisisobutyronitrile for the formation of fluorinated radicals **I**.

Recently, photocatalysis has emerged as a powerful tool to produce fluorinated open-shell species (**I**) under mild reaction conditions.[7,16–18] The working mechanisms of these systems capitalize on the photochemical activity of precious metal-based complexes or fully organic photoredox catalysts. Alternatively, suitable electron donors can interact with the radical sources (**2**) through the formation of EDA complexes. The photochemical activity of these new chemical entities can lead to the formation of key radicals (**I**) upon light irradiation. However, in most cases, these photocatalysts and additives were employed in relatively high loading (from 1 to 300 mol%) under UV-visible light irradiation. Among them, the best performing system turned out to be a Ru-based photocatalyst. (Figure 4).[19–28]

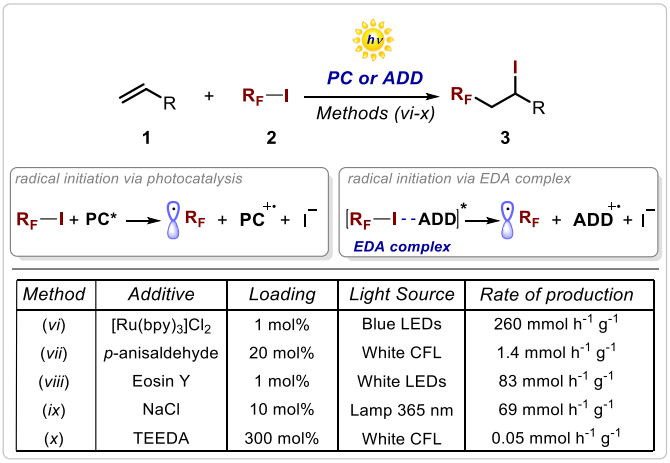

Method	Additive	Loading	Light Source	Rate of production
(*vi*)	$[Ru(bpy)_3]Cl_2$	1 mol%	Blue LEDs	260 mmol h^{-1} g^{-1}
(*vii*)	*p*-anisaldehyde	20 mol%	White CFL	1.4 mmol h^{-1} g^{-1}
(*viii*)	Eosin Y	1 mol%	White LEDs	83 mmol h^{-1} g^{-1}
(*ix*)	NaCl	10 mol%	Lamp 365 nm	69 mmol h^{-1} g^{-1}
(*x*)	TEEDA	300 mol%	White CFL	0.05 mmol h^{-1} g^{-1}

Figure 4. Representative examples of the use of photocatalytic systems for the formation of fluorinated radicals **I**. PC = photocatalyst, ADD = additive, LEDs = light-emitting diodes, CFL = compact fluorescent lamp, TEEDA = *N*,*N*,*N*',*N*'-tetraethylethylenediamine, rate of production = yield of **3** x reaction time^{-1} x weight of photoactive species^{-1}.

Therefore, the general feeling is that a further advance within this field would require the development of novel metal-free photocatalytic systems capable of working under visible light irradiation in low loading.[29] In addition, these systems have to be efficient, inexpensive, safe and readily available through straightforward synthetic protocols. In our studies, we found out that

perylene diimides (PDIs), a class of dyes historically utilized as pigments in the textile industry,[30] fulfil these requirements due to their excellent optical and redox properties.[31,32] Thus, we envisaged their use as effective photocatalysts for the iodoperfluoroalkylation of olefins under visible light irradiation.

For this reason, it is important to first introduce the nature and the photochemical properties of this notable class of organic chromophores before proceeding with the discussion of the results.

2.2 Perylene Diimides (PDIs) as Organic Photoredox Catalysts

Perylene-3,4:9,10-bis(dicarboximide)s, commonly known as perylene diimides (PDIs), have become one of the most widely used organic dyes in the family of polycyclic aromatic compounds.[31,33] They consist of a rigid perylene scaffold (aromatic core) substituted with two dicarboxylic acid imide groups at the 3,4- and 9,10-peri-positions (Figure 5).[31] Among their distinctive features, it is worth mentioning the chemical and thermal stability along with the photochemical properties of PDIs.[31,33–35] In the past, PDIs were merely employed as pigments for the automotive and textile industries due to the successful combination of their insolubility, photothermal inertness and weather resistance.[30,32,36] Nowadays, the development of a variety of synthetic methodologies, that allow for the chemical transformation of the whole PDI structure, has paved the way to the exploration of novel fields of application. Concerning their optical properties, PDIs are characterized by a strong absorption maximum centered at around 525 nm (absorptivity up to 10^5 M^{-1} cm^{-1}) and a bright emission with a small Stock shift.[31] Typically, the fluorescence quantum yields (Φ) are close to unity and the excited-state lifetimes are reasonably long, in the order of nanoseconds.[31,32,36] In general, these optical features of PDIs can be modulated through a suitable functionalization of the aromatic core, whereas the solubility of these dyes relies on the substitution at the *N*,*N*' *imide* positions.[31,35–37] In parallel, the redox features of PDIs can be tuned by installing electron-donating or withdrawing groups in their core. This results in a significant variation of both the oxidation and reduction potentials, despite similar overall bandgaps.[31,35,36] In light of the abovementioned properties, PDIs have found a wide range of applications in many fields of sciences. These applications span from optoelectronics (e.g., transistors, organic light-emitting diodes, solar cells, dye lasers), pigments, sensors, energy production. (Figure 5).[31,36–42]

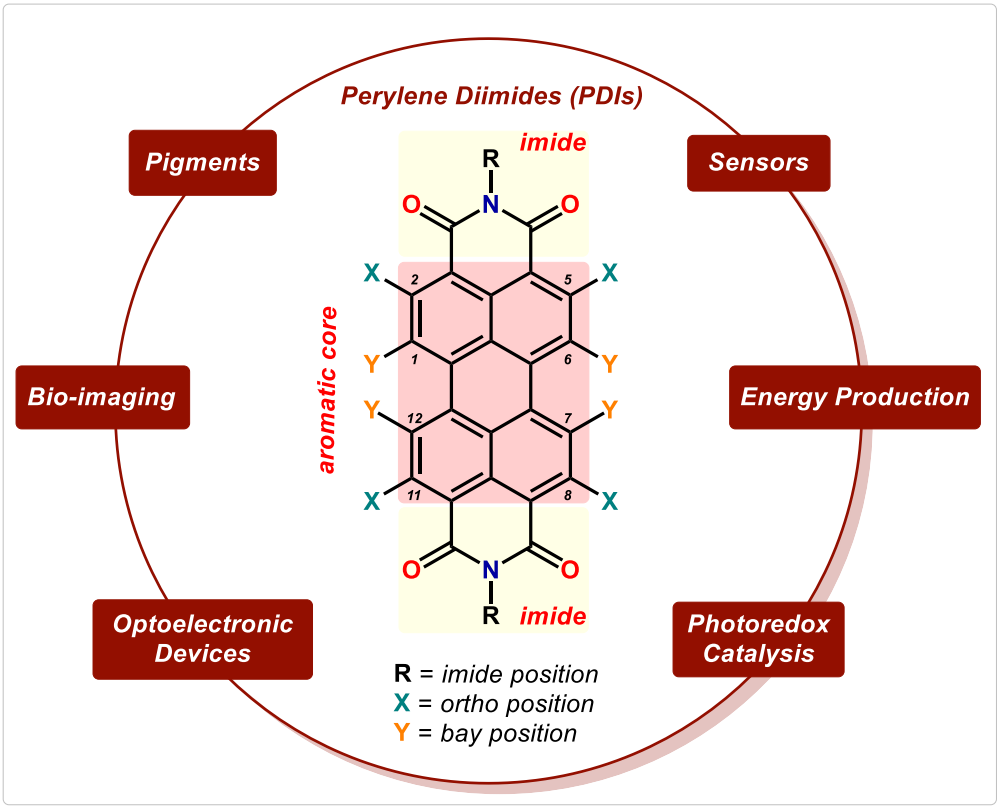

Figure 5. PDIs molecular structure and their main applications.

However, despite their outstanding physicochemical features, PDIs have found very few applications in synthetic photoredox catalysis and, currently, have been limited to the reduction of aryl halides and oxidation of sulfides.[37,43–45] In this regard, a simple symmetrical PDI, **A** (Figure 6), turned out to be the dye of choice to drive most of the cited organic photochemical reactions. **A** is prepared from perylene-3,4,9,10-tetracarboxylic dianhydride (PDA) by imidization with 2,6-diisopropylaniline at high temperature (Figure 6a).[33] Structurally, the presence of bulky groups on the *imide* positions provides better solubility in organic solvents by preventing aggregation in solution.[46] Furthermore, **A** exhibits excellent optical and redox properties, showing a strong absorption in the visible region ($\varepsilon_{\mathbf{A}\ \lambda=450\ nm}$ = 11000 M^{-1} cm^{-1}, Figure 6b).[1]

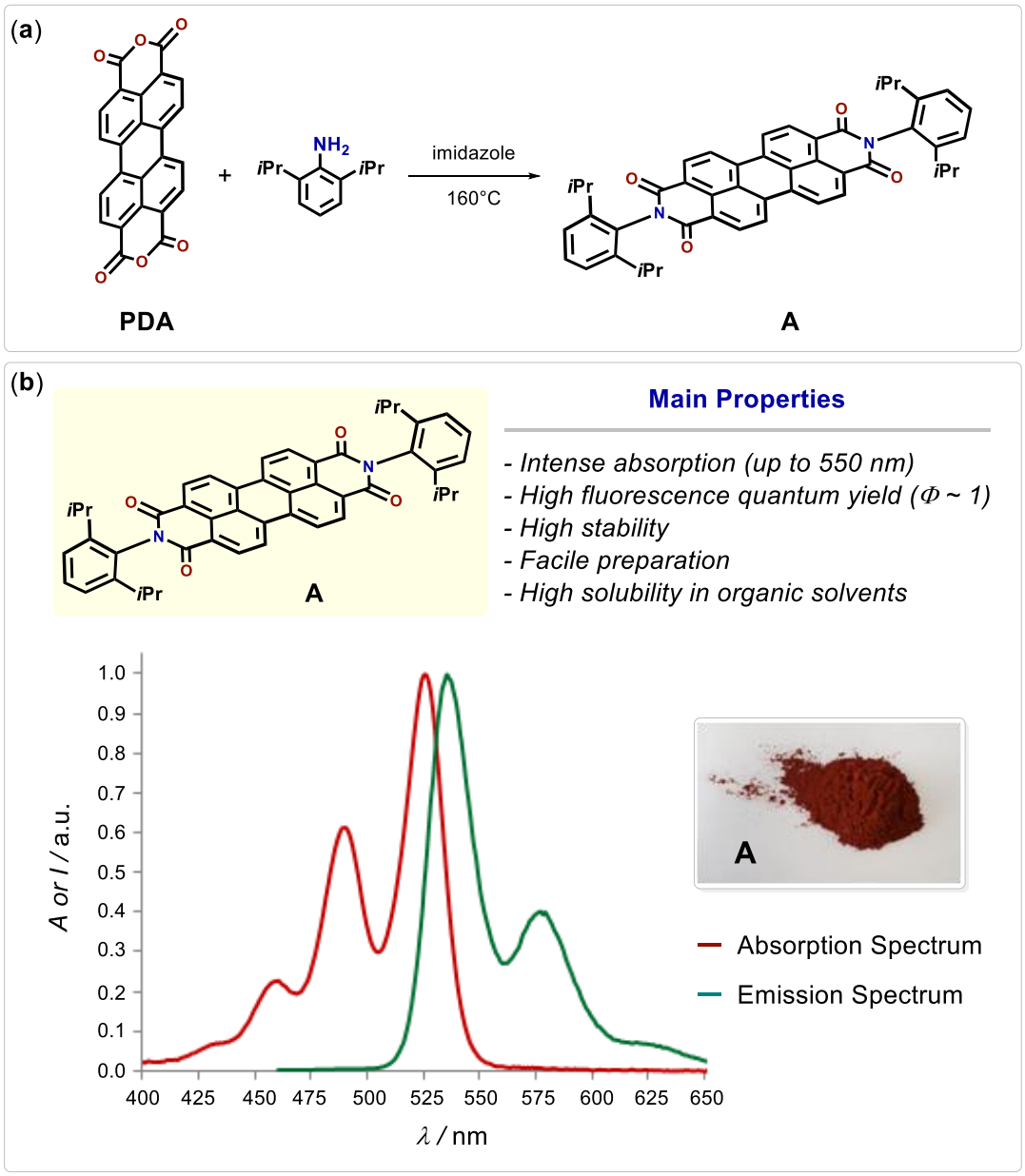

Figure 6. (**a**) Preparation of photocatalyst A from PDA. (**b**) Main physicochemical properties of PDI **A**.

Specifically, upon light absorption, **A** becomes a strong oxidant in the excited state (**A***), with a reduction potential for the couple **A***/**A**$^{\bullet-}$ of +1.97 V (*versus* saturated calomel electrode, SCE), according to Rehm-Weller equation (Figure 7).[47,48] Therefore, **A*** can effectively drive photo-oxidation reactions with suitable electron donors (ED), generating its corresponding radical anion (**A**$^{\bullet-}$, E = –0.37 V *vs* SCE for the couple **A**/**A**$^{\bullet-}$).[41,49] In addition, the reduced species is still redox active and can further carry out reductive transformations in the presence of appropriate electron-acceptors (EA).[40] Alternatively, **A**$^{\bullet-}$, due to its color and persistency in deaerated solutions,[50] can in principle absorb another visible photon reaching its highly energetic excited state (**A**$^{\bullet-}$*, E = –1.87 V *vs* SCE for the couple **A**$^{\bullet-}$*/**A**).[43,51] This species (**A**$^{\bullet-}$*) is thus able to reduce strongly unreactive acceptors.[37]

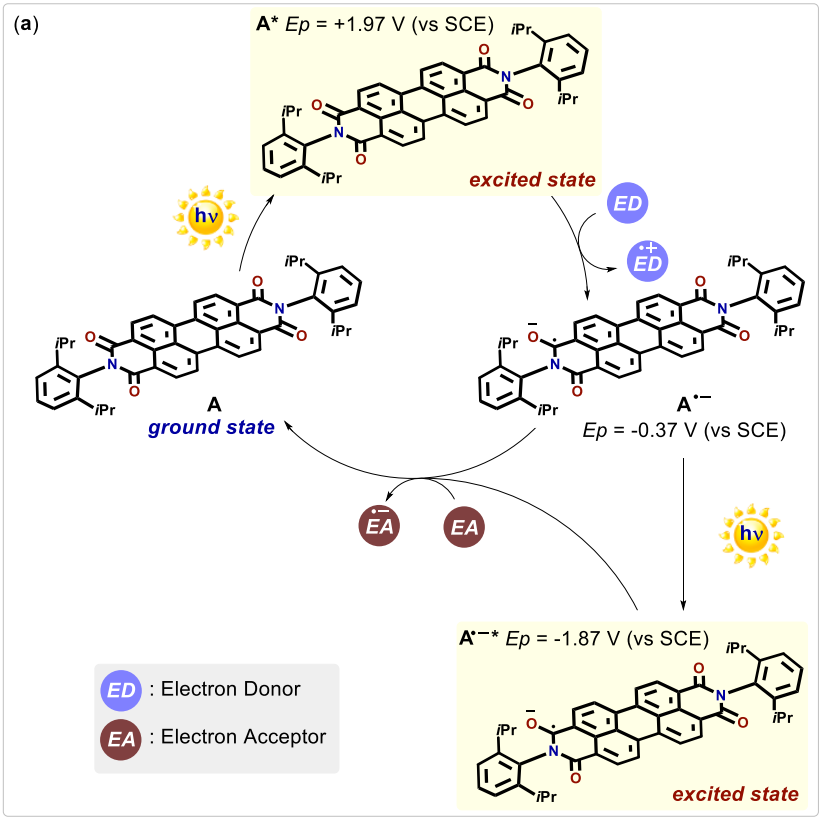

Figure 7. Possible mode of catalysis of the photoactive organic dye **A**.

In fact, a milestone in the use of PDI **A** in synthetic photochemistry is represented by the work of König and co-workers, published in 2014 (Figure 8).[43] The authors described an efficient route for the reduction of stable aryl halides in the presence of **A** under blue light irradiation (455 nm). Remarkably, these transformations are receiving growing attention as complementary methods to standard transition metal-catalyzed functionalization.[52] In addition, dehalogenation reactions might find application in wastewater treatment, since chlorinated and brominated aromatics are ubiquitous environmental contaminants.[53,54] The breakthrough of this method was the possibility of transforming even unreactive aryl chlorides (E < –1.7 V vs SCE) by means of highly energetic $\mathbf{A}^{\bullet-}$* (E = –1.87 V *vs* SCE). This led the formation of aryl radicals (Figure 8a). These useful open–shell intermediates can be then trapped by hydrogen atom donors or used in C–C bond forming reactions (Figure 8a-b).

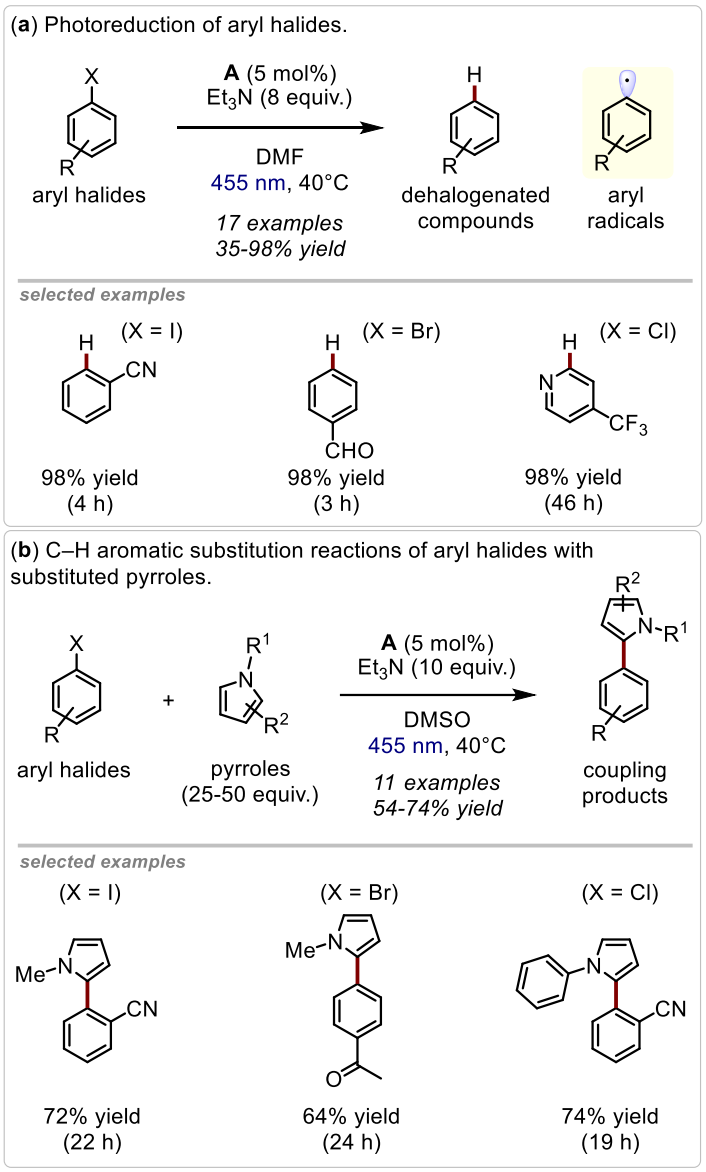

Figure 8. (**a**) Use of **A** as photocatalyst for the reduction of aryl halides. (**b**) Use of **A** to photocatalyze C–H aromatic substitution reactions.

An analogous approach was adopted by Duan, Chen and co-workers. The authors employed heterogeneous PDI-based materials, such as metal-organic polymers or silica nanoparticles, for the same abovementioned catalytic purposes.[55,56] Moreover, the group of Lin illustrated how the structural modifications of **A** at the *bay* position may affect the photocatalytic performance for the reduction of aryl halides. This was attributed to the different reduction potential and electron transfer ability of a variety of PDIs substituted with electron-donating or electron-withdrawing groups.[44]

Concerning the mechanism of the benchmark aryl dehalogenation reaction, other mechanistic hypotheses that differ from the consecutive two-photon pathway (Figure 9a) has been presented. In particular, Cozzi, Ceroni and co-workers observed that $\mathbf{A}^{\bullet-*}$ is not stable under the reaction conditions used for the dehalogenation of aryl halides.[47] Through a deep spectroscopic and electrochemical study, the authors highlighted that $\mathbf{A}^{\bullet-*}$ does not seem to be a catalytic

intermediate since, apparently, the reactivity was driven by its decomposition products (Figure 9b). These conclusions were supported by the very short lifetime of $\mathbf{A}^{\bullet-*}$ (145 ps) that does not allow for an effective PET.[50] Furthermore, at the selected irradiation wavelength (455 nm), $\mathbf{A}^{\bullet-}$ absorbs around 9 times less than **A**.[50] Based on these pieces of evidence, the authors claimed that $\mathbf{A}^{\bullet-*}$ degradation species are the real radical initiators of this transformation. Nevertheless, the exact structure of these species has never been identified.

Another possible explanation for the mode of catalysis of **A** was suggested by Nicewicz and co-workers in 2016.[49] The authors reasoned that a preassociation between $\mathbf{A}^{\bullet-}$ and aryl halides could be at play. This ground-state aggregation, namely EDA complex, could be held together by non-covalent interactions between the electron rich donor $\mathbf{A}^{\bullet-}$ and the electron poor acceptor.[57] Therefore, a PET from the donor to the acceptor might occur, leading to the formation of reactive open–shell intermediates (Figure 9c).[57] In this way, the issue of the redox potential matching between the reaction partners can be overcome, thus explaining the unpredicted reactivity of some case studies. Later on, Gschwind and co-workers implemented an in-situ combination of Nuclear Magnetic Resonance (NMR) and Ultraviolet/Visible (UV/Vis) spectroscopy under light irradiation, to allow the simultaneous and time-resolved detection of paramagnetic and diamagnetic species.[58] Using this setup, the authors attempted to confirm the consecutive PET mechanism asserted by König for the dehalogenation of aryl halides. Thereby, they easily observed the concomitant formation of both $\mathbf{A}^{\bullet-}$ and the reduction products over the time by shining blue light. However, no direct evidence for the involvement of $\mathbf{A}^{\bullet-*}$ in the reaction pathway has been provided.

Conversely, Zhang, Schanze and co-workers have recently reported the use of picosecond time-resolved transient absorption spectroscopy to monitor the formation of $\mathbf{A}^{\bullet-*}$ and its bimolecular quenching by aryl halides through Stern–Volmer studies.[51] The authors found that $\mathbf{A}^{\bullet-*}$ underwent efficient PET with electron poor halides having reduction potential > –1.7 V *vs* SCE. Besides, they calculated the potential for the couple $\mathbf{A}^{\bullet-*}/\mathbf{A}$ as −1.87 V *vs* SCE. However, a variety of unreactive halides (E < –1.8 V *vs* SCE) that are still effectively converted into the corresponding dehalogenated compounds, did not show any quenching of $\mathbf{A}^{\bullet-*}$. This can be attributed to a too slow electron transfer compared to the rapid decay of $\mathbf{A}^{\bullet-*}$. In this case, the authors suggested that a thermally activated reaction between ground-state $\mathbf{A}^{\bullet-}$ and the substrates could take place, despite its endothermicity of more than 1 eV. According to them, this process might be feasible because the dehalogenation of the corresponding aryl halide radical anion is very fast, thus making the slow electron transfer reaction irreversible.[37,59]

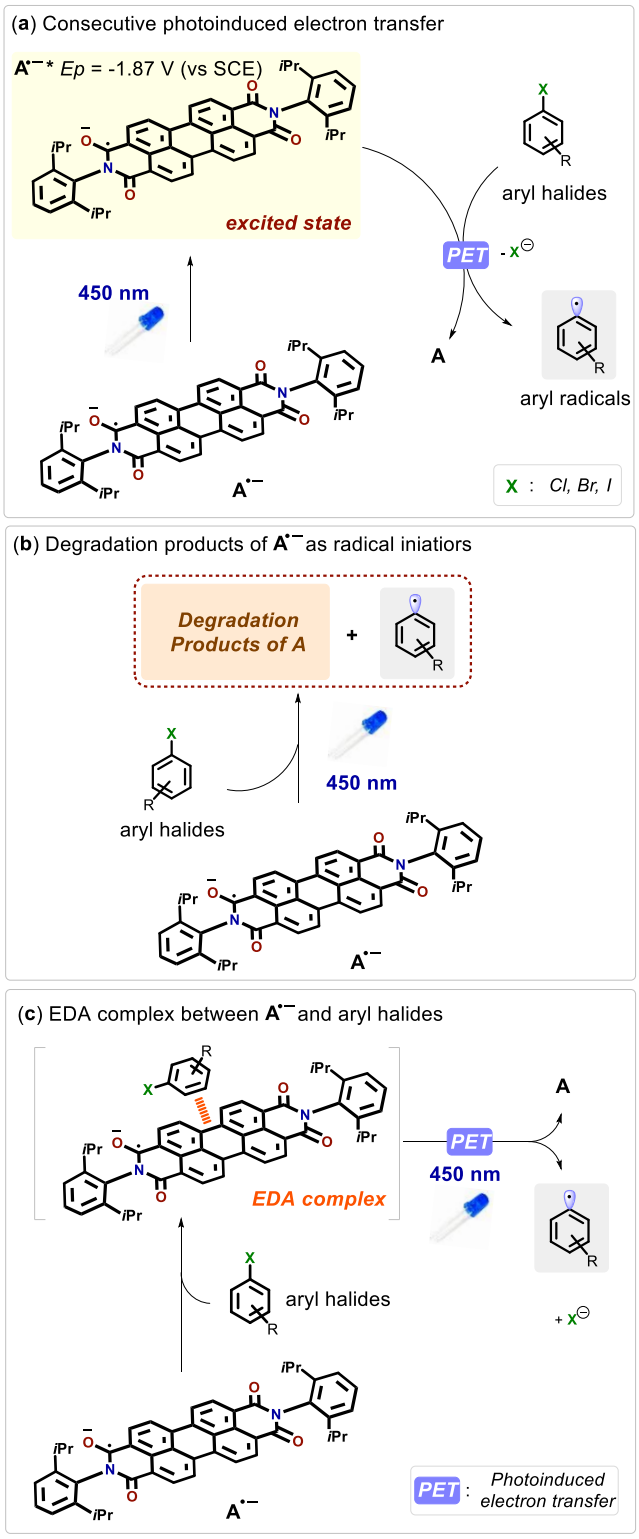

Figure 9. Suggested photochemical mechanisms for the production of aryl radicals.

Beside the described photoreduction reactions, it should be recalled that **A** is a strong oxidant in the excited state and can therefore also initiate photo-oxidation reactions or even photo-oxygenations in the presence of molecular oxygen. O_2 is probably the greenest oxidant available for organic synthesis, therefore its utilization is becoming increasingly significant for academia and industry.[60,61] To this regard, Zhang, Fan, and co-workers reported the aerobic oxidation of sulfides to sulfoxides by means of the photochemical activity of **A** under blue light irradiation (Figure 10).[45] This

transformation has practical application in the preparation of valuable biologically active sulfoxide derivatives. Remarkably, the authors found that two different reaction mechanisms could be operative. Indeed, both electron transfer and energy transfer pathways could, in principle, lead to the conversion of sulfides to sulfoxides through the formation of superoxide radical anion ($O_2^{\bullet-}$) or singlet oxygen ($^1O_2$), respectively.[37]

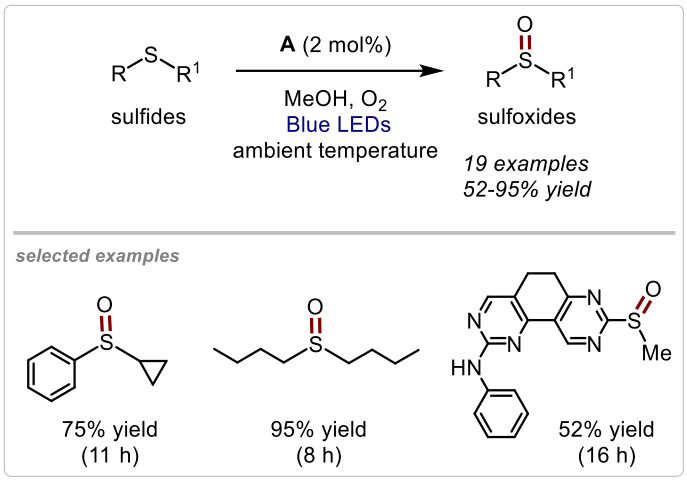

Figure 10. Use of **A** as photocatalyst for the oxidation of sulfides to sulfoxides.

2.3 Objective of the Research Project and Initial Results

As mentioned in the previous section, we were motivated by the perceived need of novel procedures for the preparation of the valuable iodoperfluoroalkyl compounds **3** in an effective and sustainable way. To this aim, we envisioned the possibility of using PDI **A** as an organic photoredox catalyst to prompt the formation of the key fluorinated radicals **I** needed for the ATRA process (Figure 11a). Therefore, we tested the initial feasibility of our idea by reacting 1-hexene (**1a**) and perfluorohexyl iodide (**2a**, 2 equiv.) in the presence of **A** as photocatalyst (5 mol%) under blue light irradiation (450 nm light-emitting diodes, LEDs). Moreover, triethylamine was employed as sacrificial electron donor (Et_3N, 2 equiv.) in a mixture of acetonitrile/methanol 4:3 as solvent (CH_3CN/CH_3OH 4:3, 0.017 M). Interestingly, this experiment provided the corresponding iodoperfluoroalkyl product **3a** in excellent yield (95% NMR yield, Figure 11b).

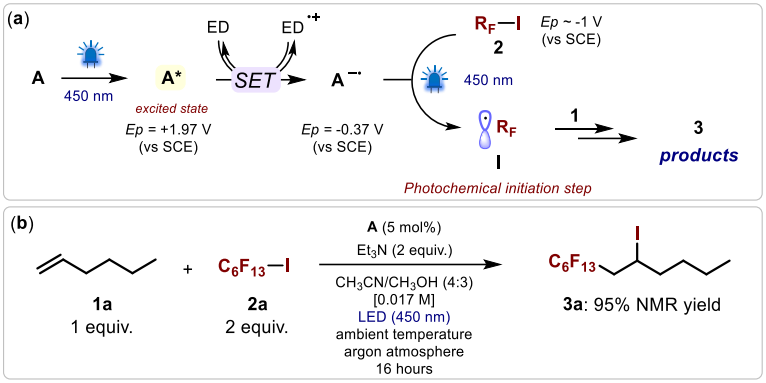

Figure 11. (**a**) Initial idea: using PDI **A** as photocatalyst to trigger the formation of perfluorinated radicals **I**. (**b**) The initial experiment with the reaction conditions. E_p = redox potential, ED = electron donor, SET = single electron transfer.

2.4 Results and Discussion

Prompted by these intriguing results, we performed an optimization study of the reaction conditions in order to improve the rate of production of the iodoperfluorohexylation of **1a** (defined as: yield of **3a** x reaction time^{-1} x weight of **A**$^{-1}$). Thus, starting from the initial conditions, the whole process can become more sustainable (Table 1-2).

First, other common sacrificial electron donors, such as aliphatic and aromatic amines, were tested for this transformation (entries 1-3, Table 1). A total suppression of the ATRA process was detected with 4-methoxy-*N*,*N*-diphenylaniline (entry 2, Table 1), likely since it is not able to reduce **A** to its corresponding radical anion. On the contrary, sodium ascorbate was found to be an excellent candidate in this case-study, providing quantitative NMR yield of product **3a** (entry 3, Table 1). Based on the higher activity and the environmentally benign character of sodium ascorbate, compared to triethylamine, it was selected for our further investigations. Then, we attempted to reduce as much as possible the loading of the different reaction components, in order to increase the sustainability of the process. Surprisingly, the considered photocatalytic system was capable of maintaining its exceptional performance even when the loading of photocatalyst **A** was decreased to 0.05 mol% (corresponding to 500 parts per million, ppm, entry 4, Table 1). However, it is worth noting that employing loadings of **A** below this threshold value, the reactivity was completely suppressed (entry 5, Table 1). In addition, the quantity of the sacrificial electron donor was successfully reduced to sub-stoichiometric amounts without any loss of reactivity (entry 6, Table 1).

Interestingly, the iodoperfluoroalkylation reaction was found to be complete in 4 hours of irradiation instead of 16 hours, indicating the efficiency of the studied methodology (entry 7, Table 1). Lastly, the concentration was effectively doubled to ensure a higher productivity without concurrently hampering the light penetration inside the reaction vessel (entry 8, Table 1).

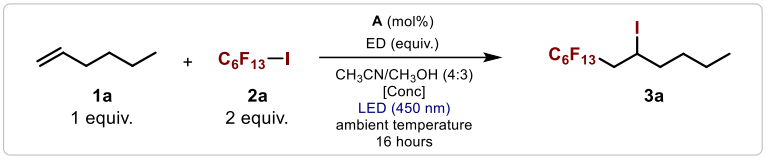

Entry	**A**	Electron Donor (ED)	Concentration	Yield[a]
1	5 mol%	Triethylamine (2 equiv.)	0.017 M	95%
2	5 mol%	4-methoxy-*N*,*N*-diphenylaniline (2 equiv.)	0.017 M	0%
3	5 mol%	Sodium Ascorbate (2 equiv.)	0.017 M	>99%
4	0.05 mol%	Sodium Ascorbate (2 equiv.)	0.017 M	>99%
5	0.005 mol%	Sodium Ascorbate (2 equiv.)	0.017 M	0%
6	0.05 mol%	Sodium Ascorbate (0.5 equiv.)	0.017 M	>99%
7[b]	0.05 mol%	Sodium Ascorbate (0.5 equiv.)	0.017 M	>99%
8[b]	0.05 mol%	Sodium Ascorbate (0.5 equiv.)	0.034 M	>99%

Table 1. Reactions performed on 0.1 mmol scale. [a] Yield determined by ^{1}H-NMR spectroscopy using 1,1,2-trichloroethene as the internal standard. [b] Reactions performed over 4 hours of irradiation.

The performance of the iodoperfluoroalkylation methodology was investigated with respect to the solvent (Table 2). Highly polar solvents such as dimethylformamide (DMF), CH_3OH and a mixture of CH_3CN/CH_3OH (4:3) or CH_3CN/H_2O (95:5) provided the desired product **3a** from 85 to 99% NMR yield. Surprisingly, in pure CH_3CN we did not observed any reactivity, perhaps due to the poor solubility of sodium ascorbate.[62] The solvent of choice for the following studies was CH_3CN/H_2O (95:5, entry 5, Table 2) because it provides for a better reaction mixture homogeneity.

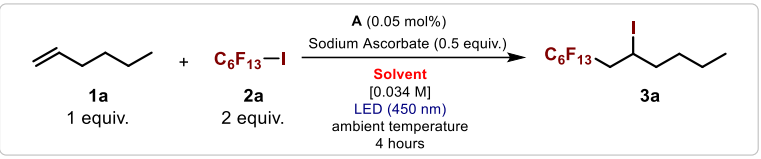

Entry	Solvent	Yield[a]
1	DMF	85%
2	CH_3CN	0%
3	CH_3OH	>99%
4	CH_3CN/CH_3OH (4:3)	>99%
5	CH_3CN/H_2O (95:5)	>99%

Table 2. Reactions performed on 0.1 mmol scale. [a] Yield determined by ^{1}H-NMR spectroscopy using 1,1,2-trichloroethene as the internal standard.

Under these conditions, an excellent isolated yield of **3a** was obtained (98% yield, entry 1, Table 3). Interestingly, our photocatalytic process turned out to be extremely convenient, since it proceeds with a very high rate of production (700 $mmol_{\mathbf{3a}}h^{-1}g_{\mathbf{A}}^{-1}$). Such a high level of reactivity outperforms current available methods.[20] At this point, a series of control experiments was performed to elucidate the nature of this approach (entry 2-9, Table 3). No reaction occurs either in the dark or in the absence of **A** (entries 2-3, Table 3), confirming that the studied transformation is driven by the photochemical activity of the PDI. This mechanistic scenario was consistent with the experiment carried out using a LED at 365 nm (a wavelength that could not be absorbed by **A**) since the product **3a** was not detected (entry 4, Table 3). In a similar fashion, a complete inhibition of reactivity was observed without sodium ascorbate as well as in presence of TEMPO (2,2,6,6-tetramethylpiperidine 1-oxyl, 1 equiv.) or air (entries 5-7, Table 3). These last two experiments were consistent with a radical mechanism. Interestingly, by shining green light to the reaction vessel, the product **3a** was also obtained in high overall yield, as well as using a solar simulator (entry 8-9, Table 3), suggesting that our methodology could efficiently work under direct sunlight irradiation.

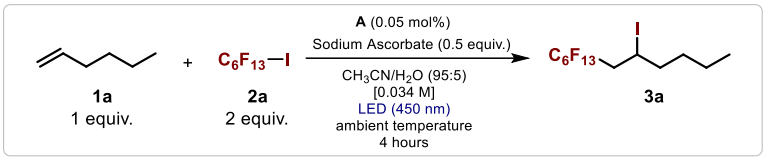

Entry	Deviation from standard conditions	Yield[a]
1	None	>99% (98%)[b]
2	In the dark	0%
3	No PDI **A**	0%
4	LED at 365 nm	0%
5	No Sodium Ascorbate	0%
6	TEMPO (1 equiv.)	0%
7	In air	0%
8	Solar Simulator[c]	>99%
9	LED at 525 nm	90%

Table 3. Reactions performed on 0.1 mmol scale. [a] Yield determined by ^{1}H-NMR spectroscopy using 1,1,2-trichloroethene as the internal standard. [b] Isolated yield is shown is parenthesis. [c] Source of photons: Lot-Oriel solar simulator equipped with a 300 W xenon lamp and an integrated Atmospheric Edge Filter with a cut-off at 300 nm.

Finally, different PDI photocatalysts have been evaluated in the best conditions found (Table 4). Specifically, **A** was compared with a more electron poor PDI derivative bearing four bromines at the *bay* positions (entry 2, Table 4). This derivative possesses a stronger photo-oxidating character but a weaker photo-reducing ability with respect to **A**. Furthermore, a PDI having branched alkyl substituents at the *imide* positions instead of bulky aryl groups has been assessed (entry 3, Table 4). All the examined photocatalysts showed the same catalytic activity of **A** towards the iodoperfluoroalkylation reactions. Therefore, PDI **A** was selected as the photocatalyst of choice due to its stronger blue light absorption, higher solubility, and easier preparation with respect to the others.

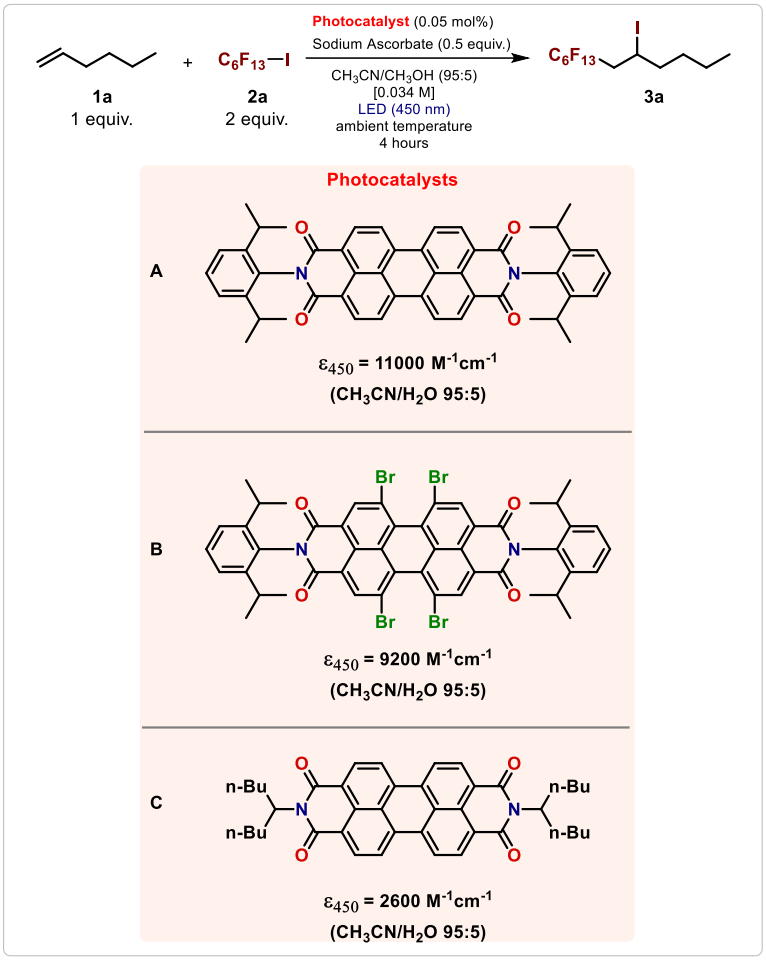

Entry	Photocatalyst	Yield[a]
1	**A**	>99%
2	**B**	>99%
3	**C**	>99%

Table 4. Reactions performed on 0.1 mmol scale. [a] Yield determined by ^{1}H-NMR spectroscopy using 1,1,2-trichloroethene as the internal standard.

With the optimized conditions in hand (entry 1, Table 3), we demonstrated that our iodoperfluorohexylation reaction is general in scope with respect to the alkene component (Figure 12). Indeed, the reaction could efficiently tolerate various terminal olefins (**1a-i**) bearing alkyl chains, halogens, alcohol, ester, ether, imide, and sulfone moieties. These experiments provided the corresponding iodoperfluorohexyl derivatives (**3a-i**) from very high to excellent isolated yields (up to 98% yield). A sulfide-containing alkene (**1j**) was also moderately functionalized under the reaction conditions to give compound **3j** in reasonable overall yield (58% yield). In addition to the perfluorohexyl chain (product **3e**), either a shorter or a longer perfluorinated substituent were installed in excellent yields to afford **3k** and **3l**, respectively (up to 96% yield). In the case of heptafluoro-2-iodopropane (**2d**) to obtain **3m**, a drop in yield was observed, possibly due to the steric effects rather than redox features (56% yield).[14] Moreover, our attempts to react iodopentafluorobenzene (**2e**) under our standard conditions failed. A terminal alkyne (**4a**) was also efficiently transformed into the corresponding unsaturated iodoperfluorohexyl compound (**5a**) in

good overall yield (70% yield, 4:1 *E*/*Z*). Notwithstanding, it should be mentioned that this procedure is not effective for the perfuoroalkylation of arenes through an homolytic aromatic substitution pathway, probably because of their lower reactivity compared to alkenes.[7]

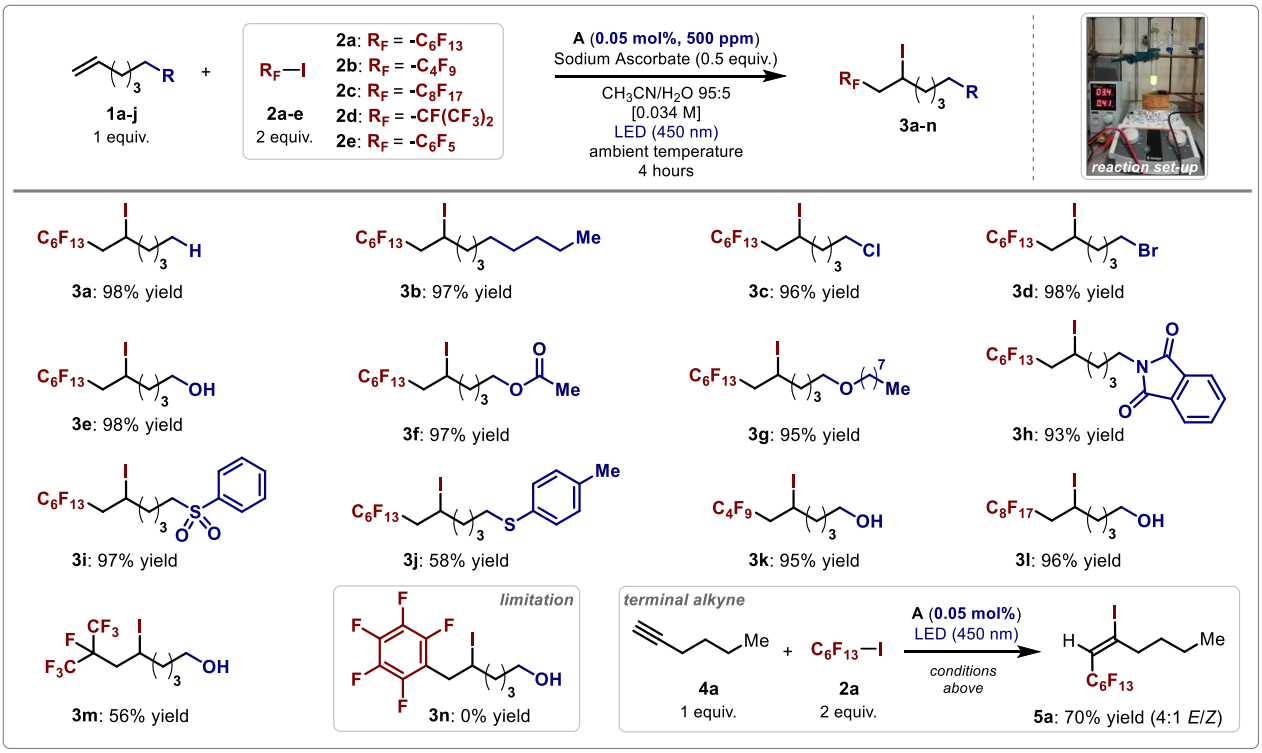

Figure 12. Evaluation of the scope of the photochemical ATRA reaction. Survey of the olefins and perfluoroalkyl iodides which can participate in the process. Conditions: reactions conducted in Schlenk tubes in CH_3CN/H_2O (95:5, 0.034 M) on 0.1 mmol scale of alkene **1**, 0.2 mmol of perfluoroalkyl iodide **2**, 0.05 mmol of sodium ascorbate and 0.05 mol% of **A**, degassed by freeze-pump-thaw cycles and irradiated for 4 hours by a single blue LED (450 nm) at ≈3 cm from the tube.

2.5 Mechanistic Investigations of the PDI-photocatalyzed Iodoperfluoroalkylation of Olefins

We then sought to clarify the role of catalyst **A** in the present photochemical transformation. Initially, we recorded the absorption spectra of the single reaction components, confirming that the only species capable of absorbing visible light at 450 nm is the photocatalyst **A**. Moreover, no ground-state association between the perylene diimide (**A**) and the radical precursor (**2a**) were detected, since their combination does not lead to relevant change of the absorption spectra (Figure 13).

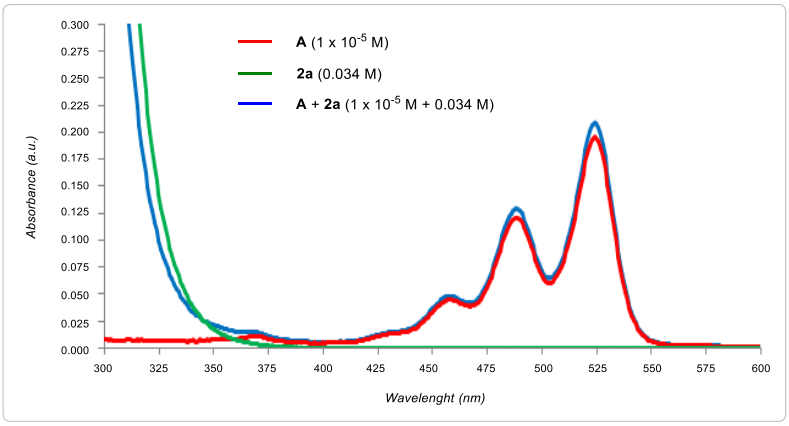

Figure 13. Optical absorption spectra recorded in CH_3CN/H_2O (95:5) of photocatalyst (**A**, red line), perfluorohexyl iodide (**2a**, green line) and their combination (blue line), optical path length = 1 cm.

As anticipated, **A** is a strong oxidant in the excited state (**A***), with a reduction potential for the couple **A***/**A**$^{\bullet-}$ of +1.97 V *vs* SCE. Indeed, in the presence of sodium ascorbate, **A*** is reductively quenched providing the corresponding radical anion (**A**$^{\bullet-}$). This chemical species has a redox potential of -0.37 V (*vs* SCE, for the couple **A**/**A**$^{\bullet-}$)[43] and thus it is not able to directly reduce the perfluorohexyl iodide (**2a**, E ≈ -1 V *vs* SCE).[20] Despite its deep blue color, the sequential absorption of another photon by **A**$^{\bullet-}$ could be difficult to achieve according to the short lifetime (τ=145 ps) of the excited state (**A**$^{\bullet-}$*), that does not allow for an effective PET, and its poor photo-stability.[47] Furthermore, at the selected irradiation wavelength (450 nm), **A**$^{\bullet-}$ absorbs around 9 times less than **A**.[50] On the other hand, **A**$^{\bullet-}$ is known to be an electron-rich persistent radical anion in deaerated solutions.[50,58] Besides, **2a** is already recognized for its high tendency to give ground-state associations with transiently generated anions.[63–68] For these reasons it does seem feasible that an EDA complex, formed upon aggregation of **A**$^{\bullet-}$ with electron-poor **2a**, could be at play.[49] A light-driven electron transfer from the donor to the acceptor, might therefore form the fluorinated radical **Ia**. This electrophilic open-shell species then reacts with 1-hexene (**1a**), leading to the formation of the ATRA product (**3a**) through a classical radical chain propagation mechanism (Figure 14).[13] In this way, the issue of the redox potential matching between the reaction partners can be overcome, thus explaining the observed reactivity of this case-study. Notwithstanding, there is no direct spectroscopic evidence that demonstrates the formation of such a complex, due to the intrinsic difficulties in carrying out photochemical studies on **A**$^{\bullet-}$.[47]

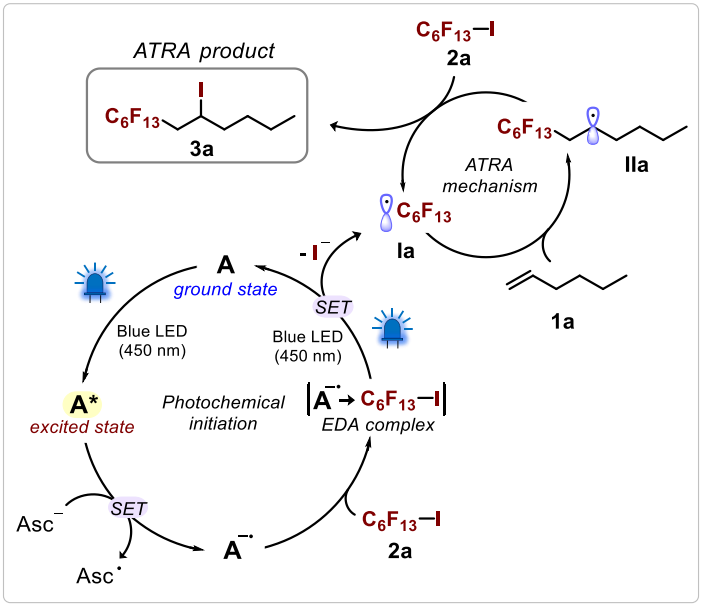

Figure 14. The proposed reaction mechanism which drives the photocatalytic iodoperfluoroalkylation of olefins. SET = Single Electron Transfer, Asc^- = ascorbate, EDA complex = Electron Donor-Acceptor complex.

Although **A** has shown to be an effective photoredox catalyst for the studied transformation, bleaching of the organic dye has been observed over the reaction time. This has suggested that a degradative pathway, which decreases the lifespan of **A**, is operative. We thus undertook a series of control experiments trying to rationalize the nature of this lateral route. When a mixture of **A** and sodium ascorbate in CH_3CN/H_2O (95:5) was irradiated over 4 hours, no degradation of **A** was detected, showing that the radical anion ($\mathbf{A}^{\bullet-}$) formation is reversible (Figure 15a*i*). In addition, the photocatalyst was fully recovered after mixing **A**, sodium ascorbate and perfluorohexyl iodide (**2a**) in the dark (Figure 15a*ii*). On the contrary, when the very same mixture was illuminated, a partial degradation of **A** occurred (Figure 15a*iii*). These experiments clearly demonstrate that both light and the radical source **2a** are involved in the degradative pathway of **A**. Subsequently, we ran a 1 mmol scale reaction using a higher amount of photocatalyst **A** (35 mg, 5 mol%) over 16 hours, attempting to isolate some of the resulting by-products to get more clues about this lateral mechanism (Figure 15b). Compound **3a** was obtained in 85% yield and we also recovered 28% (10 mg) of unreacted **A** by chromatography on silica gel. The partial recovery of **A** suggests that this species actually acts as a photocatalyst,[69] which feeds in fluorinated radicals (**Ia**) from outside the ATRA mechanism (Figure 14). Furthermore, two additional fractions, that presumably contained the degradation species of **A**, have been isolated. ^{1}H-NMR analysis indicated that they are constituted by complex mixtures of different chemical entities. ^{19}F-NMR investigation pointed out the presence of fluorine in both of the latter fractions, confirmed also by Fourier-transform infrared spectroscopy. For these reasons, we assume that the fluorinated open-shell species (**Ia**), could react with the aromatic moieties of **A**, thus inducing its radical decomposition.[70,71]

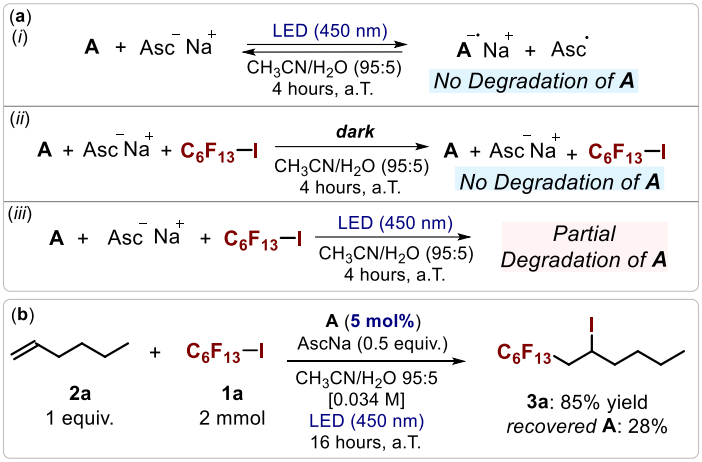

Figure 15. (**a**) Degradation studies on **A**. (**a**i) Condition: experiment was conducted on 2.5 µmol (1.8 mg) of **A**, 200 µmol of sodium ascorbate in Schlenk tube in CH_3CN/H_2O (95:5, 0.034 M), degassed by freeze-pump-thaw cycles and irradiated over 4 hours by a single blue LED (450 nm) at ≈3 cm from the tube. Alternatively, 200 µmol of perfluorohexyl iodide **2a** was added to the abovementioned mixture, either in the dark (**a**ii) or under illumination (**a**iii). (**b**) 1 mmol scale control experiment using a catalytic loading of 5 mol% of **A** under 8 blue LEDs system irradiation (450 nm). AscNa = sodium ascorbate, a.T. = ambient temperature.

2.6 Reaction Scale-up towards Continuous Flow Technology

As discussed before, iodoperfluoroalkyl compounds (**3**) can be easily converted into valuable pharmaceutical, agrochemical, or industrial intermediates. To this aim, a preparative scale process is necessary. However, batch photochemical transformations frequently have limited scale-up potential because they can be hampered by significant light attenuation as the size of a reaction vessel increases (*vide supra*, Chapter I, Section 1.2.7). In fact, when we attempted to increase the scale of the described model reaction by 10-folds, we observed a drastic drop in the formation of product **3a**, from 98% to 57% yield (Figure 16).

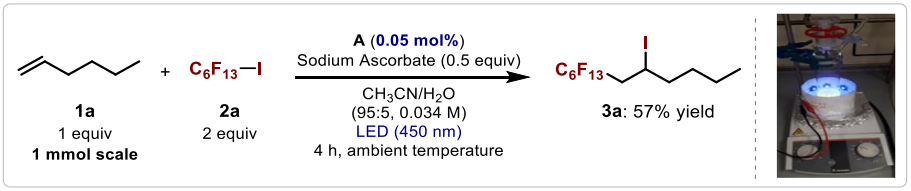

Figure 16. 10-folds reaction scale. Conditions: reaction conducted in 100 mL Schlenk tube in CH_3CN/H_2O (95:5, 0.034 M) on 1 mmol scale of alkene **1**, 2 mmol of perfluoroalkyl iodide **2**, 0,5 mmol of sodium ascorbate and 0.05 mol% of **A**, degassed by freeze-pump-thaw cycles and irradiated for 4 hours by an 8 blue LEDs system.

Continuous flow photochemistry can alleviate this limitation by using a short irradiated path length to improve photochemical efficiency, leading to shorter reaction times and higher productivity (*vide supra*, Chapter I, Section 1.2.7). Therefore, we envisaged the possibility to start a collaboration with Prof. Oliver Kappe (University of Graz, Austria), a leading expert in the field of flow chemistry. In his laboratories, we achieved the translation of our batch photochemical methodology into continuous flow, by using a commercially available plate-based photoreactor (Corning Advanced-Flow Lab Photo Reactor, 2.8 mL volume, Figure 17).[72–75]

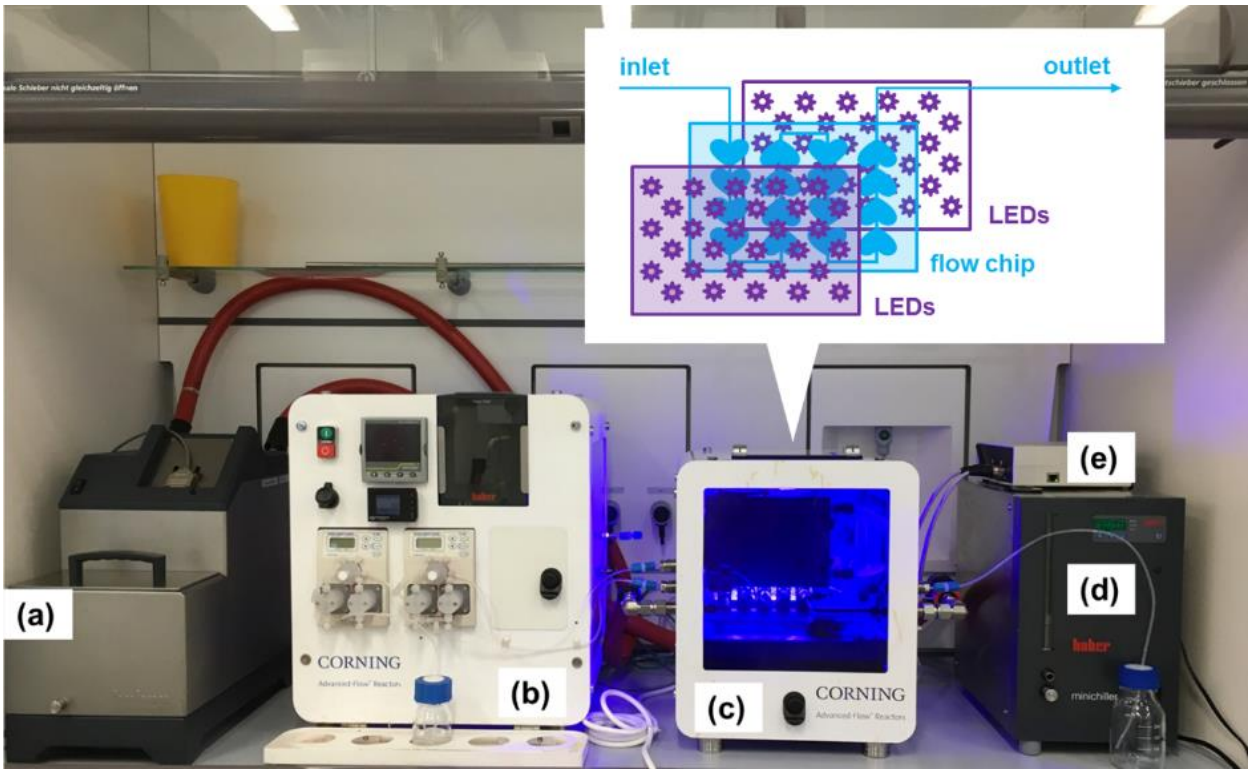

Figure 17. Photograph of commercial photoreactor setup: a) temperature control for reaction plate; b) control module, containing pumps, mass flow controller, Huber controller and data logger; c) fluidic module housing, with tinted plastic panels for light containment; d) temperature control for LED panels; e) wireless receiver for LED control.

The previous system, which used sodium ascorbate as a sub-stoichiometric electron donor, was unsuitable for flow processing, due to its heterogeneity. Accordingly, it was decided to employ triethylamine (Et_3N) as an alternative organic-soluble reductant. Additionally, the solvent of choice for the flow procedure was a mixture of CH_3CN/CH_3OH (4:3), since it is known to be effective for this transformation from our preceding studies (Table 1). Preliminary re-optimization (Table 5) was performed on the iodoperfluoroalkylation of 1-octene (**1k**, $[\mathbf{1k}]_0$ = 0.1 M, 0.5 mmol scale) by perfluorohexyl iodide (**2a**, 2 equiv.) in the presence of **A** (0.05 mol%) as photocatalyst and Et_3N (0.2 equiv.). Under blue light irradiation (450 nm) the ATRA product **3o** was observed in 95% yield, in a residence time of only 5 min (entry 1, Table 5). Further reducing the amount of Et_3N or the residence time was detrimental for the reactivity (entries 2-3, Table 5). A series of control experiments confirmed that no reaction occurs in absence of **A** nor when using 610 nm (red) light (entries 4-5, Table 5). However, green light (540 nm) was found to be only marginally less effective in promoting the reaction, resulting in 88% yield of **3o** (entry 6, Table 5). Reducing the loading of perfluorohexyl iodide (**2a**, 1.2 equiv.) lowered the yield of **3o** to 83%, but this was restored to its original level (entries 7,9, Table 5) by increasing the concentration to 0.2 M. Under these conditions, a 90% yield of the ATRA product **3o** was isolated, translating to a high throughput of 6.1 g h^{-1}. The so-obtained productivity value, compared with 0.013 g h^{-1} for the batch procedure, demonstrated that the aim of converting our previously developed methodology has been successfully achieved by simply changing few reaction parameters. This paves the way to an easy scale-up in continuous flow.

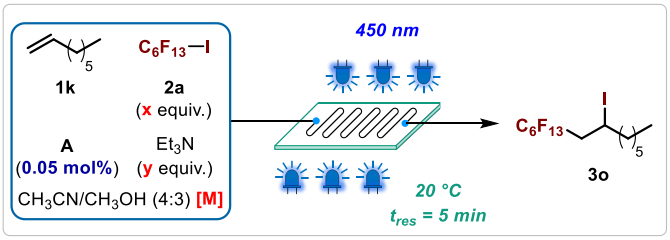

Entry	**2a** (equiv.)	Et_3N (equiv.)	Time (min)	Concentration (M)	Yield[a]
1	2	0.2	5	0.1	95%
2	2	0.1	5	0.1	93%
3	2	0.2	2.5	0.1	90%
4[b]	2	0.2	5	0.1	0%
5[c]	2	0.2	5	0.1	0%
6[d]	2	0.2	5	0.1	88%
7	1.2	0.2	5	0.1	83%
8	1.2	0.2	5	0.2	95% (90%)[e]

Table 5. Re-optimization of the reaction conditions in flow. Reactions were performed using a 5 mL sample loop and a 5 min residence time (0.56 mL/min). [a] Yields determined by GC-FID using *n*-dodecane as the internal standard. [b] Reaction conducted in the absence of **A**. [c] Reaction conduction by shining red light (610 nm). [d] Reaction conducted by shining green light (540 nm). [e] Isolated yield is shown in parentheses.

Interestingly, upon undertaking a more detailed screen of irradiation wavelengths, reactivity was observed even in the absence of **A**, when using irradiation wavelengths of 422 nm or shorter. This result can be attributed to the photoactivation of perfluoroalkyl iodide **2a** by Et_3N, through the formation of a halogen-bonded electron donor-acceptor (EDA) complex (Figure 18).[26,76,77] Such complexes absorb most strongly in the deep UV region, but can often be exploited at UVA or even some visible wavelengths by using suitable electron donors. More mechanistic details will be illustrated in the dedicated section (2.7 Mechanistic Investigations of the Catalyst-free Flow Iodoperfluoroalkylation of Olefins).

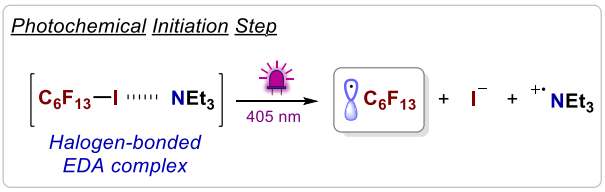

Figure 18. Photochemical initiation step through the formation of a halogen-bonded EDA complex between **2a** and Et_3N.

Encouraged by this scenario, a second iodoperfluoroalkylation protocol was optimized under purple light irradiation, in the absence of any photocatalyst (Table 6). Primary investigations examined the wavelength-dependence, highlighting a complete lack of reactivity at 450 nm (entry 1, Table 6),

moderate response at 422 nm (34% yield, entry 2, Table 6) and finally a 94% yield of **3o** at 405 nm in 5 min residence time (entry 3, Table 6). A control experiment ascertained the need for the amine additive, since no ATRA product (**3o**) was detected in the absence of Et_3N (entry 4, Table 6). Reducing the loading of perfluorohexyl iodide **2a** (1.2 equiv.) decreased the yield of **3o** to 82% (entry 5, Table 6), but was partially restored by changing the solvent to only CH_3CN (92%, entry 6, Table 6). Finally, almost quantitative yield of **3o** was observed by increasing the reaction concentration to 0.25 M, resulting in a 95% isolated yield (entry 7, Table 6).

Thanks to the increased reaction concentration allowed by this protocol, a further increase in productivity was accessed, versus the PDI-catalyzed method (7.6 g h^{-1} *vs* 6.1 g h^{-1}). For this reason, and the simplified reaction composition, we opted to further explore this method under purple light irradiation (405 nm). However, in cases with light-sensitive substrates, the PDI-catalyzed method may prove advantageous, since it allows reaction at less energetic wavelengths, even down to green light (540 nm). This corroborates the complementarity of the 405 nm protocol with respect to the 450 nm approach. It is noteworthy that our purple light transformation outperforms in terms of productivity and sustainability the currently available iodoperfluoroalkylation methods based on the photoactivation of the radical source via halogen-bonding. Indeed, the previously reported methodology required a large excess of expensive amine additives and long reaction time or the use of UV radiation (< 400 nm).[25,26]

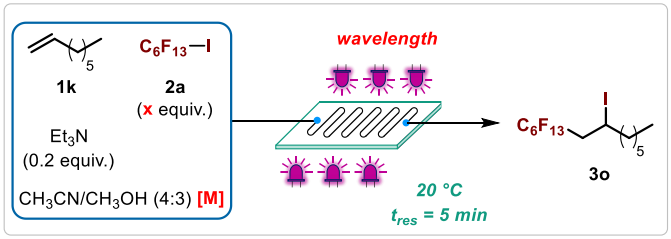

Entry	Wavelength (nm)	**2a** (equiv.)	Concentration (M)	Yield[a]
1	450	2	0.1	0%
2	422	2	0.1	34%
3	405	2	0.1	94%
4[b]	405	2	0.1	0%
5	405	1.2	0.1	82%
6[c]	405	1.2	0.1	92%
7[c]	405	1.2	0.25	98% (95%)[d]

Table 6. Optimization of the reaction conditions in flow in absence of PDI **A**. Reactions were performed using a 5 mL sample loop and a 5 min residence time (0.56 mL/min). [a] Yields determined by GC-FID using *n*-dodecane as the internal standard. [b] Reaction conducted in the absence of Et_3N. [c] Reaction was performed using only CH_3CN as solvent. [d] Isolated yield is shown in parentheses.

The synthetic potential of the catalyst-free flow procedure was then examined (Figure 19), demonstrating its generality with respect to both the olefin (**1** or **4**) and perfluoroalkyl iodide

components (**2**). A standard residence time of 5 min was found to be suitable for most alkene substrates when paired with the highly reactive perfluoroalkyl iodide **2a**. Less reactive alkenes **1l** and **1m**, required elongated residence times to reach full conversion, whereby **3p** was isolated in a modest 52% yield as a 3:1 mixture of diastereomers. Diphenylacetylene derivative **4b** proved to be completely unreactive, as has been observed previously for styrene-type substrates in ATRA reactions.[20] A slightly shorter perfluorinated chain (iodide **2b**) provided products **3s** and **3t** in synthetically useful yields. However, the sterically hindered iodide **2d** required longer residence times to achieve good yields in both examined cases (**3u** and **3v**). Furthermore, as the perfluoroalkyl chain on iodide substrate **2** was shortened further, longer reaction times were required due to the less polarized (and therefore stronger) C–I bond. Gaseous iodide reagents **2f** and **2g** were used as solutions in CH_3CN and a small back pressure of 3 bar was applied to the reactor to prevent gassing out. These reagents warranted a larger excess (4 equiv.), but also afforded their corresponding products with various olefins (**3w** to **3aa** or **5c**) in good to excellent yields.

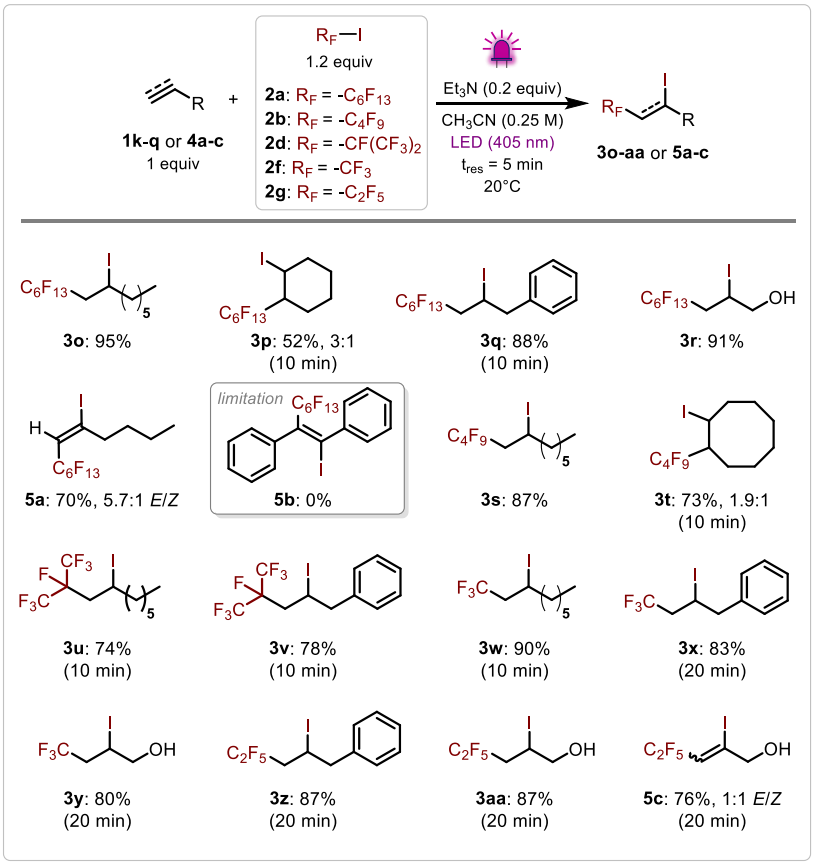

Figure 19. Evaluation of the scope of the flow photochemical ATRA reaction under purple light irradiation. Survey of the olefins and perfluoroalkyl iodides which can participate in the process. Reaction conditions: alkene or alkyne (**1**, 1 equiv.), perfluoroalkyl iodide (**2a-b,d,f-g**: 1.2 equiv., or **2f-g**: 4 equiv) and Et_3N (0.2 equiv) in CH_3CN (0.25 M). Reactions were performed on 1.25 mmol (5 mL) scale in 5 min residence time, unless otherwise specified. *E/Z* ratio and *d.r.* determined by ^{1}H-NMR spectroscopy of the crude reaction mixture.

Lastly, we envisaged that this protocol could be used in the preparation of a perfluorinated side chain, for active pharmaceutical ingredient (API) preparation (Figure 20).[78,79] In particular, breast cancer drug Fulvestrant contains a perfluorinated side chain,[80] synthesized from intermediate alcohol **6**, which, in turn can be reached by hydrogenation/dehalogenation (hydrogenolysis) of

products **3aa** or **5c**. During commercial route development for Fulvestrant, the supply and cost of intermediate **6** was noted as a main concern,[79] which highlights the need for a scalable synthesis, such as this flow methodology.

The required dehalogenation reaction was carried out in a continuous manner using an H-Cube Pro reactor equipped with a platinum oxide hydrogenation catalyst cartridge. For this manipulation, the crude mixture from the photochemical reactor was diluted to 0.1 M (to avoid precipitation), sparged with argon (to remove the excess of perfluoroalkyl iodide), and additional Et_3N (2 equiv.) was added. Complete conversion of **3aa** into the deiodinated product **6** was observed in less than 1 min residence time (50 °C, 20 bar). The obtained pentafluoropentanol (**6**) is the desired side chain of Fulvestrant,[79] but, due to its volatility, it was decided to functionalize this intermediate further as its benzoyl ester **7** for isolation. To demonstrate the scalability of this protocol, a long run experiment was successfully performed. These experiments consist of continuously running the flow apparatus over the time in order to collect relevant amounts of the desired product, without modifying the dimensionality of the flow system.[81] In this way, starting from a large feedstock solution of alkene **1o**, the final compound **7** was isolated in gram-scale over three steps (1.23 g, 73% yield over three steps), with only a single chromatographic purification.

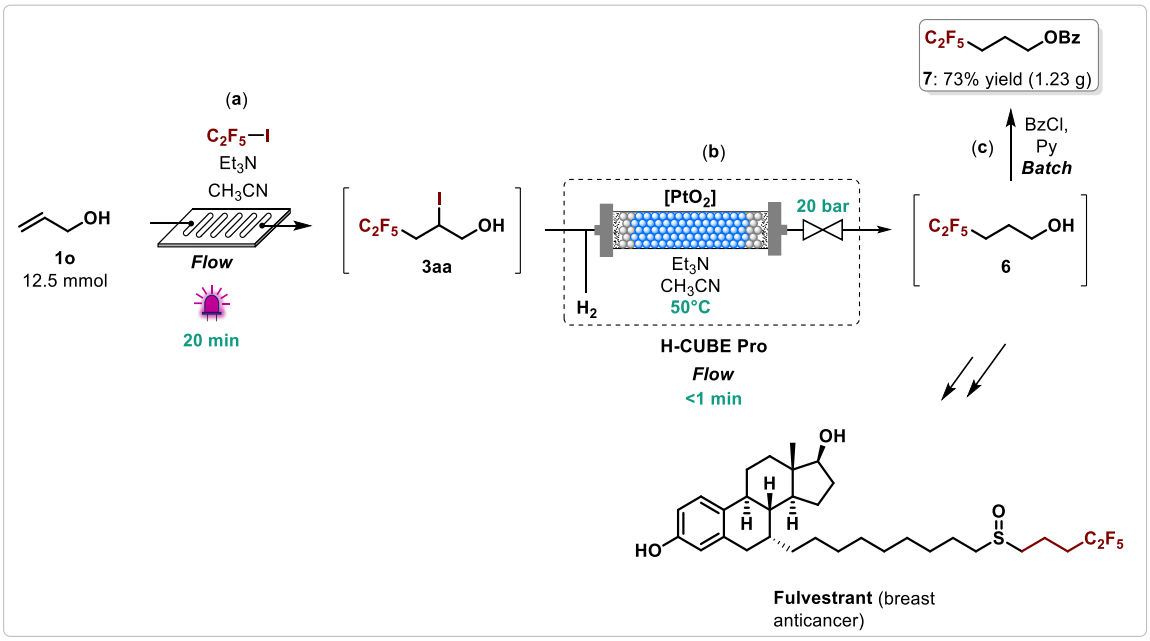

Figure 20. Fulvestrant precursor preparation. Reaction conditions: (**a**) as specified for **3ab** in Figure 19; (**b**) crude mixture from previous transformation, sparged with argon, added Et_3N (2 equiv.) and diluted to 0.1 M in CH_3CN, 50 °C, 20 bar pressure, 1 mL/min flow rate; (**c**) crude mixture from previous transformation, added benzoyl chloride (5 equiv.) and pyridine (8 equiv.), stirred at rt for 16 h.

2.7 Mechanistic Investigations of the Catalyst-free Flow Iodoperfluoroalkylation of Olefins

For further mechanistic insight, we sought to confirm the halogen-bonding activation of this ATRA reaction system. A series of ^{19}F-NMR experiments were performed using different ratios of perfluorohexyl iodide (**2a**) and Et_3N in CD_3CN, whereby a Job's plot analysis verified the formation of a 1:1 halogen-bonded complex (x_{max} = 0.5, Figure 21).[26,76,77] Particularly, the total amount of **2a** and Et_3N was kept constant to a certain value. The amount of **2a** was varied from 0 to 1 molar ratio. The chemical shift difference (Δδ) between $–CF_2I$ in the different mixtures *vs* an internal standard was calculated and the binding stoichiometry was then determined plotting [**2a**]/[**2a** + Et_3N] vs [**2a**] × Δδ. Previous reports have implied that involvement of solvent is required,[26] which may also be the case in our system.

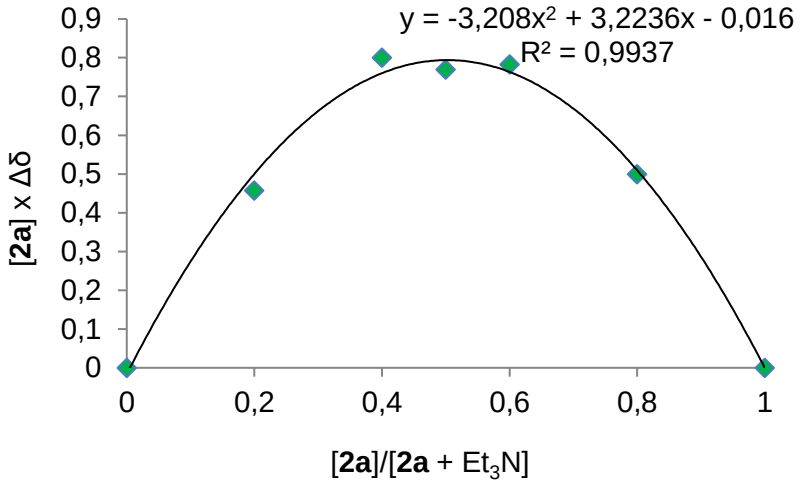

Figure 21. Job's plot analysis.

$$x_{max} = \frac{3.223}{-2 \times (-3.208)} = 0.50$$

In addition, an association constant of 1.57 M^{-1} was determined in CD_3CN using Hanna and Ashbaugh's method (Figure 22).[82] Also in this case, ^{19}F spectra of different mixtures of **2a** and Et_3N were recorded in CD_3CN. On the other hand, the amount of **2a** was kept constant and the amount of Et_3N was varied from 0 to 30 equivalents with respect to **2a**. The chemical shift difference (Δδ) between $–CF_2I$ in the different mixtures *vs* an internal standard was calculated, and the binding stoichiometry was then determined plotting 1/[Et_3N] *vs* 1/Δδ. This value is consistent with previously reported halogen bond complexes between perfluoroalkyl iodides and Et_3N in Lewis basic solvents.[83,84]

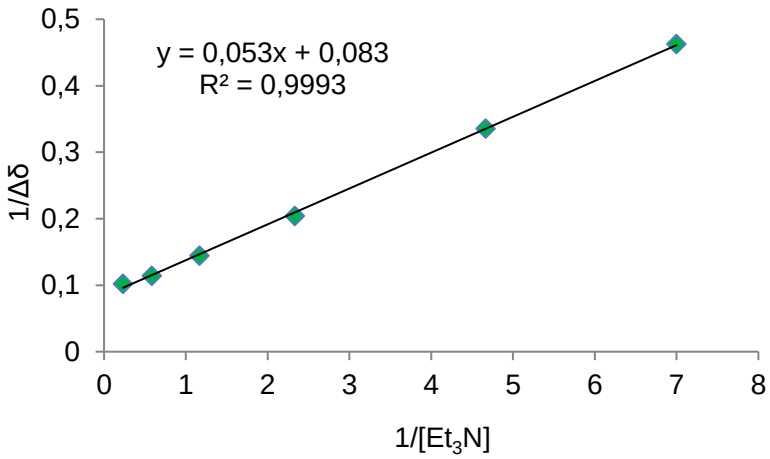

Figure 22. Association constant determination.

$$K_a = \frac{intercept}{slope} = \frac{0.053}{0.083} = 1.57\ M^{-1}$$

Furthermore, the kinetic profile of the model reaction between **1k** and **2a** revealed an induction period of at least 30 seconds, likely corresponding to the time taken to cleave enough C–I bonds for effective radical chain conjugation (Figure 23).[13]

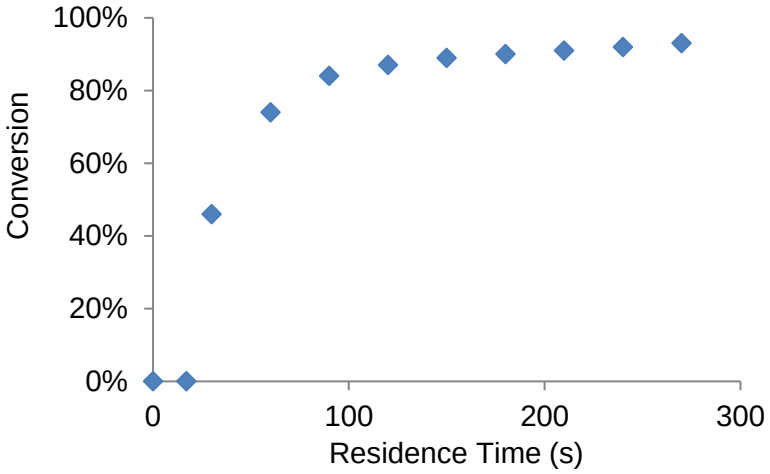

Figure 23. Kinetic profile of the model reaction performed in flow, irradiated at 405 nm in the absence of **A**.

Finally, UV-Vis experiments of the crude mixture in acetonitrile highlighted the formation of five different bands during the reaction progress. These spectroscopic measurements were carried out on the reaction crude output immediately after shining light, upon appropriate dilution. Two of such bands are present in the UV region (250 and 350 nm) and three are centered in the visible (440, 500 and 570 nm). The first set of signals is observed using a concentration of 0.0025 M with respect to the alkene **1a** and the second set is clearly observable at 0.025 M (Figure 24a-b). For comparison, the spectrum of the pure product **3o** is also shown (λ_{max} = 265 nm, Figure 24c).

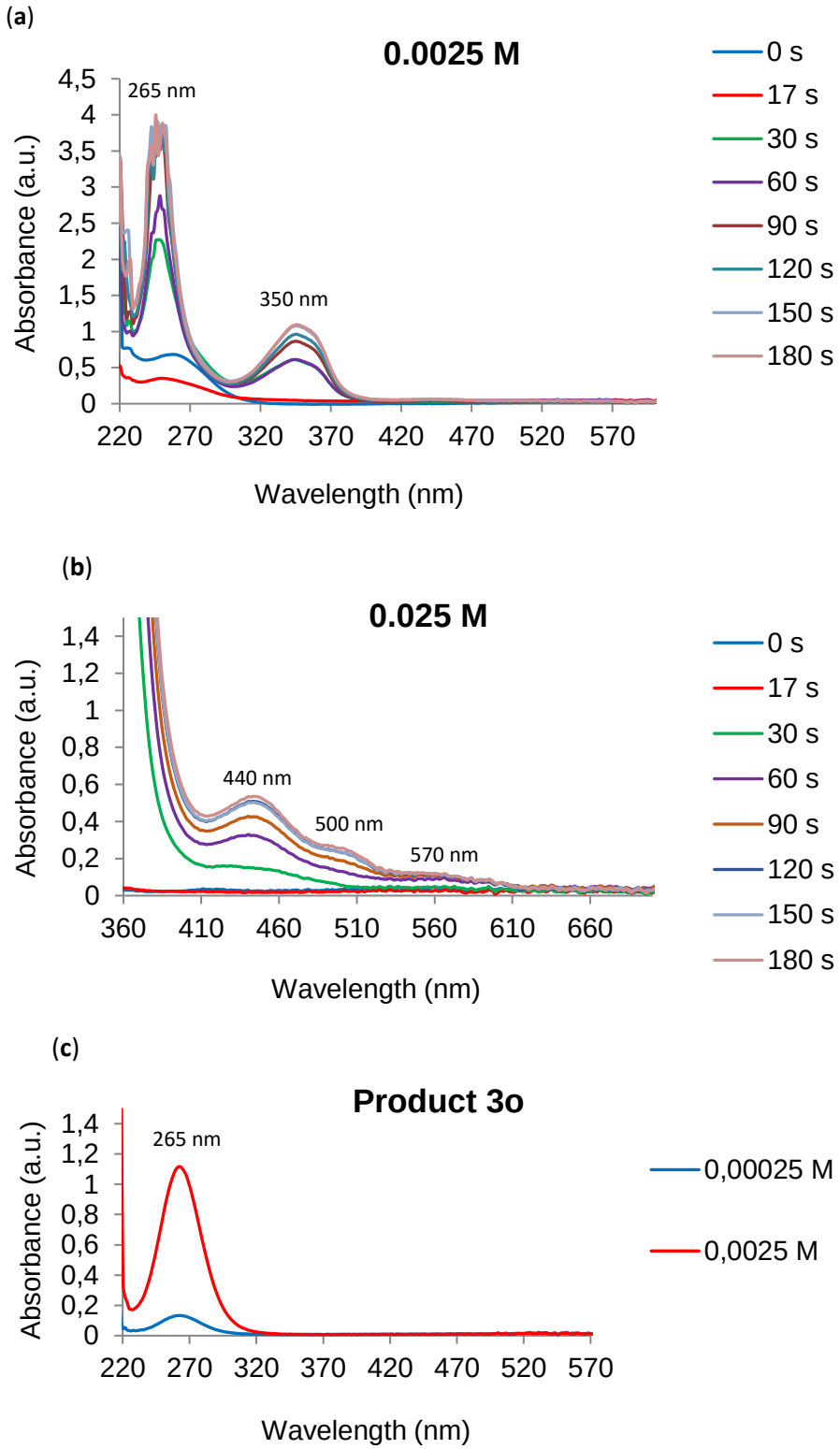

Figure 24. (**a**) Optical absorption spectra recorded in acetonitrile. Optical path length 1 cm. (**a**) Spectra of the reaction output obtained at different residence times (0.0025 M). (**b**) Spectra of the reaction output obtained at different residence times (0.025 M). (**c**) Spectra of the pure product **3o** in acetonitrile at 0.00025 M (blue line) and 0.0025 M (red line).

2.8 Conclusions

In summary, we first developed an efficient batch methodology for the direct iodoperfluoroalkylation of alkenes (**2**). The chemistry was driven by the photochemical activity of a simple perylene diimide (**A**), which was used in extremely low catalytic loading (0.05 mol% = 500 ppm) under visible light irradiation. Products **3** have been isolated in very high overall yields (up to 98% yield) employing mild reaction conditions. Remarkably, the studied protocol far surpasses the state of the art in terms of rate of production (about 700 *vs* 260 $mmol_{\mathbf{3a}}h^{-1}g_{\mathbf{A}}^{-1}$ for the Ru-based photocatalytic system).[20] In addition, preliminary mechanistic studies have suggested the existence of a radical degradation pathway of catalyst **A**.

Successively, due to the synthetic relevance of iodoperfluoroalkyl compounds **3**, we envisaged a preparative scale production by means of continuous flow technology. To this aim, we established two complementary flow methods, with productivity up to 7.6 g h^{-1}. The ATRA reaction can be achieved under irradiation at 405 nm, using substoichiometric loading of an inexpensive amine base. Alternatively, reaction can also be achieved by irradiation at a longer wavelength (450 nm), in the presence of a low loading of PDI **A** dye. In situations with light-sensitive substrates, this method could also prove to be of importance. Mechanistic insights were gained regarding the halogen-bond photoactivation of perfluoroalkyl iodides by Et_3N. Lastly, a gram-scale preparation of a fluorinated API intermediate was demonstrated in two flow steps from inexpensive starting materials, substantiating our initial hypothesis. Interestingly, our approach was further developed within the scientific community, since a number of different halogen-bond-activated perfluoroalkylation procedures have been developed in the following year (e.g., by using phosphines, ketones, etc. as electron donors).[85–87]

2.9 Experimental Section

2.9.1 General Information

NMR spectra were recorded on Varian 400 spectrometer (^{1}H: 400 MHz, ^{13}C: 100.5 MHz and 376 MHz for ^{19}F), or on Bruker 300 MHz spectrometer (^{1}H: 300 MHz, ^{13}C: 75 MHz and 282 MHz for ^{19}F). The chemical shifts (δ) for ^{1}H, ^{13}C and ^{19}F are given in ppm relative to residual signals of the solvent ($CHCl_3$ at 7.26 ppm ^{1}H-NMR and 77.16 ppm ^{13}C-NMR). Coupling constants are given in Hertz (Hz). The following abbreviations are used to indicate the multiplicity: s, singlet; d, doublet; t, triplet; q, quartet; dd, doublet of doublets; ddd, doublet of doublet of doublets; m, multiplet.

Gas chromatography with flame ionization detector (GC-FID) analyses were performed on a ThermoFisher Focus GC with a flame ionization detector, using a TR-5MS column (30 m × 0.25 mm ID × 0.25 µm) and helium as carrier gas (1 mL min^{-1} constant flow). The injector temperature was set to 280 °C. After 1 min at 50 °C, the temperature was increased by 25 °C/min to 300 °C and kept constant at 300 °C for 4 min. The detector gases used for flame ionization were hydrogen and synthetic air (5.0 quality).

High resolution mass spectra (HRMS) were obtained on Bruker micrOTOF-Q (ESI-TOF) or by using using a Q-Exactive Hybrid Quadrupole-Orbitrap MS following flow injection analysis of the re-

dissolved sample with a Dionex Ultimate 3000 series HPLC-system (Thermo Fisher Sci., Erlangen, Germany). The injection volume was 5 µL and the flow was 200 µL min^{-1} of acetonitrile (>99.9 % HPLC-grade; Chem-Lab NV, Zedelgem, Germany). The HR-MS was fitted with, either a HESI-II atmospheric pressure electrospray ionization source, or a combination of an APCI Ion Max heated probe source with an APPI Photo Mate® UV light source for mixed atmospheric pressure chemical and photo ionization. Nitrogen was used as nebulizer and drying gas.

ESI measurements were performed in negative ionization mode using the following settings: spray voltage -2.5 kV, capillary temperature 250 °C, sheath gas flow rate 45 instrument units (IU), auxiliary gas temperature 300 °C, auxiliary gas flow rate 10 IU, automatic gain control target 3e6, maximum injection time 100 ms, and the resolution was 70000 (FWHM).

APCI+APPI measurements were performed in positive ionization mode using the following settings: corona discharge current +4 µA, sheath gas flow rate 20 IU, auxiliary gas flow rate 5 IU, and the remaining settings were the same as for ESI. High resolution mass spectra were extracted from a scanned mass range of m/z 220-390 in both ionization modes.

UV-Vis measurements for the mechanistic investigations of the batch transformation were carried out on PerkinElmer Lambda 35 UV-Vis spectrophotometer. All the spectra were recorded at room temperature using 10 mm path-length cuvettes. UV-Vis spectra for the mechanistic investigations of the flow transformation were recorded using a fiber-coupled Avantes Starline AvaSpec-2048 spectrometer, with an Avantes AvaLight-DHc lamp as the light source. These spectra were processed using Avasoft 8.7 software.

Infrared (IR) spectra were measured on a Bruker alpha p instrument, using attenuated total reflectance (ATR). Spectra were processed using OPUS v6.5 software.

Simulated sunlight reaction was driven on a Lot-Oriel solar simulator equipped with a 300W xenon lamp and an integrated Atmospheric Edge Filter with a cut-off at 300 nm.

Dehalogenation reactions using PtO_2 catalyst (commercially available 70 mm CatCart®, supplied by Thales Nano) under continuous flow were performed using an H-CUBE Pro® system from ThalesNano, with a Knauer HPLC pump.

General Procedures in Batch

All reactions were set up under an argon atmosphere in Schlenk tubes, unless otherwise stated. Synthesis grade and anhydrous solvents were used as purchased. Chromatographic purification of products was accomplished using flash chromatography on silica gel (35-70 mesh). For thin layer chromatography (TLC) analysis throughout this work, Merck pre-coated TLC plates (silica gel 60 GF_{254}, 0.25 mm) were employed, using UV light as the visualizing agent (254 nm), basic aqueous potassium permanganate ($KMnO_4$) stain solution, and heat as developing agents. Organic solutions were concentrated under reduced pressure on a Büchi rotatory evaporator. The light source used to illuminate the reaction mixture consisted of a single blue LED (450-455 nm, 10 mm, 3.5 V and 700 mA controlled by an external power supply, Figure 25) produced and purchased by Addicore™ (for

more details, see: https://www.addicore.com/3W-Royal-Blue-LED-on-Star-Board-Heatsink-p/ad425.htm).

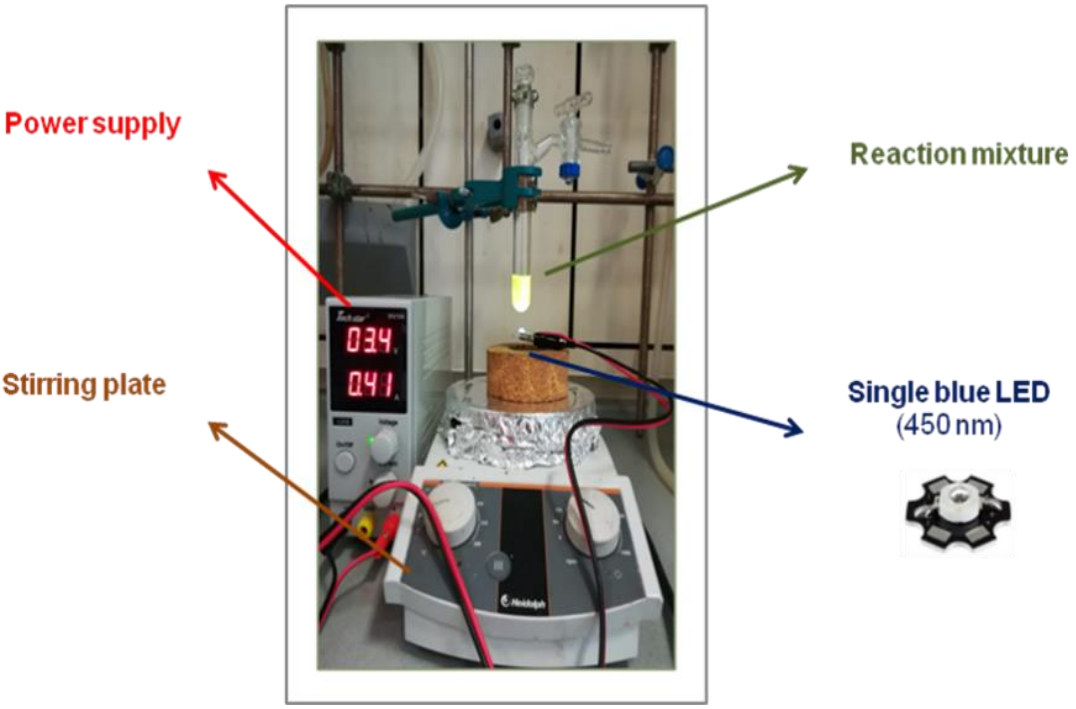

Figure 25. Reaction set-up of the photochemical iodoperfluoroalkylations of alkenes in batch. The power supply controls the light intensity.

General Procedures in Continuous Flow

All photochemical reactions were conducted in a commercial continuous-flow reactor: Corning AdvancedFlow Lab Photo Reactor (Figure 17).

Reactor module (G1 "low flow" fluidic module): A compact glass fluidic module (155 × 125 × 8 mm size, 0.3 mm channel depth, 2.77 mL internal volume), encased within a high-capacity heat exchange channel (20 mL volume).

Light source: LED panels were mounted on both sides of the fluidic module (40 mm from the center of the reaction layer). Each LED panel was equipped with 20 LEDs of 6 different wavelengths (120 LEDs in total) and a heat exchanger (T = 15 °C). The LED wavelength and intensity were controlled externally using a web-based interface, connected wirelessly to a router.

Two separate panels were used for various experiments in this study (panel 1 = 340, 375, 395, 422, 450, 540 nm; panel 2 = 365, 385, 405, 485, 610 nm and "4000K" white light).

Temperature control: Thermal regulation of the LED panels was carried out using a Huber Minichiller 280 filled with 30% ethylene glycol in water. Thermal regulation of the glass fluidic module was carried out using a Huber Ministat 230 filled with silicon oil (–20 °C to 195 °C).

Pumps: The feed solution was conveyed to the photoreactor using a FLOM UI 22-110DC HPLC pump (0.01-10 mL/min; wetted-parts: PTFE, PCTFE, FFKM and ruby).

Backpressure regulator: For experiments using gaseous perfluoroalkyl iodides, a dome-type backpressure regulator (BPR-10, Zaiput Flow Technologies) was installed after the reactor exit with a set point of 3 bar.
General connections: Connection between the pumps, fluidic module input and output was achieved using 1/8" (external diameter) PFA tubing (Swagelok), using metal-free connectors (Swagelok MS-GC-2 swaging system). Other connections used 1/16" (external diameter) PFA tubing, with PEEK fittings.
Sample loop: For optimization and substrate scope experiments, an Upchurch 6-way switching valve was used (part # V-450, https://www.idex-hs.com/store/injection-valve-2-postion-6-port-040-black.html), with a 5 mL sample loop (made from 1/16" outer diameter, 0.8 mm internal diameter PFA tubing) installed.

Chromatographic purification of products obtained in flow was accomplished using a Biotage Isolera automated flash chromatography system with cartridges packed with KP-SIL, 60 Å (32–63 µm particle size).

Materials
Commercial reagents and solvents were purchased Sigma-Aldrich, Fluka, Alfa Aesar, Fluorochem or TCI and used as received, without further purification, unless otherwise stated. 1-hexene (**1a**), 1-decen (**1b**), 6-chloro-1-hexene (**1c**), 6-bromo-1-hexene (**1d**), 5-hexen-1-ol (**1e**), 1-octene (**1k**), cyclohexene (**1l**), cyclooctene (**1m**), allylbenzene (**1n**), allyl alcohol (**1o**), 1-hexyne (**4a**), diphenylacetylene (**4b**), propargyl alcohol (**4c**), perfluorohexyl iodide (**2a**), nonafluoro-1-iodobutane (**2b**), heptadecafluoro-1-iodooctane (**2c**), heptafluoro-2-iodopropane (**2d**), iodopentafluorobenzene (**2e**), trifluoroiodomethane (**2f**), pentafluoroiodoethane (**2g**), triethylamine, 4-methoxy-N,N-diphenylaniline, (+)-sodium L-ascorbate, pyridine, and benzoyl chloride were all commercially available. The preparation of olefins **1f-j** is detailed in Section 2.9.2.

*^{1}H NMR, ^{13}C and ^{19}F NMR traces and spectra are available in the published manuscripts[1,2] and are not reported in the present thesis. Due to the C-F coupling, some carbon signals of the perfluorinated products **3** were not detectable.*

2.9.2 Synthesis of the Photocatalyst A-C and the Starting Materials

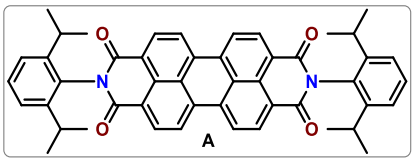

PDI **A** was prepared according to the modified literature procedure.[88] A mixture of 2,6-diisopropylaniline (2.07 mL, 11 mmol), perylene-3,4:9,10-tetracarboxylic dianhydride (1.96 g, 5 mmol) and imidazole (10 g) was stirred at 160°C for 4 h, then diluted with ethanol. This was followed by the addition of HCl (2 M, 200 mL). The reaction mixture was then allowed to settle. The precipitate thus formed was collected through vacuum filtration. Further purification by silica gel

chromatography using dichloromethane as the eluent provided the desired product (**A**) in 75% yield (2.70 g). The characterization of the compound matches the data reported in the literature.[88]

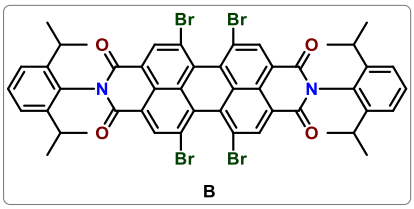

B

PDI **B** was prepared according to the modified literature procedures in two steps.[89,90] A mixture of perylene-3,4,9,10-tetracarboxylic acid dianhydride (PDA, 19.6 g, 50 mmol) and sulfuric acid (220 mL, 98 wt%) was stirred at room temperature for 12 h. The mixture was then heated to 80°C and I_2 (0.31 g, 1.2 mmol) was added. Subsequently, Br_2 (5.4 mL, 105 mmol, 2.1 equiv.) was added dropwise over 8 h and the reaction mixture was heated for 24 h at 80°C. The addition of I_2 and Br_2 was repeated and the reaction temperature was raised to 100 °C for 80 hours. After being cooled to room temperature, the excess bromine was removed by a gentle stream of N_2 gas, and ice was added slowly (80 g). The resultant precipitate was filtered, washed with sulfuric acid (200 mL, 86 %) and a large amount of water until the filtrate became neutral. The solid residue was dried in a vacuum at 120 °C for 8 h to give the corresponding tetrabrominated PDA as a red-brown powder (30 g, 85 % yield). The crude product was used directly in the later reaction without further purification. 2,6-Diisopropylaniline (2.0 g, 11.3 mmol) was added to a mixture of tetrabrominated PDA (2.0 g, 2.8 mmol, 4 equiv.) and propionic acid (40 mL) under an N_2 atmosphere, then the reaction mixture was stirred and heated at 140°C for 10 h. After being cooled to room temperature, the solvent was removed under reduced pressure, and the crude product was purified by flash column chromatography (petroleum ether/dichloromethane) to yield PDI **B** as a red-brown solid (2.2 g, 82% yield). The characterization of the compound matches the data reported in the literature.[90]

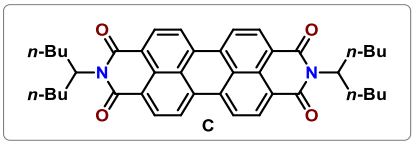

C

PDI **C** was prepared according to the modified literature procedure.[91] A mixture of perylene-3,4,9,10-tetracarboxylic dianhydride (PDA, 5.88 g, 15 mmol), 5-nonanamine (10.26 g, 60 mmol), and imidazole (60 g) was stirred at 160 °C for 4 h under argon. After cooling, the mixture was poured into 2 M HCl (350 mL) and stirred overnight. The product was extracted with DCM, washed with water, dried over sodium sulfate. The solvent was removed under reduced pressure. The crude product was purified by flash column chromatography (DCM) to give the corresponding PDI **C** (9.3 g, 88% yield). The characterization of the compound matches the data reported in the literature.[91]

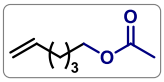

Synthesis of hex-5-en-1-yl acetate (1f). In a two-neck round-bottomed flask, purged under argon, a solution of 5-hexen-1-ol **1e** (420 µL, 3.5 mmol, 1 equiv.) and 2,6-lutidine (408 µL, 3.5 mmol, 1 equiv.) in dry THF (10 mL) was stirred at 0°C for 10 minutes. Acetyl bromide (260 µL, 3.5 mmol, 1 equiv.) was added dropwise and the solution was stirred at room temperature over 3 hours. The reaction was quenched by the addition of water (10 mL) and then extracted with diethyl ether (3 x 10 mL). The organic phases were combined and washed with brine

(10 mL) and then dried over sodium sulfate. The solvent was removed under reduced pressure to give the corresponding alkene **1f** as a pale-yellow oil (141 mg, 28% yield). The characterization of the compound matches with the data reported in the literature.[92]

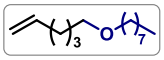

Synthesis of 1-(hex-5-en-1-yloxy)octane (1g). In a two-neck round-bottomed flask, purged under argon, a solution of 5-hexen-1-ol **1e** (420 µL, 3.5 mmol, 1 equiv.) and 1-bromooctane (610 µL, 3.5 mmol, 1 equiv.) in dry THF (14 mL) was stirred at 0°C for 10 minutes. Sodium hydride (170 mg, 4.2 mmol, 1.2 equiv.) was added portion wise and the solution was heated up to reflux and stirred overnight. The reaction was quenched by the addition of ammonium chloride (10 mL) and then extracted with ethyl acetate (3 x 10 mL). The organic phases were combined and washed with brine (10 mL) and then dried over sodium sulfate. The solvent was removed under reduced pressure and the residue was purified by flash column chromatography (n-hexane/ethyl acetate 95:5) to give the corresponding alkene **1g** as a pale-yellow oil (494 mg, 67% yield).

^{1}H-NMR (400 MHz, $CDCl_3$) δ 5.79 (ddt, *J* = 16.9, 10.2, 6.7 Hz, 1H), 5.06–4.89 (m, 2H), 3.38 (td, *J* = 6.6, 4.9 Hz, 4H), 2.12–2.01 (m, 2H), 1.56 (dp, *J* = 9.6, 6.8 Hz, 4H), 1.49–1.38 (m, 2H), 1.38–1.22 (m, 10H); ^{13}C-NMR (101 MHz, $CDCl_3$) δ 138.85 (s), 114.52 (s), 71.09 (s), 70.80 (s), 33.71 (s), 31.97 (s), 29.92 (s), 29.60 (s), 29.41 (s), 29.38 (s), 26.34 (s), 25.66 (s), 22.78 (s), 14.19 (s); HRMS calculated for $C_{14}H_{28}O$ (M-Na): 235.2038, found: 235.2032.

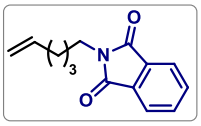

Synthesis of 2-(hex-5-en-1-yl)isoindoline-1,3-dione (1h). In a two neck round-bottomed flask, purged under argon, a mixture of 6-chloro-1-hexene **1c** (400 µL, 3 mmol, 1 equiv.), potassium phthalimide (610 mg, 3.3 mmol, 1.1 equiv.) and potassium iodide (50 mg, 0.3 mmol, 0.1 equiv.) in dry DMF (5 mL) was heated up to 90°C and stirred overnight. The reaction was quenched by the addition of water (10 mL) and then extracted with dichloromethane (3 x 10 mL). The organic phases were combined and washed with KOH 0.2 M (10 mL), brine (10 mL) and then dried over sodium sulfate. The solvent was removed under reduced pressure and the residue was purified by flash column chromatography (n-hexane/ethyl acetate 9:1) to give the corresponding alkene **1g** as a pale-yellow oil (506 mg, 74% yield). The characterization of the compound matches with the data reported in the literature.[26]

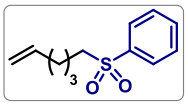

Synthesis of (hex-5-en-1-ylsulfonyl)benzene (1i). In a two-neck round-bottomed flask, purged under argon, a mixture of 6-bromo-1-hexene **1d** (260 µL, 2 mmol, 1 equiv.), sodium benzenesulfinate (391 mg, 2.4 mmol, 1.2 equiv.) tetrabutylammonium iodide (74 mg, 0.2 mmol, 0.1 equiv.) in dry DMF (2 mL) was heated up to 60°C and stirred over 5 hours. The reaction was quenched by the addition of brine (5 mL) and then extracted with ethyl acetate (3 x 5 mL). The organic phases were combined and washed with brine (5 mL) and then dried over sodium sulfate. The solvent was removed under reduced pressure and the residue was purified by flash column chromatography (n-hexane/ethyl acetate 9:1) to give the corresponding alkene **1i** as a colorless oil (372 mg, 83% yield). The characterization of the compound matches with the data reported in the literature.[93]

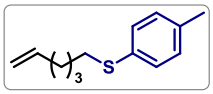

Synthesis of hex-5-en-1-yl(p-tolyl)sulfane (1j). Prepared according to a modified literature procedure.[94] 4-methylbenzenethiol (186 mg, 1.5 mmol, 1.5 equiv.) was added to a degassed solution of sodium hydroxide (120 mg, 3 mmol, 3 equiv.) in water (10 mL). The solution was stirred for 30 minutes until it had reached room temperature. Thereafter, 6-bromo-1-hexene **1d** (130 µL, 1 mmol, 1 equiv.) was added dropwise. The reaction mixture was stirred at room temperature overnight. The product was extracted with diethyl ether (3 x 10 mL) and then washed with water (10 mL) and brine (10 mL) and dried over sodium sulfate. After evaporation of the solvent, the crude product **1j** was collected as a light-yellow oil (148 mg, 72% yield).

^{1}H-NMR (400 MHz, $CDCl_3$) δ 7.33–7.27 (m, 2H), 7.14 (d, *J* = 7.9 Hz, 2H), 5.84 (ddt, *J*=16.9, 10.2, 6.7 Hz, 1H), 5.13–4.94 (m, 2H), 3.01–2.86 (m, 2H), 2.36 (s, 3H), 2.18–2.06 (m, 2H), 1.75–1.64 (m, 2H), 1.63–1.45 (m, 2H); ^{13}C-NMR (101 MHz, $CDCl_3$) δ 138.45 (s), 135.81 (s), 133.20 (s), 129.81 (s), 129.64 (s), 114.73 (s), 34.20 (s), 33.31 (s), 28.74 (s), 28.02 (s), 21.03 (s); It was not possible to measure the HRMS (ESI-MS) of compound **1j** due to its poor tendency to ionize.

2.9.3 General Procedures for the Iodoperfluoroalkylation of Alkenes in Batch and Characterization Data

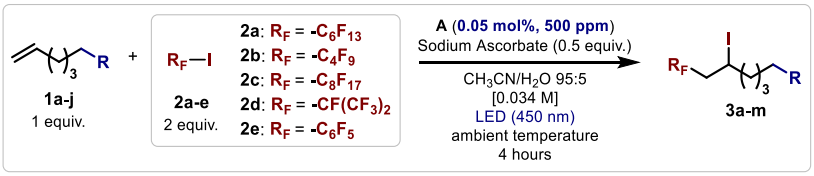

A 20 mL Schlenk tube was charged with the appropriate alkene **1** (0.1 mmol, 1 equiv.), perfluoroalkyl iodide **2** (0.2 mmol, 2 equiv.), sodium ascorbate (0.05 mmol, 0.5 equiv.) and the photocatalyst **A** (0.05 mol% = 500 ppm, with respect to the alkene **1**, 35 µg). To this suspension was then added a solution of acetonitrile and water in 95:5 ratio (3 mL, $[\mathbf{1}]_0$=0.034 M). The reaction mixture was thoroughly degassed via freeze-pump-thaw cycles (x 3) and the Schlenk tube was filled with argon and placed at 3 cm on top of a single blue LED (450 nm, 3.5V and 700 mA controlled by an external power supply). Stirring was maintained for 4 hours and then the irradiation was stopped. The reaction crude was diluted with dichloromethane and filtered through sodium sulfate. The solvent was removed under reduced pressure and the residue was purified by column chromatography (eluent: *n*-hexane/ethyl acetate) to give the corresponding iodoperfluoroalkyl compound **3**.

Characterization Data

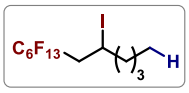

1,1,1,2,2,3,3,4,4,5,5,6,6-tridecafluoro-8-iododododecane (3a). Prepared according to the general procedure using 1-hexene **1a** (0.1 mmol, 13 µL) and perfluorohexyl iodide **2a** (0.2 mmol, 44 µL). The product **3a** was obtained as colorless oil (52 mg, 98% yield). The characterization of the compound matches with the data reported in the literature.[95]

1 mmol scale reaction. The model reaction was replicated on a more synthetically useful scale using an 8 blue LEDs system and a different reaction vessel (see picture to the right). A 100 mL Schlenk tube was charged with 1-hexene **1a** (1 mmol, 124 µL, 1 equiv.), perfluorohexyl iodide **2a** (2 mmol, 432 µL, 2 equiv.), sodium ascorbate (0.5 mmol, 99 mg, 0.5 equiv.) and the photocatalyst **A** (0.05 mol% = 500 ppm, with respect to the alkene **1a**, 0.35 mg). To this suspension was then added a solution of acetonitrile and water in 95:5 ratio (30 mL, $[\mathbf{1a}]_0$=0.034 M). The reaction mixture was thoroughly degassed via freeze-pump-thaw cycles (x 4) and the Schlenk tube was filled with argon and placed in the center of an 8 blue LEDs system (450 nm, 3.5V and 700 mA controlled by an external power supply). Stirring was maintained for 4 hours and then the irradiation was stopped. The reaction crude was diluted with dichloromethane and filtered through sodium sulfate. The solvent was removed under reduced pressure and the residue was purified by column chromatography (eluent: *n*-hexane/ethyl acetate) to give the corresponding iodoperfluorohexyl compound **3a** (300 mg, 57% yield).

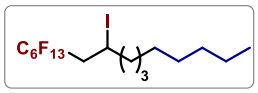

1,1,1,2,2,3,3,4,4,5,5,6,6-tridecafluoro-8-iodohexadecane (3b). Prepared according to the general procedure using 1-decen **1b** (0.1 mmol, 19 µL) and perfluorohexyl iodide **2a** (0.2 mmol, 44 µL). The product **3b** was obtained as colorless oil (57 mg, 97% yield). The characterization of the compound matches with the data reported in the literature.[28]

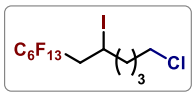

12-chloro-1,1,1,2,2,3,3,4,4,5,5,6,6-tridecafluoro-8-iododododecane (3c). Prepared according to the general procedure using 6-chloro-1-hexene **1c** (0.1 mmol, 13 µL) and perfluorohexyl iodide **2a** (0.2 mmol, 44 µL). The product **3c** was obtained as colorless oil (54 mg, 96% yield).

^{1}H-NMR (400 MHz, $CDCl_3$) δ 4.33 (ddd, *J* = 13.5, 8.4, 5.2 Hz, 1H), 3.56 (t, *J* = 6.5 Hz, 2H), 3.05–2.65 (m, 2H), 1.92–1.52 (m, 6H) ; ^{13}C-NMR (101 MHz, $CDCl_3$) δ 44.61 (s), 41.80 (s), 39.63 (s), 31.58 (s), 27.21 (s), 20.02 (s) ; ^{19}F-NMR decoupled ^{1}H (376 MHz, $CDCl_3$) δ -80.85 (m, 3F), -111.68 (m, 1F), -114.67 (m, 1F), -121.84 (m, 2F), -122.92 (m, 2F), -123.65 (m, 2F), -126.18 (m, 2F); It was not possible to measure the HRMS (ESI-MS) of compound **3c** due to its poor tendency to ionize.

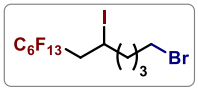

12-bromo-1,1,1,2,2,3,3,4,4,5,5,6,6-tridecafluoro-8-iododododecane (3d). Prepared according to the general procedure using 6-bromo-1-hexene **1d** (0.1 mmol, 14 µL) and perfluorohexyl iodide **2a** (0.2 mmol, 44 µL). The product **3d** was obtained as colorless oil (60 mg, 98% yield).

^{1}H-NMR (400 MHz, $CDCl_3$) δ 4.40–4.25 (m, 1H), 3.43 (t, *J* = 6.7 Hz, 1H), 3.27–3.15 (m, 1H), 3.05–2.67 (m, 2H), 2.05–1.59 (m, 6H); ^{13}C-NMR (101 MHz, $CDCl_3$) δ 33.12 (s), 32.43 (s), 31.72 (s), 30.77 (s), 28.47 (s), 19.78 (s); ^{19}F-NMR decoupled ^{1}H (376 MHz, $CDCl_3$) δ -80.85 (m, 3F), -111.62 (m, 1F), -114.65 (m, 1F), -121.81 (s, 2F), -122.89 (m, 2F), -123.65 (m, 2F), -126.18 (m, 2F); It was not possible to measure the HRMS (ESI-MS) of compound **3d** due to its poor tendency to ionize.

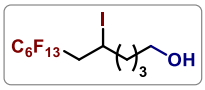

7,7,8,8,9,9,10,10,11,11,12,12,12-tridecafluoro-5-iododododecan-1-ol (3e). Prepared according to the general procedure using 5-hexen-1-ol **1e** (0.1 mmol, 12 µL) and perfluorohexyl iodide **2a** (0.2 mmol, 44 µL). The product **3e** was obtained as colorless oil (53 mg, 98% yield). The characterization of the compound matches with the data reported in the literature.[27]

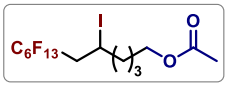

7,7,8,8,9,9,10,10,11,11,12,12,12-tridecafluoro-5-iododododecyl acetate (3f). Prepared according to the general procedure using hex-5-en-1-yl acetate **1f** (0.1 mmol, 14 mg) and perfluorohexyl iodide **2a** (0.2 mmol, 44 µL). The product **3f** was obtained as colorless oil (57 mg, 97% yield).

^{1}H-NMR (400 MHz, $CDCl_3$) δ 4.32 (ddd, *J* = 13.4, 8.5, 5.1 Hz, 1H), 4.08 (t, *J* = 6.3 Hz, 2H), 3.02–2.68 (m, 2H), 2.05 (s, 3H), 1.91–1.43 (m, 6H); ^{13}C-NMR (101 MHz, $CDCl_3$) δ 171.26 (s), 64.12 (s), 41.82 (t, *J* = 20.6 Hz), 39.90 (s), 27.67 (s), 26.35 (s), 21.08 (s), 20.29 (s); ^{19}F-NMR decoupled ^{1}H (376 MHz, $CDCl_3$) δ -80.85 (m, 3F), -111.63 (m, 1F), -114.68 (m, 1F), -121.83 (m, 2F), -122.89 (m, 2F), -123.66 (m, 2F), -126.17 (m, 2F); HRMS calculated for $C_{14}H_{14}F_{13}IO_2$ (M-Na): 610.9728, found: 610.9723.

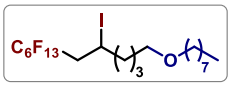

1,1,1,2,2,3,3,4,4,5,5,6,6-tridecafluoro-8-iodo-12-(octyloxy)dodecane (3g). Prepared according to the general procedure using 1-(hex-5-en-1-yloxy)octane **1g** (0.1 mmol, 21 mg) and perfluorohexyl iodide **2a** (0.2 mmol, 44 µL). The product **3g** was obtained as colorless oil (62 mg, 95% yield).

^{1}H-NMR (400 MHz, $CDCl_3$) δ 4.45–4.24 (m, 1H), 3.51–3.34 (m, 4H), 3.04–2.68 (m, 2H), 1.95–1.74 (m, 2H), 1.71–1.44 (m, 6H), 1.40–1.20 (m, 10H), 0.88 (t, *J* = 6.9 Hz, 3H); ^{13}C-NMR (101 MHz, $CDCl_3$) δ 71.25 (s), 70.46 (s), 41.81 (t, *J* = 20.9 Hz), 40.31 (s), 32.00 (s), 29.91 (s), 29.62 (s), 29.43 (s), 28.80 (s), 26.62 (s), 26.37 (s), 22.81 (s), 20.67 (s), 14.23 (s); ^{19}F-NMR decoupled ^{1}H (376 MHz, $CDCl_3$) δ -80.82 (tt, *J* = 9.9, 2.2 Hz, 3F), -111.82 (m, 1F), -114.61 (m, 1F), -121.81 (m, 2F), -122.88 (m, 2F), -123.66 (m, 2F), -126.17 (m, 2F); HRMS calculated for $C_{20}H_{28}F_{13}IO$ (M-Na): 681.0875, found: 681.0870.

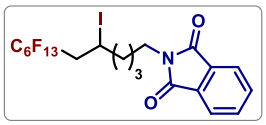

2-(7,7,8,8,9,9,10,10,11,11,12,12,12-tridecafluoro-5-iododododecyl)isoindoline-1,3-dione(3h). Prepared according to the general procedure using 2-(hex-5-en-1-yl)isoindoline-1,3-dione **1h** (0.1 mmol, 23 mg) and perfluorohexyl iodide **2a** (0.2 mmol, 44 µL). The product **3h** was obtained as colorless oil (63 mg, 93% yield).

^{1}H-NMR (400 MHz, $CDCl_3$) δ 7.84 (dd, *J* = 5.5, 3.0 Hz, 2H), 7.71 (dd, *J* = 5.4, 3.1 Hz, 2H), 4.30 (ddd, *J* = 16.8, 8.3, 5.3 Hz, 1H), 3.71 (t, *J* = 7.2 Hz, 2H), 3.00–2.68 (m, 2H), 1.95–1.39 (m, 6H) ; ^{13}C-NMR (101 MHz, $CDCl_3$) δ 168.51 (s), 134.07 (s), 132.23 (s), 123.36 (s), 39.82 (d, *J* = 1.9 Hz), 37.66 (s), 29.84 (s), 27.60 (s), 27.09 (s), 20.12 (s); ^{19}F-NMR decoupled ^{1}H (376 MHz, $CDCl_3$) δ -80.87 (tt, *J* = 10.0, 2.2 Hz, 3F), -111.77 (m, 1F), -114.63 (m, 1F), -121.83 (m, 2F), -122.93 (m, 2F), -123.69 (m, 2F), -126.20 (m, 2F); HRMS calculated for $C_{20}H_{15}F_{13}INO_2$ (M-Na): 697.9837, found: 697.9832.

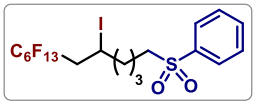

((7,7,8,8,9,9,10,10,11,11,12,12,12-tridecafluoro-5-iodododecyl)sulfonyl)benzene (3i). Prepared according to the general procedure using (hex-5-en-1-ylsulfonyl)benzene **1i** (0.1 mmol, 22 mg) and perfluorohexyl iodide **2a** (0.2 mmol, 44 µL). The product **3i** was obtained as colorless oil (65 mg, 97% yield).

^{1}H-NMR (400 MHz, $CDCl_3$) δ 7.95–7.88 (m, 2H), 7.71–7.64 (m, 1H), 7.58 (t, *J* = 7.6 Hz, 2H), 4.26 (ddd, *J* = 13.3, 8.5, 5.2 Hz, 1H), 3.15–3.08 (m, 2H), 2.99–2.62 (m, 2H), 1.87–1.70 (m, 4H), 1.71–1.60 (m, 1H), 1.56–1.45 (m, 1H); ^{13}C-NMR (101 MHz, $CDCl_3$) δ 139.20 (s), 133.93 (s), 129.50 (s), 128.19 (s), 56.08 (s), 41.75 (t, *J* = 20.9 Hz), 39.65 (d, *J* = 2.3 Hz), 28.58 (s), 21.87 (s), 19.54 (s); ^{19}F-NMR decoupled ^{1}H (376 MHz, $CDCl_3$) δ -80.80 (m, 3F), -111.52 (m, 1F), -114.69 (m, 1F), -121.80 (m, 2F), -122.85 (m, 2F), -123.61 (m, 2F), -126.09 (m, 2F); HRMS calculated for $C_{18}H_{16}F_{13}IO_2S$ (M-Na): 692.9606, found: 692.9600.

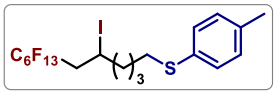

***p*-tolyl(7,7,8,8,9,9,10,10,11,11,12,12,12-tridecafluoro-5-iodododecyl)sulfane (3j).** Prepared according to the general procedure using hex-5-en-1-yl(p-tolyl)sulfane **1j** (0.1 mmol, 21 mg) and perfluorohexyl iodide **2a** (0.2 mmol, 44 µL). The product **3j** was obtained as colorless oil (38 mg, 58% yield).

^{1}H-NMR (400 MHz, $CDCl_3$) δ 7.34–7.19 (m, 2H), 7.10 (d, *J* = 7.9 Hz, 2H), 4.30 (ddd, *J* = 12.9, 7.0, 4.8 Hz, 1H), 3.07–2.64 (m, 4H), 2.32 (s, 3H), 1.90–1.50 (m, 6H); ^{13}C-NMR (101 MHz, $CDCl_3$) δ 136.40 (s), 132.64 (s), 130.39 (s), 129.84 (s), 39.92 (s), 34.37 (s), 29.86 (s), 28.87 (s), 28.32 (s), 21.13 (s), 20.30 (s); ^{19}F-NMR decoupled ^{1}H (376 MHz, $CDCl_3$) δ -80.79 (m, 2F), -111.68 (m, 1F), -114.60 (m, 1F), -121.79 (m, 2F), -122.85 (m, 2F), -123.64 (m, 2F), -126.13 (m, 2F); It was not possible to measure the HRMS (ESI-MS) of compound **3j** due to its poor tendency to ionize.

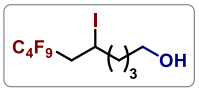

7,7,8,8,9,9,10,10,10-nonafluoro-5-iododecan-1-ol (3k). Prepared according to the general procedure using 5-hexen-1-ol **1e** (0.1 mmol, 12 µL) and nonafluoro-1-iodobutane **2b** (0.2 mmol, 34 µL). The product **3k** was obtained as colorless oil (42 mg, 95% yield). The characterization of the compound matches with the data reported in the literature.[96]

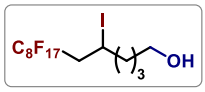

7,7,8,8,9,9,10,10,11,11,12,12,13,13,14,14,14-heptadecafluoro-5-iodotetradecan-1-ol (3l). Prepared according to the general procedure using 5-hexen-1-ol **1e** (0.1 mmol, 12 µL) and heptadecafluoro-1-iodooctane **2c** (0.2 mmol, 53 µL). The product **3l** was obtained as colorless oil (62 mg, 96% yield). The characterization of the compound matches with the data reported in the literature.[20]

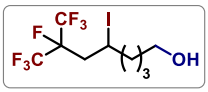

7,8,8,8-tetrafluoro-5-iodo-7-(trifluoromethyl)octan-1-ol (3m). Prepared according to the general procedure using 5-hexen-1-ol **1e** (0.1 mmol, 12 µL) and heptafluoro-2-iodopropane **2d** (0.2 mmol, 28 µL). The product **3m** was obtained as colorless oil (22 mg, 56% yield). The characterization of the compound matches with the data reported in the literature.[20]

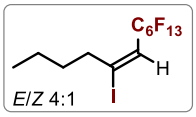

(*E*)-7,7,8,8,9,9,10,10,11,11,12,12,12-tridecafluoro-5-iodododec-5-ene (5a). Prepared according to the general procedure using 1-hexyne **4a** (0.1 mmol, 12 µL) and perfluorohexyl iodide **2a** (0.2 mmol, 44 µL). The product **5a** was obtained as colorless oil (36 mg, 70% yield, 4:1 *E*/*Z*). The characterization of the compound matches with the data reported in the literature.[97]

2.9.4 General Procedure for the Iodoperfluoroalkylation of Alkenes in Flow at 450 nm with Photocatalyst A (G1) and Characterization Data

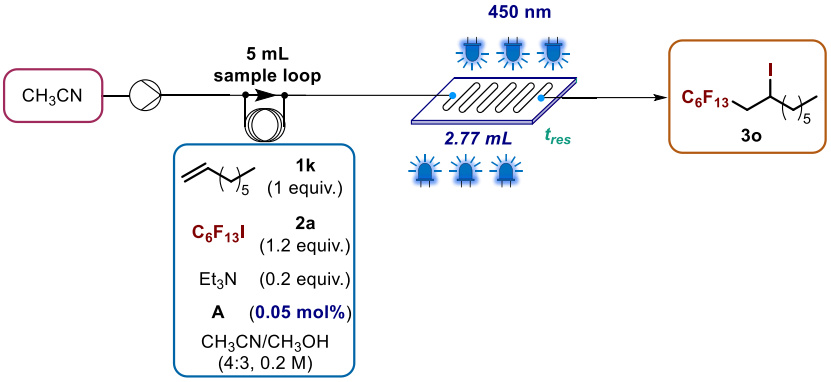

The 40 LED array was switched on at 450 nm and its thermal fluid was set to 15 °C. The reaction plate thermostat was set to 20 °C. A solution of 1-octene **1k** (1 mmol, 1 equiv) perfluorohexyl iodide **2a** (1.2 mmol, 1.2 equiv), PDI (0.05 mol% = 500 ppm, with respect to alkene **1k**, 0.35 mg) and triethylamine (0.2 mmol, 0.2 equiv) was made up in degassed acetonitrile/methanol in 4:3 ratio (5 mL total volume in a volumetric flask, solvent was degassed prior to use by sparging with argon for 15 minutes, $[\mathbf{1k}]_0$ = 0.2 M), then loaded into a 5 mL injection loop (fitted to an Upchurch 6-way valve). Acetonitrile was pumped through the 2.77 mL reaction plate at 0.554 mL/min flow rate, corresponding to 5 min residence time. After allowing the reactor to equilibrate for roughly 15 min, the reaction mixture was injected from the sample loop. The central 1 mL portion of this sample was collected for analysis by gas chromatography (GC-FID). For the isolation run, additional volume was collected to ensure that none of the 5 mL reaction mixture was lost due to longitudinal diffusion. The solvent was removed under reduced pressure and the residue was purified by column chromatography (eluent: petroleum ether/ethyl acetate) to give the corresponding iodoperfluoroalkyl compound **3o**.

Characterization Data

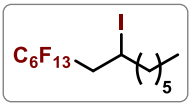

1,1,1,2,2,3,3,4,4,5,5,6,6-tridecafluoro-8-iodotetradecane (3o). Prepared according to the general procedure **G1** using 1-octene **1k** (1 mmol, 157 µL) and perfluorohexyl iodide **2a** (1.2 mmol, 260 µL). The product **3o** was obtained as colorless oil (503 mg, 90% yield). The characterization of the compound matches the data reported in the literature.[98]

2.9.5 General Procedure for the Iodoperfluoroalkylation of Alkenes in Flow at 450 nm with Photocatalyst A (G2) and Characterization Data

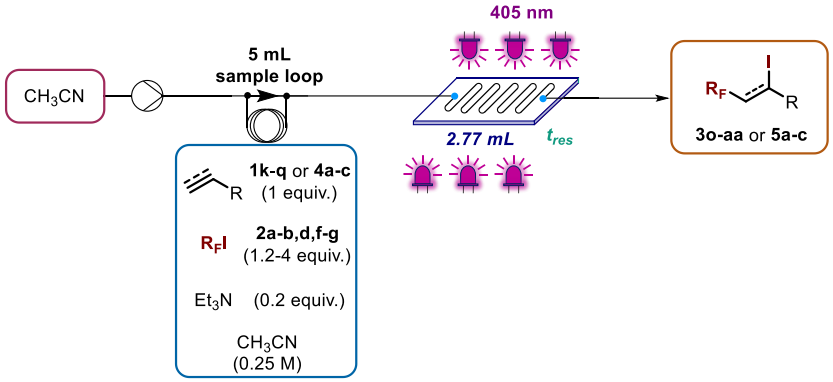

The 40 LED array was switched on at 405 nm and its thermal fluid was set to 15 °C. The reaction plate thermostat was set to 20 °C. A solution of olefin **1** or **4** (1.25 mmol, 1 equiv.) perfluoroalkyl iodide **2** (1.5 mmol, 1.2 equiv., for **2f** and **2g**: 5 mmol, 4 equiv. from a 2 M solution in acetonitrile), and triethylamine (0.25 mmol, 0.2 equiv.) was made up in degassed acetonitrile (5 mL total volume in a volumetric flask, solvent was degassed prior to use by sparging with argon for 15 minutes, $[\mathbf{1}]_0$ = 0.25 M), then loaded into a 5 mL injection loop (fitted to an Upchurch 6-way valve). Using a Zaiput backpressure regulator, a pressure of 3 bar was set before using perfluoroalkyl iodides **2f** and **2g**. Acetonitrile was pumped through the 2.77 mL reaction plate at 0.554 to 0.139 mL/min flow rate, corresponding to 5, 10 or 20 min residence time. After allowing the reactor to equilibrate for roughly 15 min, the reaction mixture was injected from the sample loop. The central 1 mL portion of this sample was collected for analysis by gas chromatography (GC-FID). For the isolation run, additional volume was collected to ensure that none of the 5 mL reaction mixture was lost due to longitudinal diffusion. The solvent was removed under reduced pressure and the residue was purified by column chromatography (eluent: petroleum ether/ethyl acetate) to give the corresponding iodoperfluoroalkyl compound **3** or **5**.

Characterization Data

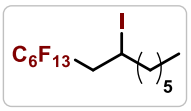

1,1,1,2,2,3,3,4,4,5,5,6,6-tridecafluoro-8-iodotetradecane (3o). Prepared according to the general procedure **G2** using 1-octene **1k** (1.25 mmol, 196 µL) and perfluorohexyl iodide **2a** (1.5 mmol, 325 µL) in a residence time of 5 min. The product **3o** was obtained as colorless oil (660 mg, 95% yield). The characterization of the compound matches the data reported in the literature.[98]

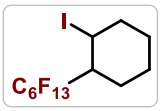

1-iodo-2-(perfluorohexyl)cyclohexane (3p). Prepared according to the general procedure **G2** using cyclohexene **1l** (1.25 mmol, 127 µL) and perfluorohexyl iodide **2a** (1.5 mmol, 325 µL) in a residence time of 10 min. The product **3p** was obtained as colorless oil (340 mg, 52% yield *d.r.* = 3:1). The characterization of the compound matches the data reported in the literature.[99]

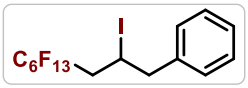

(4,4,5,5,6,6,7,7,8,8,9,9,9-tridecafluoro-2-iodononyl)benzene (3q). Prepared according to the general procedure **G2** using allylbenzene **1n** (1.25 mmol, 166

µL) and perfluorohexyl iodide **2a** (1.5 mmol, 325 µL) in a residence time of 10 min. The product **3q** was obtained as colorless oil (618 mg, 88% yield). The characterization of the compound matches the data reported in the literature.[28]

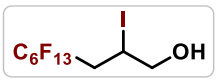

4,4,5,5,6,6,7,7,8,8,9,9,9-tridecafluoro-2-iodononan-1-ol (3r). Prepared according to the general procedure **G2** using allyl alcohol **1o** (1.25 mmol, 85 µL) and perfluorohexyl iodide **2a** (1.5 mmol, 325 µL) in a residence time of 5 min. The product **3r** was obtained as white solid (573 mg, 91% yield). The characterization of the compound matches the data reported in the literature.[100]

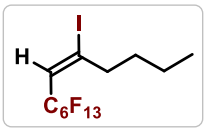

(*E*)-7,7,8,8,9,9,10,10,11,11,12,12,12-tridecafluoro-5-iodododec-5-ene (5a). Prepared according to the general procedure **G2** using 1-hexyne **4a** (1.25 mmol, 144 µL) and perfluorohexyl iodide **2a** (1.5 mmol, 325 µL) in a residence time of 5 min. The product **5a** was obtained as colorless oil (465 mg, 70% yield, *E/Z ratio* = 5.7:1). The characterization of the compound matches the data reported in the literature.[97]

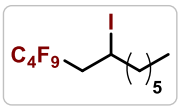

1,1,1,2,2,3,3,4,4-nonafluoro-6-iodododecane (3s). Prepared according to the general procedure **G2** using 1-octene **1k** (1.25 mmol, 196 µL) and nonafluoro-1-iodobutane **2b** (1.5 mmol, 258 µL) in a residence time of 5 min. The product **3s** was obtained as colorless oil (499 mg, 87% yield). The characterization of the compound matches the data reported in the literature.[101]

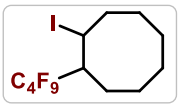

1-iodo-2-(perfluorobutyl)cyclooctane (3t). Prepared according to the general procedure **G2** using cyclooctene **1m** (1.25 mmol, 162 µL) and nonafluoro-1-iodobutane **2b** (1.5 mmol, 258 µL) in a residence time of 10 min. The product **3t** was obtained as colorless oil (417 mg, 73% yield, *d.r.* = 1.9:1). The characterization of the compound matches the data reported in the literature.[25]

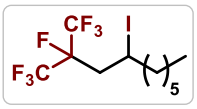

1,1,1,2-tetrafluoro-4-iodo-2-(trifluoromethyl)decane (3u). Prepared according to the general procedure **G2** using 1-octene **1k** (1.25 mmol, 196 µL) and heptafluoro-2-iodopropane **2d** (1.5 mmol, 213 µL) in a residence time of 10 min. The product **3u** was obtained as colorless oil (378 mg, 74% yield). The characterization of the compound matches the data reported in the literature.[102]

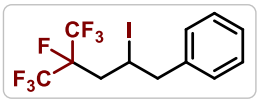

(4,5,5,5-tetrafluoro-2-iodo-4-(trifluoromethyl)pentyl)benzene (3v). Prepared according to the general procedure **G2** using allylbenzene **1n** (1.25 mmol, 166 µL) and heptafluoro-2-iodopropane **2c** (1.5 mmol, 213 µL) in a residence time of 10 min. The product **3v** was obtained as colorless oil (405 mg, 78% yield). The characterization of the compound matches the data reported in the literature.[103]

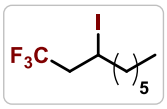

1,1,1-trifluoro-3-iodononane (3w). Prepared according to the general procedure **G2** using 1-octene **1k** (1.25 mmol, 196 µL) and trifluoroiodomethane **2f** (5 mmol, 2.5 mL of a 2 M solution in acetonitrile) in a residence time of 10 min. The product **3w** was obtained as colorless oil (348 mg, 90% yield). The characterization of the compound matches the data reported in the literature.[104]

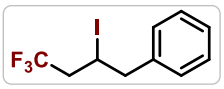

(4,4,4-trifluoro-2-iodobutyl)benzene (3x). Prepared according to the general procedure **G2** using allylbenzene **1n** (1.25 mmol, 166 µL) and trifluoroiodomethane **2f** (5 mmol, 2.5 mL of a 2 M solution in acetonitrile) in a residence time of 20 min. The product **3x** was obtained as colorless oil (327 mg, 83% yield). The characterization of the compound matches the data reported in the literature.[21]

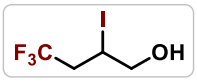

4,4,4-trifluoro-2-iodobutan-1-ol (3y). Prepared according to the general procedure **G2** using allyl alcohol **1o** (1.25 mmol, 85 µL) and trifluoroiodomethane **2f** (5 mmol, 2.5 mL of a 2 M solution in acetonitrile) in a residence time of 20 min. The product **3y** was obtained as colorless oil (255 mg, 80% yield). ^{1}H-NMR (300 MHz, $CDCl_3$) δ 4.33–4.22 (m, 1H), 3.77 (t, *J* = 4.9 Hz, 2H), 3.10–2.64 (m, 2H), 2.49 (s, 1H); ^{13}C-NMR (75 MHz, $CDCl_3$) δ 125.62 (q, *J* = 278.1 Hz), 67.59 (d, *J* = 0.7 Hz), 40.75 (q, *J* = 29.1 Hz), 22.75 (q, *J* = 2.6 Hz); ^{19}F-NMR (282 MHz, $CDCl_3$) δ -64.26 (t, *J* = 10.3 Hz, 3F); IR (ATR, neat, cm^{-1}): 3371, 1250, 1136, 1111, 1069, 1040, 1006; HRMS (ESI, negative mode) calculated for $C_4H_5OF_3I$ $[M-H]^-$: 252.9337, found: 252.9344.

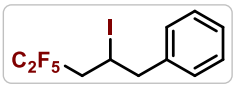

(4,4,5,5,5-pentafluoro-2-iodopentyl)benzene (3z). Prepared according to the general procedure **G2** using allylbenzene **1n** (1.25 mmol, 166 µL) and pentafluoroiodoethane **2g** (5 mmol, 2.5 mL of a 2 M solution in acetonitrile) in a residence time of 20 min. The product **3z** was obtained as colorless oil (394 mg, 87% yield). ^{1}H-NMR (300 MHz, $CDCl_3$) δ 7.41–7.29 (m, 3H), 7.25–7.18 (m, 2H), 4.47 (ddd, *J* = 12.8, 8.8, 6.4 Hz, 1H), 3.26 (ddd, *J* = 23.4, 14.6, 7.3 Hz, 2H), 3.02–2.71 (m, 2H).); ^{13}C-NMR (75 MHz, $CDCl_3$) δ 138.70 (s), 129.09 (s), 128.78 (s), 127.48 (s), 47.06 (d, *J* = 1.6 Hz), 40.77 (t, *J* = 20.8 Hz), 19.54 (s); ^{19}F-NMR (282 MHz, $CDCl_3$) δ -85.79 (s, 3F), -115.88 (ddd, *J* = 265.0, 24.7, 12.2 Hz, 1F), -117.91 (ddd, *J* = 265.1, 22.7, 11.7 Hz, 1F); IR (ATR, neat, cm^{-1}): 1318, 1188, 1115, 1009, 743, 697, 508; HRMS (APCI+APPI, positive mode) calculated for $C_{11}H_{10}F_5I$ $[M]^+$: 363.9747, found: 363.9732; HRMS (APCI+APPI, positive mode) calculated for $C_{11}H_{10}F_5$ $[M-I]^+$: 237.0703, found: 237.0694.

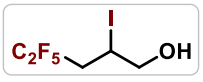

4,4,5,5,5-pentafluoro-2-iodopentan-1-ol (3aa). Prepared according to the general procedure **G2** using allyl alcohol **1o** (1.25 mmol, 85 µL) and pentafluoroiodoethane **2g** (5 mmol, 2.5 mL of a 2 M solution in acetonitrile) in a residence time of 20 min. The product **3aa** was obtained as pale-yellow oil (330 mg, 87% yield). ^{1}H-NMR (300 MHz, $CDCl_3$) δ 4.47–4.32 (m, 1H), 3.80 (s, 2H), 3.09–2.56 (m, 2H), 2.44 (s, 1H); ^{13}C-NMR (75 MHz, $CDCl_3$) δ 67.96 (d, *J* = 2.1 Hz), 37.36 (t, *J* = 21.0 Hz), 21.64 (s); ^{19}F-NMR (282 MHz, $CDCl_3$) δ -85.90 (s, 3F), -116.73 (ddd, *J* = 264.9, 28.4, 9.1 Hz, 1F), -118.47 (ddd, *J* = 264.9, 26.1, 8.9 Hz, 1F); IR (ATR, neat, cm^{-1}): 3410, 2924, 2853, 1193, 1029, 722; HRMS (ESI, negative mode) calculated for $C_5H_5OF_5I$ $[M-H]^-$: 302.9305, found: 302.9314.

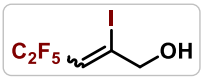

4,4,5,5,5-pentafluoro-2-iodopent-2-en-1-ol (5c). Prepared according to the general procedure **G2** using propargyl alcohol **4c** (1.25 mmol, 73 µL) and pentafluoroiodoethane **2g** (5 mmol, 2.5 mL of a 2 M solution in acetonitrile) in a residence time of 20 min. The product **5c** was obtained as pale-yellow oil (287 mg, 76% yield, *E/Z ratio* = 1:1). The characterization of the compound matches the data reported in the literature.[78]

2.9.6 Fulvestrant Side Chain Synthesis

Flow Dehalogenation of 3aa

The H-CUBE Pro (ThalesNano Inc.) system was used for this procedure. The H-CUBE Pro has an internal hydrogen generator, then this hydrogen is introduced into the reaction mixture, that is pumped by an HPLC pump, prior to catalyst contact. The pressure of the system is dictated by the adjustable BPR (back-pressure regulator). The system can be summarized by the following scheme:

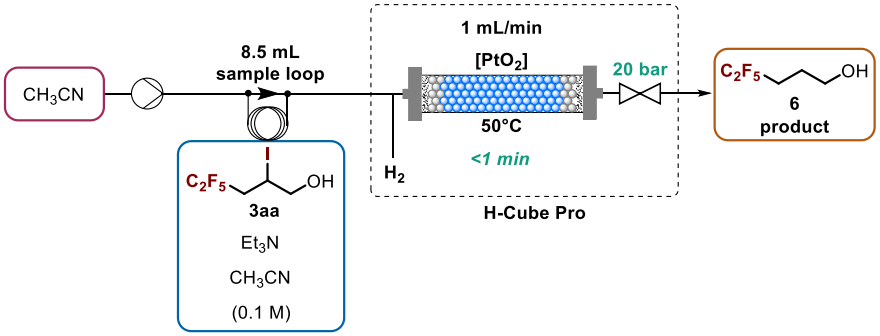

The crude mixture of **3aa** in acetonitrile (theoretically 1.25 mmol, 1 equiv.) coming from the Corning Photo-Reactor was diluted with acetonitrile to 0.1 M and sparged with argon for 30 min to remove the unreacted trifluoroiodomethane. Triethylamine (2.5 mmol, 348 µL, 2 equiv.) was then added and the resulting solution was loaded into an 8.5 mL injection loop (fitted to an Upchurch 6-way valve). Acetonitrile was pumped through the H-CUBE Pro reactor at 1 mL/min flow rate, corresponding to less than 1 min residence time. The system was equipped with a PtO_2 cartridge (70 mm, 4 mm diameter), heated up to 50 °C, pressurized to 20 bar by the adjustable back pressure regulator and set to "100% hydrogen amount". After allowing the reactor to equilibrate for roughly 30 min, the reaction mixture was injected from the sample loop. The output was collected and used directly in the following step without isolation nor purification of the dehalogenated alcohol **6**.

Dehalogenation of 6 Performed in Batch

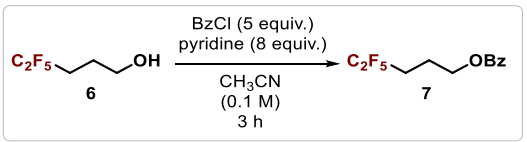

To the crude mixture of **6** in acetonitrile (theoretically 1,25 mmol, 1 equiv.) coming from the H-CUBE Pro reactor was added pyridine (10 mmol, 809 µL, 8 equiv.) and the solution was stirred at 0 °C for 10 min. Benzoyl chloride (6.25 mmol, 726 µL, 5 equiv.) was added dropwise and the solution was stirred at room temperature for 3 hours. The reaction was quenched by the addition of HCl 1 M (20 mL) and then extracted with ethyl acetate (3 × 20 mL). The organic phases were combined and dried

over sodium sulfate. The solvent was removed under reduced pressure and the residue was purified by column chromatography (petroleum ether/ethyl acetate 95:5) to give the corresponding benzoylated alcohol **7** as a pale-yellow oil (253 mg, 72% overall yield).
^{1}H-NMR (300 MHz, $CDCl_3$) δ 8.08–8.01 (m, 2H), 7.62–7.53 (m, 1H), 7.49–7.41 (m, 2H), 4.40 (t, *J* = 6.1 Hz, 2H), 2.33–2.02 (m, 4H); ^{13}C-NMR (75 MHz, $CDCl_3$) δ 166.44 (s), 133.26 (s), 129.67 (s), 128.56 (s), 63.49 (s), 27.84 (t, *J* = 22.3 Hz), 20.35 (t, *J* = 3.8 Hz); ^{19}F (282 MHz, $CDCl_3$) δ -85.51 (s), -118.32 (t, *J* = 17.8 Hz); IR (ATR, neat, cm^{-1}): 1720, 1271, 1188, 1109, 1025, 997, 705; HRMS (APCI+APPI, positive mode) calculated for $C_{12}H_{12}O_2F_5$ $[M+H]^+$: 283.0757, found: 283.0748.

Long Run Synthesis of 7

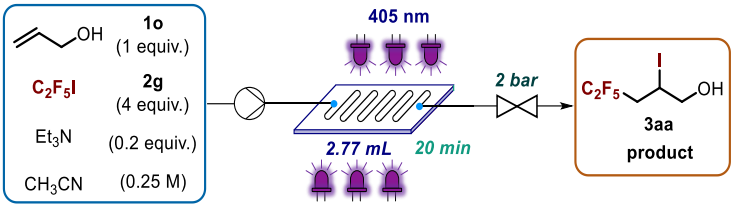

The 40 LED array was switched on at 405 nm and its thermal fluid was set to 15 °C. The reaction plate thermostat was set to 20 °C. A solution of allyl alcohol **1o** (12.5 mmol, 1 equiv), pentafluoroiodoethane **2g** (50 mmol, 4 equiv, taken from a 2 M solution in acetonitrile), and triethylamine (2.5 mmol, 0.2 equiv) was made up in degassed acetonitrile (50 mL total volume in a volumetric flask, solvent was degassed prior to use by sparging with argon for 15 minutes, $[\mathbf{1o}]_0$ = 0.25 M). Using a Zaiput back pressure regulator, a pressure of 3 bar was set. The reaction solution was pumped through the 2.77 mL reaction plate at 0.139 mL/min flow rate, corresponding to 20 min residence time. After allowing the reactor to equilibrate for roughly 15 min, the processed mixture, containing compound **3aa**, was collected over a run time of 173 min (24 mL, 6 mmol theoretical yield).

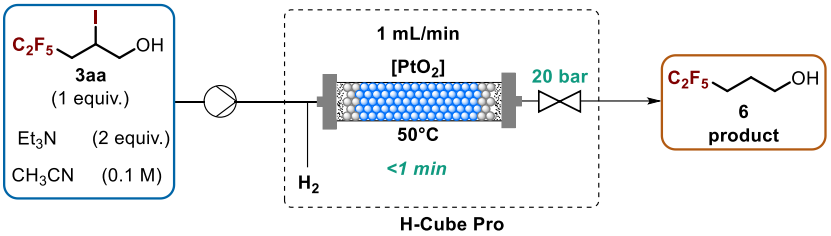

The crude mixture of **3aa** in acetonitrile (24 mL, theoretically 6 mmol, 1 equiv.) coming from the Corning Photo-Reactor was diluted with acetonitrile to 0.1 M and sparged with argon for 30 min to remove the unreacted pentafluoroiodoethane **2g**. Triethylamine (12 mmol, 1.67 mL, 2 equiv.) was then added and the resulting solution was pumped through the H-CUBE Pro reactor at 1 mL/min flow rate, corresponding to less than 1 min residence time. The system was equipped with a PtO_2 cartridge (70 mm, 4 mm diameter), heated to 50 °C, pressurized to 20 bar by the adjustable back-pressure regulator and set to “100% hydrogen amount”. The output was collected and used directly in the following step without isolation nor purification of the dehalogenated alcohol **6** (6 mmol theoretical yield).

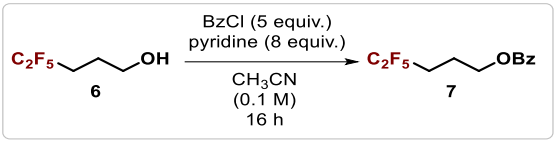

To the crude mixture of **6** in acetonitrile (6 mmol, 1 equiv.) coming from the H-CUBE Pro reactor was added pyridine (48 mmol, 3.88 mL, 8 equiv.) and stirred at 0 °C for 10 min. Benzoyl chloride (30 mmol, 3.49 mL, 5 equiv.) was added dropwise and the solution was stirred at room temperature for 16 h. The reaction was quenched by the addition of HCl (1 M, 100 mL) and then extracted with ethyl acetate (3 × 100 mL). The organic phases were combined and dried over sodium sulfate. The solvent was removed under reduced pressure and the residue was purified by column chromatography (petroleum ether/ethyl acetate 95:5) to give the corresponding benzoylated alcohol **7** as a pale-yellow oil (1.23 g, 73% yield over 3 steps).

2.10 References Chapter II

(1) Rosso, C.; Filippini, G.; Cozzi, P. G.; Gualandi, A.; Prato, M. Highly Performing Iodoperfluoroalkylation of Alkenes Triggered by the Photochemical Activity of Perylene Diimides. *ChemPhotoChem* **2019**, *3*, 193–197.

(2) Rosso, C.; Williams, J. D.; Filippini, G.; Prato, M.; Kappe, C. O. Visible-Light-Mediated Iodoperfluoroalkylation of Alkenes in Flow and Its Application to the Synthesis of a Key Fulvestrant Intermediate. *Org. Lett.* **2019**, *21*, 5341–5345.

(3) Pintauer, T.; Matyjaszewski, K. *Encyclopedia of Radicals*; Wiley, H., Ed.; 2012.

(4) Wang, J.; Sànchez-Rosellò, M.; Aceña, J. L.; del Pozo, C.; Sorochinsky, A. E.; Fustero, S.; Soloshonok, V. A.; Liu, H. Fluorine in Pharmaceutical Industry : Fluorine-Containing Drugs Introduced to the Market in the Last Decade (2001 − 2011). *Chem. Rev.* **2014**, *114*, 2432–2506.

(5) Zhou, Y.; Wang, J.; Gu, Z.; Wang, S.; Zhu, W.; Aceña, J. L.; Soloshonok, V. A.; Izawa, K.; Liu, H. Next Generation of Fluorine-Containing Pharmaceuticals , Compounds Currently in Phase II − III Clinical Trials of Major Pharmaceutical Companies : New Structural Trends and Therapeutic Areas. *Chem. Rev.* **2016**, *116*, 422–518.

(6) Berger, R.; Resnati, G.; Metrangolo, P.; Weber, E.; Hulliger, J. Organic Fluorine Compounds : A Great Opportunity for Enhanced Materials Properties. *Chem. Soc. Rev.* **2011**, *40*, 3496–3508.

(7) Barata-Vallejo, S.; Cooke, M. V.; Postigo, A. Radical Fluoroalkylation Reactions. *ACS Catal.* **2018**, *8*, 7287–7307.

(8) Lewandowski, G.; Meissner, E.; Milchert, E. Special Applications of Fluorinated Organic Compounds. *J. Hazard. Mater.* **2006**, *136*, 385–391.

(9) Muller, K.; Faeh, C.; Diederich, F. Fluorine in Pharmaceuticals : Looking Beyond Intuition. *Science* **2007**, *317*, 1881–1886.

(10) Purser, S.; Moore, P. R.; Swallow, S.; Gouverneur, V. Fluorine in Medicinal Chemistry. *Chem. Soc. Rev.* **2008**, *37*, 320–330.

(11) Fujiwara, T.; O'Hagan, D. Successful Fluorine-Containing Herbicide Agrochemicals. *J. Fluor. Chem.* **2014**, *167*, 16–29.

(12) Haszeldine, R. N. The Reactions of Fluorocarbon Radicals. Part II. The Reaction of Trifluoroiodomethane with Acetylene. *J. Chem. Soc.* **1950**, 3037–3041.

(13) Studer, A.; Curran, D. P. Catalysis of Radical Reactions: A Radical Chemistry Perspective. *Angew. Chem. Int. Ed.* **2016**, *55*, 58–102.

(14) Dolbier, W. R. Structure, Reactivity, and Chemistry of Fluoroalkyl Radicals. *Chem. Rev.* **1996**, *96*, 1557–1584.

(15) Brace, N. O. Syntheses with Perfluoroalkyl Radicals from Perfluoroalkyl Iodides. A Rapid Survey of Synthetic Possibilities with Emphasis on Practical Applications. Part One: Alkenes, Alkynes and Allylic Compounds. *J. Fluor. Chem.* **1999**, *93*, 1–25.

(16) Chatterjee, T.; Iqbal, N.; You, Y.; Cho, E. J. Controlled Fluoroalkylation Reactions by Visible-Light Photoredox Catalysis. *Acc. Chem. Res.* **2016**, *49*, 2284–2294.

(17) Nagib, D. A.; MacMillan, D. W. C. Trifluoromethylation of Arenes and Heteroarenes by Means of Photoredox Catalysis. *Nature* **2011**, *480*, 224–228.

(18) Petzold, D.; Giedyk, M.; Chatterjee, A.; König, B. A Retrosynthetic Approach for Photocatalysis. *Eur. J. Org. Chem.* **2020**, No. 10, 1193–1244.

(19) Nguyen, J. D.; Tucker, J. W.; Konieczynska, M. D.; Stephenson, C. R. J. Intermolecular Atom Transfer Radical Addition to Olefins Mediated by Oxidative Quenching of Photoredox Catalysts. *J. Am. Chem. Soc.* **2011**, *133*, 4160–4163.

(20) Wallentin, C.; Nguyen, J. D.; Finkbeiner, P.; Stephenson, C. R. J. Visible Light-Mediated Atom Transfer Radical Addition via Oxidative and Reductive Quenching of Photocatalysts. *J. Am. Chem. Soc.* **2012**, *134*, 8875–8884.

(21) Beniazza, R.; Douarre, M.; Lastécouères, D.; Vincent, J. M. Metal-Free and Light-Promoted Radical Iodotrifluoromethylation of Alkenes with Togni Reagent as the Source of CF3 and Iodine. *Chem. Commun.* **2017**, *53*, 3547–3550.

(22) Zhang, T.; Wang, P.; Gao, Z.; An, Y.; He, C.; Duan, C. Pyrene-Based Metal-Organic Framework NU-1000 Photocatalysed Atom-Transfer Radical Addition for Iodoperfluoroalkylation and (Z)-Selective Perfluoroalkylation of Olefins by Visible-Light Irradiation. *RSC Adv.* **2018**, *8*, 32610–32620.

(23) Magagnano, G.; Gualandi, A.; Marchini, M.; Mengozzi, L.; Ceroni, P.; Cozzi, P. G. Photocatalytic ATRA Reaction Promoted by Iodo-Bodipy and Sodium Ascorbate. *Chem. Commun.* **2017**, *53*, 1591–1594.

(24) Rawner, T.; Lutsker, E.; Kaiser, C. A.; Reiser, O. The Different Faces of Photoredox Catalysts: Visible-Light-Mediated Atom Transfer Radical Addition (ATRA) Reactions of Perfluoroalkyl Iodides with Styrenes and Phenylacetylenes. *ACS Catal.* **2018**, *8*, 3950–3956.

(25) Beniazza, R.; Remisse, L.; Jardel, D.; Lastécouères, D.; Vincent, J.-M. Light-Mediated Iodoperfluoroalkylation of Alkenes / Alkynes Catalyzed by Chloride Ions : Role of Halogen Bonding. *Chem. Commun.* **2018**, *54*, 7451–7454.

(26) Wang, Y.; Wang, J.; Li, G.; He, G.; Chen, G. Halogen-Bond-Promoted Photoactivation of Perfluoroalkyl Iodides: A Photochemical Protocol for Perfluoroalkylation Reactions. *Org. Lett.* **2017**, *19*, 1442–1445.

(27) Arceo, E.; Montroni, E.; Melchiorre, P. Photo-Organocatalysis of Atom-Transfer Radical Additions to Alkenes. *Angew. Chem. Int. Ed.* **2014**, *53*, 12064–12068.

(28) Yajima, T.; Ikegami, M. Metal-Free Visible-Light Radical Iodoperfluoroalkylation of Terminal Alkenes and Alkynes. *Eur. J. Org. Chem.* **2017**, 2126–2129.

(29) König, B. Photocatalysis in Organic Synthesis – Past, Present, and Future. *Eur. J. Org. Chem.* **2017**, 1979–1981.

(30) Herbst, W.; Hunger, K. *Industrial Organic Pigments: Production, Properties, Applications*; Wiley-VCH, **1997**.

(31) Würthner, F.; Saha-Möller, C. R.; Fimmel, B.; Ogi, S.; Leowanawat, P.; Schmidt, D. Perylene Bisimide Dye Assemblies as Archetype Functional Supramolecular Materials. *Chem. Rev.* **2016**, *116*, 962–1052.

(32) Würthner, F. Perylene Bisimide Dyes as Versatile Building Blocks for Functional Supramolecular Architectures. *Chem. Commun.* **2004**, 1564–1579.

(33) Nowak-Król, A.; Würthner, F. Progress in the Synthesis of Perylene Bisimide Dyes. *Org. Chem. Front.* **2019**, *6*, 1272–1318.

(34) Lee, S. K.; Zu, Y.; Herrmann, A.; Geerts, Y.; Müllen, K.; Bard, A. J. Electrochemistry, Spectroscopy and Electrogenerated Chemiluminescence of Perylene, Terrylene, and Quaterrylene Diimides in Aprotic Solution. *J. Am. Chem. Soc.* **1999**, *121*, 3513–3520.

(35) Zink-Lorre, N.; Font-Sanchis, E.; Sastre-Santos, Á.; Fernández-Lázaro, F. Perylenediimides as More than Just Non-Fullerene Acceptors: Versatile Components in Organic, Hybrid and Perovskite Solar Cells. *Chem. Commun.* **2020**, *56*, 3824–3838.

(36) Huang, C.; Barlow, S.; Marder, S. R. Perylene-3,4,9,10-Tetracarboxylic Acid Diimides: Synthesis, Physical Properties, and Use in Organic Electronics. *J. Org. Chem.* **2011**, *76*, 2386–2407.

(37) Rosso, C.; Filippini, G.; Prato, M. Use of Perylene Diimides in Synthetic Photochemistry. *Eur. J. Org. Chem.* **2021**, DOI: 10.1002/ejoc.202001616.

(38) Zhan, X.; Facchetti, A.; Barlow, S.; Marks, T. J.; Ratner, M. A.; Wasielewski, M. R.; Marder, S. R. Rylene and Related Diimides for Organic Electronics. *Adv. Mater.* **2011**, *23*, 268–284.

(39) Weil, T.; Vosch, T.; Hofkens, J.; Peneva, K.; Müllen, K. The Rylene Colorant Family-Tailored Nanoemitters for Photonics Research and Applications. *Angew. Chem. Int. Ed.* **2010**, *49*, 9068–9093.

(40) Ghosh, I. Excited Radical Anions and Excited Anions in Visible Light Photoredox Catalysis. *Phys. Sci. Rev.* **2019**, 20170185.

(41) Glaser, F.; Kerzig, C.; Wenger, O. S. Multi-Photon Excitation in Photoredox Catalysis: Concepts, Applications, Methods. *Angew. Chem. Int. Ed.* **2020**, *59*, 10266–10284.

(42) Bonchio, M.; Syrgiannis, Z.; Burian, M.; Marino, N.; Pizzolato, E.; Dirian, K.; Rigodanza, F.; Volpato, G. A.; La Ganga, G.; Demitri, N.; Berardi, S.; Amenitsch, H.; Guldi, D. M.; Caramori, S.; Bignozzi, C. A.; Sartorel, A.; Prato, M. Hierarchical Organization of Perylene Bisimides and Polyoxometalates for Photo-Assisted Water Oxidation. *Nat. Chem.* **2019**, *11*, 146–153.

(43) Ghosh, I.; Ghosh, T.; Bardagi, J. I.; Konig, B. Reduction of Aryl Halides by Consecutive Visible Light-Induced Electron Transfer Processes. *Science* **2014**, *346*, 725–728.

(44) Gong, H.; Cao, Z.; Li, M.; Liao, S.; Lin, M. Photoexcited Perylene Diimide Radical Anions for the Reduction of Aryl Halides : A Bay-Substituent Effect. *Org. Chem. Front.* **2018**, *5*, 2296–2302.

(45) Gao, Y.; Xu, H.; Zhang, S.; Zhang, Y.; Tang, C.; Fan, W. Visible-Light Photocatalytic Aerobic Oxidation of Sulfides to Sulfoxides with a Perylene Diimide Photocatalyst. *Org. Biomol. Chem.* **2019**, *17*, 7144–7149.

(46) Chen, Z.; Fimmel, B.; Würthner, F. Solvent and Substituent Effects on Aggregation Constants of Perylene Bisimide π-Stacks - A Linear Free Energy Relationship Analysis. *Org. Biomol. Chem.* **2012**, *10*, 5845–5855.

(47) Marchini, M.; Gualandi, A.; Lucarini, M.; Cozzi, P. G.; Mengozzi, L.; Franchi, P.; Balzani, V.; Ceroni, P. Mechanistic Insights into Two-Photon-Driven Photocatalysis in Organic Synthesis. *Phys. Chem. Chem. Phys.* **2018**, *20*, 8071–8076.

(48) Rehm, D.; Weller, A. Kinetics of Fluorescence Quenching by Electron and H-Atom Transfer. *Isr. J. Chem.* **1970**, *8*, 259–271.

(49) Romero, N. A.; Nicewicz, D. A. Organic Photoredox Catalysis. *Chem. Rev.* **2016**, *116*, 10075–10166.

(50) Gosztola, D.; Niemczyk, M. P.; Svec, W.; Lukas, A. S.; Wasielewski, M. R. Excited Doublet States of Electrochemically Generated Aromatic Imide and Diimide Radical Anions. *J. Phys. Chem. A* **2000**, *104*, 6545–6551.

(51) Zeman, C. J.; Kim, S.; Zhang, F.; Schanze, K. S. Direct Observation of the Reduction of Aryl Halides by a Photoexcited Perylene Diimide Radical Anion. *J. Am. Chem. Soc.* **2020**, *142*, 2204–2207.

(52) Wang, C. S.; Dixneuf, P. H.; Soulé, J. F. Photoredox Catalysis for Building C-C Bonds from C(Sp2)-H Bonds. *Chem. Rev.* **2018**, *118*, 7532–7585.

(53) Descorme, C. Catalytic Wastewater Treatment: Oxidation and Reduction Processes. Recent Studies on Chlorophenols. *Catal. Today* **2017**, *297*, 324–334.

(54) Sadowsky, D.; McNeill, K.; Cramer, C. J. Dehalogenation of Aromatics by Nucleophilic Aromatic Substitution. *Environ. Sci. Technol.* **2014**, *48*, 10904–10911.

(55) Zeng, L.; Liu, T.; He, C.; Shi, D.; Zhang, F.; Duan, C. Organized Aggregation Makes Insoluble Perylene Diimide Efficient for the Reduction of Aryl Halides via Consecutive Visible Light-Induced Electron-Transfer Processes. *J. Am. Chem. Soc.* **2016**, *138*, 3958–3961.

(56) Shang, J.; Tang, H.; Ji, H.; Ma, W.; Chen, C.; Zhao, J. Synthesis, Characterization, and Activity of a Covalently Anchored Heterogeneous Perylene Diimide Photocatalyst. *Cuihua Xuebao/Chinese J. Catal.* **2017**, *38*, 2094–2101.

(57) Yuan, Y.; Majumder, S.; Yang, M.; Guo, S. Recent Advances in Catalyst-Free Photochemical Reactions via Electron-Donor-Acceptor (EDA) Complex Process. *Tetrahedron Lett.* **2020**, *61*, 151506.

(58) Seegerer, A.; Nitschke, P.; Gschwind, R. M. Spectroscopic Methods Combined In Situ Illumination-NMR-UV / Vis Spectroscopy : A New Mechanistic Tool in Photochemistry. *Angew. Chem. Int. Ed.* **2018**, *57*, 7493–7497.

(59) Perrin, C. L. How Can an Electron-Transfer Mechanism Be Operative When the Electron Transfer Is Endothermic? *J. Phys. Chem.* **1984**, *88*, 3611–3615.

(60) Cavani, F.; Teles, J. H. Sustainability in Catalytic Oxidation: An Alternative Approach or a Structural Evolution? *ChemSusChem* **2009**, *2*, 508–534.

(61) Hone, C. A.; Kappe, C. O. The Use of Molecular Oxygen for Liquid Phase Aerobic Oxidations in Continuous Flow. *Top. Curr. Chem.* **2019**, *377*, 2.

(62) Taylor, M. J. W.; Eckenhoff, W. T.; Pintauer, T. Copper-Catalyzed Atom Transfer Radical Addition (ATRA) and Cyclization (ATRC) Reactions in the Presence of Environmentally Benign Ascorbic Acid as a Reducing Agent. *Dalt. Trans.* **2010**, *39*, 11475–11482.

(63) Nappi, M.; Bergonzini, G.; Melchiorre, P. Metal-Free Photochemical Aromatic Perfluoroalkylation of α-Cyano Arylacetates. *Angew. Chem. Int. Ed.* **2014**, *53*, 4921–4925.

(64) Filippini, G.; Nappi, M.; Melchiorre, P. Photochemical Direct Perfluoroalkylation of Phenols. *Tetrahedron* **2015**, *71*, 4535–4542.

(65) Woźniak, Ł.; Murphy, J. J.; Melchiorre, P. Photo-Organocatalytic Enantioselective Perfluoroalkylation of β-Ketoesters. *J. Am. Chem. Soc.* **2015**, *137*, 5678–5681.

(66) Guo, Q.; Wang, M.; Liu, H.; Wang, R.; Xu, Z. Visible-Light-Promoted Dearomative Fluoroalkylation of β-Naphthols through Intermolecular Charge Transfer. *Angew. Chem. Int. Ed.* **2018**, *57*, 4747–4751.

(67) Yang, C.; Zhang, W.; Li, Y.-H.; Xue, X.-S.; Li, X.; Cheng, J.-P. Origin of Stereoselectivity of the Photoinduced Asymmetric Phase- Transfer-Catalyzed Per Fl Uoroalkylation of β - Ketoesters. *J. Org. Chem.* **2017**, *82*, 9321–9327.

(68) Fernàndez-Alvarez, V. M.; Nappi, M.; Melchiorre, P.; Maseras, F. Computational Study with DFT and Kinetic Models on the Mechanism of Photoinitiated Aromatic Per Fl Uoroalkylations. *Org. Lett.* **2015**, *17*, 2676–2679.

(69) Albini, A.; Fagnoni, M. *Handbook of Synthetic Photochemistry*; 2010.

(70) Johansson, K. O.; Head-Gordon, M. P.; Schrader, P. E.; Wilson, K. R.; Michelsen, H. A. Resonance-Stabilized Hydrocarbon- Radical Chain Reactions May Explain Soot Inception and Growth. *Science* **2018**, *361*, 997–1000.

(71) Lub, J.; van Hal, P. A.; Smits, R.; Malassenet, L.; Pikkemaat, J.; Hikmet, R. A. M. On the Photo-Oxidation of Perylene Bisimide Dyes in Alcoholic Solutions. *J. Lumin.* **2019**, *207*, 585–588.

(72) Williams, J. D.; Nakano, M.; Gérardy, R.; Rincón, J. A.; De Frutos, Ó.; Mateos, C.; Monbaliu, J. C. M.; Kappe, C. O. Finding the Perfect Match: A Combined Computational and Experimental Study toward Efficient and Scalable Photosensitized [2 + 2] Cycloadditions in Flow. *Org. Process Res. Dev.* **2019**.

(73) Emmanuel, N.; Mendoza, C.; Winter, M.; Horn, C. R.; Vizza, A.; Dreesen, L.; Heinrichs, B.; Monbaliu, J. C. M. Scalable Photocatalytic Oxidation of Methionine under Continuous-Flow Conditions. *Org. Process Res. Dev.* **2017**, *21*, 1435–1438.

(74) Gérardy, R.; Winter, M.; Horn, C. R.; Vizza, A.; Van Hecke, K.; Monbaliu, J. C. M. Continuous-Flow Preparation of γ-Butyrolactone Scaffolds from Renewable Fumaric and Itaconic Acids under Photosensitized Conditions. *Org. Process Res. Dev.* **2017**, *21*, 2012–2017.

(75) Steiner, A.; Williams, J. D.; Mateos, C.; Kappe, C. O. Continuous Photochemical Benzylic Bromination Using in Situ Generated Br2: Process Intensification towards Optimal PMI and Throughput. *Green Chem.* **2020**.

(76) Liu, Y.; Chen, X.-L.; Sun, K.; Li, X.-Y.; Zeng, F.-L.; Liu, X.-C.; Qu, L.-B.; Zhao, Y.-F.; Yu, B. Visible-Light Induced Radical Perfluoroalkylation/Cyclization Strategy To Access 2-Perfluoroalkylbenzothiazoles/Benzoselenazoles by EDA Complex. *Org. Lett.* **2019**, DOI: 10.1021/acs.orglett.9b01175.

(77) Sun, X.; Wang, W.; Li, Y.; Ma, J.; Yu, S. Halogen-Bond-Promoted Double Radical Isocyanide Insertion under Visible-Light Irradiation: Synthesis of 2-Fluoroalkylated Quinoxalines. *Org. Lett.* **2016**, *18*, 4638–4641.

(78) Li, X.; Provencher, L.; Singh, S. M. Laboratory Scale Preparation of 4,4,5,5,5-Pentafluoropentan-1-Thiol: An Important Chain of Anti-Breast Cancer Agents. *Tetrahedron Lett.* **1994**, *35*, 9141–9144.

(79) Brazier, E. J.; Hogan, P. J.; Leung, C. W.; Kearney-mcmullan, A. O.; Norton, A. K.; Powell, L.; Robinson, G. E.; Williams, E. G. Fulvestrant : From the Laboratory to Commercial-Scale Manufacture Abstract : *Org. Process Res. Dev.* **2010**, *14*, 544–552.

(80) Bundred, N.; Howell, A. Fulvestrant (Faslodex^{TM}): Current Status in the Therapy of Breast Cancer. *Expert Rev. Anticancer Ther.* **2002**, *2*, 151–160.

(81) Plutschack, M. B.; Pieber, B.; Gilmore, K.; Seeberger, P. H. The Hitchhiker's Guide to Flow Chemistry. *Chem. Rev.* **2017**, *117*, 11796–11893.

(82) Hanna, M. W.; Ashbaugh, A. L. Nuclear Magnetic Resonance Study of Molecular Complexes of 7,7,8,8-Tetracyanoquinodimethane and Aromatic Donors 1,2. *J. Phys. Chem.* **1964**, *68*, 811–816.

(83) Sarwar, M. G.; Dragisic, B.; Salsberg, L. J.; Gouliaras, C.; Taylor, M. S. Thermodynamics of Halogen Bonding in Solution: Substituent, Structural, and Solvent Effects. *J. Am. Chem. Soc.* **2010**, *132*, 1646–1653.

(84) Beale, T. M.; Chudzinski, M. G.; Sarwar, M. G.; Taylor, M. S. Halogen Bonding in Solution: Thermodynamics and Applications. *Chem. Soc. Rev.* **2013**, *42*, 1667–1680.

(85) Bag, D.; Kour, H.; Sawant, S. D. Photo-Induced 1,2-Carbohalofunctionalization of C-C Multiple Bonds: Via ATRA Pathway. *Org. Biomol. Chem.* **2020**, *18*, 8278–8293.

(86) Lu, H.; Wang, D. Y.; Zhang, A. Visible Light-Promoted Phosphine-Catalyzed Difluoroalkylation of Arenes and Heterocycles. *J. Org. Chem.* **2020**, *85*, 942–951.

(87) Mao, T.; Ma, M. J.; Zhao, L.; Xue, D. P.; Yu, Y.; Gu, J.; He, C. Y. A General and Green Fluoroalkylation Reaction Promoted: Via Noncovalent Interactions between Acetone and Fluoroalkyl Iodides. *Chem. Commun.* **2020**, *56*, 1815–1818.

(88) Regar, R.; Mishra, R.; Mondal, P. K.; Sankar, J. Metal-Free Annulation at the Ortho- and Bay-Positions of Perylene Bisimide Leading to Lateral π-Extension with Strong NIR Absorption. *J. Org. Chem.* **2018**, *83*, 9547–9552.

(89) Qiu, W.; Chen, S.; Sun, X.; Liu, Y.; Zhu, D. Suzuki Coupling Reaction of 1,6,7,12-Tetrabromoperylene Bisimide. *Org. Lett.* **2006**, *8*, 867–870.

(90) Ren, H.; Li, J.; Wang, R.; Wang, Q.; Liu, D. Synthesis and Characterization of Novel Perylenediimide-Cored Dendrimer with Fluorinated Shell. *Synth. Commun.* **2010**, *40*, 759–

765.

(91) Hu, Y.; Chen, S.; Zhang, L.; Zhang, Y.; Yuan, Z.; Zhao, X.; Chen, Y. Facile Approach to Perylenemonoimide with Short Side Chains for Nonfullerene Solar Cells. *J. Org. Chem.* **2017**, *82*, 5926–5931.

(92) Vasilikogiannaki, E.; Titilas, I.; Vassilikogiannakis, G.; Stratakis, M. Cis-Semihydrogenation of Alkynes with Amine Borane Complexes Catalyzed by Gold Nanoparticles under Mild Conditions. *Chem. Commun.* **2015**, *51*, 2384–2387.

(93) Yang, H.; Carter, R. G. Synthesis of All-Carbon, Quaternary Center-Containing Cyclohexenones through an Organocatalyzed, Multicomponent Coupling. *Org. Lett.* **2010**, *12*, 3108–3111.

(94) Kleimark, J.; Johansson, C.; Olsson, S.; Hakansson, M.; Hansson, S.; Akermark, B.; Norrby, P. Sterically Governed Selectivity in Palladium-Assisted Allylic Alkylation. *Organometallics* **2011**, *30*, 230–238.

(95) Huang, W.-Y.; Zhang, H.-Z. Reaction of Perfluoroalkyl Iodides with Alkenes Initiated by Organophosphine and Related Compounds. *J. Fluor. Chem.* **1990**, *50*, 133–140.

(96) Kohlmeier, A.; Janietz, D. Hydrogen-Bonded Polyphilic Block Mesogens with Semiperfluorinated Segments. *Chem. Mater.* **2006**, *18*, 59–68.

(97) Vázquez, A. J.; Nudelman, N. S. Perfluoroalkylation of Alkenes and Alkynes in Water. *Arkivoc* **2015**, 190–201.

(98) Cao, L.; Li, C. P-MeOC6H4N2+ BF4-/TiCl3: A Novel Initiator for Halogen Atom-Transfer Radical Reactions in Aqueous Media. *Tetrahedron Lett.* **2008**, *49*, 7380–7382.

(99) Davis, C. R.; Burton, D. J.; Yang, Z. Y. Titanium-Catalyzed Addition of Perfluoroalkyl Iodides to Alkenes. *J. Fluor. Chem.* **1995**, *70*, 135–140.

(100) Lahiouhel, D.; Ameduri, B.; Boutevin, B. A Telechelic Fluorinated Diol from 1,6-Diiodoperfluorohexane. *J. Fluor. Chem.* **2001**, *107*, 81–88.

(101) Zeng, R.; Fu, C.; Ma, S. Formal Alkylation of Allenes through Highly Selective Radical Cyclizations of Allene-Enes. *Angew. Chem. Int. Ed.* **2012**, *51*, 3888–3891.

(102) Deng, W.; Li, Y.; Li, Y. G.; Bao, H. Iron-Catalyzed Carboiodination of Alkynes. *Synthesis* **2018**, *50*, 2974–2980.

(103) Yoshioka, E.; Kohtani, S.; Jichu, T.; Fukazawa, T.; Nagai, T.; Kawashima, A.; Takemoto, Y.; Miyabe, H. Aqueous-Medium Carbon − Carbon Bond-Forming Radical Reactions Catalyzed by Excited Rhodamine B as a Metal-Free Organic Dye under Visible Light Irradiation. *J. Org. Chem.* **2016**, *81*, 7217–7229.

(104) Du, Y.; Pearson, R. M.; Lim, C. H.; Sartor, S. M.; Ryan, M. D.; Yang, H.; Damrauer, N. H.; Miyake, G. M. Strongly Reducing, Visible-Light Organic Photoredox Catalysts as Sustainable Alternatives to Precious Metals. *Chem. Eur. J.* **2017**, *23*, 10962–10968.

Chapter III

Fluoroalkylation of Organic Compounds by Means of the Photochemical Activity of Carbon Dots

Abstract

Chapter III discusses the development of fluoroalkylation reactions of electron-rich organic compounds by means of the photochemical activity of nitrogen-doped carbon dots. This project was inspired by the photoactivation of the radical source **2** by a simple amine (triethylamine), illustrated in Chapter II, that was then further developed towards light-absorbing amine-rich carbon-based nanoparticles **D**. These photoactive materials possess peculiar physicochemical properties and display higher sustainability with respect to the commonly used molecular photocatalytic systems. In addition, besides alkene derivatives, this approach also allowed the functionalization of arenes and heteroarenes in a straightforward way. Mechanistic studies confirmed the pre-association of the radical source **2** with the amino groups present on the surface of **D** *via* halogen-bonding. This work was conducted within the Prato group, together with *Prof. Maurizio Prato*, who supervised the project, and with *Dr. Giacomo Filippini*, who conceived the idea and performed some of the experiments. A significant part of this work has been published in 2019.[1] Moreover, we illustrated these results in a review article regarding the use of carbon-based nanoparticles as nano-organocatalysts, published in 2020.[2] Adapted with permission from *ACS Catal*. **2020**, *10*, 8090−8105. Copyright 2020 American Chemical Society.

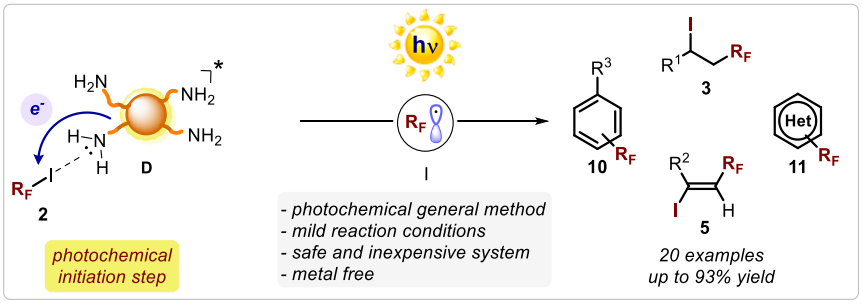

3.1 Introduction

As described in Chapter II, fluoroalkylation reactions of organic compounds are pivotal for the preparation of valuable derivatives for a wide range of applications, especially for pharmaceutics (Figure 1c).[3–6] Besides the depicted ATRA pathway for the functionalization of olefins, another important mechanism can be exploited for the perfluoroalkylation of arenes and heteroarenes (**8** or **9**, Figure 1a). This approach is known as homolytic aromatic substitution (HAS).[6,7]

Similarly to the ATRA reactivity, direct perfluoroalkylation of arenes through HAS pathway typically relies on radical chemistry and the strongly electrophilic nature of perfluoroalkyl radicals ($R_F^{\bullet}$, **I**).

The formation of such fluorinated open-shell species may be achieved through the very same general activation modes, starting from suitable radical precursors: (*i*) thermal activation or (*ii*) photochemical activation (Figure 1a). Those electron-poor radicals (**I**) can react with arenes forming a radical σ-complex (Figure 1b).[7] Many reactions defined as homolytic aromatic substitution involve an oxidative step to convert the radical σ-complex into a cationic σ-complex, followed by the rapid loss of a proton to restore aromaticity. When perfluoroalkyl halides (e.g., R_FI, **2**) are used as radical precursors, these electron-poor species themselves can often oxidize the radical σ-complexes to the corresponding cationic σ-complex. Subsequently, the mesolytic cleavage of the C–X bond, within the resulting radical anion, leads to the formation of a new fluorinated radical, which can react with another electron-rich arene molecule, thus starting a self-propagating radical chain process.[8]

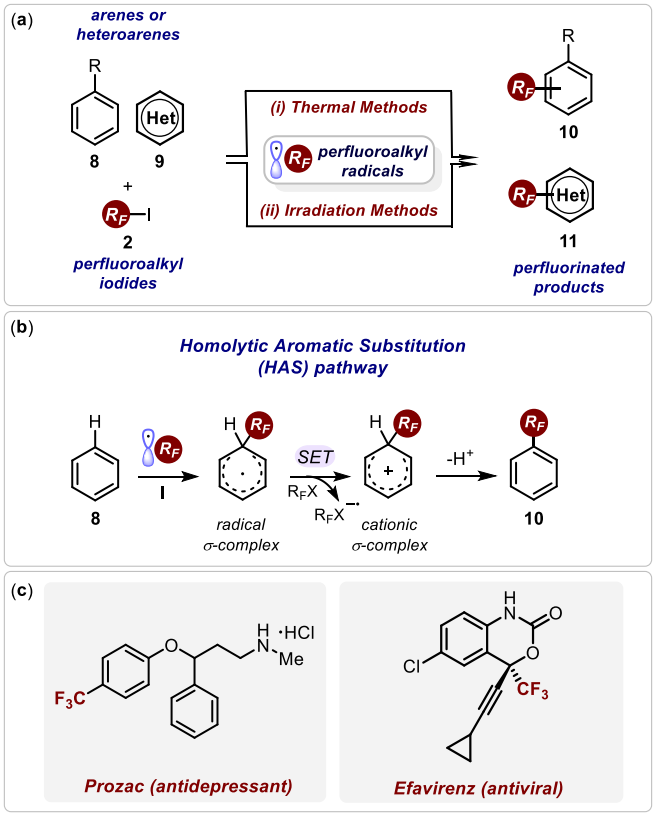

Figure 1. (**a**) General methods for the fluorinated radicals I formation. (**b**) Classical homolytic aromatic substitution (HAS) pathway. SET = single electron transfer. (**c**) Pharmaceutically relevant compounds containing fluorinated moieties.

Due to the synthetic relevance of the fluoroalkylation reactions, a plethora of different radical methodologies have been reported over the last decades, as summarized in a recent review.[6] In this Section, this important research topic is presented through the analysis of some explicative examples in order to describe its historical evolution. The advancement of the methodologies for the generation of radicals **I** for the HAS transformations followed a common path with those for the ATRA reactivity. Indeed, thermal approaches that required harsh conditions, such as high temperatures or the use of potentially explosive initiators, have been practically supplanted with the advent of photocatalysis (Figure 2a).[6,9,10] Among the latter photochemical methods, it is worth mentioning the seminal work reported by MacMillan and co-workers where they employed a Ru- or Ir-based photocatalyst (at 1-2 mol% loading) to trigger the direct trifluoromethylation of unactivated

arenes and heteroarenes under visible light irradiation (Figure 2b).[11] Similarly, Itoh and colleagues utilized an anthraquinone derivative as organic photoredox catalyst (at 5 mol% loading) to promote the formation of the perfluoroalkyl radicals **I** for the same synthetic puposes (Figure 2c).[12] Later on, the Melchiorre group developed a different strategy for the photochemical perfluoroalkylation of arenes (Figure 2d). Specifically, the authors exploited the formation of a photon-absorbing EDA complex, generated upon association of perfluoroalkyl iodides **2** with α-cyano arylacetate anions. This approach required the use of 1,1,3,3-tetramethylguanidine (TMG, 2.5 equiv.) as base to deprotonate the α-cyano substate, thus affording a suitable electron-rich donor for the formation of such colored complexes.[13] Afterwards, the same research group expanded this procedure towards the direct excitation of colored reaction intermediates in order to install perfluoroalkyl moieties on the corresponding substrates (Figure 2e).[14] In this case, the TMG base (2.5 equiv.) provided the formation of light-absorbing phenolate anions that triggered the generation of radicals **I** from **2**. Lastly, Chen and co-workers utilized the photochemical activity of EDA complexes directly formed between organic bases (e.g., TEEDA = *N,N,N',N'*-tetraethylethylenediamine, 3 equiv.) and **2** with the assistance of Lewis-basic solvent (such as tetrahydrofuran, THF) for the perfluoroalkylation of arenes (Figure 2f).[15] As evidenced, in most cases, these photocatalysts and additives were employed in relatively high loading (from 1 to 300 mol%) under UV-visible light irradiation.

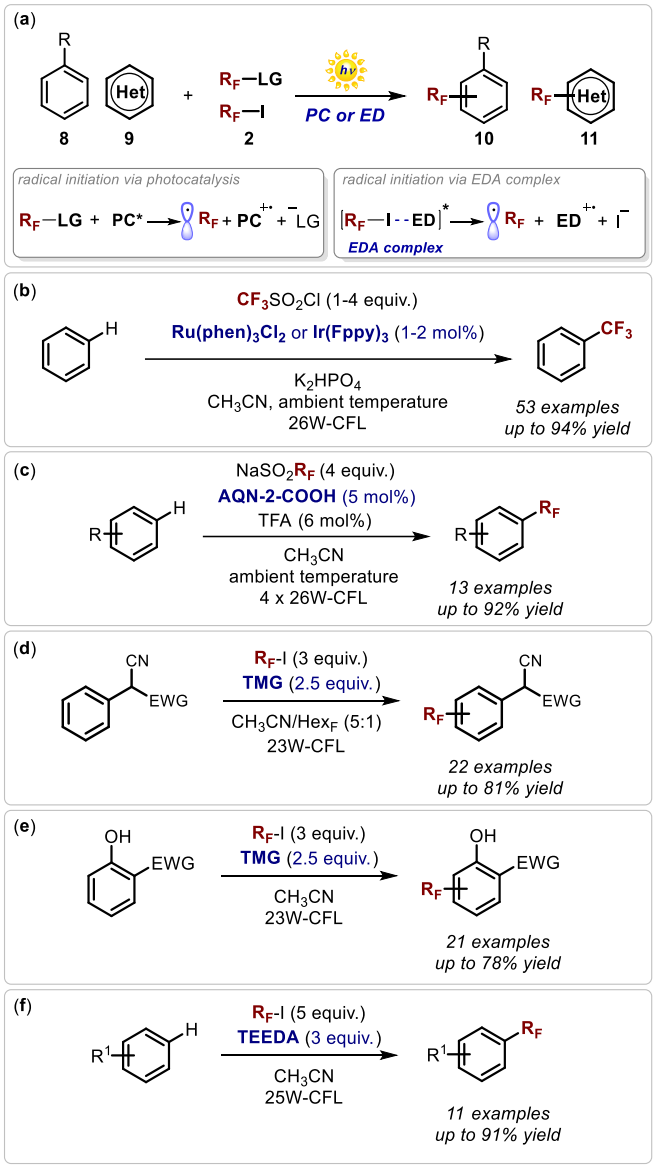

Figure 2. Representative examples of the use of photocatalytic systems for the perfluoroalkylation of arenes **8** and heteroarenes **9**. LG = leaving group, PC = photocatalyst, ED = electron donor, CFL = compact fluorescent lamp, AQN-2-COOH = anthraquinone-2-carboxylic acid, TMG = 1,1,3,3-tetramethylguanidine, EWG = electron-withdrawing group, TEEDA = *N,N,N',N'*-tetraethylethylenediamine.

Therefore, the general feeling is that a further advance within this field is represented by the development of novel metal-free photocatalytic systems capable of working under visible light irradiation, possibly in low loading.[16] In addition, these systems have to be efficient, inexpensive, safe and readily available through straightforward preparation protocols. To this aim, we took inspiration from the ability of simple amines to photoactivate perfluoroalkyl iodides (**2**) *via* halogen bonding, thus generating reactive fluorinated radicals (**I**, *vide supra*, Chapter II).[17] In addition, our group recently reported the preparation of safe and non-toxic photoactive carbon-based nanoparticles, namely carbon dots, bearing numerous amino groups on their surface.[18,19] Hence, we envisaged the possibility to exploit these light-absorbing and highly functional nanoparticles as effective sustainable nano-photocatalysts for the perfluoroalkylation of organic compounds, including arenes and heteroarenes.

For this reason, it is important to first introduce the nature and the photochemical properties of this prominent class of carbon-based nanomaterials before proceeding with the discussion of the results.

3.2 Carbon Dots (CDs): Synthesis, Properties and Applications

Carbon dots (CDs) are a new class of fluorescent carbon-based nanomaterials consisting of quasi-spherical nanoparticles, with dimensions smaller than 10 nm.[20,21] Specifically, CDs can be divided into different subgroups depending on the nature of the nanostructures obtained during the synthesis. Namely, graphene quantum dots (GQDs), carbon quantum dots (CQDs), carbon nanodots (CNDs), and polymer-like dots (PDs).[20] Notwithstanding, discerning between CQDs and CNDs is often challenging because the relative contributions from the structure and the excitation states can be difficult to unravel. In this regard, the general term carbon dots (CDs) has been recommended to describe all of the quasi-spherical carbon nanoparticles, including those with molecular-like behavior and delocalized electronic structure.[18,22] Generally, CDs consist of carbon cores that can be surrounded by shells containing numerous polar groups such as carboxylic acids, alcohols, and amines.[20] The nature of these heteroatom functionalities arises from the precursors and the operative conditions employed in the CD synthesis. Importantly, these surface groups play a pivotal role in determining the overall chemical behavior of the whole nanoparticles.[21,23] Moreover, CDs have been found to have excellent optical and luminescence properties, considerable solubility in polar solvents (including water), high chemical and photostability, as well as low toxicity and excellent biocompatibility.[23] The ever-growing popularity of these nanoparticles is also substantiated by their fast and facile preparation from economic raw materials (including natural renewable sources or waste), their scalability for large-scale productions, and their tailorable surfaces.[24,25] Furthermore, specific precursors/additives, including heteroatom-containing species or metal complexes, can be used to fine-tune the properties of CDs to make them ideal for a wide range of applications.[23,26] Indeed, the luminescence, redox properties, and chirality of CDs can be controlled at least to some extent with a proper choice of the molecular precursors.[18] These characteristics have generated a broad, interdisciplinary research interest, spanning over chemistry, materials science, biology, and medicine (Figure 3a).[27] Consequently, since their discovery in 2004,[28] CDs have found numerous applications in optoelectronic devices, functional materials, catalysis, agriculture, bioimaging, sensors, and drug delivery.[20,23,27,29–31] Among the above-mentioned areas of application of CDs, catalysis and photocatalysis are extremely appealing fields for chemists. Explicitly, the presence of reactive surface groups on light-absorbing CDs have paved the way to new catalytic possibilities, enabling the preparation of valuable organic compounds under mild operating conditions by means of classical polar or (light-driven) radical reactivities.[23,32–36] CDs are therefore emerging as promising nanocatalytic platforms that fulfill the sustainability requirements of nontoxic, water-compatible, readily available, and potentially recyclable catalysts for green chemical production. Specifically, CDs have been profitably applied in acid-base catalysis, aminocatalysis, hydrogen-bond catalysis and photoredox catalysis (Figure 3b).[2,25,37] This has resulted in an ascending interest, both academic and industrial, in CD-catalyzed synthetic routes. This is reinforced by the ever-increasing pressure on the chemical industry for a rapid swing to new sustainable synthetic routes to access chemicals of widespread use.[37–40]

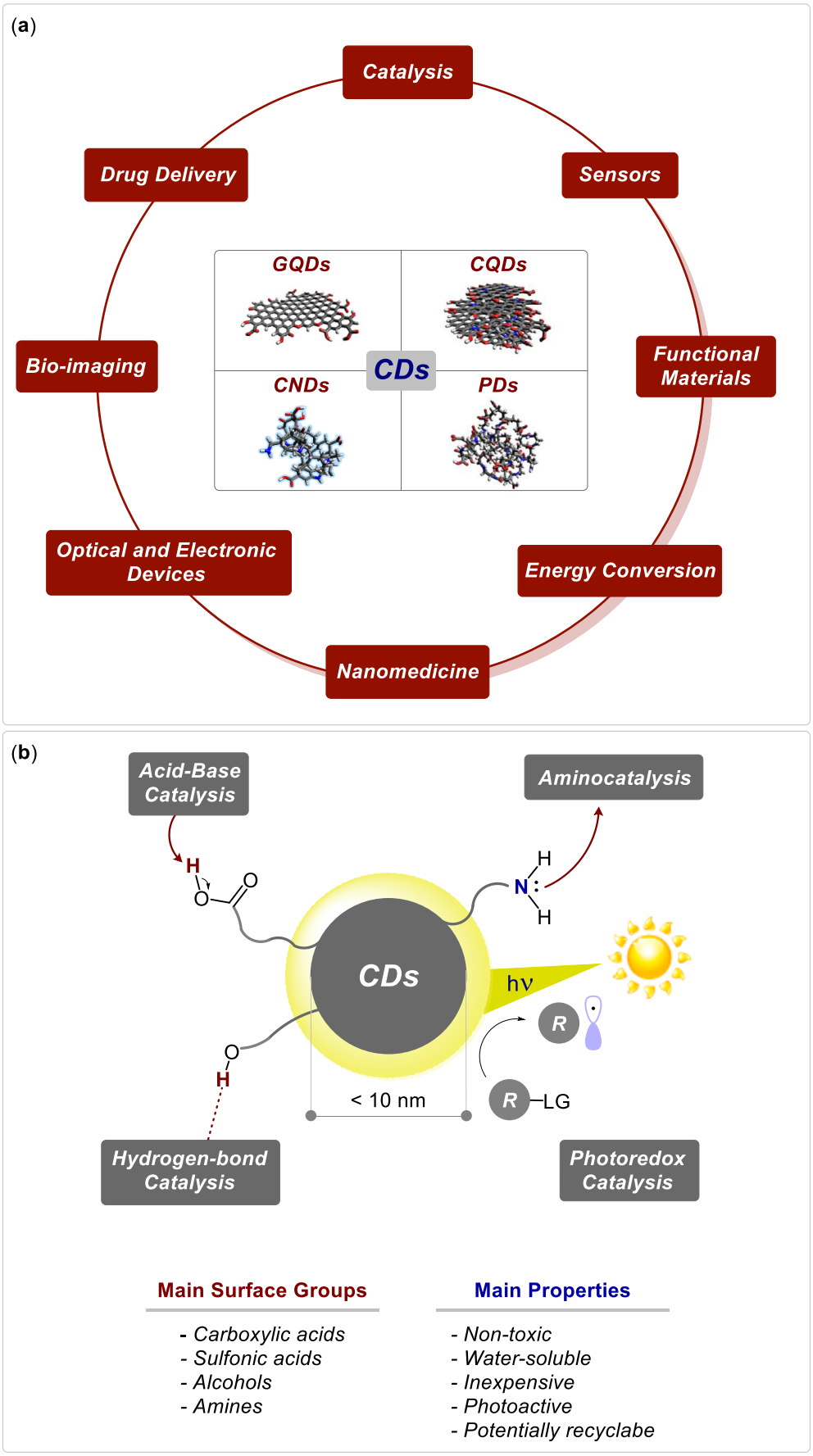

Figure 3. (**a**) Main applications of CDs. GQDs = graphene quantum dots, CQDs = carbon quantum dots, CNDs = carbon nanodots, PDs = polymer-like dots. (**b**) CDs as promising nano-catalytic platform.

3.2.1 CDs as Organic Nano-photocatalysts

The physicochemical features of CDs make them attractive for green and sustainable light-driven transformations in organic chemistry. In particular, CDs show a strong absorption centered in the UV region with a long tail extending into the visible region (π–π*or n–π* transitions), which varies depending on the CD nature and preparation.[41–43] More importantly, the vast majority of the CDs have a peculiar photoluminescence (PL) which involves a strong blue emission, which rapidly declines in the red region, generally characterized by dependence from excitation wavelength.[18,26,44] The emission properties of CDs rely on the composition of fluorophores and on the arrangements of structural domains.[45] The PL of CDs can be effectively quenched by either electron donor or acceptor species through the formation of charge-transfer systems, paving the way for photocatalytic applications in organic synthesis and solar fuel production.[35,36,46–49] Precisely, upon light absorption, the photoexcited CDs are able to undergo single-electron-transfer processes with a variety of either organic or inorganic substrates, thus allowing photocatalysis (Figure 4).[2,50,51]

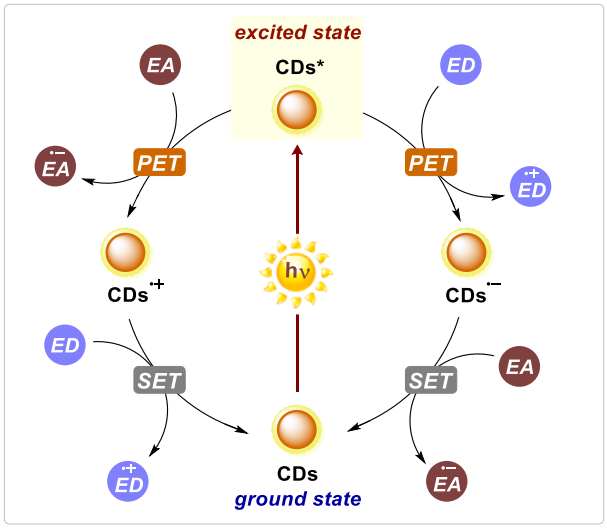

Figure 4. Possible modes of catalysis of generic CDs bearing surface functionalities. ED = electron donor, EA = electron acceptor, PET = photoinduced electron transfer, SET = single electron transfer.

One of the first examples of the application of CDs in nano-photocatalysis was reported by Liu, Kang, and coworkers.[52] These carbon nanoparticles were prepared by electro-chemical ablation of graphite in water (30 V for 120 h) and purified by filtration and centrifugation. The so-obtained materials were classified as CQDs, possessing a uniform-dispersed diameter centered at 5 nm (determined by transmission electron microscopy, TEM). Despite the pure carbon composition of the precursor, these CDs show the presence of hydroxyl and carboxyl groups on their surface, formed during the synthesis in water. The quantification of these functionalities has been obtained through acid-base titration, resulting in a total concentration of 10.1 µmol/g. By using these carbon-based nanoparticles as photocatalysts in relatively high loading (30 mg/mL), the authors described photo-enhanced aldol condensation reactions under light irradiation (Figure 5a).

In a similar case study, MacFarlane and colleagues reported the use of sulfonated CDs as a photoswitchable acid catalyst for ring-opening reactions (Figure 5b).[53] The carbonaceous core of these CDs was prepared by electrochemical ablation of graphite rods in water (15-60 V for 6 days),

then purified by filtration and centrifugation. The sulfur decoration was then introduced using sulfuric acid. The obtained nanoparticles were classified as water-dispersible CQDs, having a spherical shape and size in the range of 2-9 nm (determined by TEM). The presence of -SO_3H groups on CDs surface was demonstrated by FT-IR and energy-dispersive X-ray (EDX) spectroscopy and the sulfur content was quantified by elemental analysis (1.97 wt%). Moreover, these CDs showed a PL centered at 560 nm (upon excitation at 485 nm), which can be efficiently quenched by electron-donors in solution, demonstrating the electron-acceptor nature of these sulfonated carbon nanoparticles. Thus, these sulfonated-CDs were employed to drive photochemical ring-opening reactions of styrene oxide in methanol in low catalytic loading (0.5 mg/mL).

Another example of using *S*-doped-CDs was reported by Sarma and co-workers.[54] They described photoinduced cross dehydrogenative coupling reactions taking advantage of the surface acidity and the photochemical properties of sulfonated CDs (Figure 5c). In this case, the carbon nanoparticles were prepared by microwave-assisted carbonization of glucose in oleic acid at 180°C for 7 min and purified by extraction and dialysis against water. Then, the sulfate functionalities were introduced by treating the material with fuming sulfuric acid. The resulting nanoparticles had an average diameter in the range of 3.2±1.5 nm (determined by TEM). The presence of -OSO_3H groups on CDs surface was quantified by acid-base titration (400 µmol/L, while the amount of -OH and -COOH groups was found to be 3.5 and 1.25 times higher, respectively), confirming their surface acidity. Furthermore, these CDs showed excitation-dependent emission properties centered at 424 nm (upon excitation at 300 nm), which can be quenched in the presence of either electron acceptor or electron donor molecules in solution. These data show the dual photo-oxidizing and reducing nature of the nanomaterial. By using these carbon-based nanoparticles as photocatalysts in relatively low loading (10 mg/mmol), the authors described aerobic cross-coupling reactions under light irradiation (Figure 5a).

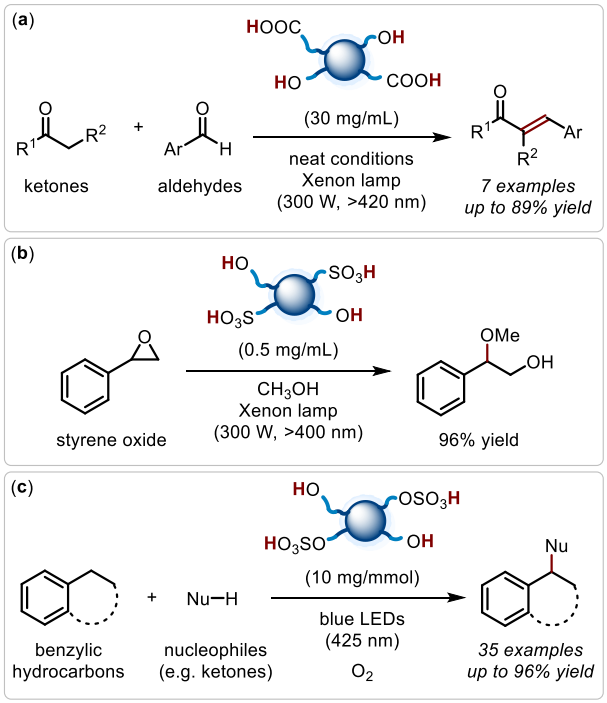

Figure 5. Use of CDs as nano-photocatalysts in: (**a**) photo-enhanced aldol condensation reactions; (**b**) photo-ring-opening reactions; (**c**) dehydrogenative coupling reactions.

Beside the described examples, no further applications of CDs as nano-photocatalysts have been reported at that time, confirming that this is an exciting new research field.

3.3 Objective of the Research Project and Initial Results

In particular, we envisaged to contemporary exploit the activation of radical source **2** by means of the amino groups present on such CDs, along with the intrinsic photo-reducing features of these carbon nanoparticles. In this way, we hypothesized to achieve a more efficient generation of radicals of the type of **I**, thus making feasible even the perfluoroalkylation of less reactive arenes and heteroarenes **8-9** through an HAS pathway.

To this regard, we selected an amine-rich *N*-doped-CDs, namely **D**, previously prepared within our group as a possible nano-photocatalyst. **D** was obtained through microwave-assisted hydrothermal synthesis from arginine (Arg) and ethylenediamine (EdA) at 240 °C for 3 min, followed by filtration and dialysis purification against water (Figure 6a).[19,55] The resulting amorphous carbon nanoparticles show a narrow size distribution of 2.47 ± 0.84 nm (determined by atomic force microscopy, AFM) and an amino-rich surface, confirmed by a positive Kaiser test (KT) of 1350 µmol g^{-1} performed at 120 °C.[19,56] These CDs **D** have been exploited by our group for several applications, spanning from nanomedicine to energy conversion.[18,42,55,57–60] The presence of abundant surface functionalities, in which the majority are amines, increases the solubility of **D** both in water and polar organic solvents. These superficial groups are readily accessible for further chemical derivatization, thus allowing the formation of composite nanohybrids.[18,61–63] Concerning the optical properties, a solution of **D** in *N*,*N*-dimethylformamide (DMF) appears slightly yellow in daylight, since it presents an absorption tale up to about λ = 410 nm (see Section 3.5). In addition, **D** exhibits a peculiar wavelength-dependent emission in the blue region upon light absorption (see Section 3.5). Furthermore, **D** was supposed to be a strong reductant in the excited state (**D***) as implied by its reduction potential, which was estimated as about -2 V *vs* SCE for the couple $\mathbf{D}^{\bullet+}$/**D*** (see Section 3.5 for details).[61,64] Hence, we figured out that **D*** could trigger the formation of reactive radicals **I** from perfluoroalkyl iodides (**2**, $E^0 \approx -1$ V *vs* SCE).[65] These event could in principle initiate the desired perfluoroalkylation reactions onto electron-rich arenes (Figure 6b).

We tested the feasibility of our strategy by reacting 1,3,5-trimethoxybenzene (**8a**) and perfluorohexyl iodide (**2a**, 6 equiv.) in the presence of **D** as nano-photocatalyst (0.7% w/v) under visible light irradiation (395 nm LEDs).[66] Moreover, potassium carbonate was employed as base (K_2CO_3, 1 equiv.) in DMF as solvent (0.25 M). Interestingly, this experiment provided the corresponding perfluoroalkyl product **10a** in excellent yield (>99% NMR yield, Figure 6c).

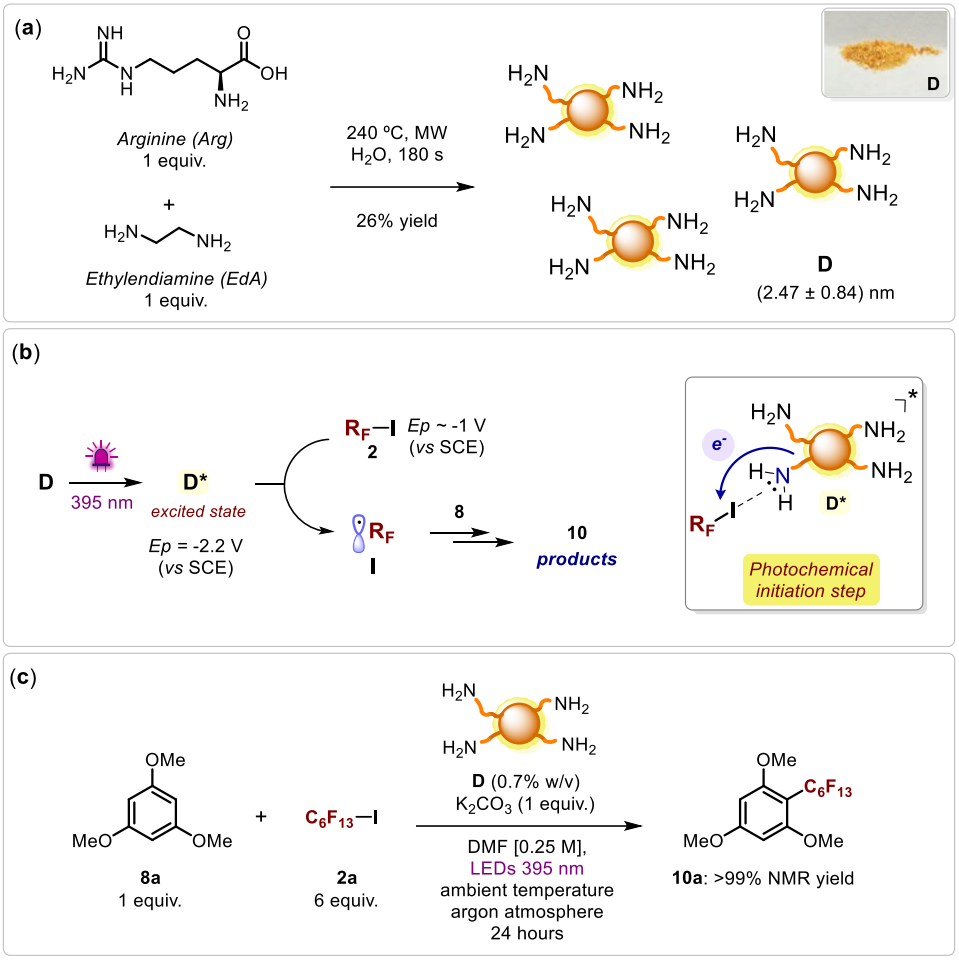

Figure 6. (**a**) Synthesis of nano-photocatalyst **D**. (**b**) Initial idea: using CDs **D** as nano-photocatalyst to trigger the formation of perfluorinated radicals **I**. (**c**) The initial experiment with the reaction conditions. Ep = redox potential.

3.4 Results and Discussion

Starting from the satisfying initial conditions, we attempted to perform an optimization study of the reaction conditions in order to improve the sustainability of the perfluorohexylation of **8a** (entry 1, Table 1).

First, we sought to reduce the excess of the radical source **2a** initially employed (6 equiv.) but, regrettably, this turned out to be detrimental for the reactivity. In fact, by using 3 equiv. of **2a** the yield of the HAS product **10a** decreased to 36%, while an exact stoichiometric amount of **2a** gave only a detectable quantity of the desired product **10a** (11% yield, entries 2-3, Table 1).

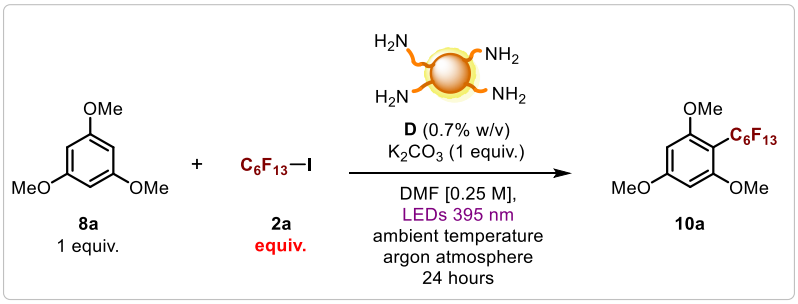

Entry	**2a** (equiv.)	Yield[a]
1	6	>99%
2	3	36%
3	1	11%

Table 1. Reactions performed on 0.1 mmol scale. [a] Yield determined by ^{1}H-NMR spectroscopy using 1,1,2-trichloroethene as the internal standard.

The generality of the perfluoroalkylation methodology was then investigated with respect to the solvent, starting from the initial point (Table 2). Water would be a green and sustainable option for the solubilization of the nano-photocatalyst **D** (solubility up to 80 mg mL^{-1}).[55,67] Nevertheless, H_2O was not able to dissolve the substrate **8a** and the reagent **2a**. The same applied for a less polar solvent, such as dichloromethane (DCM), since it was capable of bringing in solution the starting materials but not the photocatalyst **D**, which tended to aggregate. For these reasons, it was not surprising that both water and DCM provided almost negligible amounts of the HAS product **10a** (entries 2-3, Table 2). Therefore, DMF was kept as reaction medium for the following investigations, considering that it guarantees the correct compromise for the solubilization of the nanoparticles **D** and the reaction components.

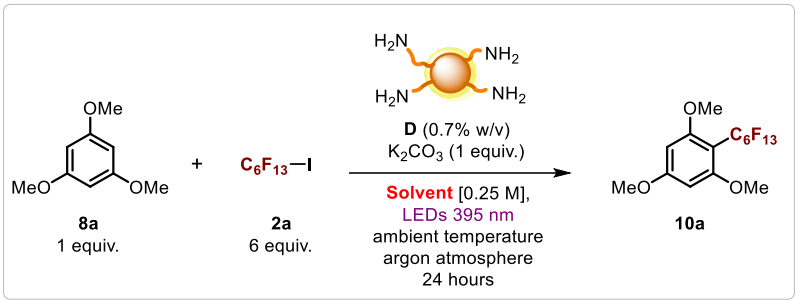

Entry	Solvent	Yield[a]
1	DMF	>99%
2	H_2O	<5%
3	DCM	<5%

Table 2. Reactions performed on 0.1 mmol scale. [a] Yield determined by ^{1}H-NMR spectroscopy using 1,1,2-trichloroethene as the internal standard.

Under these optimized conditions, a high isolated yield of **10a** was obtained (82% yield, entry 1, Table 3). Subsequently, a series of control experiments was carried out in order to obtain more

mechanistic clues (entries 2-8, Table 3). An experiment revealed how the exclusion of light completely suppressed the process, therefore establishing the photochemical nature of the transformation (entry 2, Table 3). In addition, we confirmed that the photochemical activity of **D** is essential for the reactivity, since no reaction occurs in the absence of the nanoparticles (entry 3, Table 3). This mechanistic hypothesis was also congruent with the experiment performed using LEDs at 525 nm (a wavelength that could not be absorbed by **D**, see Section 3.5 for details), in which the fluorinated adduct **10a** was not formed (entry 4, Table 3). The inhibition of the reaction observed under aerobic atmosphere was consonant with a radical mechanism (entry 5, Table 3). This was further corroborated by the experiment conducted in the presence of 2,2,6,6-tetramethylpiperidine 1-oxyl (TEMPO, 1 equiv.), since the product **10a** was not detected (entry 6, Table 3). The use of 1 equiv. of an acid scavenger was needed to quench hydrogen iodide (HI), which is stoichiometrically formed after the mesolytic cleavage of **2a** to furnish the radical intermediate. In line with this notion, performing the reaction in the absence of K_2CO_3 resulted in a lack of reactivity (entry 7, Table 3). Interestingly, this reaction worked well using a solar simulator (entry 8, Table 3), suggesting that our methodology could effectively be conducted under direct sunlight irradiation.

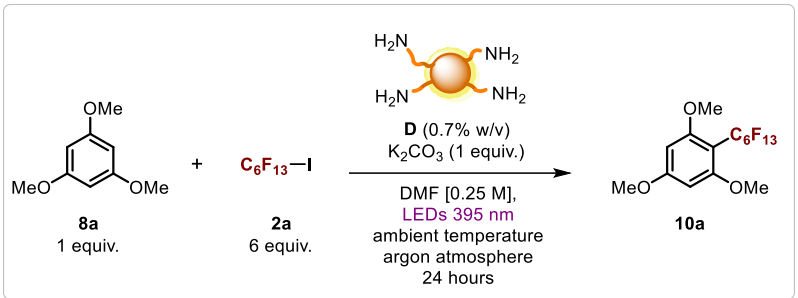

Entry	Deviation from standard conditions	Yield[a]
1	None	>99% (82%)[b]
2	In the dark	0%
3	No CDs **D**	0%
4	LED at 525 nm	0%
5	In air	0%
6	TEMPO (1 equiv.)	0%
7	No K_2CO_3	<5%
8	Solar Simulator[c]	>99%

Table 3. Reactions performed on 0.1 mmol scale. [a] Yield determined by ^{1}H-NMR spectroscopy using 1,1,2-trichloroethene as the internal standard. [b] Isolated yield is shown is parenthesis. [c] Source of photons: Lot-Oriel solar simulator equipped with a 300 W xenon lamp and an integrated Atmospheric Edge Filter with a cut-off at 300 nm.

With the optimized conditions in hand (entry 1, Table 3), we evaluated the synthetic potential of our photochemical perfluoroalkylation strategy (Figure 7), by reacting differently electron-rich aromatic compounds (**8-9**) with perfluoroalkyl iodides (**2**). In addition to the perfluorohexyl moiety (product **10a**), either a shorter or a longer perfluorinated chain were installed in good yield to afford **10b** and **10c**, respectively (up to 93% yield). Interestingly, this particular photochemical process is amenable to scale-up (1 mmol, product **10a**) without any erosion of the chemical yield (85% yield). Mesitylene was also a suitable starting material, and the resulting fluorinated adduct **10d** was isolated in moderate yield (53%). However, our attempts to react benzene under our standard conditions resulted in poor yield (22% yield). This is consonant with the classical HAS reactivity, where the absence of strongly electron-donating groups on **8** greatly decreases the efficiency of the reaction, because of the reduced electron density on the aromatic moiety.[7] The perfluoroalkylation of 2,6-diisopropylaniline (**8d**) led to the sole formation of the para-adduct **10f** in high yield (85%). A phenol derivative (**8e**) was also perfluoroalkylated at the ortho-position to afford **10g** in a moderate isolated yield (31%). The photochemical method was useful to directly functionalize heteroaromatic compounds such as caffeine (**9a**), providing the corresponding fluorinated product **11a** in decent overall yield (40%). In addition, we found that nano-photocatalyst **D** can also be used to photochemically initiate ATRA reactions between alkenes (**1**) and perfluoroalkyl iodides (**2**) to prepare iodoperfluoroalkyl compounds (as well as the photocatalytic systems described in Chapter II). The reaction could efficiently tolerate various terminal olefins (**1a-g**, **i**) bearing alkyl chains, halogens, ether, ester, sulfone and alcohol moieties. These experiments provided the corresponding derivatives (**3a-g**, **i**) from good to excellent isolated yields (up to 90% yield). Lastly, a terminal alkyne (**4a**) was also efficiently transformed into the corresponding unsaturated iodoperfluorohexyl compound (**5a**) in good yield (76% yield, 4:1 *E/Z*).

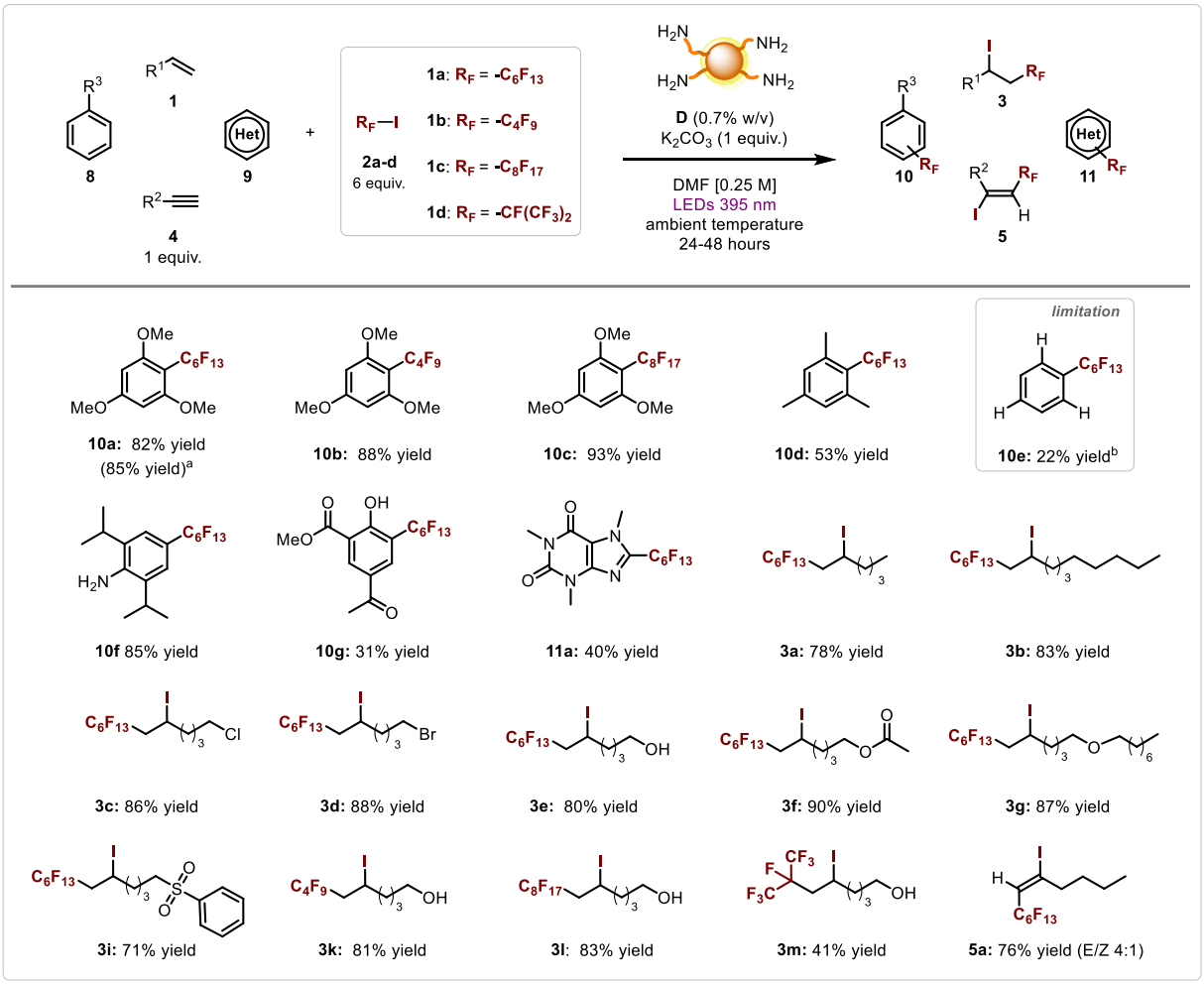

Figure 7. Evaluation of the scope of the photochemical reaction. Survey of the organic compounds and perfluoroalkyl iodides which can participate in the process. Conditions: reactions conducted in Schlenk tubes in DMF (0.25 M) on 0.1 mmol scale of **3-4**,**8-9**, 0.6 mmol of perfluoroalkyl iodide **2**, 0.1 mmol of K_2CO_3 and 0.7 % w/v of **D**, degassed by freeze-pump-thaw cycles and irradiated for 24-48 hours by a LED strip (395 nm). For the synthesis of compounds **10d**, **10e**, **10g** and **11a** reactions were performed over 48 hours. [a] 1 mmol scale reaction. [b] Yield determined by ^{1}H-NMR spectroscopy using 1,1,2-trichloroethene as the internal standard.

3.5 Mechanistic Investigations of the Nano-photocatalyzed Perfluoroalkylation of Electron-rich Organic Compounds

We then sought to demonstrate the role of nano-photocatalyst **D** in the present transformation. Initially, we recorded the absorption spectra of single reaction components, confirming that the only species capable of absorbing visible light at 395 nm is the photocatalyst **D** (red line in Figure 8).

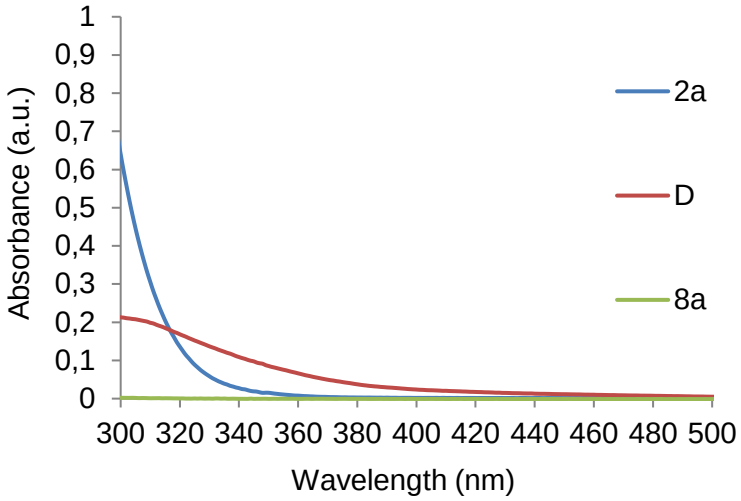

Figure 8. Optical absorption spectra recorded in DMF of the radical source **2a** (0.04 M, blue line), nano-photocatalyst **D** (0.1 mg mL^{-1}, red line), substrate **8a** (0.033 M, green line).

Moreover, we performed a series of Stern-Volmer quenching studies between the nano-photocatalyst (**D**) and the quencher (**2a**) at a wavelength where the quencher does not absorb. Indeed, the emission spectrum of **D** after excitation at 370 nm was recorded (Figure 9a, maximum emission at 430 nm), and we observed that **2a** effectively quenched the emission, and therefore the excited state of the carbon-based nanoparticles (**D***). In particular, the quenching of the emission of **D** was correlated with the concentration of the quencher (**2a**) added to its solution. Therefore, the resulting Stern-Volmer constant (K_{sv}) was represented by the slope of the so-obtained straight, corresponding to 2.14 M^{-1} (Figure 9b).

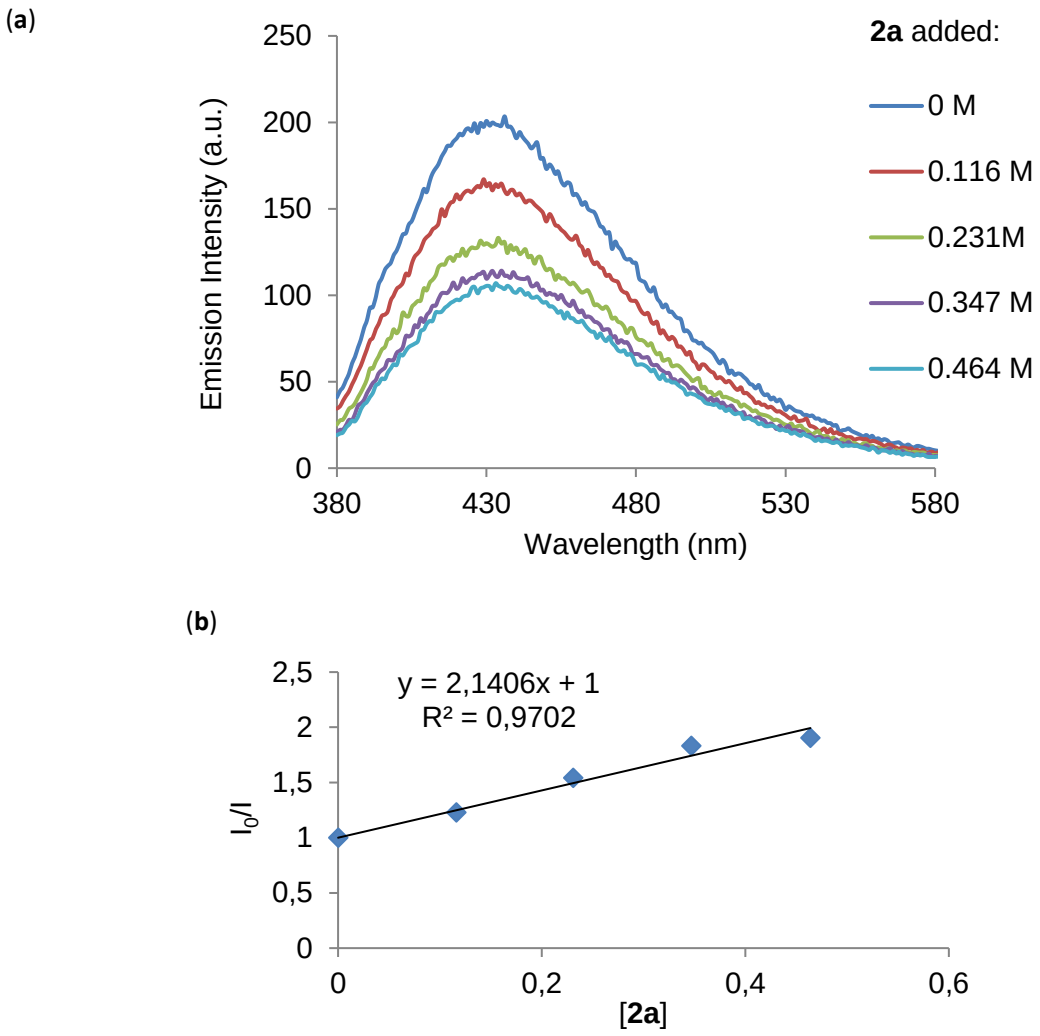

Figure 9. (**a**) Quenching of **D** emission (0.1 mg mL^{-1} in DMF, excitation at 370 nm) in the presence of increasing amounts of perfluorohexyl iodide (**2a**). (**b**) Stern-Volmer constant determination. I_0 = initial emission, I = emission after the addition of the quencher (**2a**).

Additionally, the redox potential of the excited **D** (for the couple $\mathbf{D}^{\bullet+}/\mathbf{D}^*$), was calculated by means of the Rehm-Weller equation (*vide supra*, Section 1.2.3). The reduction potential of **D** in the ground-state (for the couple $\mathbf{D}^{\bullet+}/\mathbf{D}$) was known to correspond to +1.14 V *vs* SCE,[55] and excitation energy (E_{00}) has been estimated spectroscopically from the position of long wavelength tail of the absorption spectrum of **D**. Practically, this was evaluated to be roughly 405 nm, which translates into E_{00} of about 3 V for **D**. Thus, the resulting redox potential of the excited nano-photocatalyst (**D***) turned out to be approximately -2 V *vs* SCE (calculated with *eq. 8*, Section 1.2.3).[68] These studies strongly suggested that a productive PET from **D*** to **2a** could be viable at ambient temperature ($E^0_{\mathbf{2a}} \approx$ -1 V *vs* SCE),[65] thus triggering the formation of fluorinated radical species (**Ia**).

Furthermore, we verified that no ground-state aggregation occurs between the reaction substrate **8a** and the radical source **2a**, since their combination does not lead to any change of the absorption spectra (Figure 10).

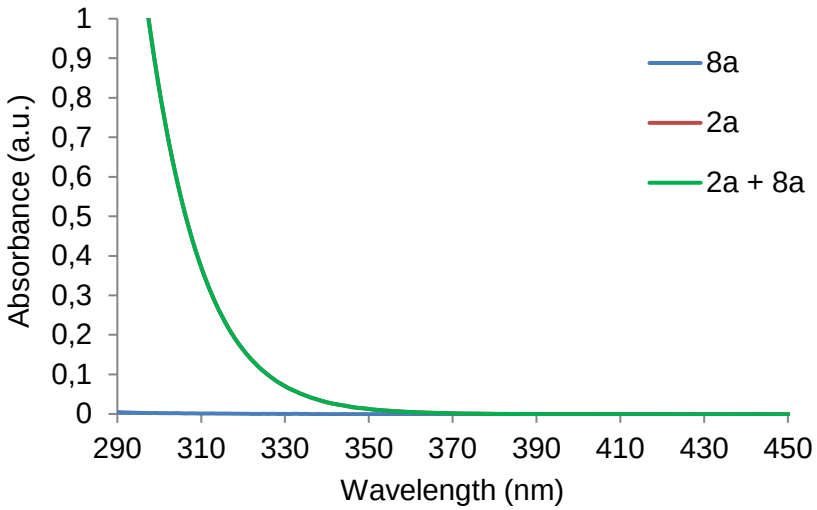

Figure 10. Optical absorption spectra recorded in DMF of the substrate (**8a**, 0.033 M, blue line), perfluorohexyl iodide (**2a**, 0.033 M, red line) and their combination (0.033 M + 0.033 M, green line), optical path length = 1 cm.

For further mechanistic insight, we sought to confirm the hypothesized halogen-bonding activation of the perfluorohexyl iodide (**2a**) by the amine functionalities present on the surface of the nano-photocatalyst **D**. Therefore, we have chosen *n*-butylamine (*n*Bu-NH_2) as model compound to mimic the chemical behavior of the numerous primary surface amino groups, despite it should be mentioned that even less present nitrogen and oxygen containing functionalities might act as halogen-bond acceptors.[15,69] A series of ^{19}F-NMR studies in deuterated DMF (DMF-*d*), demonstrated that *n*Bu-NH_2 may behave as acceptor in the formation of halogen-bonded derivatives with **2a**.[70] Specifically, the total amount of **2a** was kept constant at 0.09 mmol. The amount of *n*-butylamine was varied from 0 to 0.91 mmol. The chemical shift difference (Δδ) between $-CF_2I$ in the different mixtures was calculated and the binding constant (K) of the complex has been determined by numerical fitting of the binding isothermal, plotting $[amine]_{tot}/[\mathbf{2a}]_{tot}$ *vs* Δδ (Figure 11). The so-obtained value corresponded to 2.13 M^{-1}.

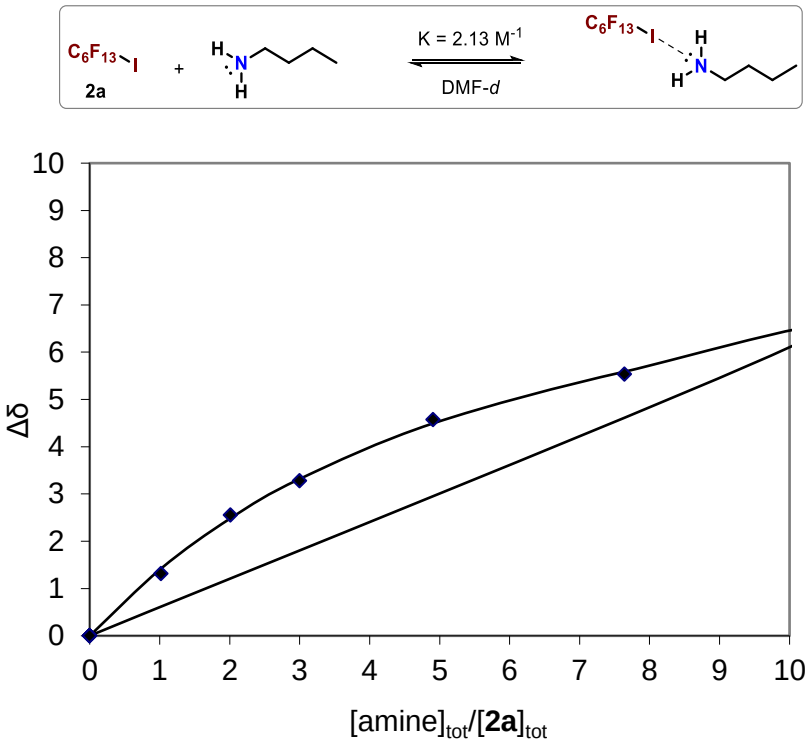

Figure 11. Binding isothermal diagram.

Therefore, the amine-rich **D** used are likely engaged in halogen bonding interaction with **2a**. Supporting this hypothesis is the fact that the presence of **D** induced a detectable shift of the $-CF_2I$ signal in **2a** toward higher ^{19}F-NMR field. In particular, the NMR signal observed after mixing **2a** and **D** turned out to be more resolved and with a different shape than that of **2a** alone (Figure 12). It is worth mentioning that these experiments were carried out at the highest concentration possible of **D** in DMF-*d*, corresponding to 0.33 mg mL^{-1}, to avoid precipitation.

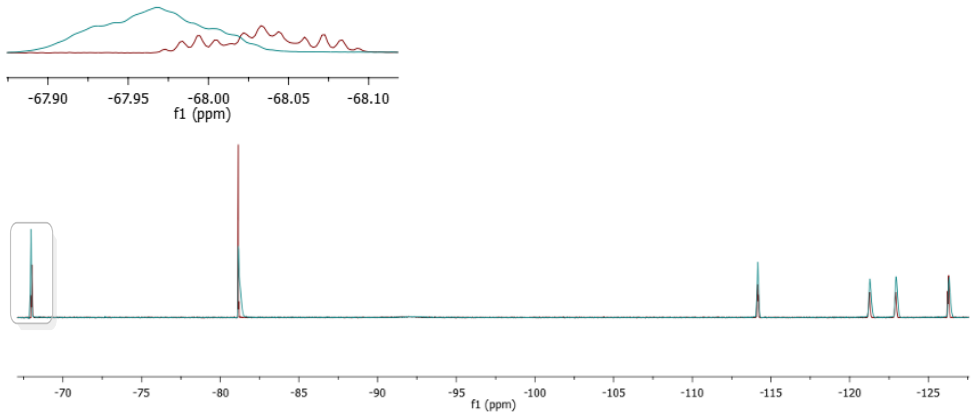

Figure 12. Superimposed ^{19}F spectra of a solution of **2a** (green line, 0.025 M) and **2a** + **D** (red line, **D** = 0.33 mg mL^{-1}) in DMF-*d* with highlighted the enlargement of the -CF_2I group region.

Anyway, it should be noted that the *n*Bu-NH_2 (0.7% w/v) was not catalytically active under the optimized reaction conditions (Entry 2, Table 4). This might be attributed to a lower electron donating character with respect to triethylamine or, alternatively, to the lower absorptivity of the corresponding halogen-bonded complex at the irradiation wavelength.[15,17] In addition, the chemical

yield of the model transformation dropped down to 88% (Entry 3, Table 4) by using a mixture of **D** (0.7% w/v) and *n*Bu-NH_2 (1.4% w/v). This last experiment revealed how the presence of a photocatalytically inactive halogen-bond acceptor is detrimental for the reactivity because it could partly decrease the amount of available **2a** in solution.

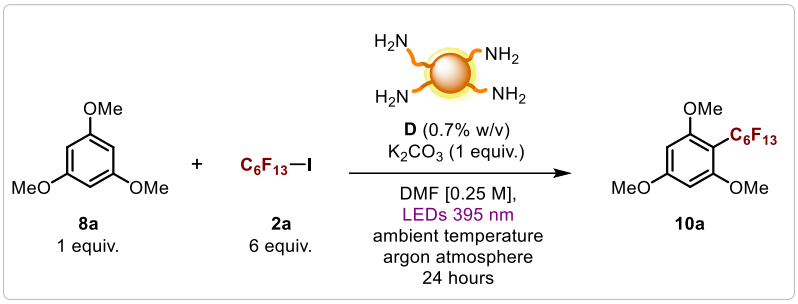

Entry	Deviation from standard conditions	Yield[a]
1	None	>99%
2	*n*Bu-NH_2 (0.7% w/v)	0%
3	**D** (0.7% w/v) + *n*Bu-NH_2 (1.4% w/v)	88%

Table 4. Reactions performed on 0.1 mmol scale. [a] Yield determined by ^{1}H-NMR spectroscopy using 1,1,2-trichloroethene as the internal standard.

On the basis of all these experimental observations, we thus propose the mechanism depicted in Figure 13. Halogen-bond formation brings the nano-photocatalyst **D** and the radical source **2a** in close proximity, thus producing the corresponding adduct **IIIa**. Afterwards, under irradiation with light **D** reaches an electronically excited-state (**D***). The photoexcited nanoparticle induces the reductive cleavage of the adjacent C-I bond in **2a** by PET, giving the oxidized photocatalyst ($\mathbf{D}^{\bullet+}$) and the electrophilic radical **Ia**. The addition of the radical to the aromatic compound **8a** provides the cyclohexadienyl radical **IVa**, which could be oxidized by $\mathbf{D}^{\bullet+}$. The photocatalytic cycle is thus closed. Alternatively, **IVa** could also initiate a radical chain process by reducing **2a**, thereby regenerating **Ia**. Deprotonation of the positively charged intermediate **Va** finally furnishes the desired fluorinated arene **10a**.

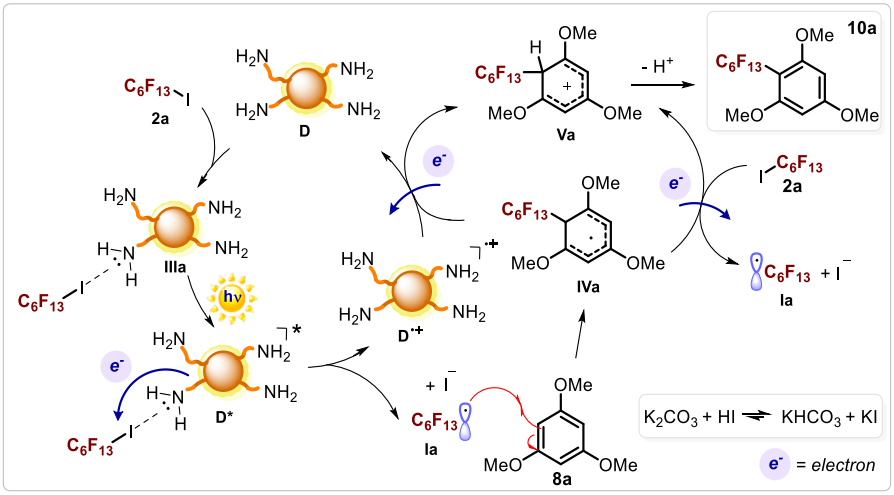

Figure 13. The plausible reaction mechanism which drives the photocatalytic perfluorohexylation of **10a**.

3.6 Conclusions

In summary, we have used amine-rich carbon dots **D** to effectively install perfluoroalkyl groups onto electron-rich organic compounds, including arenes and heteroarenes. The reaction protocol is operationally simple, conducted at ambient temperature with readily available substrates and reagents, and using visible light LEDs as the photon source. This work demonstrates the ability of **D** to intercept the perfluoroalkyl iodides though the formation of halogen-bonded complexes and furthermore to act as a photo-reducing agent upon light excitation. Thus, these carbon-based nanoparticles trigger the formation valuable C-C bonds in an efficient and sustainable manner.

3.7 Experimental Section

3.7.1 General Information

The NMR spectra were recorded on Varian 400 spectrometer (^{1}H: 400 MHz and 376 MHz for ^{19}F). UV-Vis measurements were carried out on PerkinElmer Lambda 35 UV-Vis spectrophotometer. All the spectra were recorded at room temperature using 10 mm path-length cuvettes. Simulated sunlight reaction was driven on a Lot-Oriel solar simulator equipped with a 300 W xenon lamp and an integrated Atmospheric Edge Filter with a cut-off at 300 nm.

General Procedures

All reactions were set up under an argon atmosphere in Schlenk tubes, unless otherwise stated. Synthesis grade and anhydrous solvents were used as purchased. Chromatographic purification of products was accomplished using flash chromatography on silica gel (35-70 mesh). For thin layer chromatography (TLC) analysis throughout this work, Merck pre-coated TLC plates (silica gel 60 GF_{254}, 0.25 mm) were employed, using UV light as the visualizing agent (254 nm), basic aqueous potassium permanganate ($KMnO_4$) stain solution or iodine, and heat as developing agents. Organic solutions were concentrated under reduced pressure on a Büchi rotatory evaporator. The light source used to illuminate the reaction mixture consisted of a 20 UV LEDs strip (390-400 nm, 3.4 V, 20 mA, Figure 14).

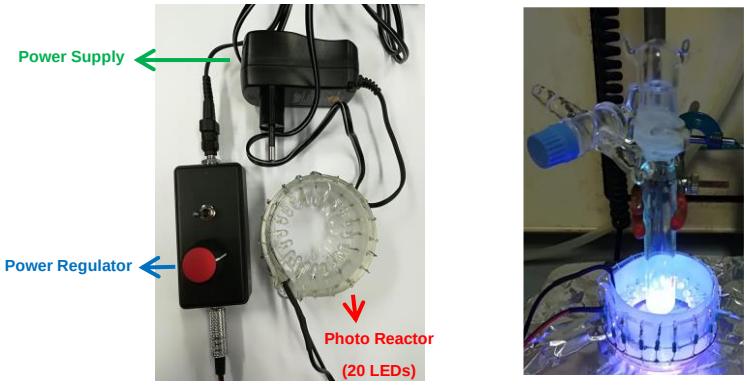

Figure 14. LEDs system and reaction set-up for the photochemical perfluoroalkylations of organic compounds.

Materials

Commercial reagents and solvents were purchased Sigma-Aldrich, Fluka, Alfa Aesar, Fluorochem, VWR and used as received, without further purification, unless otherwise stated. *L*-arginine, ethylenediamine, *n*-butylamine, 1-hexene (**1a**), 1-decen (**1b**), 6-chloro-1-hexene (**1c**), 6-bromo-1-hexene (**1d**), 5-hexen-1-ol (**1e**), perfluorohexyl iodide (**2a**), nonafluoro-1-iodobutane (**2b**), heptadecafluoro-1-iodooctane (**2c**), heptafluoro-2-iodopropane (**2d**), 1-hexyne (**4a**), 1,3,5-trimethoxybenzene (**8a**), mesitylene (**8b**), benzene (**8c**), 2,6-diisopropylaniline (**8d**), methyl 5-acetylsalicylate (**8e**), caffeine (**9a**) and potassium carbonate are all commercially available. The preparation of olefins **1f-g,i** is detailed in the Experimental Section of the preceding chapter (Chapter II, Section 2.9.2).

*^{1}H NMR, ^{13}C and ^{19}F NMR traces and spectra are available in the published manuscript[1] and are not reported in the present thesis. Due to the C-F coupling, some carbon signals of the perfluorinated products **3** and **10** were not detectable.*

3.7.2 Synthesis of the Nano-photocatalyst D and the Starting Materials

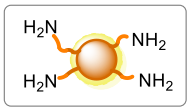

D was prepared according to the literature procedure.[1] *N*-doped CDs (**D**) were obtained via microwave irradiation of an aqueous solution of *L*-Arginine (Arg) and ethylenendiamine (EdA, 1:1 mol/mol). Typically, Arg (87.0 mg), EdA (33.0 µL) and Milli-Q water (100.0 µL) were heated at 240 °C, 26 bar and 200 W for 180 seconds. In the process of microwave heating, the solution changes color from transparent to brown as a result of formation of CDs **D**. The solution was diluted with water and was filtered through a 0.1 µm microporous membrane separating a deep yellow solution that was dialyzed against pure water through a dialysis membrane for 2 days. The aqueous solution of **D** was lyophilized giving a brownish solid (**D**: 23.0 mg). The characterization of the nanoparticles matches with the data reported in the literature.[19,55]

3.7.3 General Procedures for the Photocatalytic Fluoroalkylation of Organic Compounds and Characterization Data

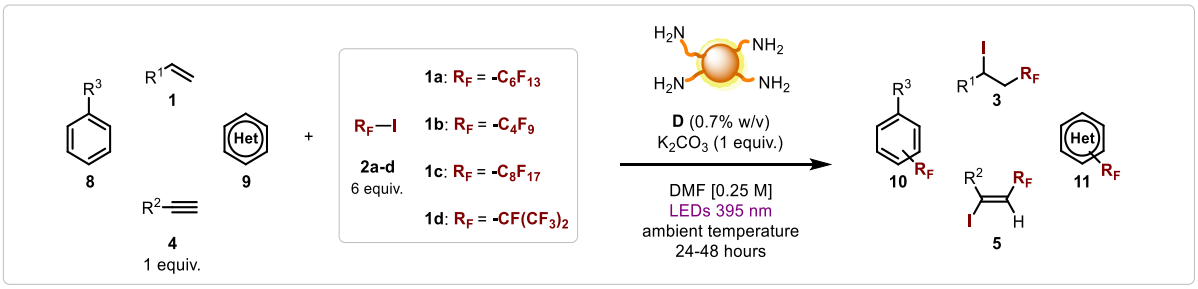

A 10 mL Schlenk tube was charged with the appropriate electron-rich organic compound **1,4,8-9** (0.1 mmol, 1 equiv.), perfluoroalkyl iodide **2** (0.6 mmol, 6 equiv.), potassium carbonate (0.1 mmol, 1 equiv.) and **D** (0.7 w/v, 3.6 mg). To this suspension was then added *N*,*N*-dimethylformamide (0.4 mL, $[substrate]_0$ = 0.25 M). The reaction mixture was thoroughly degassed via freeze-pump-thaw cycles (x 3) and the Schlenk tube was filled with argon and placed in the center of an LED strip (395 nm). Stirring was maintained for 24 hours (48 hours for compounds **10d**, **10e**, **10g** and **11a**) and then the irradiation was stopped. The reaction crude was diluted with a 5% lithium chloride solution and extracted with ethyl acetate (three times). The organic phase was filtered through sodium sulfate. The solvent was removed under reduced pressure and the residue was purified by column chromatography (eluent: *n*-hexane/ethyl acetate) to give the corresponding fluoroalkyl compound **3,5,10-11**.

Characterization Data

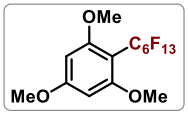

1,3,5-trimethoxy-2-(perfluorohexyl)benzene (10a). Prepared according to the general procedure using 1,3,5-trimethoxybenzene **8a** (0.1 mmol, 17 mg) and perfluorohexyl iodide **2a** (0.6 mmol, 130 µL). The product **10a** was obtained as

white solid (40 mg, 82% yield). The characterization of the compound matches with the data reported in the literature.[12]

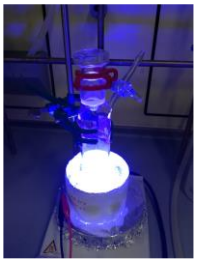

1 mmol scale reaction. The model reaction was replicated on a more synthetically useful scale using a different reaction vessel (20 mL). A 20 mL Schlenk tube was charged with 1,3,5-trimethoxybenzene **8a** (1 mmol, 170 mg), perfluorohexyl iodide **1a** (6 mmol, 1.30 mL), potassium carbonate (1 mmol, 138 mg) and **D** (0.7 w/v, 36 mg). To this suspension was then added *N,N*-dimethylformamide (4 mL, $[\mathbf{8a}]_0$ = 0.25 M). The reaction mixture was thoroughly degassed via freeze-pump-thaw cycles (x 3) and the Schlenk tube was filled with argon and placed in the centre of an LED strip (395 nm). Stirring was maintained for 24 hours and then the irradiation was stopped. The reaction crude was diluted with a 5% lithium chloride solution and extracted with ethyl acetate (three times). The organic phase was filtered through sodium sulfate. The solvent was removed under reduced pressure and the residue was purified by column chromatography (eluent: *n*-hexane/ethyl acetate) to give the corresponding fluoroalkyl compound **10a** (410 mg, 85%).

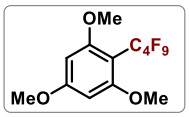

1,3,5-trimethoxy-2-(perfluorobutyl)benzene (10b). Prepared according to the general procedure using 1,3,5-trimethoxybenzene **8a** (0.1 mmol, 17 mg) and nonafluoro-1-iodobutane **2b** (0.6 mmol, 103 µL). The product **10b** was obtained as white solid (34 mg, 88% yield). The characterization of the compound matches with the data reported in the literature.[15]

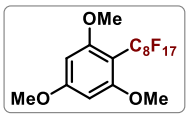

1,3,5-trimethoxy-2-(perfluorooctyl)benzene (10c). Prepared according to the general procedure using 1,3,5-trimethoxybenzene **8a** (0.1 mmol, 17 mg) and heptadecafluoro-1-iodooctane **2c** (0.6 mmol, 158 µL). The product **10c** was obtained as white solid (54 mg, 93% yield). The characterization of the compound matches with the data reported in the literature.[12]

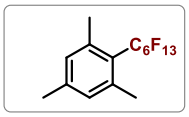

1,3,5-trimethyl-2-(perfluorohexyl)benzene (10d). Prepared according to the general procedure using mesitylene **8b** (0.1 mmol, 14 µL) and perfluorohexyl iodide **2a** (0.6 mmol, 130 µL) over 48 hours of irradiation. The product **10d** was obtained as white solid (23 mg, 53% yield). The characterization of the compound matches with the data reported in the literature.[71]

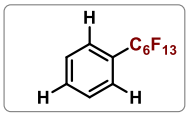

(perfluorohexyl)benzene (10e). Prepared according to the general procedure using benzene **8e** (0.1 mmol, 9 µL) and perfluorohexyl iodide **2a** (0.6 mmol, 130 µL) over 48 hours of irradiation. The yield of **10e** was determined by ^{1}H-NMR spectroscopy to be 22%, in reference to 1,1,2-trichloroethylene (δ 6.5, s, 1H). The characterization of the compound matches with the data reported in the literature.[71] The compound was not isolated due to the paucity of reactivity.

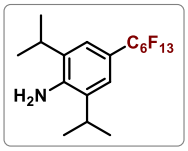

2,6-diisopropyl-4-(perfluorohexyl)aniline (10f). Prepared according to the general procedure using 2,6-diisopropylaniline **8d** (0.1 mmol, 19 µL) and perfluorohexyl iodide **2a** (0.6 mmol, 130 µL). The product **10f** was obtained as white solid (42 mg,

85% yield). The characterization of the compound matches with the data reported in the literature.[72]

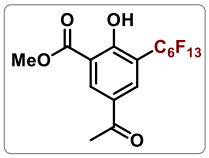

Methyl 5-acetyl-2-hydroxy-3-(perfluorohexyl)benzoate (10g). Prepared according to the general procedure using methyl 5-acetylsalicylate **8e** (0.1 mmol, 19 mg) and perfluorohexyl iodide **2a** (0.6 mmol, 130 µL). The product **10g** was obtained as white solid (16 mg, 31% yield). The characterization of the compound matches with the data reported in the literature.[14]

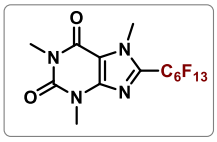

1,3,7-trimethyl-8-(perfluorohexyl)-3,7-dihydro-1*H*-purine-2,6-dione (11a). Prepared according to the general procedure using caffeine **9a** (0.1 mmol, 19 mg) and perfluorohexyl iodide **2a** (0.6 mmol, 130 µL) over 48 hours of irradiation. The product **11a** was obtained as white solid (20 mg, 40% yield). The characterization of the compound matches with the data reported in the literature.[73]

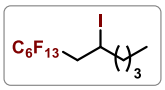

1,1,1,2,2,3,3,4,4,5,5,6,6-tridecafluoro-8-iodododecane (3a). Prepared according to the general procedure using 1-hexene **1a** (0.1 mmol, 13 µL) and perfluorohexyl iodide **2a** (0.6 mmol, 130 µL). The product **3a** was obtained as colorless oil (41 mg, 78% yield). The characterization of the compound matches with the data reported in the literature.[74]

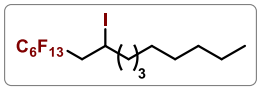

1,1,1,2,2,3,3,4,4,5,5,6,6-tridecafluoro-8-iodohexadecane (3b). Prepared according to the general procedure using 1-decen **1b** (0.1 mmol, 19 µL) and perfluorohexyl iodide **2a** (0.6 mmol, 130 µL). The product **3b** was obtained as colorless oil (49 mg, 83% yield). The characterization of the compound matches with the data reported in the literature.[75]

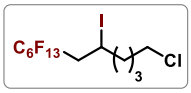

12-chloro-1,1,1,2,2,3,3,4,4,5,5,6,6-tridecafluoro-8-iodododecane (3c). Prepared according to the general procedure using 6-chloro-1-hexene **1c** (0.1 mmol, 13 µL) and perfluorohexyl iodide **2a** (0.6 mmol, 130 µL). The product **3c** was obtained as colorless oil (49 mg, 86% yield). The characterization of the compound matches with the data reported in the literature.[76]

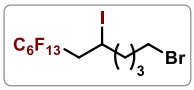

12-bromo-1,1,1,2,2,3,3,4,4,5,5,6,6-tridecafluoro-8-iodododecane (3d). Prepared according to the general procedure using 6-bromo-1-hexene **1d** (0.1 mmol, 14 µL) and perfluorohexyl iodide **2a** (0.6 mmol, 130 µL). The product **3d** was obtained as colorless oil (54 mg, 88% yield). The characterization of the compound matches with the data reported in the literature.[76]

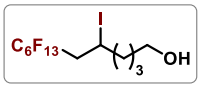

7,7,8,8,9,9,10,10,11,11,12,12,12-tridecafluoro-5-iododecan-1-ol (3e). Prepared according to the general procedure using 5-hexen-1-ol **1e** (0.1 mmol, 12 µL) and perfluorohexyl iodide **2a** (0.6 mmol, 130 µL). The product **3e** was obtained as colorless oil (44 mg, 80% yield). The characterization of the compound matches with the data reported in the literature.[77]

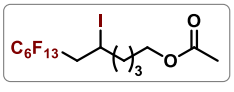

7,7,8,8,9,9,10,10,11,11,12,12,12-tridecafluoro-5-iododecyl acetate (3f). Prepared according to the general procedure using hex-5-en-1-yl acetate **1f** (0.1

mmol, 14 mg) and perfluorohexyl iodide **2a** (0.6 mmol, 130 µL). The product **3f** was obtained as colorless oil (53 mg, 90% yield). The characterization of the compound matches with the data reported in the literature.[76]

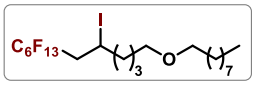

1,1,1,2,2,3,3,4,4,5,5,6,6-tridecafluoro-8-iodo-12-(octyloxy)dodecane (3g). Prepared according to the general procedure using 1-(hex-5-en-1-yloxy)octane **1g** (0.1 mmol, 21 mg) and perfluorohexyl iodide **2a** (0.6 mmol, 130 µL). The product **3g** was obtained as colorless oil (57 mg, 87% yield). The characterization of the compound matches with the data reported in the literature.[76]

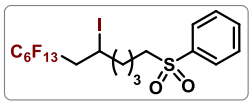

((7,7,8,8,9,9,10,10,11,11,12,12,12-tridecafluoro-5-iodododecyl)sulfonyl)benzene (3i). Prepared according to the general procedure using (hex-5-en-1-ylsulfonyl)benzene **2i** (0.1 mmol, 22 mg) and perfluorohexyl iodide **2a** (0.6 mmol, 130 µL). The product **3i** was obtained as colorless oil (48 mg, 71% yield). The characterization of the compound matches with the data reported in the literature.[76]

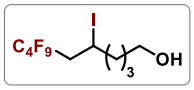

7,7,8,8,9,9,10,10,10-nonafluoro-5-iododecan-1-ol (3k). Prepared according to the general procedure using 5-hexen-1-ol **1e** (0.1 mmol, 12 µL) and nonafluoro-1-iodobutane **2b** (0.6 mmol, 103 µL). The product **3k** was obtained as colorless oil (36 mg, 81% yield). The characterization of the compound matches with the data reported in the literature.[78]

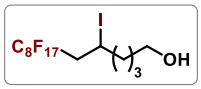

7,7,8,8,9,9,10,10,11,11,12,12,13,13,14,14,14-heptadecafluoro-5-iodotetradecan-1-ol (3l). Prepared according to the general procedure using 5-hexen-1-ol **1e** (0.1 mmol, 12 µL) and heptadecafluoro-1-iodooctane **2c** (0.6 mmol, 158 µL). The product **3l** was obtained as colorless oil (54 mg, 83% yield). The characterization of the compound matches with the data reported in the literature.[65]

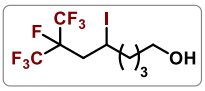

7,8,8,8-tetrafluoro-5-iodo-7-(trifluoromethyl)octan-1-ol (3m). Prepared according to the general procedure using 5-hexen-1-ol **1e** (0.1 mmol, 12 µL) and heptafluoro-2-iodopropane **2d** (0.6 mmol, 85 µL). The product **3m** was obtained as colorless oil (16 mg, 41% yield). The characterization of the compound matches with the data reported in the literature.[65]

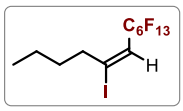

(*E*)-7,7,8,8,9,9,10,10,11,11,12,12,12-tridecafluoro-5-iodododec-5-ene (5a). Prepared according to the general procedure using 1-hexyne **4a** (0.1 mmol, 12 µL) and perfluorohexyl iodide **2a** (0.6 mmol, 130 µL). The product **5a** was obtained as colorless oil (40 mg, 76% yield, 4:1 *E*/*Z*). The characterization of the compound matches with the data reported in the literature.[79]

3.8 References Chapter III

(1) Rosso, C.; Filippini, G.; Prato, M. Use of Nitrogen-Doped Carbon Nanodots for the Photocatalytic Fluoroalkylation of Organic Compounds. *Chem. Eur. J.* **2019**, *25*, 16032–16036.

(2) Rosso, C.; Filippini, G.; Prato, M. Carbon Dots as Nano-Organocatalysts for Synthetic Applications. *ACS Catal.* **2020**, *10*, 8090–8105.

(3) Wang, J.; Sànchez-Rosellò, M.; Aceña, J. L.; del Pozo, C.; Sorochinsky, A. E.; Fustero, S.; Soloshonok, V. A.; Liu, H. Fluorine in Pharmaceutical Industry : Fluorine-Containing Drugs Introduced to the Market in the Last Decade (2001 − 2011). *Chem. Rev.* **2014**, *114*, 2432–2506.

(4) Zhou, Y.; Wang, J.; Gu, Z.; Wang, S.; Zhu, W.; Aceña, J. L.; Soloshonok, V. A.; Izawa, K.; Liu, H. Next Generation of Fluorine-Containing Pharmaceuticals , Compounds Currently in Phase II − III Clinical Trials of Major Pharmaceutical Companies : New Structural Trends and Therapeutic Areas. *Chem. Rev.* **2016**, *116*, 422–518.

(5) Berger, R.; Resnati, G.; Metrangolo, P.; Weber, E.; Hulliger, J. Organic Fluorine Compounds : A Great Opportunity for Enhanced Materials Properties. *Chem. Soc. Rev.* **2011**, *40*, 3496–3508.

(6) Barata-Vallejo, S.; Cooke, M. V.; Postigo, A. Radical Fluoroalkylation Reactions. *ACS Catal.* **2018**, *8*, 7287–7307.

(7) Bowman, W. R.; Storey, J. M. D. Synthesis Using Aromatic Homolytic Substitution - Recent Advances. *Chem. Soc. Rev.* **2007**, *36*, 1803–1822.

(8) Studer, A.; Curran, D. P. Catalysis of Radical Reactions: A Radical Chemistry Perspective. *Angew. Chem. Int. Ed.* **2016**, *55*, 58–102.

(9) Chatterjee, T.; Iqbal, N.; You, Y.; Cho, E. J. Controlled Fluoroalkylation Reactions by Visible-Light Photoredox Catalysis. *Acc. Chem. Res.* **2016**, *49*, 2284–2294.

(10) Petzold, D.; Giedyk, M.; Chatterjee, A.; König, B. A Retrosynthetic Approach for Photocatalysis. *Eur. J. Org. Chem.* **2020**, No. 10, 1193–1244.

(11) Nagib, D. A.; MacMillan, D. W. C. Trifluoromethylation of Arenes and Heteroarenes by Means of Photoredox Catalysis. *Nature* **2011**, *480*, 224–228.

(12) Cui, L.; Matusaki, Y.; Tada, N.; Miura, T.; Uno, B.; Itoh, A. Metal-Free Direct C-H Perfluoroalkylation of Arenes and Heteroarenes Using a Photoredox Organocatalyst. *Adv. Synth. Catal.* **2013**, *355*, 2203–2207.

(13) Nappi, M.; Bergonzini, G.; Melchiorre, P. Metal-Free Photochemical Aromatic Perfluoroalkylation of α-Cyano Arylacetates. *Angew. Chem. Int. Ed.* **2014**, *53*, 4921–4925.

(14) Filippini, G.; Nappi, M.; Melchiorre, P. Photochemical Direct Perfluoroalkylation of Phenols. *Tetrahedron* **2015**, *71*, 4535–4542.

(15) Wang, Y.; Wang, J.; Li, G.; He, G.; Chen, G. Halogen-Bond-Promoted Photoactivation of Perfluoroalkyl Iodides: A Photochemical Protocol for Perfluoroalkylation Reactions. *Org. Lett.* **2017**, *19*, 1442–1445.

(16) König, B. Photocatalysis in Organic Synthesis – Past, Present, and Future. *Eur. J. Org. Chem.* **2017**, 1979–1981.

(17) Rosso, C.; Williams, J. D.; Filippini, G.; Prato, M.; Kappe, C. O. Visible-Light-Mediated Iodoperfluoroalkylation of Alkenes in Flow and Its Application to the Synthesis of a Key Fulvestrant Intermediate. *Org. Lett.* **2019**, *21*, 5341–5345.

(18) Arcudi, F.; Đorđević, L.; Prato, M. Design, Synthesis, and Functionalization Strategies of Tailored Carbon Nanodots. *Acc. Chem. Res.* **2019**, *52*, 2070–2079.

(19) Đorđević, L.; Arcudi, F.; Prato, M. Preparation, Functionalization and Characterization of Engineered Carbon Nanodots. *Nat. Protoc.* **2019**, *14*, 2931–2953.

(20) Kang, Z.; Lee, S. T. Carbon Dots: Advances in Nanocarbon Applications. *Nanoscale* **2019**, *11*, 19214–19224.

(21) Gao, J.; Zhu, M.; Huang, H.; Liu, Y.; Kang, Z. Advances, Challenges and Promises of Carbon Dots. *Inorg. Chem. Front.* **2017**, *4*, 1963–1986.

(22) Cayuela, A.; Soriano, M. L.; Carrillo-Carrión, C.; Valcárcel, M. Semiconductor and Carbon-Based Fluorescent Nanodots: The Need for Consistency. *Chem. Commun.* **2016**, *52*, 1311–1326.

(23) Dhenadhayalan, N.; Lin, K. C.; Saleh, T. A. Recent Advances in Functionalized Carbon Dots toward the Design of Efficient Materials for Sensing and Catalysis Applications. *Small* **2020**, *16*, 1905767.

(24) Li, H.; Liu, R.; Lian, S.; Liu, Y.; Huang, H.; Kang, Z. Near-Infrared Light Controlled Photocatalytic Activity of Carbon Quantum Dots for Highly Selective Oxidation Reaction. *Nanoscale* **2013**, *5*, 3289–3297.

(25) Tejwan, N.; Saha, S. K.; Das, J. Multifaceted Applications of Green Carbon Dots Synthesized from Renewable Sources. *Adv. Colloid Interface Sci.* **2020**, *275*, 102046.

(26) Li, F.; Yang, D.; Xu, H. Non-Metal-Heteroatom-Doped Carbon Dots: Synthesis and Properties. *Chem. Eur. J.* **2019**, *25*, 1165–1176.

(27) Yu, H.; Shi, R.; Zhao, Y.; Waterhouse, G. I. N.; Wu, L. Z.; Tung, C. H.; Zhang, T. Smart Utilization of Carbon Dots in Semiconductor Photocatalysis. *Adv. Mater.* **2016**, *28*, 9454–9477.

(28) Xu, X.; Ray, R.; Gu, Y.; Ploehn, H. J.; Gearheart, L.; Raker, K.; Scrivens, W. A. Electrophoretic Analysis and Purification of Fluorescent Single-Walled Carbon Nanotube Fragments. *J. Am. Chem. Soc.* **2004**, *126*, 12736–12737.

(29) Han, M.; Zhu, S.; Lu, S.; Song, Y.; Feng, T.; Tao, S.; Liu, J.; Yang, B. Recent Progress on the Photocatalysis of Carbon Dots: Classification, Mechanism and Applications. *Nano Today* **2018**, *19*, 201–218.

(30) Sharma, A.; Das, J. Small Molecules Derived Carbon Dots: Synthesis and Applications in Sensing, Catalysis, Imaging, and Biomedicine. *J. Nanobiotechnology* **2019**, *17*, 92.

(31) Wang, R.; Lu, K. Q.; Tang, Z. R.; Xu, Y. J. Recent Progress in Carbon Quantum Dots: Synthesis, Properties and Applications in Photocatalysis. *J. Mater. Chem. A* **2017**, *5*, 3717–3734.

(32) Bertelsen, S.; Jørgensen, K. A. Organocatalysis—after the Gold Rush. *Chem. Soc. Rev.* **2009**, *38*, 2178–2189.

(33) Alemán, J.; Cabrera, S. Applications of Asymmetric Organocatalysis in Medicinal Chemistry. *Chem. Soc. Rev.* **2013**, *42*, 774–793.

(34) Yoon, T. P.; Ischay, M. A.; Du, J. Visible Light Photocatalysis as a Greener Approach to Photochemical Synthesis. *Nat. Chem.* **2010**, *2*, 527–532.

(35) Testa, C.; Zammataro, A.; Pappalardo, A.; Trusso Sfrazzetto, G. Catalysis with Carbon Nanoparticles. *RSC Adv.* **2019**, *9*, 27659–27664.

(36) Zammataro, A.; Sfrazzetto, G. T. Carbon Dots as Catalysts: A New Class of Nanozymes. *Curr. Organocatalysis* **2019**, *7*, 3–6.

(37) Burgman, M.; Tennant, M.; Voulvoulis, N.; Makuch, K.; Madani, K. Facilitating the Transition to Sustainable Green Chemistry. *Curr. Opin. Green Sustain. Chem.* **2018**, *13*, 130–136.

(38) Michelin, C.; Hoffmann, N. Photocatalysis Applied to Organic Synthesis – A Green Chemistry Approach. *Curr. Opin. Green Sustain. Chem.* **2018**, *10*, 40–45.

(39) Rothenberg, G. *Catalysis: Concepts and Green Applications*; Wiley-VCH, 2017.

(40) Crisenza, G. E. M.; Melchiorre, P. Chemistry Glows Green with Photoredox Catalysis. *Nat. Commun.* **2020**, *11*, 8–11.

(41) Miao, X.; Qu, D.; Yang, D.; Nie, B.; Zhao, Y.; Fan, H.; Sun, Z. Synthesis of Carbon Dots with Multiple Color Emission by Controlled Graphitization and Surface Functionalization. *Adv. Mater.* **2018**, *30*, 1704740.

(42) Arcudi, F.; Đorđević, L.; Prato, M. Rationally Designed Carbon Nanodots towards Pure White-Light Emission. *Angew. Chem. Int. Ed.* **2017**, *56*, 4170–4173.

(43) Lu, S.; Xiao, G.; Sui, L.; Feng, T.; Yong, X.; Zhu, S.; Li, B.; Liu, Z.; Zou, B.; Jin, M.; Tse, J. S.; Yan, H.; Yang, B. Piezochromic Carbon Dots with Two-Photon Fluorescence. *Angew. Chem. Int. Ed.* **2017**, *56*, 6187–6191.

(44) Sun, Y. P.; Zhou, B.; Lin, Y.; Wang, W.; Fernando, K. A. S.; Pathak, P.; Meziani, M. J.; Harruff, B. A.; Wang, X.; Wang, H.; Luo, P. G.; Yang, H.; Kose, M. E.; Chen, B.; Veca, L. M.; Xie, S. Y. Quantum-Sized Carbon Dots for Bright and Colorful Photoluminescence. *J. Am. Chem. Soc.* **2006**, *128*, 7756–7757.

(45) Ragazzon, G.; Cadranel, A.; Ushakova, E. V.; Wang, Y.; Guldi, D. M.; Rogach, A. L.; Kotov, N. A.; Prato, M. Optical Processes in Carbon Nanocolloids. *Chem* **2020**, DOI: 10.1016/j.chempr2020.11.012.

(46) Hutton, G. A. M.; Martindale, B. C. M.; Reisner, E. Carbon Dots as Photosensitisers for Solar-Driven Catalysis. *Chem. Soc. Rev.* **2017**, *46*, 6111–6123.

(47) Hu, C.; Li, M.; Qiu, J.; Sun, Y. P. Design and Fabrication of Carbon Dots for Energy Conversion and Storage. *Chem. Soc. Rev.* **2019**, *48*, 2315–2337.

(48) Li, H.; He, X.; Kang, Z.; Huang, H.; Liu, Y.; Liu, J.; Lian, S.; Tsang, C. H. A.; Yang, X.; Lee, S. T.

Water-Soluble Fluorescent Carbon Quantum Dots and Photocatalyst Design. *Angew. Chem. Int. Ed.* **2010**, *49*, 4430–4434.

(49) Cadranel, A.; Margraf, J. T.; Strauss, V.; Clark, T.; Guldi, D. M. Carbon Nanodots for Charge-Transfer Processes. *Acc. Chem. Res.* **2019**, *52*, 955–963.

(50) Cao, L.; Shiral Fernando, K. A.; Liang, W.; Seilkop, A.; Monica Veca, L.; Sun, Y. P.; Bunker, C. E. Carbon Dots for Energy Conversion Applications. *J. Appl. Phys.* **2019**, *125*, 220903.

(51) Bhattacharyya, S.; Ehrat, F.; Urban, P.; Teves, R.; Wyrwich, R.; Döblinger, M.; Feldmann, J.; Urban, A. S.; Stolarczyk, J. K. Effect of Nitrogen Atom Positioning on the Trade-off between Emissive and Photocatalytic Properties of Carbon Dots. *Nat. Commun.* **2017**, *8*, 1401.

(52) Han, Y.; Huang, H.; Zhang, H.; Liu, Y.; Han, X.; Liu, R.; Li, H.; Kang, Z. Carbon Quantum Dots with Photoenhanced Hydrogen-Bond Catalytic Activity in Aldol Condensations. *ACS Catal.* **2014**, *4*, 781–787.

(53) Li, H.; Sun, C.; Ali, M.; Zhou, F.; Zhang, X.; MacFarlane, D. R. Sulfated Carbon Quantum Dots as Efficient Visible-Light Switchable Acid Catalysts for Room-Temperature Ring-Opening Reactions. *Angew. Chem. Int. Ed.* **2015**, *54*, 8420–8424.

(54) Sarma, D.; Majumdar, B.; Sarma, T. K. Visible-Light Induced Enhancement in the Multi-Catalytic Activity of Sulfated Carbon Dots for Aerobic Carbon-Carbon Bond Formation. *Green Chem.* **2019**, *21*, 6717–6726.

(55) Arcudi, F.; Đorđević, L.; Prato, M. Synthesis, Separation, and Characterization of Small and Highly Fluorescent Nitrogen-Doped Carbon Nanodots. *Angew. Chem. Int. Ed.* **2016**, *55*, 2107–2112.

(56) Troll, W.; Cannan, R. K. A Modified Photometric Ninhydrin Method for the Analysis of Amino and Imino Acids. *J. Biol. Chem.* **1953**, *200*, 803–811.

(57) Carrara, S.; Arcudi, F.; Prato, M.; De Cola, L. Amine-Rich Nitrogen-Doped Carbon Nanodots as a Platform for Self-Enhancing Electrochemiluminescence. *Angew. Chem. Int. Ed.* **2017**, *56*, 4757–4761.

(58) Arcudi, F.; Strauss, V.; Đorđević, L.; Cadranel, A.; Guldi, D. M.; Prato, M. Porphyrin Antennas on Carbon Nanodots: Excited State Energy and Electron Transduction. *Angew. Chem. Int. Ed.* **2017**, *56*, 12097–12101.

(59) Rizzo, C.; Arcudi, F.; Đorđević, L.; Dintcheva, N. T.; Noto, R.; D'Anna, F.; Prato, M. Nitrogen-Doped Carbon Nanodots-Ionogels: Preparation, Characterization, and Radical Scavenging Activity. *ACS Nano* **2018**, *12*, 1296–1305.

(60) Cadranel, A.; Strauss, V.; Margraf, J. T.; Winterfeld, K. A.; Vogl, C.; Đorđević, L.; Arcudi, F.; Hoelzel, H.; Jux, N.; Prato, M.; Guldi, D. M. Screening Supramolecular Interactions between Carbon Nanodots and Porphyrins. *J. Am. Chem. Soc.* **2018**, *140*, 904–907.

(61) Rigodanza, F.; Đorđević, L.; Arcudi, F.; Prato, M. Customizing the Electrochemical Properties of Carbon Nanodots by Using Quinones in Bottom-Up Synthesis. *Angew. Chem. Int. Ed.* **2018**, *57*, 5062–5067.

(62) Cacioppo, M.; Scharl, T.; Đorđević, L.; Cadranel, A.; Arcudi, F.; Guldi, D. M.; Prato, M.

Symmetry-Breaking Charge-Transfer Chromophore Interactions Supported by Carbon Nanodots. *Angew. Chem. Int. Ed.* **2020**, *59*, 12779–12784.

(63) Đorđević, L.; Haines, P.; Cacioppo, M.; Arcudi, F.; Scharl, T.; Cadranel, A.; Guldi, D. M.; Prato, M. Synthesis and Excited State Processes of Arrays Containing Amine-Rich Carbon Dots and Unsymmetrical Rylene Diimides. *Mater. Chem. Front.* **2020**, *4*, 3640–3648.

(64) Farid, S.; Dinnocenzo, J. P.; Merkel, P. B.; Young, R. H.; Shukla, D.; Guirado, G. Reexamination of the Rehm-Weller Data Set Reveals Electron Transfer Quenching That Follows a Sandros-Boltzmann Dependence on Free Energy. *J. Am. Chem. Soc.* **2011**, *133*, 11580–11587.

(65) Wallentin, C.; Nguyen, J. D.; Finkbeiner, P.; Stephenson, C. R. J. Visible Light-Mediated Atom Transfer Radical Addition via Oxidative and Reductive Quenching of Photocatalysts. *J. Am. Chem. Soc.* **2012**, *134*, 8875–8884.

(66) Sliney, D. H. What Is Light? The Visible Spectrum and Beyond. *Eye* **2016**, *30*, 222–229.

(67) van der Helm, M. P.; Klemm, B.; Eelkema, R. Organocatalysis in Aqueous Media. *Nat. Rev. Chem.* **2019**, *3*, 491–508.

(68) Buzzetti, L.; Crisenza, G. E. M.; Melchiorre, P. Mechanistic Studies in Photocatalysis. *Angew. Chem. Int. Ed.* **2019**, *58*, 3730–3747.

(69) Sun, X.; Wang, W.; Li, Y.; Ma, J.; Yu, S. Halogen-Bond-Promoted Double Radical Isocyanide Insertion under Visible-Light Irradiation: Synthesis of 2-Fluoroalkylated Quinoxalines. *Org. Lett.* **2016**, *18*, 4638–4641.

(70) Cavallo, G.; Metrangolo, P.; Milani, R.; Pilati, T.; Priimagi, A.; Resnati, G.; Terraneo, G. The Halogen Bond. *Chem. Rev.* **2016**, *116*, 2478–2601.

(71) Khrizanforov, M.; Khrizanforova, V.; Mamedov, V.; Zhukova, N.; Strekalova, S.; Grinenko, V.; Gryaznova, T.; Sinyashin, O.; Budnikova, Y. Single-Stage Synthetic Route to Perfluoroalkylated Arenes via Electrocatalytic Cross-Coupling of Organic Halides Using Co and Ni Complexes. *J. Organomet. Chem.* **2016**, *820*, 82–88.

(72) He, C. Y.; Gu, J. W.; Zhang, X. Visible-Light-Mediated Direct Perfluoroalkylation and Trifluoromethylation of Free Anilines. *Tetrahedron Lett.* **2017**, *58*, 3939–3941.

(73) Aikawa, K.; Nakamura, Y.; Yokota, Y.; Toya, W.; Mikami, K. Stable but Reactive Perfluoroalkylzinc Reagents: Application in Ligand-Free Copper-Catalyzed Perfluoroalkylation of Aryl Iodides. *Chem. Eur. J.* **2015**, *21*, 96–100.

(74) Huang, W.-Y.; Zhang, H.-Z. Reaction of Perfluoroalkyl Iodides with Alkenes Initiated by Organophosphine and Related Compounds. *J. Fluor. Chem.* **1990**, *50*, 133–140.

(75) Yajima, T.; Ikegami, M. Metal-Free Visible-Light Radical Iodoperfluoroalkylation of Terminal Alkenes and Alkynes. *Eur. J. Org. Chem.* **2017**, 2126–2129.

(76) Rosso, C.; Filippini, G.; Cozzi, P. G.; Gualandi, A.; Prato, M. Highly Performing Iodoperfluoroalkylation of Alkenes Triggered by the Photochemical Activity of Perylene Diimides. *ChemPhotoChem* **2019**, *3*, 193–197.

(77) Arceo, E.; Montroni, E.; Melchiorre, P. Photo-Organocatalysis of Atom-Transfer Radical

Additions to Alkenes. *Angew. Chem. Int. Ed.* **2014**, *53*, 12064–12068.

(78) Kohlmeier, A.; Janietz, D. Hydrogen-Bonded Polyphilic Block Mesogens with Semiperfluorinated Segments. *Chem. Mater.* **2006**, *18*, 59–68.

(79) Vázquez, A. J.; Nudelman, N. S. Perfluoroalkylation of Alkenes and Alkynes in Water. *Arkivoc* **2015**, 190–201.

Chapter IV

Surface Groups on Amine-rich Carbon Dots Enable Covalent Aminocatalysis in Aqueous Media

Abstract

Chapter IV discusses the use of the nitrogen-doped carbon dots **D** as covalent aminocatalysts through enamine or iminium ion activation in aqueous media. In particular, besides the intrinsic photochemical properties of these carbon nanoparticles, the high number of surface amino groups can be exploited in covalent organocatalysis for the α or β-functionalization of carbonyl compounds. This work demonstrated how a detailed characterization of the mentioned carbon dots (particularly by ^{19}F-tagging NMR spectroscopy, acid-base titration and Kaiser test) is instrumental to unlock their application in green synthetically relevant polar transformations. As a result of the multi-functional properties of these carbon-based nanoparticles, diverse conjugate additions (e.g., Michael, *aza*-Michael, *sulfa*-Michael reactions) and aldol reactions occurred with noteworthy efficiency. In addition, when chiral nitrogen-doped carbon dots **E** were employed, the corresponding asymmetric products were obtained with appreciable optical activity, demonstrating that the chirality can be transferred with molecular control in the catalytic process. This provided the proof of principle for the implementation of nanomaterials into chemical roles previously considered only attainable by the molecular realm.

This work was conducted within the Prato and Bonchio group, together with *Prof. Maurizio Prato* and *Prof. Marcella Bonchio*, who supervised the project; with *Dr. Giacomo Filippini*, *Dr. Giulio Ragazzon*, *Dr. Xavier Companyò*, who conceived the idea and performed some of the catalytic experiments; with *Mr. Francesco Amato*, who prepared and characterized the CDs employed; with *Dr. Alberto Vega-Peñaloza* and *Dr. Luca Dell'Amico*, who performed the ^{19}F-NMR experiments. A significant part of this work has been published in 2020.[1]

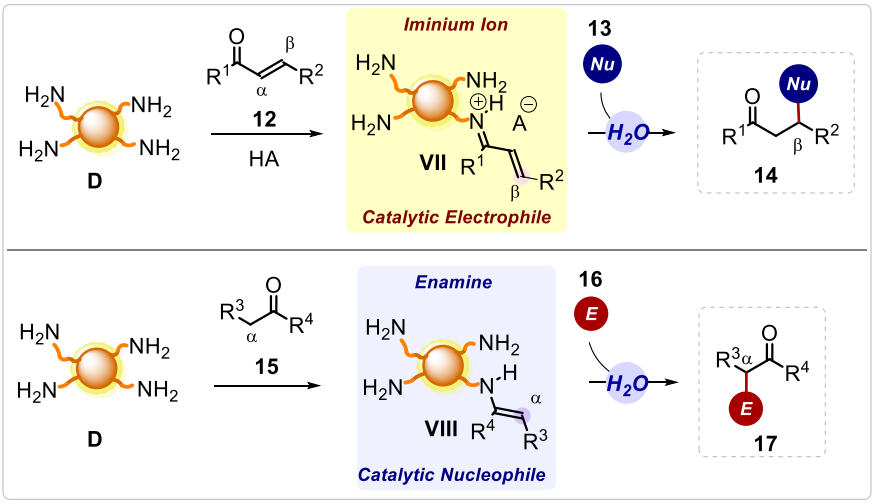

4.1 Introduction

Carbon dots (CDs) stand as the missing link between the molecular and the nanoscale world, owing to the unique molecular-like behavior emerging from their synthetic precursors. In fact, the easy programming of the multifunctional CDs surface, along with the low toxicity and fast preparation of these carbon-based nanoparticles are making them a potential game-changer for advanced technological applications.[2–4] Moreover, the successful implementation of carbon nanostructures into chemical roles so far restricted to molecular systems may open new opportunities, where the nanoscale and the molecular realms will merge and complement each other. In this context, CDs are rising as promising nano-catalytic platforms that fulfill the sustainability requirements for green chemical production.[5] Therefore, CDs may bridge the gap between homogeneous and heterogeneous catalysis, by transferring key molecular prerogatives at the horizon of nanoscale materials.

As described in Chapter III, the surface functionalities of CDs play a pivotal role in regulating the chemistry of the nanoparticles and hence their catalytic attitude. Specifically, the nature of these groups can profoundly influence the optoelectronic features of CDs and their consequent application in radical organic photochemistry. Besides, these superficial moieties can be further exploited in polar reactivities for the preparation of strategic C–C and C–heteroatom bonds under mild and green conditions. In doing so, CDs act as proper nano-organocatalysts.[5] Furthermore, the appeal of this approach relates to the straightforward synthesis, cost-efficiency, safety, potential recyclability and multifunctionality of these nanostructured particles with respect to the commonly used molecular organocatalysts.[5] Remarkably, CDs can exhibit high solubility in water without any additional post-synthetical treatment, whereas the other mentioned organocatalysts would require a proper derivatization for this purpose, generally through tedious multistep synthesis.[6–10] This is of practical importance, since organocatalytic transformations in environmentally benign solvents, such as water, are receiving growing attention with the aim of designing sustainable processes even in biological surroundings.[6] Therefore, the direct use of CDs as nano-organocatalysts in aqueous media turned out to be promptly achievable for benchmark organocatalytic transformations by means of acid-base catalysis, hydrogen-bond catalysis and aminocatalysis (Figure 1).[5]

4.2 CDs as Nano-organocatalysts

Acid-base catalysis and, specifically, Brønsted acid catalysis employs a protic acid to enhance the electrophilicity of a substrate towards a nucleophilic reagent.[11] CDs bearing carboxylic acids on their surface can act as Brønsted acid catalysts in various organic transformations. Indeed, Sarma and co-workers reported the synthesis of biologically relevant *aza*-Michael adducts and quinazolinones by exploiting the surface acidity of CDs catalysts displaying carboxyl functionalities (Figure 1a).[12] These carbon nanoparticles were obtained from β-carotene through a hydrothermal treatment in water at 180°C over 3 h under air, followed by filtration, affording spherical carbon nanoparticles with size in the range of 3.5-5.5 nm (determined by TEM and AFM). Despite the nanomaterial precursor did not contain any oxygen atom, the superficial -COOH groups were generated during the carbonization process in the presence of water and air (concentration of carboxylic groups calculated to be 145 μmol/L). By using these CDs as nano-organocatalysts, the abovementioned

condensation reactions proceeded in the order of minutes in aqueous media with low CDs loading (0.5 mg/mL).

Hydrogen bond catalysis is an alternative route to activate electrophiles by the formation of a hydrogen bond network between the proton donor and the acceptor, represented by the organocatalyst and the electrophilic reaction substrate, respectively.[13] CDs bearing hydroxyl groups on their surface can act as hydrogen bond catalysts in nucleophilic addition reactions towards the appropriate electrophiles.[14] In fact, Sing, Jang and co-workers described multi-component condensation reactions between naphthols, aldehydes and malononitriles by employing CDs embedded in micelles as proton donor species in water (Figure 1b).[15] These carbon nanoparticles were prepared by autoclave pyrolysis of an aqueous solution of citric acid at 160°C over 6 h under air and purified through centrifugation followed by dialysis against water. The obtained CDs were classified as CQDs, showing an average size range of 7.5 nm (determined by dynamic light scattering, DLS) and a high density of hydroxyl and carboxyl functionalities on the surface of the nanomaterial. These CDs were then incorporated into micelles formed by imidazolium-based ionic liquids in water. The resulting hybrid systems, having dimensions of 27-32 nm by DLS, were able to trap organic reactants in their interior cavity where the reactions take place. In this way, the condensation reactions took place in the presence of a stoichiometric amount of the hybrid CD-based system in water under sonication at room temperature.

Aminocatalysis is one of the most important branches of organocatalysis. It employs primary and secondary amines to activate the functionalization of carbonyl compounds.[16] CDs carrying amino groups on their surface are capable of driving catalytic aldol-type reactions on suitable carbonyl substrates. For instance, Wang and co-workers reported the use of amine-terminated CDs to catalyze Knoevenagel condensation reactions in a biphasic mixture of water and 1-octanol (Figure 1c).[17] These carbon nanoparticles were prepared by pyrolysis of a mixture of citric acid and suit-able diamines in 1-octanol at 180°C (over 6 h) under argon and purified by washing with water. These CDs possess aliphatic primary, secondary or tertiary amines on their surface, according to the nitrogen-rich precursor added, and they display an average particle diameter of 5.5 nm (determined by TEM). The density of surface amino groups on these CDs ranged between 2.79 to 4.06 μmol/g, calculated by thermogravimetric analysis (TGA) and X-ray photoelectron spectroscopy (XPS). By using these amine-rich carbon nanoparticles in low catalytic loadings (0.14 g/L), the authors were able to carry out the mentioned transformations. Interestingly, they demonstrated that CDs bearing primary amines are more efficient in promoting condensation reactions than those holding secondary or tertiary amines.

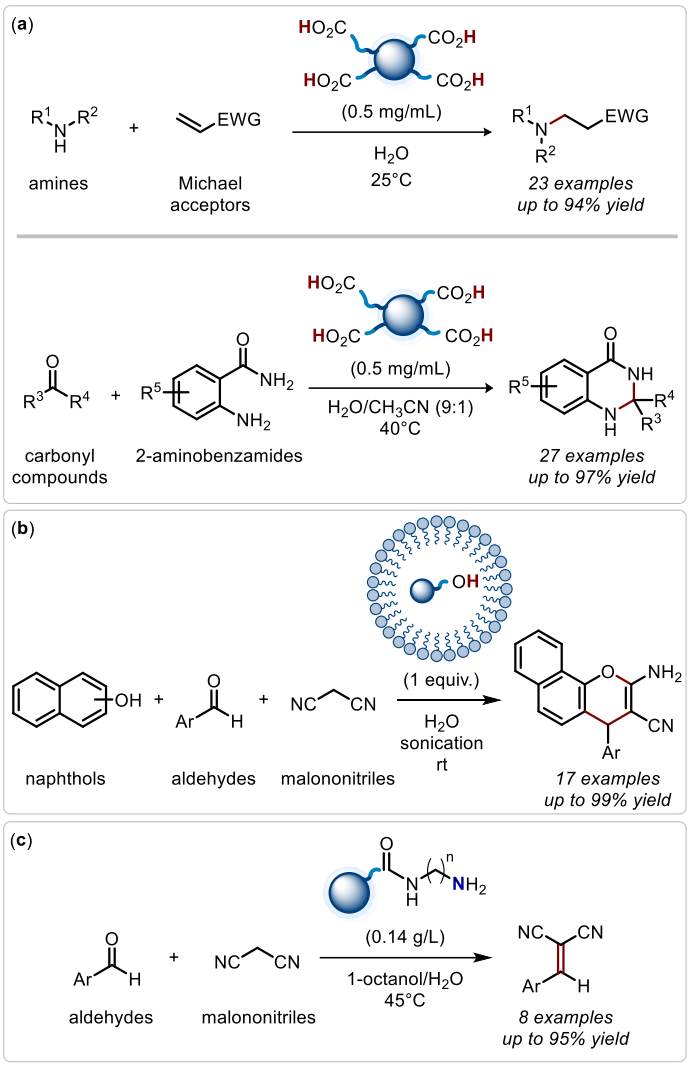

Figure 1. Use of CDs as nano-organocatalysts in: (**a**) Aza-Michael and condensation reactions; (**b**) multi-component condensation reactions; (**c**) Knoevenagel condensation reactions.

Despite their high potential, only the described exploratory applications of CDs as nano-organocatalysts have been reported at that time, proving that also this is a thrilling new field of research. Importantly, a detailed characterization and quantification of the terminal functional groups present in the CDs outer shell is crucial to enable their implementation towards a wide diversity of synthetically relevant organocatalyzed transformations. However, in some cases this aspect has been untended or not sufficiently deepened.

4.3 Objective of the Research Project and Initial Results

To this aim, we envisaged the careful deployment of multiple analytical and spectroscopic techniques to provide an accurate description of the surface amino groups present on CDs **D**, prepared from Arg and EdA (Figure 2, previously introduced in Chapter III), at unprecedented levels of detail. These characterization methods can include AFM, DLS, electrophoretic studies, KT, pH titration, thermogravimetric analysis, IR spectroscopy, and *in situ* ^{19}F-NMR analysis. The information gained through these investigations could help to address the type, amount, accessibility, and reactivity of amine terminal groups. In doing so, we envisioned the possibility to unlock the implementation of **D** as efficient covalent nano-organocatalysts capable of working in water media.

Specifically, we aimed to extend the reactivity of **D** towards the prominent branch of organocatalysis that remained largely underexplored with nanosized catalysts, namely aminocatalysis. In fact, the amine functionalities present on the surface of the **D** could in principle serve as catalysts for the functionalization of a variety of sterically hindered carbonyl compounds through enamine or iminium ion activations, respectively. This would be of great importance in synthetic chemistry, since aminocatalysis is undeniably one of the most versatile strategy for the formation of relevant C-C and C-heteroatom bonds (see Chapter I, Section 1.1.1).[16,18,19] Moreover, this approach could take advantage of the abovementioned benefits of nanocatalysts. Finally, we hypothesized the use of chiral optically active CDs **E**, prepared from Arg and (*S,S*)-1,2-cyclohexanediamine, to carry out aminocatalytic transformations in an enantioselective fashion (Figure 2).[20] This would demonstrate that the chiral information retained in the nanomaterial outer shell could be successfully transferred with molecular control, enabling the most desirable goal of enantioselective catalysis by carbon-based nanomaterials.

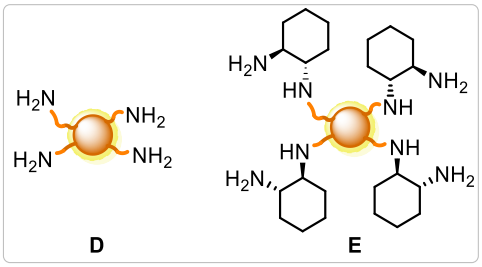

Figure 2. Amine-rich CDs **D** and their chiral optically active version **E** employed as nano-organocatalysts in this study.

We planned the first step of our investigations based on the previously reported characterization of **D**. Explicitly, these CDs possess a size of about 2.5 nm (determined by AFM) and numerous primary amines on their surface quantified in 1350 µmol g^{-1} (from KT analysis at 120 °C).[21,22] Successively, we evaluated the total number of acid/base sites present in the selected CDs. This was done using the Gran Plot analysis of simple pH back titrations,[23] and resulted in 10700 ± 800 µmol g^{-1}. Additionally, a comparison of this value with that associated with the starting materials allows the quantification of the acid/base sites retained during the synthesis. This corresponded to only about 20%, possibly because of amide-bond formation, that is reasonably occurring under hydrothermal conditions.[24] To gain additional information on the surface charge of **D**, agarose gel electrophoresis was performed at neutral pH in phosphate buffer. As expected, **D** migrated toward the cathode, indicating their positive charge at neutral pH, which could be consistent with the presence of protonated amino groups. For comparison, other frequently used *N*-doped-CDs were prepared from hydro or solvothermal protocols that employ citric acid in combination with urea (**F**) or EdA (**G**) as doping agents, as well as from the prolonged thermolysis of aspartic acid (**H**, 100 h at 320°C).[25–27] Furthermore, two other common types of non-doped CDs, obtained from citric acid, were prepared: graphitic CDs **J**, obtained in similar conditions as **H**, and amorphous CDs **K**, obtained upon a shorter thermolytic treatment at a lower temperature (40 h at 180°C) of the same precursor.[27,28] To complete the screening, the KT was performed on the various *N*-doped CDs. As expected, CDs **H** afforded a negative test, since the XPS data indicate the presence of nitrogen solely as pyrrolic or pyridinic.[27] Analysis of CDs **F-G** revealed 1000 and 1100 µmol g^{-1} of primary aliphatic amines,

respectively, both values being lower than the reference value of 1350 µmol g^{-1} associated to **D**.[21,22] Interestingly, despite a similar amount of acid/base sites (6000-11000 µmol g^{-1}), CDs **D** turned out to be superior in terms of uniformity of the net superficial charge and number of primary amino groups in the outer shell compared to CDs **F-J,K**, obtained as well from bottom-up synthetic protocols (Figure 3, see Section 4.6 for details). For these reasons, we decided to focus our further characterization and catalytic studies on **D**.

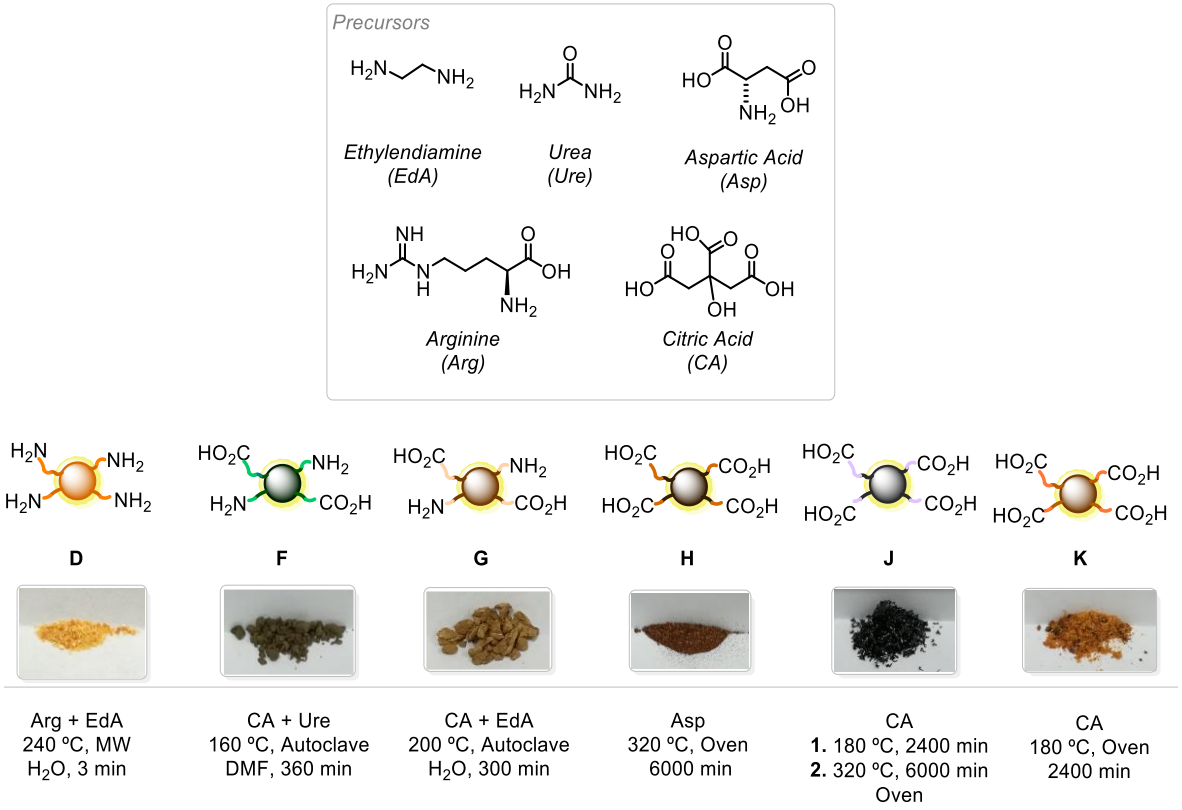

Figure 3. Precursors and synthesis of CDs **D**, **F-H**, **J-K** studied in the preliminary investigations.

4.4 Results and Discussion

The largely amorphous nature of **D** was confirmed by thermogravimetric analysis, because about 94% of weight loss was observed at 600°C under nitrogen. Focusing on the molecular features of **D**, infrared spectroscopy clearly points at the presence of N–H and O–H bonds involved in hydrogen-bond interactions, which provide solubility in water and polar solvents. A solution of **D** in ultrapure water possesses a native pH of 9.4, confirming the presence of basic sites in the sample. Upon complete deprotonation through the addition of 10.5 equiv. of NaOH with respect to the KT value at 120°C (1350 µmol g^{-1}), the back titration with HCl afforded the pH curve shown in Figure 4a. To our surprise, the minimum slope of the curve, which occurs in correspondence to the highest buffering capacity of **D**, was obtained between pH 6 and 8, indicating the presence of several functional groups with a pK_a in that range. The observed pK_a value could be tentatively ascribed to the spatial proximity of non-protonated amines with other protonated groups.[29] Alternatively, the formation of imidazole derivatives, originating from the cyclization of ethylenediamine with guanidinium groups followed by aromatization, could provide an explanation.[30] Sites with pK_a close

to physiological pH are employed by Nature as proton shuttles in a biological environment, thus **D** may offer a multi-site environment for proton transfer under physiological conditions.[31]

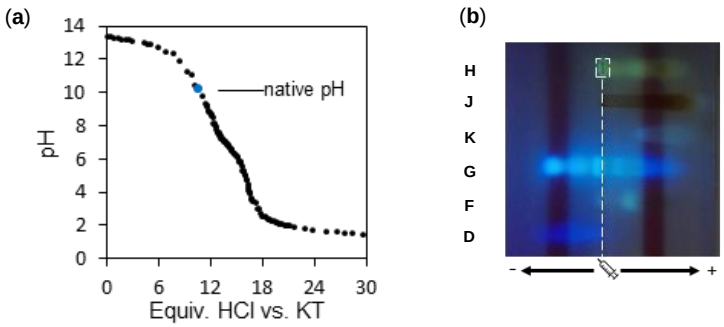

Figure 4. (**a**) pH curve observed upon back titration of **D** (4.5 mg mL^{-1}) with HCl, after the addition of 10.5 equiv of NaOH versus the KT value at 120°C. (**b**) Post-electrophoresis photograph was taken under UV light (365 nm) of the gel at pH 7 containing all the investigated CDs **D**, **F-H**, **J-K**.

The comparison between the total number of acid/base sites with the KT value in **D** indicates that the number of acid/base (10700 ± 800 µmol g^{-1}) sites is about 8 times higher with respect to the KT value at 120°C (1350 µmol g^{-1}). Therefore, several acid/base sites present on the CDs surface cannot be detected with this colorimetric experiment. In fact, this test exploits the condensation of primary aliphatic amines with ninhydrin forming an imine intermediate, thus requiring at least one hydrogen atom attached to the α-carbon of the reactive amine.[32,33] Secondary and aromatic amines are elusive under KT analysis while remaining of prominent interest as catalytic sites in organocatalytic schemes.

Therefore, in order to obtain additional information on the main amine structural types, we studied the surface groups of **D** by NMR spectroscopy. Indeed, we implemented a covalent fluorine-labeling strategy combined with ^{19}F-NMR analysis.[34] *p*-fluorocinnamaldehyde (**12a**) was selected as molecular fluorinated probe for two main reasons, since its condensation will give rise to conjugated imine or iminium ion species, the actual electrophilic catalytic intermediates involved in aminocatalyzed conjugated additions.[35–37] In fact, the in situ condensation with the surface amines of **D** would form the corresponding fluorinated imine or iminium-ion species, enabling the direct detection of the different fluorinated intermediates as a fingerprint of the surface functional groups. To validate this method, we chose a selection of model amines that are potentially representative of the population of the **D** terminals. These are namely: aniline (**18a**) and 1-naphtylamine (**18b**) as aromatic primary amines, benzylamine (**18c**) and phenylethylamine (**18d**) as aliphatic primary amines, and dibenzylamine (**18e**) and diphenylamine (**18f**) as secondary amines. The mixture of *p*-fluorocinnamaldehyde (**12a**) with the aromatic (**18a-b**) and benzylic or aliphatic (**18c-d**) model primary amines afforded the corresponding fluorinated imines **VI** (Figure 5a-d). Notably, the treatment of a solution of **D** (18 mg/mL) with 10 equiv. of **12a** in MeOH-d_4 showed, after 24 h, a set of broad resonances between -112.6 and -113.6 ppm that are ascribable to the formation of fluorinated imines by covalent interaction between the tagged probe and the reactive groups on the **D** surface (Figure 5e).

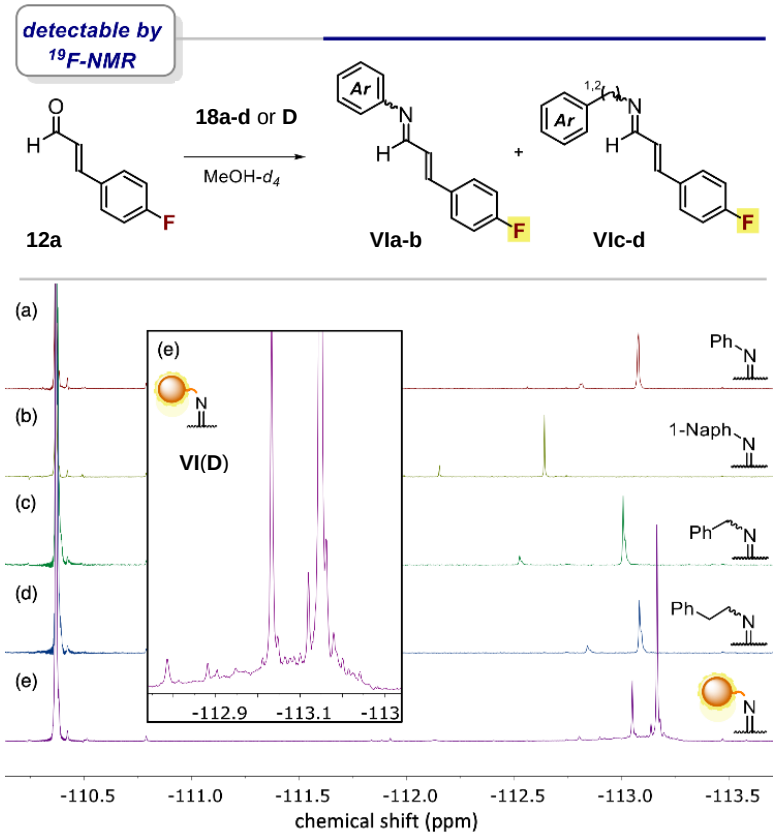

Figure 5. (**a-d**) $^{19}F\{^{1}H\}$-NMR spectra of diverse imines **VIa-d** formed in situ upon the condensation of *p*-Fcinnamaldehyde (**12a**, 10 equiv., 0.125 mmol) with the corresponding model amines (**18a-d**, 1 equiv., 0.0125 mmol) in MeOH-d_4 after 24 h. (**e**) ^{19}F-NMR spectra of **D** solution (18 mg mL^{-1}) with **12a** (0.125 mmol) in MeOH-d_4 after 24 h.

The use of *p*-fluorothioanisole as an internal standard allows a rough quantification of the surface imines that correspond to 4100 µmol g^{-1} of available primary amines at the **D** surface. Remarkably, this number is 3-fold higher compared with the KT value at 120°C (1350 µmol g^{-1}), revealing that ^{19}F-NMR analysis with a fluorinated probe is a more effective technique for the determination of the available superficial primary amines. To expand the portfolio of detectable functional groups to secondary amines, we next implemented the fluorinated probe to the in-situ generation of iminium-ion species (Figure 6). Hence, the treatment of the different primary (**18a-d**) and secondary (**18e-f**) model amines with **12a** under acidic conditions afforded the corresponding fluorinated iminium ions **VIIa-f** (Figure 6a-f). Interestingly, the $^{19}F\{^{1}H\}$-NMR signals of the iminium ions formed in solution are more sensitive to structural variations with respect to the imines. It should be mentioned that we observed a rapid decomposition of the corresponding iminium ion species under these conditions. This process hampered the possibility to performing accurate quantification experiments on iminium ion intermediates with the **D** and therefore these determinations have been carried out solely on imine derivatives. Nevertheless, the NMR analysis of a solution of **D** (18 mg mL^{-1}) with 4 equiv. of **12a** and 4 equiv. of trichloroacetic acid (TCA) in MeOH-d_4 clearly shows the appearance of a new set of signals corresponding to the iminium ions generated between the fluorinated aldehyde **12a** with the surface amine groups (**VII**(**D**), Figure 6g). By comparison with the model iminium-ions spectra (Figure 6a-f), we were able to identify three main amine types present in the **D** external surface as: (*i*) secondary aliphatic amines, (*ii*) primary aromatic amines, and (*iii*) primary aliphatic

amines. Instead, secondary aromatic amines, such as diphenylamine **18f**, are not present on **D** surface. In agreement with the imine $^{19}F\{^{1}H\}$-NMR (Figure 5) and with the titration experiments (Figure 4), the major type of reactive groups present on the **D** surface turn out to be aliphatic primary amines.

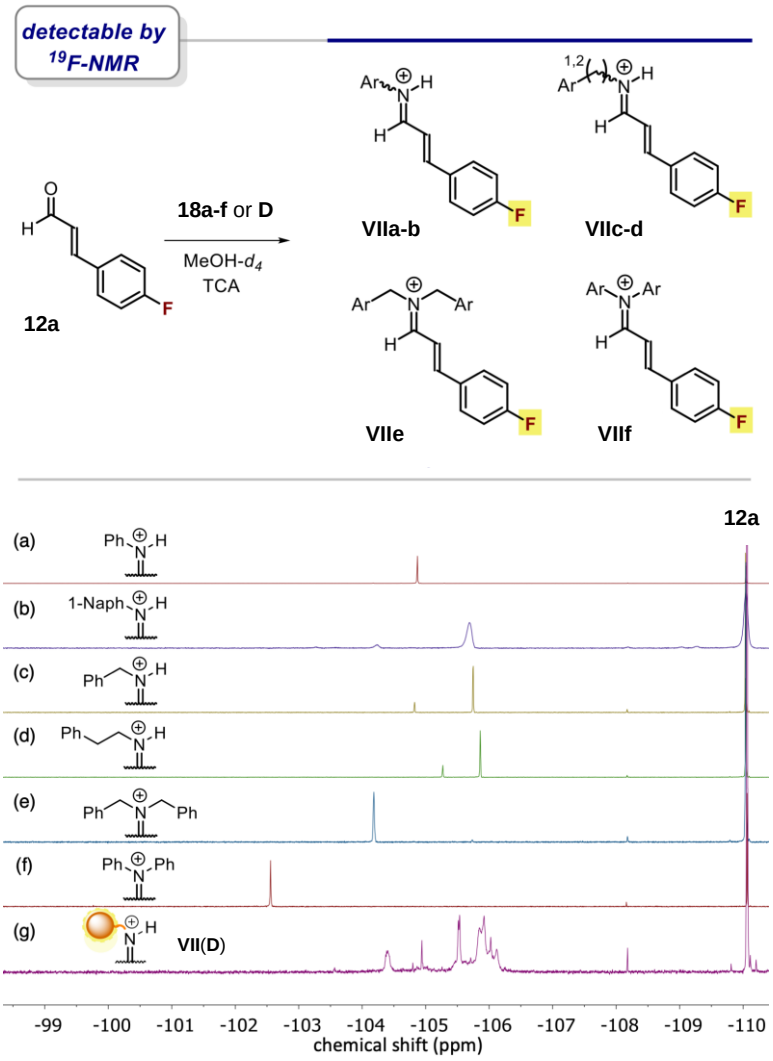

Figure 6. (**a-f**) $^{19}F\{^{1}H\}$-NMR traces of the diverse iminium ions **VIIa-f** formed upon condensation of *p*-F-cinnamaldehyde (**12a**, 4 equiv., 0.4 mmol) and trichloroacetic acid (TCA, 4 equiv., 0.4 mmol) with the corresponding model amines **18a-f** (1 equiv., 0.1 mmol). (**g**) $^{19}F\{^{1}H\}$-NMR spectra of **D** solution (18 mg mL^{-1}) with **12a** (0.4 mmol) and TCA (1 mmol) in MeOH-d_4.

As previously stated, the NMR quantification on the imines revealed a 3-fold enhancement in the determination of the amount of available reactive amine with respect to classical KT analysis and accounts approximately for the 40% of all the acid/base active sites predicted by the titration experiments. With these studies, we have established $^{19}F\{^{1}H\}$-NMR as a useful and fast technique for the determination of the amine content on the CDs surface.

To gain more information on the accessibility of the terminal amines, we performed a deeper investigation of the KT on **D** using benzylamine (**18c**) as the model amine. As expected, under the standard conditions (120°C for 15 min) both **D** and benzylamine afforded a positive test, with a quantitative conversion of the latter. To test the accessibility of amines, additional KTs were

performed at room temperature and followed in time. Under these conditions, the conversion of benzylamine remained quantitative. On the other hand, taking the results of the KT at 120°C as a reference, the conversion of D leveled off at around 64% ± 7% (Figure 7).

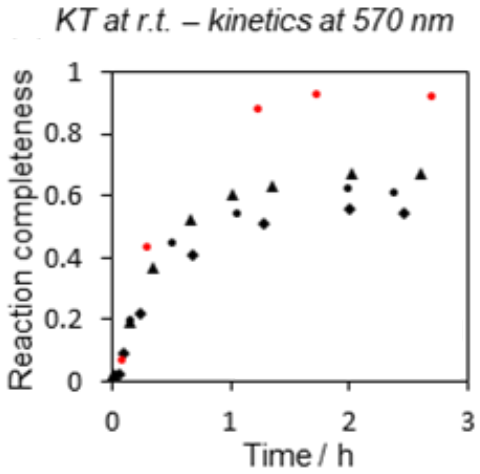

Figure 7. Representative kinetic traces observed at 570 nm while monitoring the KT at room temperature of **18c** (red dots) and three different batches of **D** (black indicators).

These experiments confirmed the hypothesis of a limited accessibility of the amines at room temperature. Therefore, the actual amount of amino groups within **D** might be even higher than the value measured through ^{19}F-NMR analysis at ambient temperature (4100 µmol g^{-1}). Thus, assuming a similar accessibility for all amino moieties (about 64%), a calculated overall value of approximately 6400 µmol g^{-1} of primary amines for **D** could be tentatively proposed. This rationalization suggests that a high portion of the acid/base active sites on the surface of **D** are primary amines, albeit some are less accessible to carbonyl compounds and, therefore, not reactive at room temperature. These deductions are also consistent with the positive charge observed with electrophoresis as well as with the elemental analysis of **D** (C 62%, H 9%, N 21%, and O 7%). These data would assign to N 9% of the total weight of **D**, and the residual 12% N content could be reasonably present in undetected moieties, such as amides, that are known to form at relatively low temperature during CDs synthesis, and heterocycles or secondary amines, that cannot be quantified via imine formation.[38] The experiments presented so far establish both the nature and the amount of available primary amines located on the surface of the **D**. Such a detailed characterization becomes of fundamental importance for the implementation of CDs in advanced applications relying on the chemical behavior of their surface, such as their utilization as nano-organocatalysts. This is unquestionably the main goal of this Chapter.

Therefore, we envisioned the use of **D** as water-soluble catalysts tackling the activation of aldehydes and ketones, which are both expected to occur vis-à-vis the structural diversity of the reactive amine groups identified by ^{19}F-NMR. Indeed, the iminium ion species detected by in situ NMR analysis are the electrophilic catalytic intermediates responsible for the LUMO-lowering activation in aminocatalysis, able to engage in conjugate addition with a series of nucleophiles (see Chapter I, Section 1.1.1).[16,39] To this aim, we first compared the reactivity of **D** with respect to the free model amines (i.e., **18a**, **18d**, **18e**, and pyrrolidine **18g**) in the conditions at which the iminium ions **VII** were

identified, as confirmation of their reactivity in that surroundings. Indeed, we performed a reaction between *p*-F-cinnamaldehyde (**12a**, 3 equiv.) and *N*-methylindole (**13a**, 1 equiv.) as biologically relevant *C*-nucleophile.[40] Deuterated methanol (0.20 M) was used as solvent in the presence of a catalytic amount of **D** (3.6% w/v, corresponding to 6 mol% of reactive amines, based on the amount of functionalities that can condense with **12a** measured through the ^{19}F-NMR studies: 4100 µmol g^{-1}) or free amines **18** (20 mol%), and trichloroacetic acid (TCA, 20 mol %). Remarkably, these experiments demonstrated that in all cases, **D** outperforms the isolated amine precursors in terms of product **14a** yield. This occurred even at the high catalytic loading at which the model amines were employed with respect to **D** (20 mol% *vs* 6 mol%, Table 1). Therefore, the synthetic potential of **D** as nano-organocatalysts can be then evaluated.

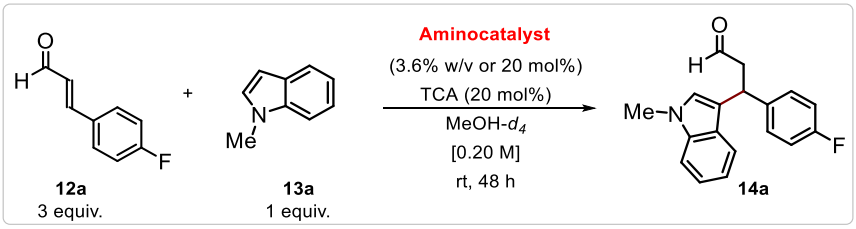

Entry	Aminocatalyst	Yield[a]
1	**D**	62%
2	-	0%
3	Aniline (**18a**)	13%
4	Phenylethylamine (**18d**)	<5%
5	Dibenzylamine (**18e**)	29%
6	Pyrrolidine (**18g**)	31%

Table 1. Reaction performed on 0.1 mmol scale. [a] Yield determined by ^{1}H-NMR spectroscopy using 1,1,2-trichloroethene as the internal standard.

After these preliminary results obtained in the operative conditions employed for the NMR studies, we found that **D** (3.6% w/v) can be also dissolved in a mixture of water-dioxane 1:1 ([**12a**]$_0$ = 0.25 M). In this case, by using TFA as protic acid (20 mol%) the reaction occurs smoothly, delivering the product **14a** in good yield (63% isolated yield, Figure 8). Similarly, when the non-fluorinated cinnamaldehyde **12b** was reacted with the same nucleophile **13a**, the corresponding Michael adduct **14b** was obtain in slightly lower isolated yield (53% yield, Figure 8). These outcomes revealed that **D** is similar in terms of performance to well-established aminocatalytic systems for this transformation.[39,41]

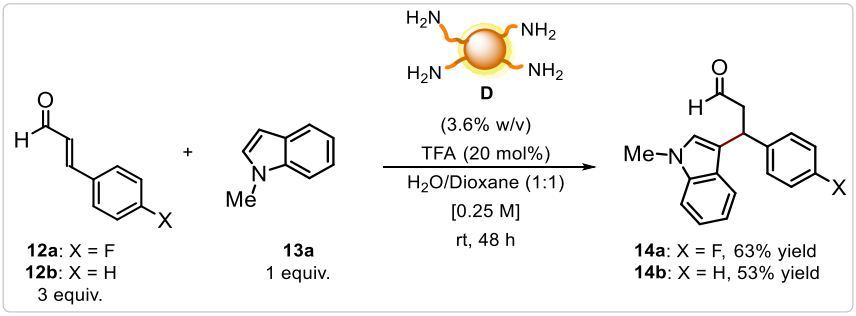

Figure 8. Reactions performed on 0.1 mmol scale using **D** as nano-organocatalysts in water/dioxane (1:1) and in the presence of TFA as protic acid.

To prove the effectiveness of **D** as a water-compatible catalytic system for iminium ion activation towards other unsaturated carbonyl compounds, such as ketones, an optimization study has been performed (Table 2). Specifically, 2-cyclohexen-1-one (**12c**, 1 equiv.) and dimethylmalonate (**13b**, 1 equiv.) were selected as model compounds. Hence, by reacting them in pure water in the presence of **D** as catalyst (3.6% w/v, $[\mathbf{12c}]_0$ = 0.25 M) and benzoic acid as additive (20 mol%), the corresponding addition product **14c** was obtained in moderate NMR yield over 24 hours (30% yield, entry 1, Table 2). Control experiments without the nano-organocatalysts **D** or, alternatively, without the protic acid, provided negligible amount of **14c** in both cases (<5% yield, entries 2-3, Table 2). This confirmed that these components together were needed in the reaction system. Furthermore, by employing the same acidic additive previosuly used for aldehydes **12a-b**, namely TFA, a poorer reactivity was observed with respect to benzoic acid (22% yield of **14c**, entry 4, Table 2). On the contrary, increasing the excess of the ketone **12c** translated into a significant improvement of the formation of **14c** (70% yield, entry 5, Table 2). Lastly, an almost quantitative yield of the desired adduct was afforded when the reaction time was extended to 48 hours (93% NMR yield, 90% isolated yield, entry 6, Table 2). It is worth mentioning that when other type of CDs (**F-H**, **J-K**) were employed as catalysts, product **14c** was not detected. Explicitly, this happened with CDs **H**, that possess nitrogen sites that are present solely as pyridinic and pyrrolic-type residues, or nitrogen-free CDs (**J**, **K**). Additionally, the same result was obtained with CDs **F** and **G**, which afforded a positive KT despite a broad structural inhomogeneity, as evidenced by their multiple-band electrophoretic behavior (Figure 4b). These experiments thus indicated that a stringent control of CD surface environment and composition is crucial for reactivity.

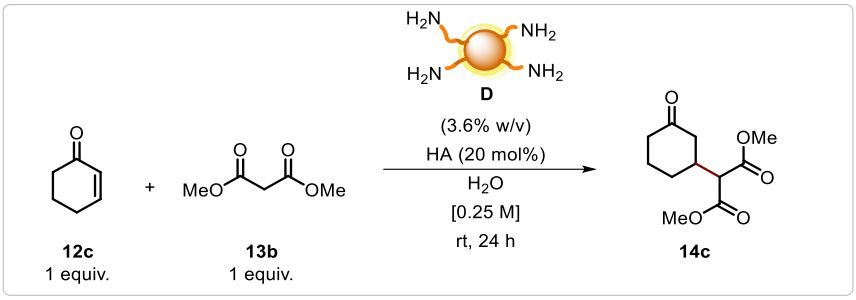

Entry	**12c** (equiv.)	Acid (mol %)	**D** (% w/v)	Yield[a]
1	1	Benzoic acid (20)	3.6	30%
2	1	Benzoic acid (20)	0	0%
3	1	Benzoic acid (0)	3.6	<5%
4	1	TFA (20)	3.6	22%
5	3	Benzoic acid (20)	3.6	70%
6[b]	3	Benzoic acid (20)	3.6	93% (90%)

Table 2. Reactions performed on 0.1 mmol scale. [a] Yield determined by ^{1}H-NMR spectroscopy using 1,1,2-trichloroethene as the internal standard. [b] Reaction performed over 48 hours.

With the optimized conditions in hand, different α,β-unsaturated carbonyl compounds (**12c–d**) and nucleophiles (**13b-e** or **18a**) were tested to prove the generality of the developed protocol. The corresponding β-functionalized products **14d-h** were afforded in isolated yields spanning from 63% to 92%. As expected from the previous investigations, by using only **18a** as nucleophile reagent without the catalyst **D**, the formation of the corresponding product **14g** was not detected (Figure 9).

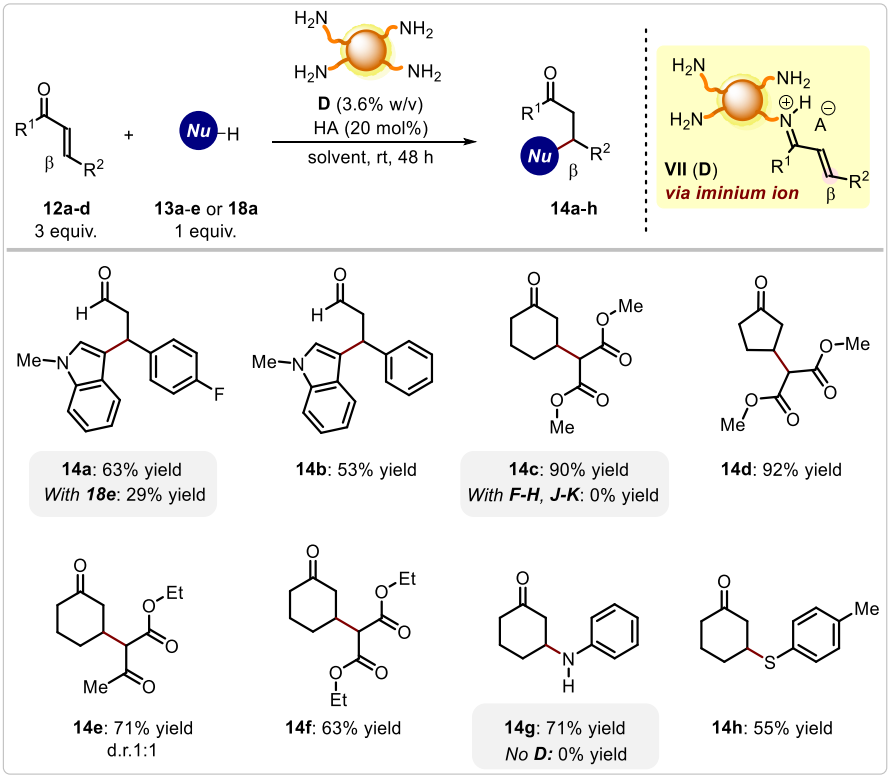

Figure 9. CDs **D**-catalyzed conjugate additions of different nucleophiles (**13a-e** or **18a**) to enals and enones **12a-d**. Reaction was performed on 0.1 mmol scale. TFA and dioxane/MilliQ water (1:1) were used for the synthesis of compounds **14a-b**. Benzoic acid (HA) and pure MilliQ water were used for the synthesis of compounds **14c-h**. Yields of the isolated products are indicated below each entry.

To expand the portfolio of catalytic activation modes performed by the **D**, we turned our attention to the formation of enamine intermediates **VIII** toward HOMO-rising catalysis.[18,42] In fact, primary and secondary amines can also be used to catalyze the enamine-mediated addition of α-enolizable aldehydes and ketones to electrophiles (see Chapter I, Section 1.1.1). During our studies, we found that the present nano-organocatalyst **D** successfully activates simple acetone (**15a**) toward aldol-type addition to isatin (**16a**) in ultrapure water. We carried out a novel optimization survey starting from the operative conditions employed for the iminium ion catalysis, apart from the protic acid that is not needed for the enamine activation mode (Table 3). Indeed, by reacting **15a** (1 equiv.) with **16a** (1 equiv.) in the presence of **D** (3.6% w/v, $[\mathbf{16a}]_0$ = 0.25 M), the corresponding aldol adduct **17a** was obtained in quantitative NMR yield over 30 hours (entry 1, Table 3). Here as well, the catalyst **D** is necessary to carry out the organic transformation, since no product **17a** was detected in his absence (entry 2, Table 3). Notwithstanding, in this procedure, the catalyst loading was lowered to 0.9% mol without any significant loss of reactivity (>99% yield, entry 3, Table 3). Parallelly, the reaction time was successfully reduced to 6 hours with a minor impact on the formation of **17a** (93% yield, entry 4, Table 3). Finally, almost quantitative production of the aldol adduct was restored by increasing the excess of the saturated carbonyl reagent (**15a**) to 7 equiv. (97% NMR yield, 96% isolated yield, entry 5, Table 3). This correction also secured a better dispersion of the insoluble isatin substrate (**16a**). Remarkably, common water sources, such as tap water and seawater, can also be used as solvents, providing **17a** in comparable excellent yields (Figure 10a). This demonstrates the robustness of the described methodology to variations of pH and ionic strength in the reaction medium.

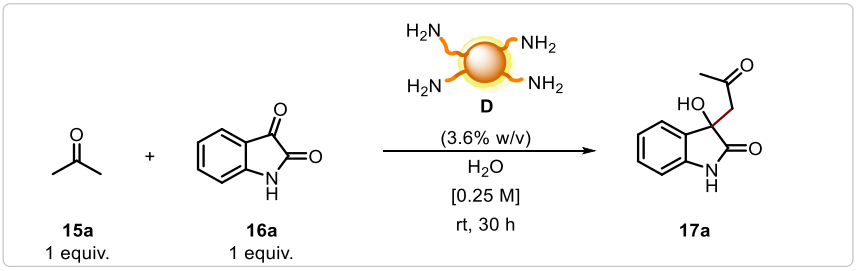

Entry	**15a** (equiv.)	**D** (% w/v)	Time (hours)	Yield[a]
1	1	3.6	30	>99%
2	1	0	30	0%
3	1	0.9	30	>99%
4	1	0.9	6	93%
5	7	0.9	6	97% (96%)

Table 3. Reactions performed on 0.1 mmol scale. [a] Yield determined by ^{1}H-NMR spectroscopy using 1,1,2-trichloroethene as the internal standard.

We then studied the generality and limitations of the proposed aldol protocol (Figure 10a). A diverse set of saturated carbonyl compounds (**15**) and isatins (**16**) was transformed into the corresponding 3,3-disubstituted oxindole derivatives (**17**). In detail, isatins **16a-e** bearing both electron-withdrawing and electron-donating substituents afforded the corresponding products **17a-e** in excellent isolated yields (81%-96%). Moreover, 2-pentanone (**15b**) and the cyclic ketones cyclohexanone (**15c**) and cycloheptanone (**15d**) actively participated in the catalytic functionalization of isatin (products **17f-h**). Interestingly, products **17g-h** were obtained with complete diastereocontrol (*d.r.* > 20:1). The observed selectivity likely originates in the increased steric hindrance of cyclic ketones **15g** and **15h**. Building on these results, we applied the **D**-catalyzed protocol to the synthesis of Convolutamydine A (**17i**) in 60% isolated yield (Figure 10b). It is worth mentioning that (*R*)-Convolutamydine A is a natural product with a potent inhibitory activity on the differentiation of HL-60 human promyelocytic leukemia cells and can be successfully synthesized as a racemic mixture using **D** as a catalyst in water.[43]

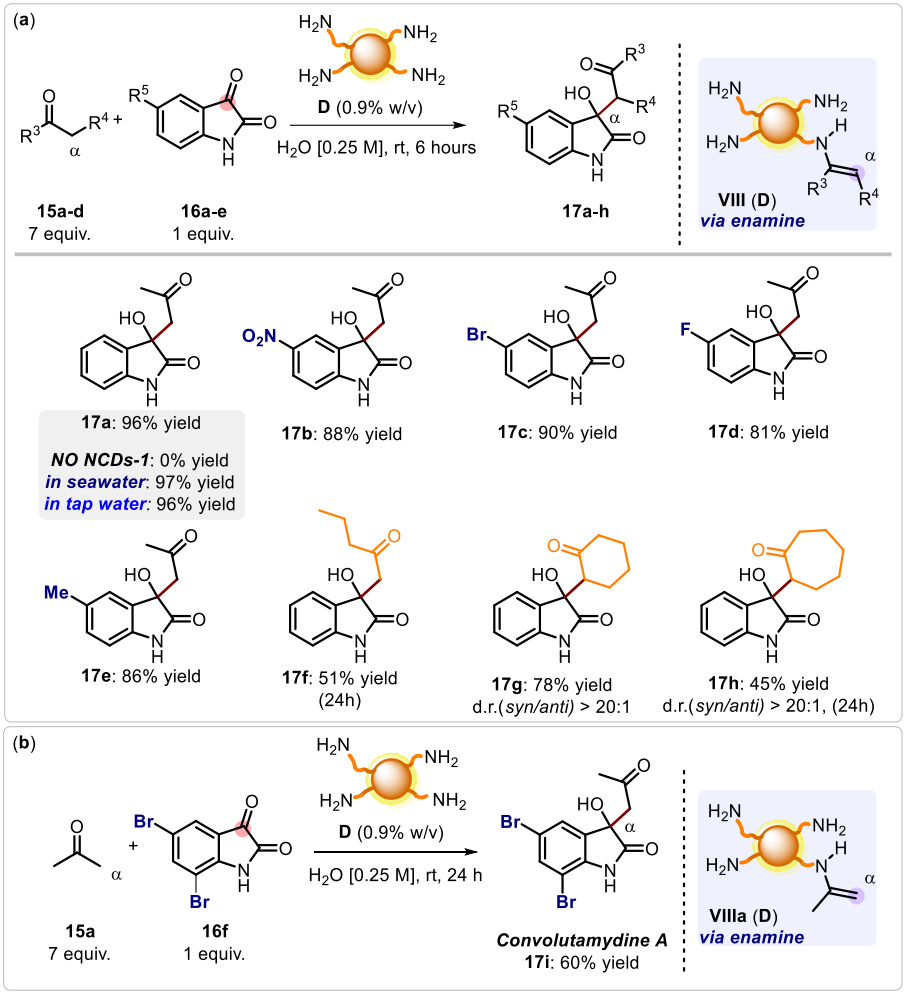

Figure 10. (**a**) **D**-catalyzed aldol additions of saturated ketones **15a-d** to isatins **16a-e**. Reactions were performed on 0.1 mmol scale using MilliQ water. Yields and diastereoselectivities of the isolated products are indicated below each entry. For the synthesis of compounds **17f** and **17h**, the reactions were performed over 24 h. (**b**) **D**-catalyzed aldol additions of acetone (**15a**) to 5,7-dibromoisatin (**16f**). The reaction was performed on 0.1 mmol scale using MilliQ water.

Finally, we turned our attention toward the challenging implementation of asymmetric catalysis by chiral CD derivatives.[5] So far, the use of carbon nanomaterials in enantioselective transformations has only been addressed relying on post-functionalization procedures.[44,45] While, due to the harsh synthetic reaction conditions, the enantiopure building blocks undergo racemization generally leading to optically inactive CDs, as in the case of **D**,[20] recently, chiral *N*-doped-CDs (**E**) have been successfully prepared by employing (*R,R*)- or (*S,S*)-1,2-cyclohexanediamine in combination with Arg as precursors (Figure 11a).[20] Therefore, we studied the catalytic behavior of (*S*)-**E** (1.5% w/v) in the aldol addition of acetone **15a** to isatin **16a** under enamine catalysis conditions (Figure 11b and Table 4).

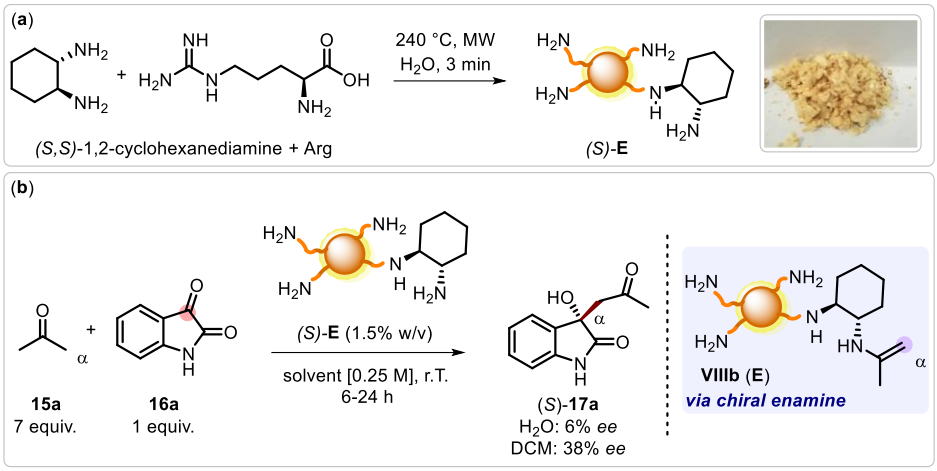

Figure 11. (**a**) Synthesis of chiral CDs (*S*)-**E**. (*S*)-**E**-catalyzed aldol addition of acetone (**15a**) to isatin (**16a**). Reactions were performed on 0.1 mmol scale.

The reaction in aqueous media at room temperature affords the aldol adduct (*S*)-**17a** quantitatively (99% NMR yield) with 6% of enantiomeric excess (*ee*) over 6 hours (entry 1, Table 4). Importantly, the direct use of (*S,S*)-1,2-cyclohexanediamine as catalyst under the same reaction conditions yields the final product in 62% yield and with *ee* as low as 4%. The poorer performance of (*S,S*)-1,2-cyclohexanediamine confirms again the superior catalytic activity of the CDs in comparison with the free-amine constituents, demonstrating that the inclusion of chiral diamines into the carbon-based nanomaterial scaffold enhances their catalytic activity while preserving a similar asymmetric induction. By lowering the reaction temperature to 0°C the enantiocontrol imparted by the chiral nanosized catalytic platform can be increased to 9%, despite a reduced overall reactivity (62% yield, entry 2, Table 4). Apolar solvents, such as toluene, or polar aprotic solvents, such as dimethylsulfoxide (DMSO) or ethyl acetate, completely suppressed the formation of aldol (*S*)-**17a** even over 24 hours, probably due to the inefficient solubilization of CDs **E** (entries 3-5, Table 4). On the contrary, solubilizing polar solvents, like ethanol, or *N,N*-dimethylformamide (DMF) led to the formation of the desired product in high yield and detectable enantioselectivity (80-85% yield, 1-6% *ee*, entries 6-7, Table 4). When the considered reaction was carried out in neat condition (**15a** as solvent), an appreciable stereoselectivity was observed, albeit a low conversion of the starting material (27% yield of (*S*)-**17a**, 8% *ee*, entry 8, Table 4). Interestingly, when dichloromethane (DCM) was used as a solvent, the final aldol adduct was formed with a remarkable and reproducible 38% *ee* and discrete yield over 24 hours (59% yield, entry 9, Table 4). It should be mentioned that in such conditions the reaction system turned out to be highly heterogenous, however the depicted reactivity was still observed. To the best of our knowledge, these results represent the first example of asymmetric catalysis promoted by a chiral CD nanomaterial, whereby molecular chirality is transferred at the nanoscale. Notably, the isolated (*S,S*)-1,2-cyclohexanediamine probed under analogous experimental conditions provides a similar enhancement of asymmetric induction (46% *ee*), albeit with a much lower product yield (25% yield). These results highlight the still unexplored potential of carbon nanomaterials for enantioselective recognition and do confirm the effective molecular encoding of CDs for asymmetric catalysis.

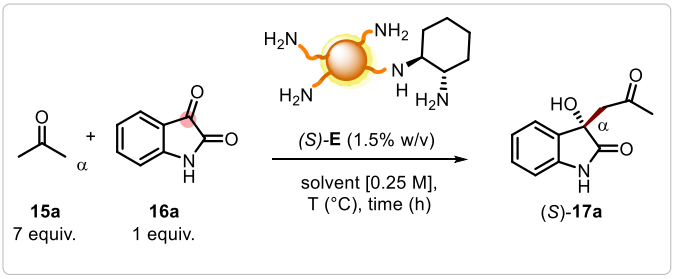

Entry	Solvent	Time (h)	Yield[a]	*ee*[b]
1	H_2O	6	99%	6%
2[c]	H_2O	6	62%	9%
3	Toluene	24	0%	-
4	DMSO	24	0%	-
5	Ethyl Acetate	24	<5%	-
6	EtOH	24	85%	6%
7	DMF	24	80%	1%
8	Acetone	24	27%	8%
9	DCM	24	59%	38%

Table 4. Reaction were performed on 0.1 mmol scale. [a] Yield determined by ^{1}H-NMR spectroscopy using 1,1,2-trichloroethene as the internal standard. [b] The enantiomeric excess was determined by HPLC analysis on a chiral column (see the Experimental Section for details). [c] Reaction performed at 0°C.

4.5 Conclusions

The use of a wide set of analytical and spectroscopic molecular techniques provides unprecedented evidence on the nature, amount, availability, and reactivity of terminal amino functionalities present in the outer shell of commonly used CDs. This knowledge reveals that nitrogen-rich CDs exhibit a unique molecular-like behavior while retaining the typical nano-colloidal features. As a result, these nanosized multifunctional materials have been successfully implemented into amino-catalyzed reactivity schemes enabling the activation of carbonyl compounds via covalent bonding in water solution. Different benchmark aminocatalytic transformations, including conjugate additions and aldol reactions, are efficiently catalyzed by amine-rich CDs catalysts proceeding via iminium ion and enamine intermediates. Furthermore, the use of optically active CDs as catalysts allows to govern the stereodetermining bond-forming event, demonstrating that the chirality retained in the CDs outer shell can be transferred with molecular control in the catalytic process. In summary, this study proves that the accurate characterization of the nanomaterial surface enables advanced applications commonly considered out of reach for nanostructures, such as covalent asymmetric catalysis, and provides the proof of principle for the implementation of nanomaterials into chemical roles previously considered only attainable by the molecular realm.

4.6 Experimental Section

4.6.1 General Information

The microwave synthesis was performed on a CEM Discover-SP. The NMR spectra were recorded on Varian 400 spectrometer (^{1}H: 400 MHz; ^{13}C: 100.5 MHz). UV-Vis measurements were carried out on PerkinElmer Lambda 35 UV-Vis spectrophotometer. All the spectra were recorded at room temperature using 10 mm path-length cuvettes. Atomic force microscopy (AFM) images were obtained with a Nanoscope IIIa, VEECO Instruments. As a general procedure to perform AFM analyses, tapping mode with a HQ:NSC19/ALBS probe (80 kHz; 0.6 N/m) (MikroMasch) from drop cast of samples in an aqueous solution (concentration in the order of μg mL^{-1}) on a mica substrate was performed. The obtained AFM-images were analyzed in S3 Gwyddion 2.35. Thermogravimentric analysis (TGA) was recorded with a TGA Q500 (TA instruments), under a flow of N_2 (90 mL/min), following a temperature program consisting in the equilibration of the sample at 100 °C followed by a ramp at 10 °C min^{-1} up to 700 °C. The sample aliquot ranged from 1 to 2 mg, exactly weighed. Fourier-transform infrared spectroscopy was performed on KBr pellets on a Spectrum 2000 FT-IR Intrument (Perkin Elmer). HPLC analysis was performed using a Phenomenex Lux 5u Cellulose-5 column, with a mobile phase of hexane/i-PrOH 80/20, a flow rate of 0.8 mL min^{-1}, and detecting the analytes at λ = 254 nm.

General Procedures

CDs **D** were synthesized in glass microwave vials. CDs **F-G** were synthetized by means of an autoclave steel reactor with teflon line of 20 mL. All organocatalytic reactions were set up in glass vials, unless otherwise stated. Synthesis grade and anhydrous solvents were used as purchased. Chromatographic purification of products was accomplished using flash chromatography on silica gel (35-70 mesh). For thin layer chromatography (TLC) analysis throughout this work, Merck pre-coated TLC plates (silica gel 60 GF_{254}, 0.25 mm) were employed, using UV light as the visualizing agent (254 nm), basic aqueous potassium permanganate ($KMnO_4$) stain solution or iodine, and heat as developing agents. Organic solutions were concentrated under reduced pressure on a Büchi rotatory evaporator.

Materials

Commercial reagents and solvents were purchased Sigma-Aldrich, Fluka, Alfa Aesar, Fluorochem, VWR, Riede-de Haën, and used as received, without further purification, unless otherwise stated. Dialysis tubes with molecular weight cutoff 0.5-1 KDa were bought from Spectrum Labs and power supply for electrophoresis was bought from Consort (Model E844). Ultrapure fresh water obtained from a Millipore water purification system (>18 MΩ Milli-Q, Millipore) was used in all experiments. *L*-arginine (Arg), ethylendiamine (EdA), Kaiser test kit, agarose, tris borate-EDTA, potassium phosphate monobasic, potassium phosphate dibasic, trichloroacetic acid (TCA), trifluoroacetic acid (TFA), 4-fluorothioanisole, *p*-fluorocinnamaldehyde **12a**, trans-cinnamaldehyde **12b**, 2-cyclohexen-1-one **12c**, 2-cyclopenten-1-one **12d**, acetone **15a**, 2-pentanone **15b**, cyclohexanone **15c**, cycloheptanone **15d**, aniline **18a**, 1-naphthylamine **18b**, benzylamine **18c**, 2-phenylethylamine **18d**, dibenzylamine **18e**, diphenylamine **18f**, pyrrolidine **18g**, 1-methylindole **13a**, dimethyl malonate **13b**, ethyl acetoacetate **13c**, diethyl malonate **13d**, 4-mercaptotoluene **13e**, isatin **16a**, 5-nitro isatin

16b, 5-bromo isatin **16c**, 5-fluoro isatin **16d**, 5-methyl isatin **16e**, 5,7-dibromo isatin **16f** are all commercially available. Seawater used for the synthesis of compound **17a** was collected in Trieste. The preparations of CDs are detailed in Section 4.6.2.

^{1}H NMR, ^{13}C and ^{19}F-NMR traces and spectra are available in the published manuscript[1] and are not reported in the present thesis.

4.6.2 Synthesis of the Nano-organocatalyst D-H, J-K

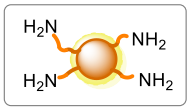

CDs **D** were synthesized by following a literature procedure.[22] Tipically, *L*-arginine (87.0 mg, 0.5 mmol, 1 equiv.), ethylenediamine (33.0 µL, 0.5 mmol, 1 equiv.) and milli-Q water (100.0 µL) were heated at 240°C, 26 bar and 200 W for 180 seconds. In the process of microwave heating, the solution changes color from transparent to brown as a result of formation of **D**. The solution was diluted with water and was filtered through a 0.1 µm microporous membrane separating a deep yellow solution that was dialyzed against milli-Q water through a dialysis membrane for 2 days. The aqueous solution of **D** was lyophilized giving a brownish solid (**D**: 23.0 mg). UV-vis absorption, fluorescence spectra, AFM data, IR spectroscopy and Kaiser test analysis are in accordance with the reported data (Figure 12).[22] Dynamic light scattering analysis excluded the presence of aggregates in aqueous solution at d > 5 nm.

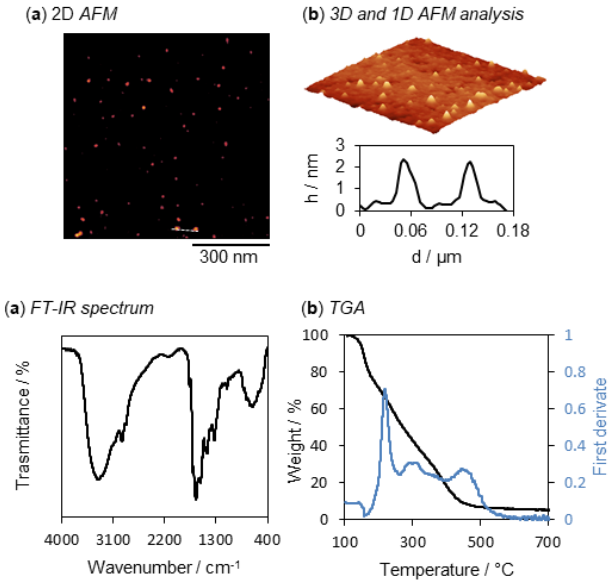

Figure 12. (**a**) Tapping mode AFM (0.8 × 0.8 µm) from a drop-cast CDs **D** aqueous solution on a mica substrate (scale bar, 300 nm). (**b**) Three-dimensional close-up AFM image (0.5 × 0.5 µm) of **D**, and height profile along the dashed line of figure (**a**). (**c**) FT-IR spectrum of **D**. (**d**) Thermogravimetric analysis of **D** under nitrogen.

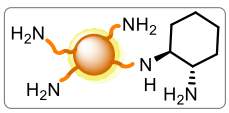

CDs **E** were synthesized by following a literature procedure.[22] Tipically, *L*-arginine (87.0 mg, 0.5 mmol, 1 equiv.), (*R,R*)- or (*S,S*)-cyclohexanediamine (57.0 mg, 0.5 mmol, 1 equiv.) and milli-Q water (100.0 µL) were heated at 240°C, and 200 W for 180 seconds. In the process of microwave heating, the solution becomes dark brown as a result of formation of **E**. The solution was diluted with water and was filtered through a 0.1 µm microporous membrane separating a deep yellow solution that was dialyzed against milli-Q water

through a dialysis membrane for 2 days. The aqueous solution of **E** was lyophilized giving a brownish solid (**E**: 21.0 mg). Kaiser test analysis afforded a value of 900 ± 100 µmol g^{-1} of primary amines, in line with the reported value; UV-Vis and fluorescence spectra are analogous to the reported ones (Figure 13).

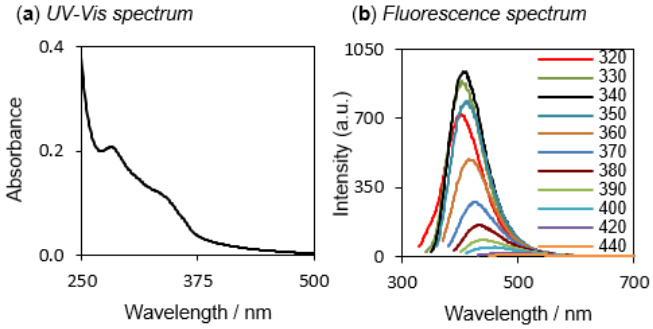

Figure 13. (**a**) UV-Vis spectrum of **E** recorded in water. Optical path = 1 cm. (**b**) Fluorescence spectrum of **E** recorded in water. The excitation wavelengths are shown inside the figure (**b**).

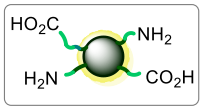

CDs **F** were synthetized by following a modified literature procedure.[25] Citric acid (1.00 g, 5.20 mmol) and urea (2 g, 33.30 mmol) were dissolved in 10 mL of DMF and then heated at 160°C for 6 h in an autoclave. After cooling down the resulting mixture to room temperature, DMF was removed by an azeotropic distillation with toluene under reduced pressure. milli-Q water was then added, and the obtained mixture was filtered through 0.1 µm microporous membrane. The filtrate was dialyzed against milli-Q water through a dialysis membrane (0.5-1 kDa cutoff) over seven days and afterwards freeze-dried to obtain a dark solid (**F**: 121.5 mg). UV-Vis and fluorescence spectra of **F** were recorded in water and the highest emission intensity was observed in the blue region of the electromagnetic spectrum (Figure 14).

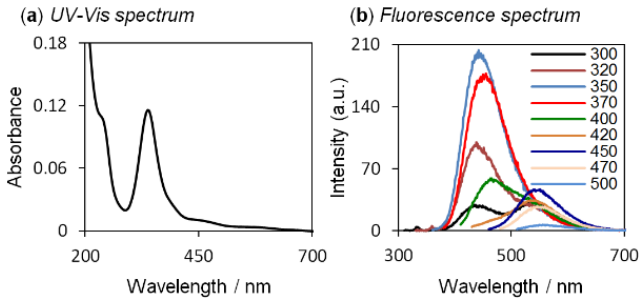

Figure 14. (**a**) UV-Vis spectrum of **F** recorded in water. Optical path = 1 cm. (**b**) Fluorescence spectrum of **F** recorded in water. The excitation wavelengths are shown inside the figure (**b**).

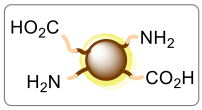

CDs **G** were synthetized by following a modified literature procedure.[26] Citric acid (1.05 g, 5.5 mmol) and ethylenediamine (330 µL, 5 mmol) were dissolved in 10 mL of milli-Q water and then heated at 200°C for 5 h in an autoclave. After cooling down the resulting mixture to room temperature, the mixture was filtered through 0.1 µm microporous membrane and dialyzed against milli-Q water through a dialysis membrane (0.5-1 kDa cutoff) over seven days. Afterwards, the mixture was freeze-dried and a brownish was collected (**G**:

81.0 mg). UV-Vis and fluorescence spectra of **G** were recorded in water and they are analogous to the reported ones (Figure 15).

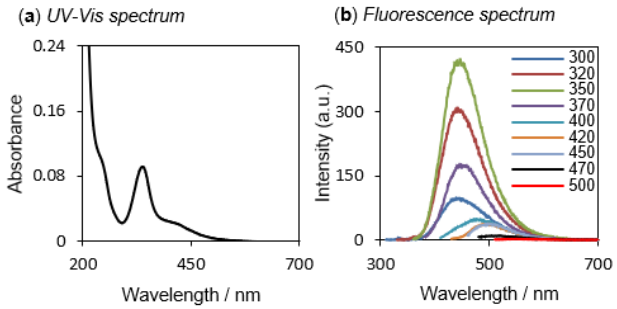

Figure 15. (**a**) UV-Vis spectrum of **G** recorded in water. Optical path = 1 cm. (**b**) Fluorescence spectrum of **G** recorded in water. The excitation wavelengths are shown inside the figure (**b**).

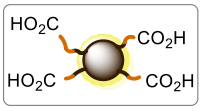

CDs **H** were synthetized by following a modified literature procedure.[27] L-aspartic acid (5 g) was heated in a muffle furnace under air at 320°C for 100 h. After this thermal treatment, the obtained solid was dispersed in milli-Q water and freeze-dried to obtain a brownish powder (**H**: 2.0 g). UV-Vis and fluorescence spectra of **H** were recorded in an aqueous solution of NaOH 0.5 M and they analogous to the reported ones (Figure 16).

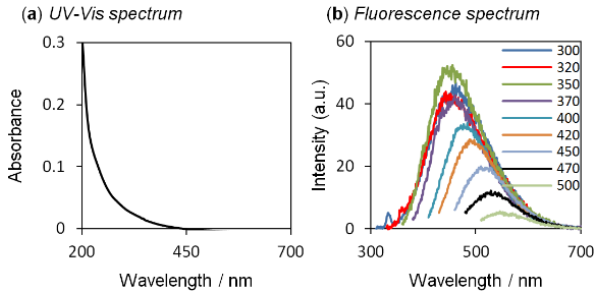

Figure 16. (**a**) UV-Vis spectrum of **H** recorded in an aqueous solution of NaOH 0.5 M. Optical path = 1 cm. (**b**) Fluorescence spectrum of **H** recorded in an aqueous solution of NaOH 0.5 M. The excitation wavelengths are shown inside the figure (**b**).

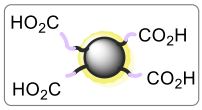

CDs **J** were synthetized by following a modified literature procedure.[27] Citric acid (20 g) was heated in a muffle furnace at 180 °C for 40 h under air. The resulting solid mixture was further heated at 320 °C for 100 h. After this second thermal treatment, the obtained solid was dispersed in milli-Q water and freeze-dried to obtain a dark powder (**J**: 2.4 g). UV-Vis and fluorescence spectra of **J** were recorded in an aqueous solution of NaOH 0.5 M and they are analogous to the reported ones (Figure 17).

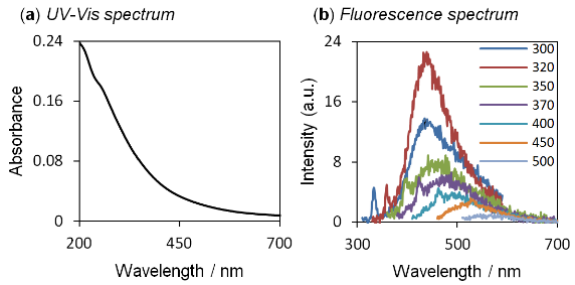

Figure 17. (**a**) UV-Vis spectrum of **J** recorded in an aqueous solution of NaOH 0.5 M. Optical path = 1 cm. (**b**) Fluorescence spectrum of **J** recorded in an aqueous solution of NaOH 0.5 M. The excitation wavelengths are shown inside the figure (**b**).

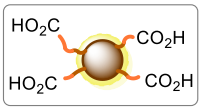

CDs **K** were synthetized by following a modified literature procedure.[27,28] Citric acid (20 g) was heated in a muffle furnace at 180 °C for 40 h under air. After this thermal treatment, the obtained solid was dispersed in milli-Q water and freeze-dried to produce an orange powder (**K**: 5.4 g). UV-Vis and fluorescence spectra of **K** were recorded in an aqueous solution of NaOH 0.5 M and they are analogous to the reported ones (Figure 18).

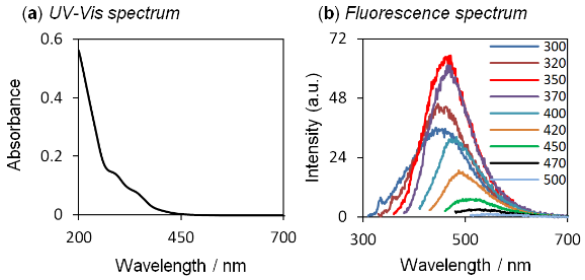

Figure 18. (**a**) UV-Vis spectrum of **K** recorded in an aqueous solution of NaOH 0.5 M. Optical path = 1 cm. (**b**) Fluorescence spectrum of **K** recorded in an aqueous solution of NaOH 0.5 M. The excitation wavelengths are shown inside the figure (**b**).

4.6.3 Kaiser Test Investigation and Acid/Base Backtitration

Kaiser Test Procedure

Kaiser tests (KTs) were performed according to a modified reported protocol by employing a commercially available kit.[46] Typically, about 1 mg of carbon dots was placed in a test tube. Then, 75 µL of a phenolic solution in ethanol, 100 µL of a KCN solution in pyridine/water and 75 µL of a ninhydrin solution in ethanol were added, in this order, to the analyzed material. This mixture was then heated at 120 °C for 10 minutes. The resulting solution was diluted with ethanol in water (60% v/v, 1:18 dilution) and its absorption spectrum was recorded. A blank solution without the analyte was used as a reference. Primary amines on the carbon dots surface were thus quantified from the absorbance value at 570 nm, considering a molar absorption coefficient for the ninhydrin derivative of 15000 M^{-1} cm^{-1} (Ruhemann's purple). For each sample, at least two independent analysis were performed. As a comparison, benzylamine (**18c**, 2 µL of an aqueous 0.5 M solution) has undergone to the same analytical procedure at 120°C, demonstrating complete conversion into the corresponding colored derivative under these conditions. On the other hand, ethylenediamine (EdA, 3 µL of an aqueous 0.15 M solution) revealed an additional – unexpected – band at 480 nm and the calculated conversion turned out to be not quantitative.

Kaiser Test at Room Temperature

In the accessibility experiments, the analyzed solution was kept at room temperature (r.T., 25 °C) over the time. Therefore, to a known amount of carbon dots (about 1 mg), the aforementioned Kaiser test solutions were added. Subsequently, the resulting mixture was diluted with ethanol in water (60%, 1:125 dilution) and its absorption spectrum was recorded. A blank solution without the analyte was used as a reference. This procedure was repeated over the time and the conversion was calculated taking into account the value of the Kaiser test performed at 120°C and the dilution factor (dil, Equation 1). As a comparison, benzylamine (**18c**, 2 µL of an aqueous 0.5 M solution) has undergone to the same analytical procedure. The conversion of 2c into the corresponding colored derivative turned out to be 95 ± 10% at r.T., over four trials.

$$Conversion\ (\%) = \frac{KT\ (r.T.)}{KT\ (120°C)} \times dil \times 100 \qquad (eq.\ 1)$$

Acid/base Backtitrations

A known amount of CDs **D**, **F-H**, **J-K** (about 10 mg) was dispersed in 4 mL of milli-Q-water. Subsequently, 1 mL of NaOH 0.5 M (Normex) was added and then the resulting solution was titrated with a 0.1 M solution of HCl (Normex). For the quantification of acid/base sites, a Gran Plot analysis was performed.[23] By plotting the µmol of H^+ and OH^- *vs* the µmol of titrant (or *vs* the equivalents of titrant with respect to the KT value at 120°C, for **D**, see Figure 19b), two linear regions were individuated. The resulting amounts of titrant at the equivalent point (μmol_{eq1} and μmol_{eq2}) were extrapolated through a linear fitting. Finally, the total number of acid/base active sites were calculated by subtracting μmol_{eq2} from μmol_{eq1} and dividing the resulting number by the amount of carbon dots analyzed. Backtitrations and Gran plot analysis were repeated at least three times (Figure 19-24).

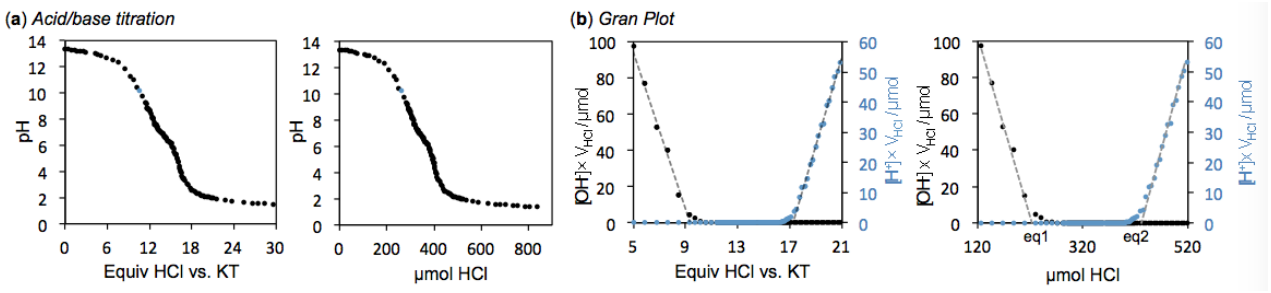

Figure 19. (**a**) pH titration curve of **D**. (**b**) Gran Plot of **D**.

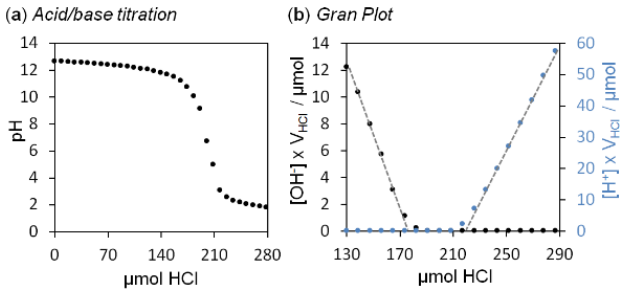

Figure 20. (**a**) pH titration curve of **F**. (**b**) Gran Plot of **F**.

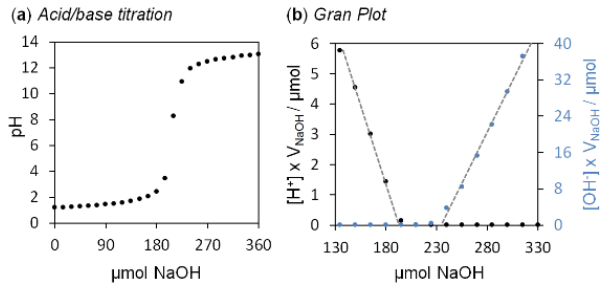

Figure 21. (**a**) pH titration curve of **G**. (**b**) Gran Plot of **G**.

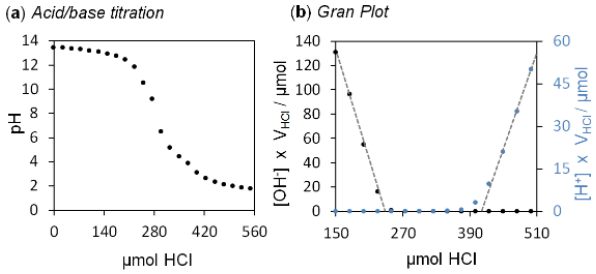

Figure 22. (**a**) pH titration curve of **H**. (**b**) Gran Plot of **H**.

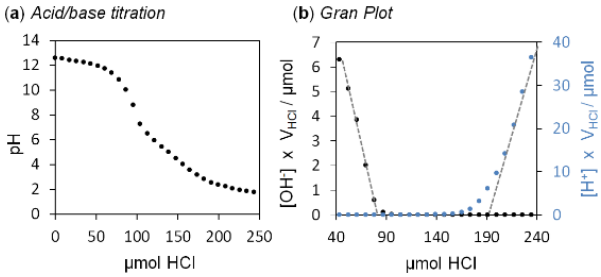

Figure 23. (**a**) pH titration curve of **J**. (**b**) Gran Plot of **J**.

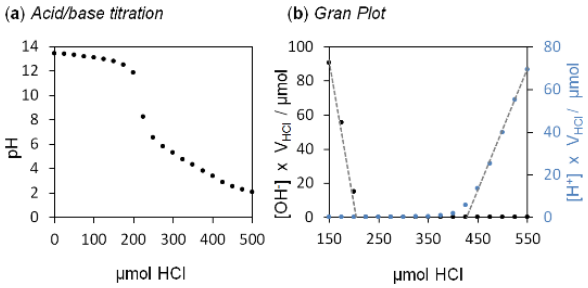

Figure 24. (**a**) pH titration curve of **K**. (**b**) Gran Plot of **K**.

Quantification of Acid/base Sites

The number of acid/base sites previously determined through the backtitrations are shown in Table 5. Moreover, the amount of retained sites was calculated by comparison with the number of acid/base sites of the starting materials. In this respect, all their carboxyl, amino and guanidinium groups were considered in the computation. In the case of **F**, a positive KT suggests that urea decomposition occurs under the synthetic conditions; since thermal decomposition of urea is known to produce ammonia and cyanic acid, two acid/base sites have been included in the calculation.[24,47]

CDs	Acid/base sites (μmol/g)	Acid/base sites of starting materials (μmol/g)	Kaiser test (μmol/g)	Acid/base retained sites
D	10700 ± 800	50500	1350 ± 100	21%
F	9200 ± 1100	48891	1000 ± 100	19%
G	7100 ± 200	48893	1100 ± 100	15%
H	9400 ± 300	22538	-	42%
J	6000 ± 800	15615	-	38%
K	11200 ± 500	15615	-	72%

Table 5. Number of acid/base sites determined through acid/base titrations and the estimation of the amount of primary aliphatic amines by means of Kaiser test on different CDs.

4.6.4 Electrophoretic Studies

For the electrophoresis studies, two agarose gels were prepared in two different buffers. The first buffer was obtained from a commercially available solution, namely tris borate-EDTA (TBE, "buffer concentrate, long run"). The concentrated solution was diluted 10 times by adding milli-Q-water, affording the desired pH of 8.9. The second buffer was prepared by dissolving potassium phosphate both mono- and dibasic in milli-Q-water (KH_2PO_4 0.01 M and K_2HPO_4 6.22 x 10^{-3} M), providing a final pH equal to 7.0. The gel precursors employed for each electrophoresis experiment, were freshly obtained mixing agarose (1 g) along with the buffer solution (50 mL, 2 wt%) and heated up at 100°C for 10 min. Therefore, the hot mixtures were placed into the electrophoresis chamber thus allowing their gelation in situ. CDs dispersions (total volume = 1 mL, concentration = 50 mg mL^{-1}) were prepared in the two different buffers for the electrophoretic studies. In particular, for carboxyl-rich CDs (**H**, **J** and **K**), a 0.5 M solution of NaOH (10% v/v with respect to the total volume) was added before the addition of the buffer solution in order to improve the solubility of the nanoparticles in the medium. As a comparison for the electrophoretic mobility, in every study a 1.68 x 10^{-4} M solution of fluorescein in the two buffers was prepared. In a typical electrophoresis experiment, 10 μL of each abovementioned mixture (CDs and fluorescein) were placed in the starting positions of the corresponding gel and the chamber was filled with the appropriate buffer solution. Then, a voltage of 300 V was applied for 6 min through a power supply, recording an electric current of 230-250 mA (Figure 25). Moreover, the effect of the CDs concentration on the electrophoretic mobility was explored. Indeed, an optimal concentration of CDs of 50 mg mL^{-1} was chosen in order to make the luminescent spots brighter under UV light irradiation at 365 nm.

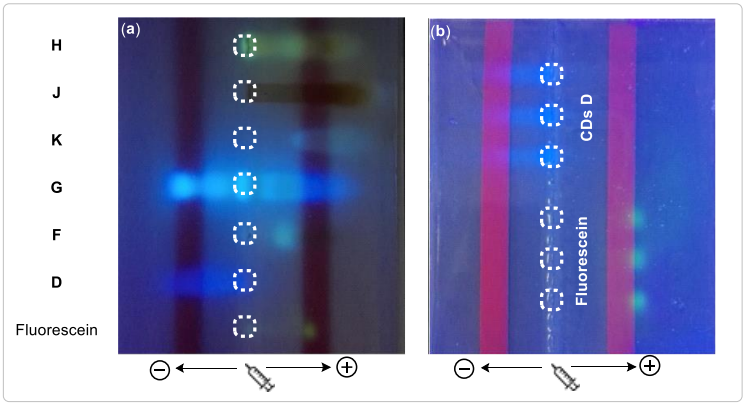

Figure 25. Post-electrophoresis photograph taken under UV light (365 nm) of the gel at pH 7 (**a**) or pH 8.9 (**b**) containing all the investigated CDs.

4.6.5 ^{19}F-NMR Quantification of Reactive Primary Amines

All the ^{19}F-NMR experiments were performed using a freshly distilled batch of *p*-fluorocinnamaldehyde (**12a**) and diverse primary aromatic and aliphatic amines. All the spectra were registered at 25 °C, [amine] = 0.25 M in MeOH-d_4. Before the generation of the diverse imine species, the corresponding imines were obtained by mixing 1 equivalent of the amine to 10 equivalents of **12a**. In order to reach a complete equilibration of the system the NMR analysis was conducted after 24 h in the presence of 4-fluorothioanisole as the internal standard (IS).

For conciseness, all the ^{19}F-NMR traces and spectra are available in the published manuscript[1] and are not reported in the present thesis.

The quantification of reactive primary amines ascertained from the abovementioned ^{19}F-NMR experiments are depicted in Table 6.

Amine	^{19}F-NMR integral area *vs* IS	NMR yield (starting amine *vs* imine)	Calculated reactive primary amines (mmol)
18a	0.218	>99%	0.0218
18b	0.210	>99%	0.0210
18c	0.209	>99%	0.0209
18d	0.180	90%	0.0180
D	0.584	-	0.0365

Table 6. Quantification of reactive primary amines summary.

4.6.6 General Procedure for β-Functionalization of Enones and Characterization Data

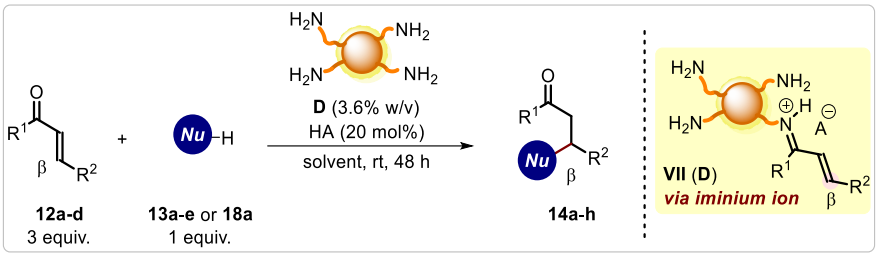

A 4 mL glass vial was charged with the appropriate nucleophile 13a-e or 18a (0.1 mmol, 1 equiv.), **D** (3.6% w/v, 14.4 mg), the appropriate enone **12a-d** (0,3 mmol, 3 equiv.), the corresponding acid (HA, 20 mol%) and solvent (final concentration: 0.25 M). The resulting mixture was stirred for the indicated time (generally 48 hours) at ambient temperature. The reaction crude was then extracted with ethyl acetate and the organic phase was filtered through sodium sulfate. The solvent was removed under reduced pressure and the residue was purified by column chromatography (eluent: hexane/ethyl acetate) to give the corresponding β-functionalized carbonyl compounds **14a-h**. TFA (HA) and milli-Q water/dioxane (1:1) were used for the synthesis of compounds **14a-b**. Benzoic acid (HA) and pure milli-Q water were used for the synthesis of compounds **14c-h**.

Characterization Data

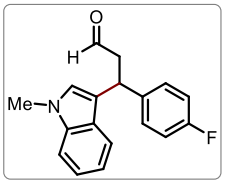

3-(4-fluorophenyl)-3-(1-methyl-1H-indol-3-yl)propanal (14a). Prepared according to the general procedure using 1-methylindole **13a** (0.1 mmol, 12 µL) and *p*-fluorocinnamaldehyde **12a** (0.3 mmol, 39 µL). Reaction time: 48 hours. The product **14a** was obtained as yellowish oil (17.7 mg, 63% yield).

^{1}H NMR (300 MHz, $CDCl_3$) δ 9.76 (t, J = 2.17 Hz, 1H, CHO), 7.33 (m, 2H, ArH), 7.36-7.28 (m, 3H, ArH), 7.01 (m, 3H, ArH), 6.85 (s, 1H, NCH), 4.85 (t, J = 7.69 Hz, 1H, ArCH), 3.76 (s, 3H, NCH_3), 3.20 (ddd, J = 2.54, 8.01, 16.5 Hz, 1H, CH_2CO); 3.05 (ddd, J = 1.86, 7.38, 16.5 Hz, 1H, CH_2CO); ^{13}C NMR (75 MHz, $CDCl_3$) δ 201.7, 131.1, 129.4, 129.23, 129.0, 126.5, 122.3, 119.6, 119.3, 115.8, 115.4, 109.6, 50.2, 36.7, 29.9.; ^{19}F NMR (75 MHz, MeOH-d_4) -120.11. HRMS (ESI) exact mass calculated for ($C_{15}H_{16}FNO$) requires m/z 281,1216, found m/z 304,1117 ($C_{15}H_{16}FNO+Na^+$).

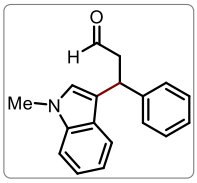

3-(1-methyl-1H-indol-3-yl)-3-phenylpropanal (14b). Prepared according to the general procedure using 1-methylindole **13a** (0.1 mmol, 12 µL) and trans-cinnamaldehyde **12b** (0.3 mmol, 38 µL). Reaction time: 48 hours. The product **14b** was obtained as yellowish oil (14.0 mg, 53% yield). The characterization of the compound matches with the data reported in the literature.[40]

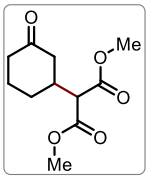

Dimethyl 2-(3-oxocyclohexyl)malonate (14c). Prepared according to the general procedure using dimethyl malonate **13b** (0.1 mmol, 12 µL) and 2-cyclohexen-1-one **12c** (0.3 mmol, 30 µL). Reaction time: 48 hours. The product **14c** was obtained as yellowish oil (20.5 mg, 90% yield). The characterization of the compound matches with the data reported in the literature.[48]

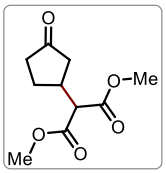

Dimethyl 2-(3-oxocyclopentyl)malonate (14d). Prepared according to the general procedure using dimethyl malonate **13b** (0.1 mmol, 12 µL) and 2-cyclopenten-1-one **12d** (0.3 mmol, 25 µL). Reaction time: 48 hours. The product **14d** was obtained as yellowish oil (19.1 mg, 92% yield). The characterization of the compound matches with the data reported in the literature.[48]

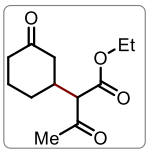

Ethyl 3-oxo-2-(3-oxocyclohexyl)butanoate (14e). Prepared according to the general procedure using methyl acetoacetate **13c** (0.1 mmol, 11 µL) and 2-cyclohexen-1-one **12c** (0.3 mmol, 30 µL). Reaction time: 48 hours. The product **14e** was obtained as yellowish oil (15.1 mg, 71% yield, d.r. 1:1). The characterization of the compound matches with the data reported in the literature.[49]

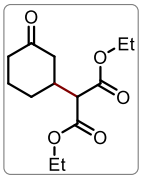

Diethyl 2-(3-oxocyclohexyl)malonate (14f). Prepared according to the general procedure using diethyl malonate **13d** (0.1 mmol, 15 µL) and 2-cyclohexen-1-one **12c** (0.3 mmol, 30 µL). Reaction time: 48 hours. The product **14f** was obtained as yellowish oil (16.1 mg, 63% yield). The characterization of the compound matches with the data reported in the literature.[50]

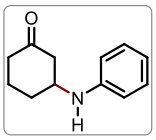

3-(phenylamino)cyclohexanone (14g). Prepared according to the general procedure using aniline **18a** (0.1 mmol, 9 µL) and 2-cyclohexen-1-one **12c** (0.3 mmol, 30 µL). Reaction time: 48 hours. The product **14g** was obtained as yellowish oil (13.4 mg, 71% yield). The characterization of the compound matches with the data reported in the literature.[51]

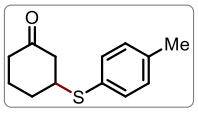

3-(p-tolylthio)cyclohexanone (14h). Prepared according to the general procedure using 4-mercaptotoluene **13e** (0.1 mmol, 12.4 mg) and 2-cyclohexen-1-one **12c** (0.3 mmol, 30 µL). Reaction time: 48 hours. The product **14h** was obtained as colorless oil (12.1 mg, 55% yield). The characterization of the compound matches with the data reported in the literature.[52]

4.6.7 General Procedure for the α-Functionalization of Ketones and Characterization Data

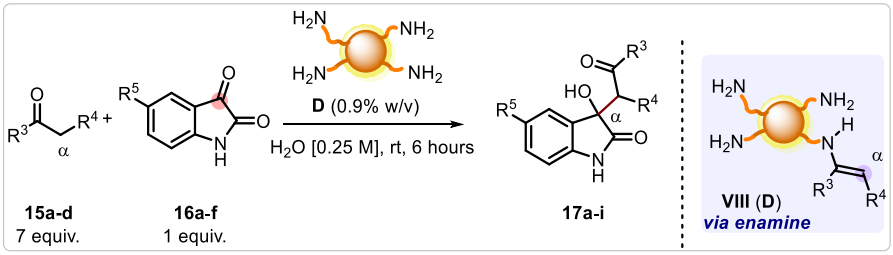

A 4 mL glass vial was charged with the appropriate isatin **16a-f** (0.1 mmol, 1 equiv.), **D** (0.9% w/v, 3.6 mg), the appropriate saturated ketone **15a-d** (0.7 mmol, 7 equiv.) and milli-Q water (final concentration: 0.25 M). The resulting mixture was stirred for the indicated time (generally 6 hours) at ambient temperature. The reaction crude was then extracted with ethyl acetate and the organic phase was filtered through sodium sulfate. The solvent was removed under reduced pressure and the residue was purified by column chromatography (eluent: hexane/ethyl acetate) to give the corresponding α-functionalized carbonyl compounds **17a-i**.

Characterization Data

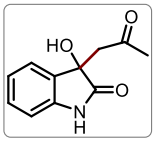

3-hydroxy-3-(2-oxopropyl)indolin-2-one (17a). Prepared according to the general procedure using isatin **16a** (0.1 mmol, 15.0 mg) and acetone **15a** (0.7 mmol, 50 µL). Reaction time: 6 hours. The product **17a** was obtained as brownish solid (19.7 mg, 96% yield). The characterization of the compound matches with the data reported in the literature.[53] Similar results were obtained using seawater or tap water instead of milli-Q water (19.9 mg, 97% yield or 19.7 mg, 96% yield, respectively).

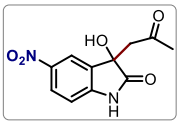

3-hydroxy-5-nitro-3-(2-oxopropyl)indolin-2-one (17b). Prepared according to the general procedure using 5-nitro isatin **16b** (0.1 mmol, 19.0 mg) and acetone **15a** (0.7 mmol, 50 µL). Reaction time: 6 hours. The product **17b** was obtained as brownish solid (22.0 mg, 88% yield). The characterization of the compound matches with the data reported in the literature.[54]

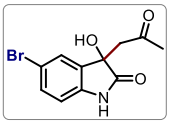

5-bromo-3-hydroxy-3-(2-oxopropyl)indolin-2-one (17c). Prepared according to the general procedure using 5-bromo isatin **16c** (0.1 mmol, 23.0 mg) and acetone **15a** (0.7 mmol, 50 µL). Reaction time: 6 hours. The product **17c** was obtained as brownish solid (25.6 mg, 90% yield). The characterization of the compound matches with the data reported in the literature.[53]

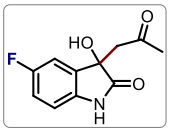

5-fluoro-3-hydroxy-3-(2-oxopropyl)indolin-2-one (17d). Prepared according to the general procedure using 5-fluoro isatin **16d** (0.1 mmol, 17.0 mg) and acetone **15a** (0.7 mmol, 50 µL). Reaction time: 6 hours. The product **17d** was obtained as brownish solid (18.1 mg, 81% yield). The characterization of the compound matches with the data reported in the literature.[53]

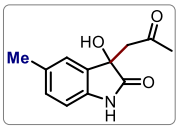

3-hydroxy-5-methyl-3-(2-oxopropyl)indolin-2-one (17e). Prepared according to the general procedure using 5-methyl isatin **16e** (0.1 mmol, 16.0 mg) and acetone **15a** (0.7 mmol, 50 µL). Reaction time: 6 hours. The product **17e** was obtained as brownish solid (18.8 mg, 86% yield). The characterization of the compound matches with the data reported in the literature.[53]

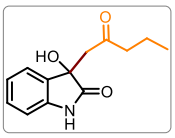

3-hydroxy-3-(2-oxopentyl)indolin-2-one (17f). Prepared according to the general procedure using isatin **16a** (0.1 mmol, 15.0 mg) and 2-pentanone **15b** (0.7 mmol, 74 µL). Reaction time: 24 hours. The product **17f** was obtained as brownish solid (11.9 mg, 51% yield). The characterization of the compound matches with the data reported in the literature.[55]

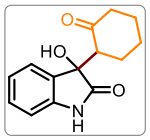

3-hydroxy-3-(2-oxocyclohexyl)indolin-2-one (17g). Prepared according to the general procedure using isatin **16a** (0.1 mmol, 15.0 mg) and cyclohexanone **15c** (0.7 mmol, 75 µL). Reaction time: 6 hours. The product **17g** was obtained as brownish solid (19.1 mg, 78% yield, d.r. 20:1). The characterization of the compound matches with the data reported in the literature.[56]

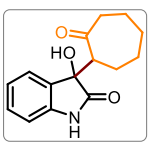

3-hydroxy-3-(2-oxocycloheptyl)indolin-2-one (17h). Prepared according to the general procedure using isatin **16a** (0.1 mmol, 15.0 mg) and cycloheptanone **15d** (0.7 mmol, 83 µL). Reaction time: 24 hours. The product **17h** was obtained as brownish

solid (11.7 mg, 45% yield, d.r. 20:1). The characterization of the compound matches with the data reported in the literature.[57]

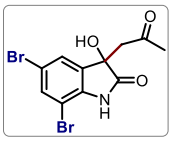

5,7-dibromo-3-hydroxy-3-(2-oxopropyl)indolin-2-one (17i). Prepared according to the general procedure using 5,7-dibromo isatin **16f** (0.1 mmol, 30.5 mg) and acetone **15a** (0.7 mmol, 50 µL). Reaction time: 24 hours. The product **17i** was obtained as brownish solid (21.8 mg, 60% yield). The characterization of the compound matches with the data reported in the literature.[54]

4.6.8 General Procedure for the Enantioselective α-Functionalization of Acetone and Characterization Data

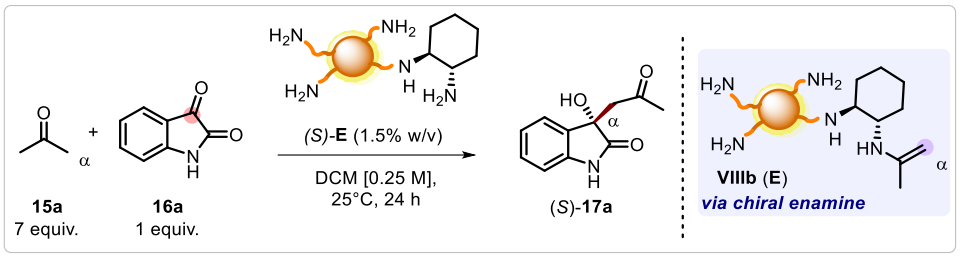

A 4 mL glass vial was charged with isatin **16a** (0.1 mmol, 1 equiv.), (*S*)-**E** (1.5% w/v, 3.6 mg), acetone **15a** (0.7 mmol, 7 equiv.) and DCM (final concentration: 0.25 M). The resulting mixture was stirred for 24 hours at room temperature. The reaction crude was then extracted with ethyl acetate and the organic phase was filtered through sodium sulfate. The solvent was removed under reduced pressure and the residue was purified by column chromatography (eluent: hexane/ethyl acetate) to give the corresponding enantioenriched α-functionalized acetone (*S*)-**17a**.

Characterization Data

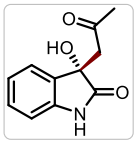

(*S*)-3-hydroxy-3-(2-oxopropyl)indolin-2-one ((*S*)-17a). Prepared according to the general procedure using isatin **16a** (0.1 mmol, 15.0 mg) and acetone **15a** (0.7 mmol, 50 µL). The product was obtained as brownish solid (12.1 mg, 59% yield). The enantiomeric excess was determined to be 38% by HPLC analysis on a Phenomenex Lux 5u Cellulose-5 column (Figure 26-27). Experimental condition: 80:20 hexane/isopropanol, flow rate 0.8 mL min^{-1}, multi wavelength detector (λ = 254 nm): τ_{Minor} =20.7 min, τ_{Major} = 22.6 min. $[\alpha]_D^{25}$ = -1.8 (c = 0.5, methanol). An (*S*) absolute configuration was inferred by comparison of the optical rotation with the value reported in the literature (Lit. $[\alpha]_D^{25}$ = -10.8 (c = 0.53, methanol, 26% *ee* for (*S*)-compound).[21] The characterization of the compound matches with the data reported in the literature.[16]

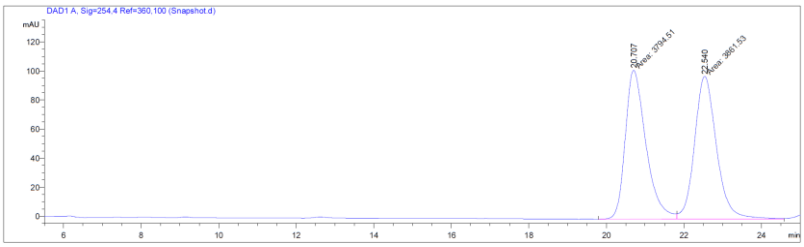

Peak #	RetTime [min]	Type	Width [min]	Area [mAU*s]	Height [mAU]	Area %
1	20.707	MF	0.6177	3794.50781	102.38261	49.5623
2	22.540	FM	0.6563	3861.53149	98.06886	50.4377

Figure 26. HPLC analysis of racemate **17a**. Retention time: t_1= 20.7 min, t_2 = 22.6 min.

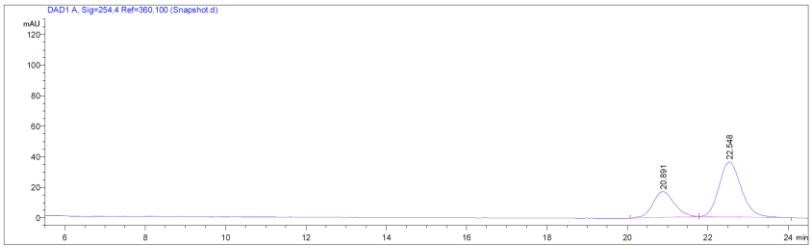

Peak #	RetTime [min]	Type	Width [min]	Area [mAU*s]	Height [mAU]	Area %
1	20.891	BB	0.5623	620.41852	16.81968	31.0010
2	22.548	BB	0.5941	1380.86853	35.95085	68.9990

Figure 27. HPLC analysis of the product obtained using (*S*)-**E**, as catalyst for the formation of (*S*)-**17a** solvent: DCM, 38% *ee*.

4.7 References Chapter IV

(1) Filippini, G.; Amato, F.; Rosso, C.; Ragazzon, G.; Vega-Peñaloza, A.; Companyó, X.; Dell'Amico, L.; Bonchio, M.; Prato, M. Mapping the Surface Groups of Amine-Rich Carbon Dots Enables Covalent Catalysis in Aqueous Media. *Chem* **2020**, *6*, 3022–3037.

(2) Kang, Z.; Lee, S. T. Carbon Dots: Advances in Nanocarbon Applications. *Nanoscale* **2019**, *11*, 19214–19224.

(3) Gao, J.; Zhu, M.; Huang, H.; Liu, Y.; Kang, Z. Advances, Challenges and Promises of Carbon Dots. *Inorg. Chem. Front.* **2017**, *4*, 1963–1986.

(4) Dhenadhayalan, N.; Lin, K. C.; Saleh, T. A. Recent Advances in Functionalized Carbon Dots toward the Design of Efficient Materials for Sensing and Catalysis Applications. *Small* **2020**, *16*, 1905767.

(5) Rosso, C.; Filippini, G.; Prato, M. Carbon Dots as Nano-Organocatalysts for Synthetic Applications. *ACS Catal.* **2020**, *10*, 8090–8105.

(6) van der Helm, M. P.; Klemm, B.; Eelkema, R. Organocatalysis in Aqueous Media. *Nat. Rev. Chem.* **2019**, *3*, 491–508.

(7) Simon, M. O.; Li, C. J. Green Chemistry Oriented Organic Synthesis in Water. *Chem. Soc. Rev.* **2012**, *41*, 1415–1427.

(8) Lindström, U. M. Stereoselective Organic Reactions in Water. *Chem. Rev.* **2002**, *102*, 2751–2772.

(9) Chanda, A.; Fokin, V. V. Organic Synthesis "on Water." *Chem. Rev.* **2009**, *109*, 725–748.

(10) Jimeno, C. Water in Asymmetric Organocatalytic Systems: A Global Perspective. *Org. Biomol. Chem.* **2016**, *14*, 6147–6164.

(11) Seayad, J.; List, B. Asymmetric Organocatalysis. *Org. Biomol. Chem.* **2005**, *3*, 719–724.

(12) Majumdar, B.; Mandani, S.; Bhattacharya, T.; Sarma, D.; Sarma, T. K. Probing Carbocatalytic Activity of Carbon Nanodots for the Synthesis of Biologically Active Dihydro/Spiro/Glyco Quinazolinones and Aza-Michael Adducts. *J. Org. Chem.* **2017**, *82*, 2097–2106.

(13) Taylor, M. S.; Jacobsen, E. N. Asymmetric Catalysis by Chiral Hydrogen-Bond Donors. *Angew. Chem. Int. Ed.* **2006**, *45*, 1520–1543.

(14) Han, Y.; Huang, H.; Zhang, H.; Liu, Y.; Han, X.; Liu, R.; Li, H.; Kang, Z. Carbon Quantum Dots with Photoenhanced Hydrogen-Bond Catalytic Activity in Aldol Condensations. *ACS Catal.* **2014**, *4*, 781–787.

(15) Mayank; Singh, A.; Kaur, N.; Singh, N.; Jang, D. O. A Carbon Quantum Dot-Encapsulated Micellar Reactor for the Synthesis of Chromene Derivatives in Water. *Mol. Catal.* **2017**, *439*, 100–107.

(16) Melchiorre, P.; Marigo, M.; Carlone, A.; Bartoli, G. Asymmetric Aminocatalysis - Gold Rush in Organic Chemistry. *Angew. Chem. Int. Ed.* **2008**, *47*, 6138–6171.

(17) Pei, X.; Xiong, D.; Wang, H.; Gao, S.; Zhang, X.; Zhang, S.; Wang, J. Reversible Phase Transfer of Carbon Dots between an Organic Phase and Aqueous Solution Triggered by CO2. *Angew. Chem. Int. Ed.* **2018**, *57*, 3687–3691.

(18) Bertelsen, S.; Jørgensen, K. A. Organocatalysis—after the Gold Rush. *Chem. Soc. Rev.* **2009**, *38*, 2178–2189.

(19) Tian, X.; Liu, Y.; Melchiorre, P. Aminocatalytic Enantioselective 1,6 Additions of Alkyl Thiols to Cyclic Dienones: Vinylogous Iminiuma Ion Activation. *Angew. Chem. Int. Ed.* **2012**, *51*, 6439–6442.

(20) Đorđević, L.; Arcudi, F.; D'Urso, A.; Cacioppo, M.; Micali, N.; Bürgi, T.; Purrello, R.; Prato, M. Design Principles of Chiral Carbon Nanodots Help Convey Chirality from Molecular to Nanoscale Level. *Nat. Commun.* **2018**, *9*, 3442.

(21) Arcudi, F.; Đorđević, L.; Prato, M. Synthesis, Separation, and Characterization of Small and Highly Fluorescent Nitrogen-Doped Carbon Nanodots. *Angew. Chem. Int. Ed.* **2016**, *55*, 2107–2112.

(22) Đorđević, L.; Arcudi, F.; Prato, M. Preparation, Functionalization and Characterization of Engineered Carbon Nanodots. *Nat. Protoc.* **2019**, *14*, 2931–2953.

(23) Boiani, J. A. The Gran Plot Analysis of an Acid Mixture: An Undergraduate Experiment to Highlight This Alternate Method. *J. Chem. Educ.* **1986**, *63*, 724.

(24) Schaber, P. M.; Colson, J.; Higgins, S.; Thielen, D.; Anspach, B.; Brauer, J. Thermal Decomposition (Pyrolysis) of Urea in an Open Reaction Vessel. *Thermochim. Acta* **2004**, *424*, 131–142.

(25) Li, D.; Jing, P.; Sun, L.; An, Y.; Shan, X.; Lu, X.; Zhou, D.; Han, D.; Shen, D.; Zhai, Y.; Qu, S.; Zbořil, R.; Rogach, A. L. Near-Infrared Excitation/Emission and Multiphoton-Induced Fluorescence of Carbon Dots. *Adv. Mater.* **2018**, *30*, 1705913.

(26) Schneider, J.; Reckmeier, C. J.; Xiong, Y.; Von Seckendorff, M.; Susha, A. S.; Kasak, P.; Rogach, A. L. Molecular Fluorescence in Citric Acid-Based Carbon Dots. *J. Phys. Chem. C* **2017**, *121*, 2014–2022.

(27) Martindale, B. C. M.; Hutton, G. A. M.; Caputo, C. A.; Prantl, S.; Godin, R.; Durrant, J. R.; Reisner, E. Enhancing Light Absorption and Charge Transfer Efficiency in Carbon Dots through Graphitization and Core Nitrogen Doping. *Angew. Chem. Int. Ed.* **2017**, *56*, 6459–6463.

(28) Martindale, B. C. M.; Hutton, G. A. M.; Caputo, C. A.; Reisner, E. Solar Hydrogen Production Using Carbon Quantum Dots and a Molecular Nickel Catalyst. *J. Am. Chem. Soc.* **2015**, *137*, 6018–6025.

(29) Nan, Z.; Tan, Z. C. Thermodynamic Investigation of the Azeotropic Binary Mixture Water + N-Propanol. *J. Chem. Eng. Data* **2005**, *50*, 6–10.

(30) Bucio-Cano, A.; Reyes-Arellano, A.; Correa-Basurto, J.; Bello, M.; Torres-Jaramillo, J.; Salgado-Zamora, H.; Curiel-Quesada, E.; Peralta-Cruz, J.; Avila-Sorrosa, A. Targeting Quorum Sensing by Designing Azoline Derivatives to Inhibit the N-Hexanoyl Homoserine Lactone-Receptor CviR: Synthesis as Well as Biological and Theoretical Evaluations. *Bioorganic Med. Chem.* **2015**, *23*, 7565–7577.

(31) Schneider, F. Histidine in Enzyme Active Centers. *Angew. Chemie Int. Ed. English* **1978**, *17*, 583–592.

(32) Troll, W.; Cannan, R. K. A Modified Photometric Ninhydrin Method for the Analysis of Amino and Imino Acids. *J. Biol. Chem.* **1953**, *200*, 803–811.

(33) Sarin, V. K.; Kent, S. B. H.; Tam, J. P.; Merrifield, R. B. Quantitative Monitoring of Solid-Phase Peptide Synthesis by the Ninhydrin Reaction. *Anal. Biochem.* **1981**, *117*, 147–157.

(34) Sun, Y.; Kunc, F.; Balhara, V.; Coleman, B.; Kodra, O.; Raza, M.; Chen, M.; Brinkmann, A.;

Lopinski, G. P.; Johnston, L. J. Quantification of Amine Functional Groups on Silica Nanoparticles: A Multi-Method Approach. *Nanoscale Adv.* **2019**, *1*, 1598–1607.

(35) Günler, Z. I.; Companyó, X.; Alfonso, I.; Burés, J.; Jimeno, C.; Pericàs, M. A. Deciphering the Roles of Multiple Additives in Organocatalyzed Michael Additions. *Chem. Commun.* **2016**, *52*, 6821–6824.

(36) Renzi, P.; Hioe, J.; Gschwind, R. M. Enamine/Dienamine and Brønsted Acid Catalysis: Elusive Intermediates, Reaction Mechanisms, and Stereoinduction Modes Based on in Situ NMR Spectroscopy and Computational Studies. *Acc. Chem. Res.* **2017**, *50*, 2936–2948.

(37) Brazier, J. B.; Jones, K. M.; Platts, J. A.; Tomkinson, N. C. O. On the Roles of Protic Solvents in Imidazolidinone-Catalyzed Transformations. *Angew. Chem. Int. Ed.* **2011**, *50*, 1613–1616.

(38) Vallan, L.; Urriolabeitia, E. P.; Ruipérez, F.; Matxain, J. M.; Canton-Vitoria, R.; Tagmatarchis, N.; Benito, A. M.; Maser, W. K. Supramolecular-Enhanced Charge Transfer within Entangled Polyamide Chains as the Origin of the Universal Blue Fluorescence of Polymer Carbon Dots. *J. Am. Chem. Soc.* **2018**, *140*, 12862–12869.

(39) Erkkilä, A.; Majander, I.; Pihko, P. M. Iminium Catalysis. *Chem. Rev.* **2007**, *107*, 5416–5470.

(40) Austin, J. F.; MacMillan, D. W. C. Enantioselective Organocatalytic Indole Alkylations. Design of a New and Highly Effective Chiral Amine for Iminium Catalysis. *J. Am. Chem. Soc.* **2002**, *124*, 1172–1173.

(41) Dalko, P. I.; Moisan, L. In the Golden Age of Organocatalysis. *Angew. Chem. Int. Ed.* **2004**, *43*, 5138–5175.

(42) Mukherjee, S.; Yang, J. W.; Hoffmann, S.; List, B. Asymmetric Enamine Catalysis. *Chem. Rev.* **2007**, *107*, 5471–5569.

(43) Kamano, Y.; Zhang, H. ping; Ichihara, Y.; Kizu, H.; Komiyama, K.; Pettit, G. R. Convolutamydine A, a Novel Bioactive Hydroxyoxindole Alkaloid from Marine Bryozoan Amathia Convoluta. *Tetrahedron Lett.* **1995**, *36*, 2783–2784.

(44) Chronopoulos, D. D.; Kokotos, C. G.; Tsakos, M.; Karousis, N.; Kokotos, G.; Tagmatarchis, N. Conjugating Proline Derivatives onto Multi-Walled Carbon Nanotubes: Preparation, Characterization and Catalytic Activity in Water. *Mater. Lett.* **2015**, *157*, 212–214.

(45) Rosso, C.; Emma, M. G.; Martinelli, A.; Lombardo, M.; Quintavalla, A.; Trombini, C.; Syrgiannis, Z.; Prato, M. A Recyclable Chiral 2-(Triphenylmethyl)Pyrrolidine Organocatalyst Anchored to [60]Fullerene. *Adv. Synth. Catal.* **2019**, *361*, 2936–2944.

(46) Iannazzo, D.; Piperno, A.; Ferlazzo, A.; Pistone, A.; Milone, C.; Lanza, M.; Cimino, F.; Speciale, A.; Trombetta, D.; Saija, A.; Galvagno, S. Functionalization of Multi-Walled Carbon Nanotubes with Coumarin Derivatives and Their Biological Evaluation. *Org. Biomol. Chem.* **2012**, *10*, 1025–1031.

(47) Kasprzyk, W.; Swiergosz, T.; Bednarz, S.; Walas, K.; Bashmakova, N.; Bogdal, D. Luminescence Phenomena of Carbon Dots Derived from Citric Acid and Urea – a Molecular Insight. *Nanoscale* **2018**, *10*, 13889–13894.

(48) Dub, P. A.; Wang, H.; Watanabe, M.; Gridnev, I. D.; Ikariya, T. A Practical Asymmetric Conjugate Addition to Cyclic Enones with Chiral Bifunctional Ru Amido Catalysts. *Tetrahedron Lett.* **2012**, *53*, 3452–3455.

(49) Majima, K.; Takita, R.; Okada, A.; Ohshima, T.; Shibasaki, M. Catalytic Asymmetric Michael

Reaction of β-Keto Esters: Effects of the Linker Heteroatom in Linked-BINOL. *J. Am. Chem. Soc.* **2003**, *125*, 15837–15845.

(50) Liu, X.; Zhang, W.; Wang, Y.; Zhang, Z. X.; Jiao, L.; Liu, Q. Cobalt-Catalyzed Regioselective Olefin Isomerization under Kinetic Control. *J. Am. Chem. Soc.* **2018**, *140*, 6873–6882.

(51) Firouzabadi, H.; Iranpoor, N.; Jafari, A. A. Micellar Solution of Sodium Dodecyl Sulfate (SDS) Catalyzes Facile Michael Addition of Amines and Thiols to α,β-Unsaturated Ketones in Water under Neutral Conditions. *Adv. Synth. Catal.* **2005**, *347*, 655–661.

(52) Rana, N. K.; Selvakumar, S.; Singh, V. K. Highly Enantioselective Organocatalytic Sulfa-Michael Addition to α, β-Unsaturated Ketones. *J. Org. Chem.* **2010**, *75*, 2089–2091.

(53) Gupta, N.; Roy, T.; Ghosh, D.; Abdi, S. H. R.; Kureshy, R. I.; Khan, N. U. H.; Bajaj, H. C. Ordered Short Channel Mesoporous Silica Modified with 1,3,5-Triazine-Piperazine as a Versatile Recyclable Basic Catalyst for Cross-Aldol, Knoevenagel and Conjugate Addition Reactions with Isatins. *RSC Adv.* **2015**, *5*, 17843–17850.

(54) Yadav, G. D.; Singh, S. N-Arylprolinamide as an Organocatalyst for the Direct Asymmetric Aldol Reaction of Acetone with Isatin. *Tetrahedron Asimm.* **2016**, *27*, 123–129.

(55) Zhong, F.; Jiang, C.; Yao, W.; Xu, L. W.; Lu, Y. Molecular Sieve Mediated Decarboxylative Mannich and Aldol Reactions of β-Ketoacids. *Tetrahedron Lett.* **2013**, *54*, 4333–4336.

(56) Guo, Q.; Zhao, J. C. G. Primary Amine Catalyzed Aldol Reaction of Isatins and Acetaldehyde. *Tetrahedron Lett.* **2012**, *53*, 1768–1771.

(57) Ogasawara, A.; Subba Reddy, U. V.; Seki, C.; Okuyama, Y.; Uwai, K.; Tokiwa, M.; Takeshita, M.; Nakano, H. 2-Azanorbornane-Based Amine Organocatalyst for Enantioselective Aldol Reaction of Isatins with Ketones. *Tetrahedron Asimm.* **2016**, *27*, 1062–1068.

Chapter V

Heterogeneous Photochemical C–N Coupling Reactions in Continuous Flow

Abstract

Chapter V discusses the development of photochemical C-N coupling reactions by means of heterogeneous carbon nitrides (CNs) **L** as photocatalyst combined with a Ni(II) source, in a continuous flow regime (Figure 15). The synthetic relevance of the C-N couplings requires the design of an efficient preparative scale process, based on sustainable catalysts. Cheap and recyclable carbon nitrides of the type of **L** fulfil these requirements. However, performing these transformations on larger scales is difficult due to the problems associated with handling solids in flow. By combining an oscillatory pump with a microstructured plug flow photoreactor, a stable suspension of the photocatalyst can be maintained, circumventing clogging of the reactor channels. In this way, upon a careful system configuration, a model aryl amino compound **20a** was prepared from the corresponding aryl bromide **19a** and amine **18g** in multi-gram scale. Furthermore, this method was applied for the gram scale synthesis of a precursor of an active pharmaceutical ingredient (**20b**).

This work was conducted within the Kappe and Pieber groups, together with *Prof. Oliver Kappe* and *Dr. Bartholomäus Pieber*, who supervised the project; with *Dr. Jason D. Williams* who configured the flow apparatus; with *Mr. Sebastian Gisbertz*, who provided the heterogeneous photocatalyst **L**; with *Dr. Hannes P. L. Gemoets* and *Dr. Wouter Debrouwer*, who provided the photoreactor and supported with its operation. A significant part of this work has been published in 2020.[1]

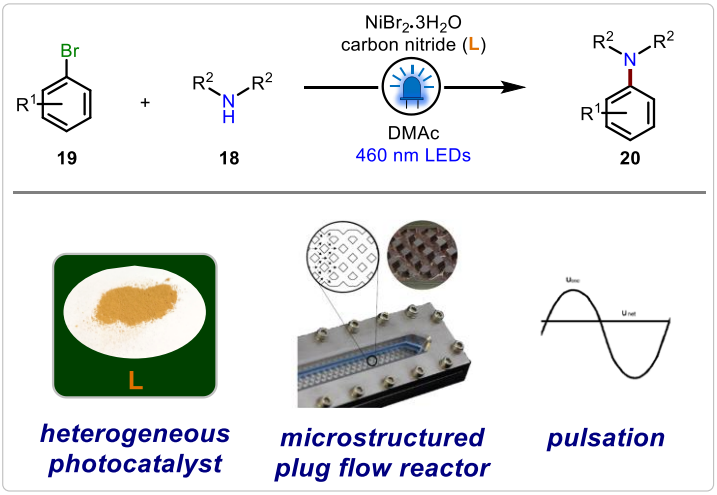

5.1 Introduction

Nowadays, aryl amino moieties (**20**) are ubiquitous in natural products and pharmaceutically relevant compounds due to their significant biological activity. To this end, C-N cross-coupling reactions between aryl halides (**19**) and amines (**18**) have become one of the most highly utilized transformations in organic synthesis (Figure 1).[2]

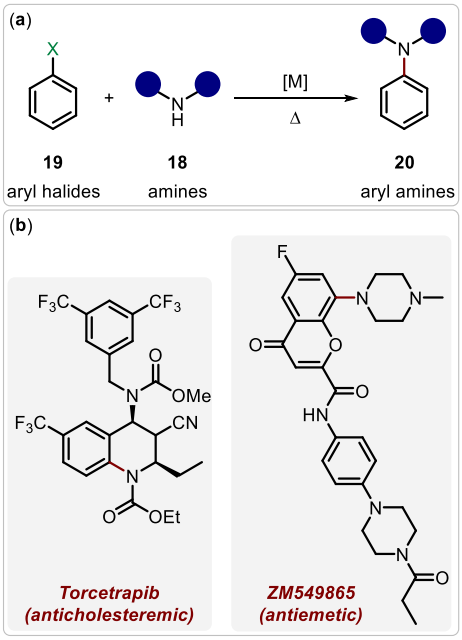

Figure 1. (**a**) General aryl amination reaction between aryl halides **19** and amines **18** to prepare the corresponding aniline derivatives **20**. (**b**) Pharmaceutically relevant compounds containing aryl amino moieties.

Originally, the introduction of the aryl amino groups in a controlled manner has been pursued by either nucleophilic aromatic substitution or Cu-mediated coupling reactions. The latter approach was first reported by Ullmann and Goldberg more than one century ago.[3,4] They used stoichiometric amounts of copper salts to activate aryl (pseudo)halides to react with amine nucleophiles (Figure 2a*i*). However, the generation of large amounts of waste and harsh reaction conditions limited the synthetic utility of these procedures. In the 1990s, Buchwald and Hartwig independently developed Pd- and Cu-catalyzed *N*-arylation reactions using suitable diamine or phosphine ligands (Figure 2a*ii*).[5,6] This breakthrough, together with subsequent efforts from both groups towards a general and efficient methodology for C-N bond formation, led to the establishment of what presently is known as the Buchwald-Hartwig amination reaction.[2,7,8] This transformation has emerged as a prominent tool for the preparation of fine chemicals, even at the industrial scale. Typically, these methodologies usually employ Pd complexes along with strong alkoxide bases and high reaction temperatures (up to 120°C, Figure 2b).[9] It is worth mentioning that also aryl organoboron compounds could be utilized as substrates for the aryl amination reaction in the presence of Cu-based catalysts. This transformation is known as Chan-Lam amination.[10]

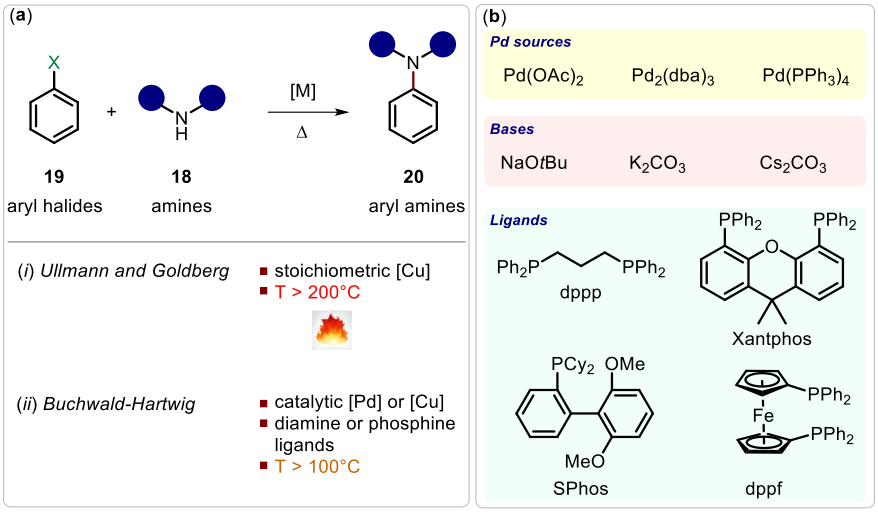

Figure 2. (**a**) Ullmann-Goldberg and Buchwald-Hartwig coupling reactions. (**b**) Some of the typical catalysts, bases and ligands employed in modern Buchwald-Hartwig aminations. dba = dibenzylideneacetone.

Despite the terrific synthetic power of the mentioned approaches, a renewed interest has recently arisen through the possibility to overcome the classic drawbacks in terms of sustainability, cost and relatively harsh conditions.[11] Nickel is an appealing alternative to palladium due to its abundancy.[12] However, in contrast with Pd, Ni is usually less prone to afford the amination products **20** in mild conditions, since reductive elimination from Ni(II) complexes is thermodynamically disfavored, unless strong bases and sophisticated ligands are used (Figure 3a).[13] Moreover, in some cases highly elaborated or air-sensitive Ni(0) complexes are required. Therefore, scientists have found a way to overcome these limitations by destabilizing the catalytic Ni(II) species through a single-electron oxidation to Ni(III) or a single-electron reduction to Ni(I) intermediates (Figure 3b-c).[14] In this way, a more facile formation of products **20** was achieved at room temperature. However, a critical challenge was immediately pointed out, namely the coexistence of a low-valent Ni catalyst to favor oxidative addition of substrates **19** with a high-valent Ni catalyst to facilitate reductive elimination of products **20**. This event prompted the development of a wide diversity of effective Ni-based catalytic systems, along with a variety of proposed mechanistic pathways belonging to each approach (Figure 4a).[14–17]

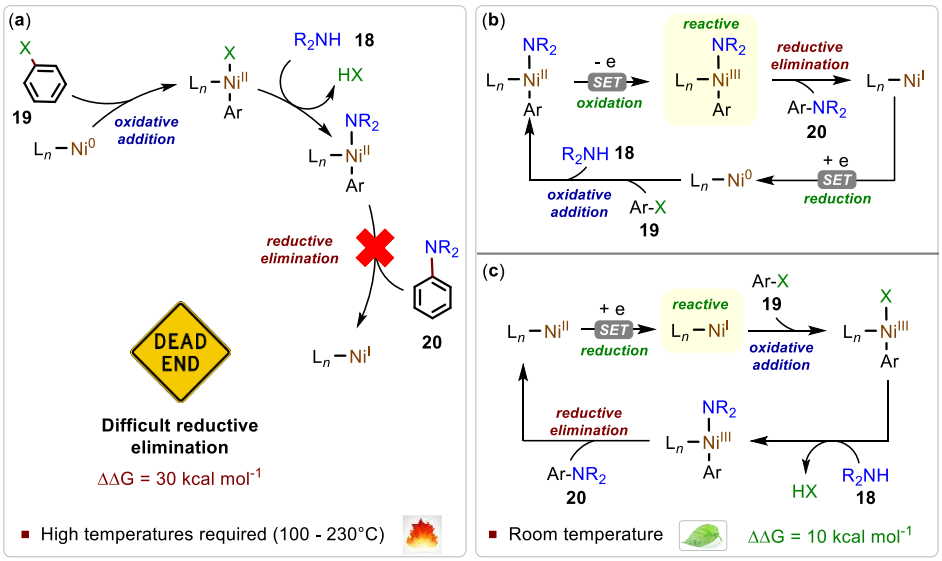

Figure 3. (**a**) Simplified Ni-catalyzed aryl amination mechanism without any external assistance. (**b**) Destabilization of the Ni(II) species through a SET oxidation process. (**c**) Destabilization of the Ni(II) species through a SET reduction process. SET = single electron transfer, L_n = generic ligands coordinated to the Ni species (e.g., solvents, halides, etc.).

Among the different systems developed so far, the most famous usually involve chemical redox active agents or, alternatively, the merging the Ni-catalysis with electro- or photocatalysis. Concerning the first approach, stoichiometric amounts of organic or inorganic oxidants (such as iodine or 1,2-dichloroisobutane) were used to destabilize the Ni(II) intermediates towards the formation of reactive Ni(III) species.[18,19] On the contrary, the use of earth-abundant zinc powder as reducing agent was recently reported to generate Ni(I) complexes from the stable Ni(II) precursors.[20] In both cases, these reactive Ni(I or III) species were capable of affording products **20** at room temperature (Figure 4b). Electrocatalysis could represent a promising alternative to the use of redox agents thanks to the simultaneous occurrence of anodic oxidations and cathodic reductions. Moreover, electrochemical reactions generally occur under mild conditions, thus reducing the consumption of chemicals and energy.[21,22] To this regard, Ni-catalysis has been merged with electrocatalysis to drive aryl amination reactions in a sustainable manner. In these methodologies, the oxidation of inert Ni(II) species occurred at the anode, whereas the concomitant reduction of Ni(I) complexes happened at the cathode to close the catalytic cycle (Figure 4c).[23,24]

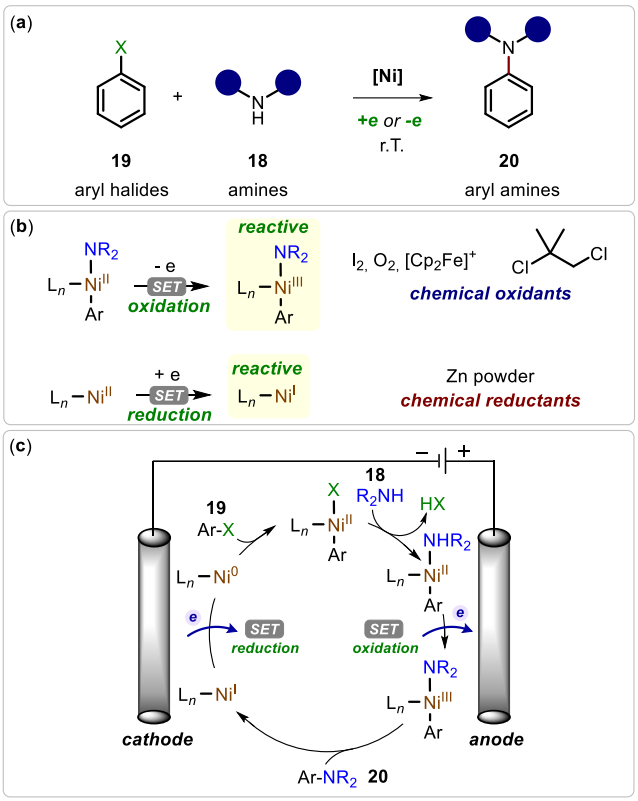

Figure 4. (**a**) General Ni-catalyzed amination reaction. (**b**) Use of chemical oxidants or reductants to destabilize the inert Ni(II) species. (**c**) Ni-catalysis merged with electrocatalysis. SET = single electron transfer, L_n = generic ligands coordinated to the Ni species (e.g., solvents, halides, etc.), Cp = cyclopentadienyl.

In a similar fashion, photocatalysis can be combined with Ni- catalysis for the same redox purposes, taking advantage of its intrinsic benign traits (Figure 5a). In this case, a photocatalyst (PC) can absorb the incident light and drive the oxidation of Ni(II) and the lateral reduction of Ni(I) species to close the combined catalytic cycle (Figure 5b).[14,25,26] Remarkably, an impressive number of examples concerning photocatalytic aryl amination reactions have been reported to date, hence demonstrating their meaningful synthetic utility.[14] Among them, a milestone within this field is represented by the work of Buchwald and MacMillan, published in 2016.[26] The authors described the use of an Ir photocatalyst in very low loading (0.02 mol%) together with a simple Ni salt and 1,4-diazabicyclo[2.2.2]octane (DABCO) as base to promote metallophotoredox aryl aminations under blue light irradiation (Figure 5c). The breakthrough of this study is represented by the possibility of functionalizing a wide range of aryl halides **19** without using sophisticated Ni ligands, because amines **18** can act both as reagent and ligand. This approach was adopted by numerous following studies from different research groups. It should be mentioned that in the considered work a Ni(II) source was employed as C-N bond forming catalyst. However, the actual species that was able to participate to the catalytic cycle was proposed to be a Ni(0) intermediate formed upon reduction of the initial complex by means of the Ir photocatalyst and a sacrificial amount of amine **18**. After that, the transformation could follow the usual pathway depicted in Figure 5b. In the following years, other possible reaction mechanisms have been proposed for this benchmark photochemical transformation. In particular, the role of the Ir photocatalyst have been reconsidered. It seems to not only initiate the reaction through Ni(II) reduction but also its presence ensures that reactivity perpetuates through continually reducing the resting state Ni(II) catalyst to its active, low-valent

form. In this scenario, the oxidative addition of aryl halides **19** could occur on the Ni(I) intermediate instead of to the Ni(0) species displayed in Figure 5b.[16] Nevertheless, the actual mechanism of the metallophotoredox aryl amination reaction is still debated and it appears to depend on the nature of the reaction components and conditions employed.[14,17,25]

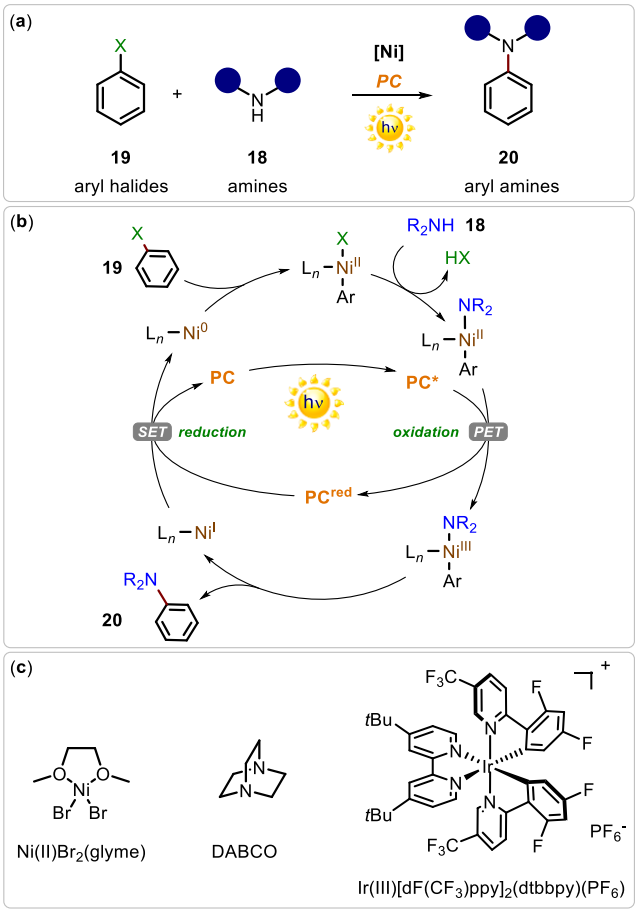

Figure 5. (**a**) General metallophotoredox aryl amination reaction. (**b**) Simplified merged metallocatalytic and photocatalytic cycle. (**c**) Reaction components utilized by Buchwald and MacMillan in 2016. PC = photocatalyst, PC^{red} = reduced form of the PC, PET = photoinduced electron transfer, SET = single electron transfer, DABCO = 1,4-diazabicyclo[2.2.2]octane, L_n = generic ligands coordinated to the Ni species (e.g., solvents, halides, etc.).

In contrast to the abovementioned SET pathways between the photocatalyst and Ni catalyst, an energy transfer pathway between them has also been proposed. In these cases, an excited state Ni(II) complex is generated via energy-transfer photosensitization. Thus, in contrast to the previous ground-state Ni(II) species, this highly energetic intermediate can readily undergo reductive elimination to deliver the C-N coupling products **20** (Figure 6). To this purpose, Miyake, Thordarson and colleagues utilized a dual catalytic system constituted by $NiBr_2$ and $[Ru(bpy)_3]Cl_2$ or organic phenoxazines as photocatalysts.[27,28] Comparably, Johannes and Escobar employed $NiBr_2$(glyme) and $Ir(ppy)_3$ to achieve the same objective.[29]

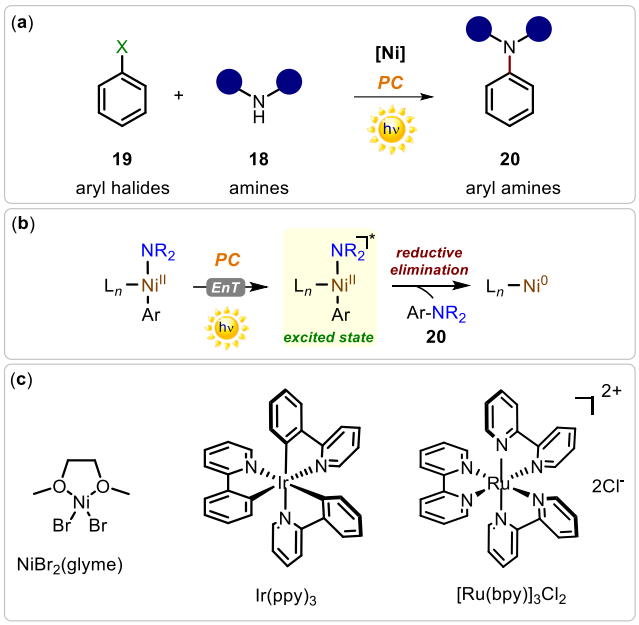

Figure 6. (**a**) General metallophotoredox aryl amination reaction. (**b**) Key mechanistic step for the formation of aryl amines **20**. (**c**) Some of the principal reaction components utilized by Miyake, Escobar and co-workers. PC = photocatalyst, EnT = energy transfer, L_n = generic ligands coordinated to the Ni species (e.g., solvents, halides, etc.).

A different approach consists of the exploitation of the intrinsic photochemical activity of the Ni(II) complexes themselves, by directly exciting them with UV light. In this mechanistic situation, the key step is represented by an intramolecular electron transfer from the ligated amine **18** to the Ni center to afford, upon deprotonation, the corresponding reactive Ni(I) intermediate and the amino radical, which can add to the aryl halide **19** to deliver the desired product **20** (Figure 7). In this context, Miyake and co-workers described the direct photoexcitation of the *in-situ* formed [$NiBr_2$(amine)$_3$] under light irradiation (365 nm).[30] Notwithstanding, a potentially harmful UV radiation must be used, whereas in the previously outlined examples a safer visible light illumination was sufficient to carry out the amination reactions.

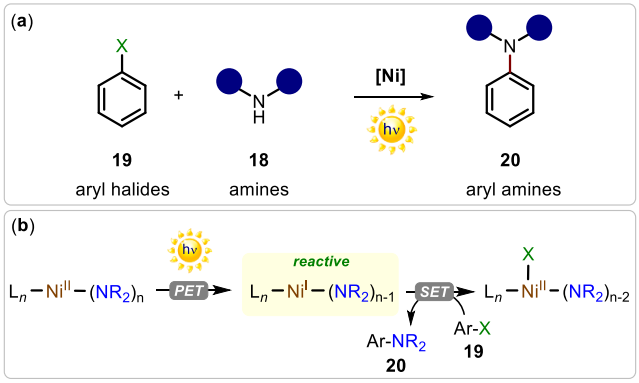

Figure 7. (**a**) General metallophotoredox aryl amination reaction without any external photocatalyst. (**b**) Key mechanistic step for the formation of aryl amines **20**. PET = photoinduced electron transfer, SET = single electron transfer, L_n = generic ligands coordinated to the Ni species (e.g., solvents, halides, etc.).

Because of the high cost and scarce abundance of Ir/Ru-based photocatalysts, there is a high demand for the development of more sustainable and equally effective photocatalysts. Organic dyes could represent a limited alternative due to their possible photobleaching under the reaction

conditions.[31] In this regard, heterogeneous photocatalysis may represent a practical and attractive solution to the listed issues, hence owing excellent optoelectronic properties, along with facile preparation and potential recyclability (see Chapter I, Section 1.3.3).[32,33] Weix, Krauss and collaborators reported the use of nanosized CdSe quantum dots (QDs) to replace the precious transition-metal photocatalysts for the studied transformation.[34] A similar approach was exploited by Xiao, Lu and co-workers that employed a bench-stable CdS semiconductor for the same photocatalytic purposes.[35] In both cases, a simple Ni(II) source was adopted as co-catalyst for the production of aryl amines **20**.

However, the presence of potentially toxic metals within the structure of the heterogeneous photocatalysts may undermine the actual sustainability and safety of their end-use.[36–38] For this reason, the development of novel metal-free photoactive materials are receiving growing attention from the scientific community. In the realm of nanosized semiconductors, the class of carbon nitrides (CNs) undoubtedly represents the most popular choice for photocatalytic applications in organic synthesis on account of their intrinsic properties.[33,39–41] Therefore, it is important to introduce the main characteristics and applications of CNs, with particular attention to the examined aryl amination reaction.

5.2 Carbon Nitrides (CNs): Synthesis, Properties and Applications

CN-based materials diversify to large extents, and various structures have been reported, building a portfolio of material sub-classes. The growing popularity of CNs arises from remarkable features that allow them to act as recyclable photoredox catalysts under visible light irradiation. Indeed, CNs have an appropriate band gap energy of about 2.7 eV and excellent thermochemical stability (Figure 8a). Moreover, they are easy to prepare in a straightforward way from economic precursors (e.g., melamine, urea, cyanamide), tolerant to numerous chemical derivatizations and, primarily, easy to recover and reuse multiple time without any deterioration.[42]

From a structural point of view, the most stable and investigated allotrope, namely graphitic-CN (*g*-CN), is proposed to be constituted of repeating *N*-bridged poly(tri-s-triazine) frameworks arranged into graphite-like π-conjugated planar layers, (although other repeating units have been proposed, such as for example *s*-triazine).[39,43,44] The C/N ratio in g-CN is theoretically 3/4, (which the typically used formula C_3N_4 in various literature indicates), albeit the experimental ratio deviates from this value depending on synthetic procedure, due to the formation of defective structures and incorporation of other elements (e.g., O). It emerges that the accurate structure of *g*-CN (and other CNs in general) is not defined in detail, and often the depiction of the structure is merely a simplification for guiding the reader.

In addition, the redox properties of CNs can be tuned in order to make them suitable for a wide range of light-driven radical transformations. In fact, the position of both valence and conduction bands (VB and CB, respectively) can be modulated on the basis of C/N ratio, polymerization degree (for example adding inorganic salts during the preparation), crystallinity and the presence of doping agents (e.g., boron, sulfur, organic additives).[42,43,45] Therefore, light absorption causes the excitation of electrons from the VB to the CB, with consequent charge separation (electrons and holes).

Depending on the specific energy positions of the VB and CB, the considered photocatalysts may provide sufficiently high redox potential and abundant surface sites to induce the desired transformations (Figure 8b). In contrast to homogeneous photocatalysis, solid-phase photoactive semiconductors can generate both oxidizing and reducing species on the same single particle and at the same time. These materials are therefore suitable for the application in organic synthesis through oxidative or reductive pathways (Figure 8a).[32,46]

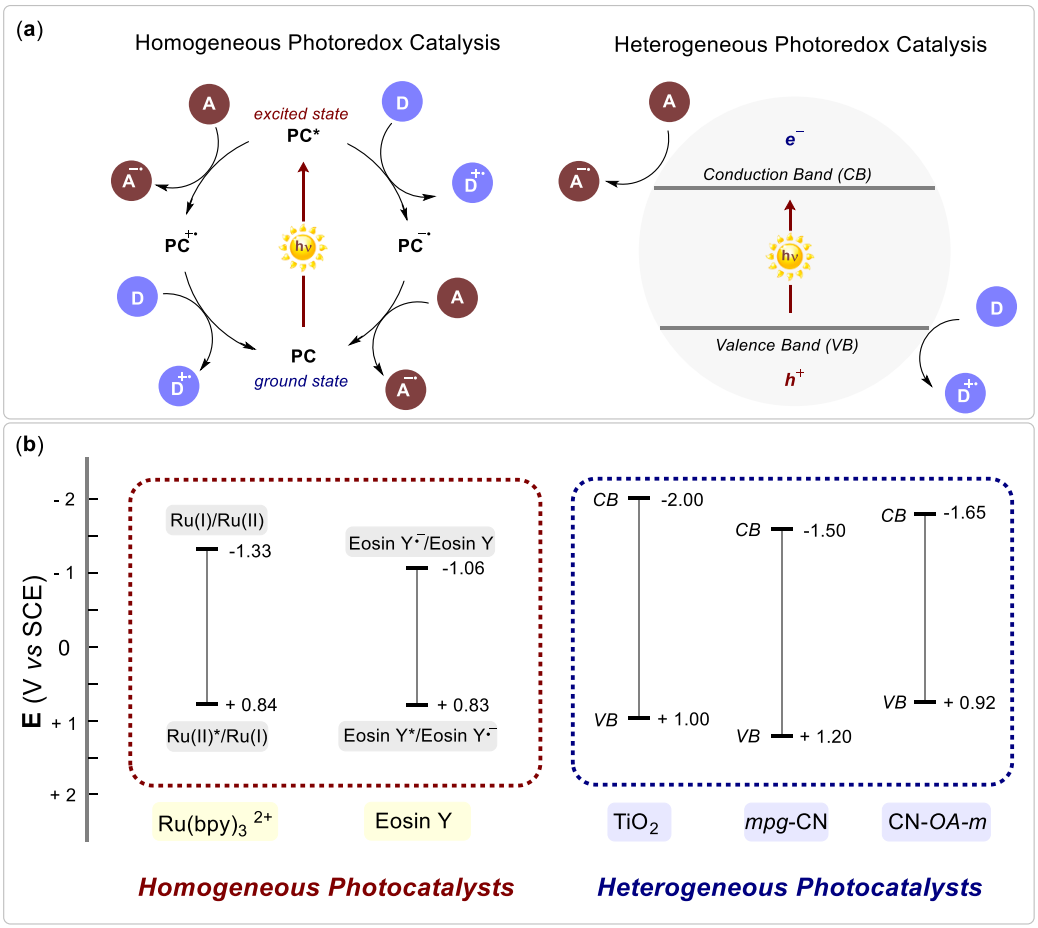

Figure 8. (**a**) Mode of catalysis of a generic homogeneous photoredox catalyst *vs* a generic heterogeneous photoredox catalyst. (**b**) Oxidation and reduction potential of common homogeneous and heterogeneous photocatalysts. PC = photocatalyst, VB = valence band, CB = conduction band.

5.2.1 CNs as Organic Nano-photocatalysts

Beside the abovementioned features, the textural properties can be tailored as well for better photocatalytic performance, as shown by the development of mesoporous carbon nitride (mpg-CN), which possesses a much higher surface area than *g*-CN.[47,48] To this regard, Antonietti, König and co-workers recently reported a seminal work in which *mpg*-CN was used as a heterogeneous photoredox catalyst for synthetically relevant functionalization of arenes, including the important aryl amination discussed in this Chapter (Figure 9).[49] The *mpg*-CN was prepared from cyanamide by thermal treatment (550°C for 4 hours under nitrogen atmosphere) in the presence of mesoporous silica matrices (Figure 9a). Removing of the silica template with ammonium hydrogen difluoride in water afforded the final material with a high specific surface area. This aspect is pivotal to ensure a sufficient number of active surface sites that translates into enhanced photocatalytic properties.[39]

In particular, as concern this Chapter, *mpg*-CN assisted C–N cross-coupling reactions between bromoarenes **19** and amines **18** in dimethylacetamide (DMAc) to afford the anilines **20** in very high yield in the presence of a Ni(II) catalyst upon blue light irradiation (up to 92%, Figure 9b). Interestingly, the *mpg*-CN photocatalyst was easily recovered by centrifugation and reused up to four times with conserved activity in sequential reactions, proving its stability towards reactive radicals and nucleophiles.

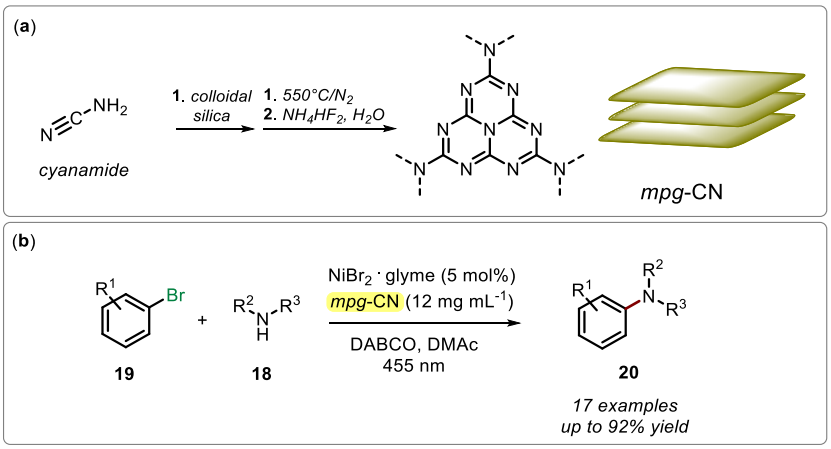

Figure 9. (**a**) *mpg*-CN preparation from cyanamide. (**b**) *mpg*-CN as photocatalyst for the aryl amination reactions. DABCO = 1,4-diazabicyclo[2.2.2]octane.

Similarly, Pieber and co-workers employed a CN derivative (CN-*OA*-*m*), synthesized by co-condensation of urea and oxamide, followed by post-calcination in molten salts (550°C in the presence of KCl and LiCl, Figure 10a) to carry out the aryl aminations.[50] Interestingly, this catalytic system was able to convert both electron-rich and electron-poor aryl halides **19** using blue or green light irradiation, avoiding catalyst deactivation *via* the formation of nickel-black (Figure 10b). Furthermore, the CN-*OA*-*m* photocatalyst turned out to be recyclable multiple times without any loss of its catalytic activity. The straightforward recycling strategies (centrifugation or filtration) of the CNs make them attractive for cost-efficient and sustainable processes. Mechanistically, this CN could assist the formation of products **20** by prompting both the oxidation of the Ni(II) to Ni(III) intermediates and the following reduction of Ni(I) to Ni(0). However, the authors could not exclude a two-step energy transfer process, as depicted in Figure 5b and 6b, respectively. A subsequent study further proposed an initial photoreduction of Ni(II) to Ni(I) by means of a modified CN, followed by a dark Ni(I)-Ni(III) cycle.[51]

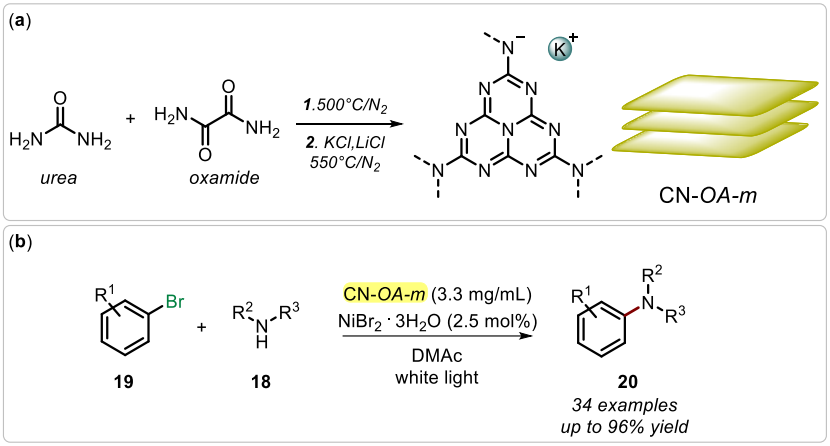

Figure 10. (**a**) CN-*OA*-*m* preparation from urea and oxamide in molten salts. (**b**) CN-*OA*-*m* as photocatalyst for the aryl amination reactions.

5.3 Objective of the Research Project and Initial Results

Considering the potential industrial relevance of these transformations, a continuous flow scale-up would be highly desirable, as explained in Section 1.2.7. However, the use of solid compounds, such as CN photocatalysts, in a flow setup remains one of the central challenges in continuous processing.[52] Indeed, complex reactor designs (agitated cells or multi-jet oscillating disk) or continuous stirred-tank reactor (CSTR) cascades have been proposed as solutions, but maintain their intrinsic limitations of complex moving parts or poor residence time distributions.[53–58] Another alternative is the use of a pulsator (oscillatory pump) that prevents settling of solid materials, without having issues surrounding the long term wear of moving reactor parts. This principle has been demonstrated in baffled and baffle-less tubular flow reactors for several applications (e.g. crystallizations, precipitations and few examples of synthetic transformations).[59–61] However, to the best of our knowledge, no successful efforts had been reported utilizing an oscillatory microstructured plug flow photoreactor to enable continuous heterogeneous catalysis at the time of this project.

Therefore, in this Chapter we investigated a way to tackle this issue by using a microstructured plug flow photoreactor in combination with oscillatory flow delivered by a pulsator (HANU™ REACTOR, CREAFLOW). The oscillation, combined with narrow channels formed by static mixing elements in the reactor, is designed to maintain a homogenized suspension of the carbon nitride particles, mitigating the risk of settling and reactor wall fouling, regardless of the net flow rate. The feasibility of this technology was evaluated for the aryl amination reaction using CN-*OA*-*m* (named **L** in the following sections) under blue light irradiation.

In particular, the flow system (Figure 11) was formed by a photoreactor composed of Hastelloy baseplate housing a flow channel with a series of cubic static mixing elements, topped with lid and glass window to allow light irradiation (15 mL internal volume, 2 × 2 mm channel depth and width). A symmetrical pulse was delivered by an oscillatory diaphragm pulsator unit, positioned between the reactor and a metering pump (which generates the net flow through the system). The static mixing elements split and recombine the process stream under the imposed pulsation. The narrow channels increase pulsation velocity and improve turbulence inside the reactor, encouraging

suspension of solids, even at low net flow rates. In addition, the excellent film refreshment promotes efficient photon utilization for photochemical transformations. The flow reactor was equipped with an integrated heat exchanger which enables temperature control. In a typical reaction, the heterogeneous reaction mixture was kept suspended in a stirred feed vessel and fed into the system through the peristaltic metering pump, under the appropriate pulsation regime. The arrangement was pressurized at 3 bar using a back pressure regulator (BPR) capable of handling solids and a pulsation dampener (air-filled tube connected by a Y-piece) was placed between the reactor and the BPR, in order to prevent cavitation or suction of air from the end of the system during the backward pulsation (see Section 5.5 for details).

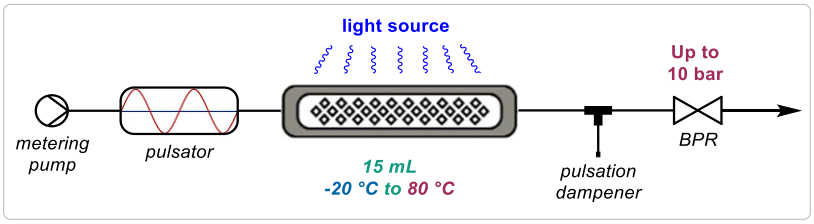

Figure 11. Schematic representation of the reaction setup including metering pump, pulsator, reaction plate, light source, pulsation dampener and BPR. For a photograph of the setup see the Experimental Section.

The amination of ethyl 4-bromobenzoate (**19a**) with pyrrolidine (**18g**, 3 equiv.) under blue light irradiation was selected as a model reaction. Initial reaction conditions were adapted from a previous publication: nickel(II) bromide trihydrate (2.5 mol%) and **L** (3.33 mg mL^{-1}) as metal and photocatalyst, respectively, in DMAc ($[\mathbf{19a}]_0$ = 0.2 M, 25 mL stock solution, 5 mmol scale). In a preliminary experiment, the pulsation amplitude was set to 70% (about 0.32 mL per stroke) and the pulsation frequency to 3 Hz (100%) (see Section 5.5). By using the specified pulsation, the solid/liquid suspension was observed to be stable along the whole system. Gratifyingly, the C-N coupling product **20a** was observed by HPLC in 66% and 77% assay yield at 40 and 50 °C respectively, using a residence time of 15 min under blue light irradiation (460 nm, Figure 12).

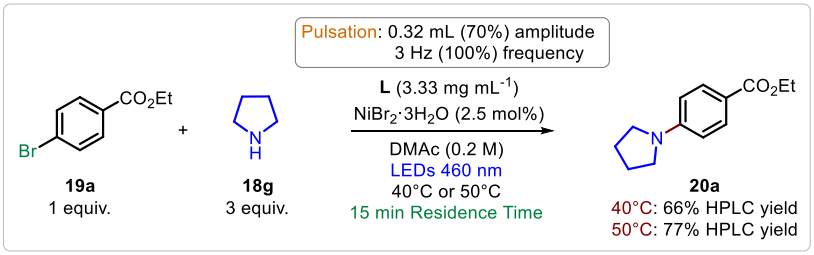

Figure 12. Reaction scheme for preliminary photochemical aryl amination experiments. Yields were determined by HPLC assay at the maximum concentration using 4-ethylbiphenyl as the internal standard.

5.4 Results and Discussion

The material exiting the reactor was monitored over time by HPLC, providing both its relative concentration at the analyzed time point (Figure 13, green line) and the assay yield of desired product **20a** (Figure 13, blue bars). Surprisingly, an unusual concentration/yield course was observed during these first trials. An ideal distribution of the two parameters over the time should follow a Gaussian-type profile, where the highest concentration corresponds to the highest yield, particularly for such concentration-dependent reactions.[50,62,63]

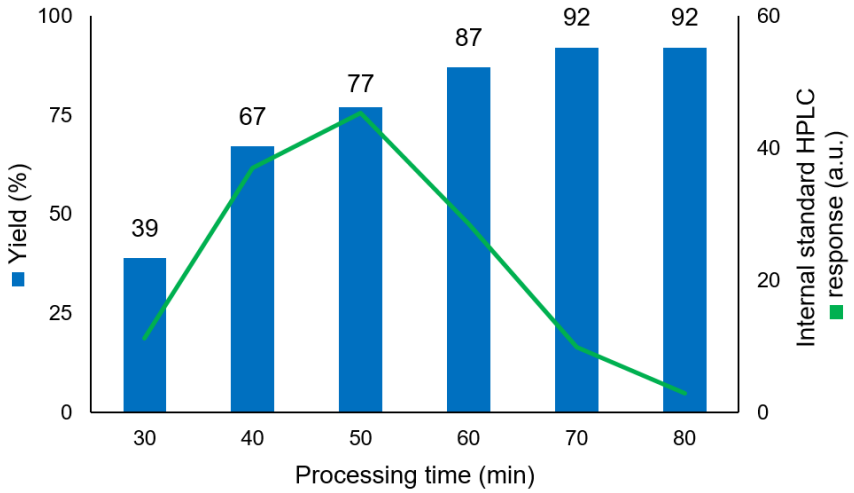

Figure 13. HPLC response of internal standard, relative to concentration (green line) and yield (blue bars) profile over the collection time, determined by HPLC using 4-ethylbiphenyl as the internal standard.

Conversely, the observed trend showed an increasing yield after the maximum concentration was reached, that is a strong deviation from the expected profile. The very same concentration/yield profile was also observed in the absence of any insoluble component (**L**), suggesting that this effect is not due to the solid photocatalyst (Figure 14a, the detectable yields were attributable to the background reaction that could occur in the absence of photocatalyst **L**). As further validation, the photocatalyst-free experiment was performed in a smaller plate-based photoreactor at the available irradiation wavelength (395 nm, Lab Photo Reactor, Corning). Albeit the yields were different in number for the two reactors (due to the different wavelength available), in the smaller volume reactor the expected concentration/yield profile was observed (Figure 14b), thus implying that this deviation is due to the reactor itself.

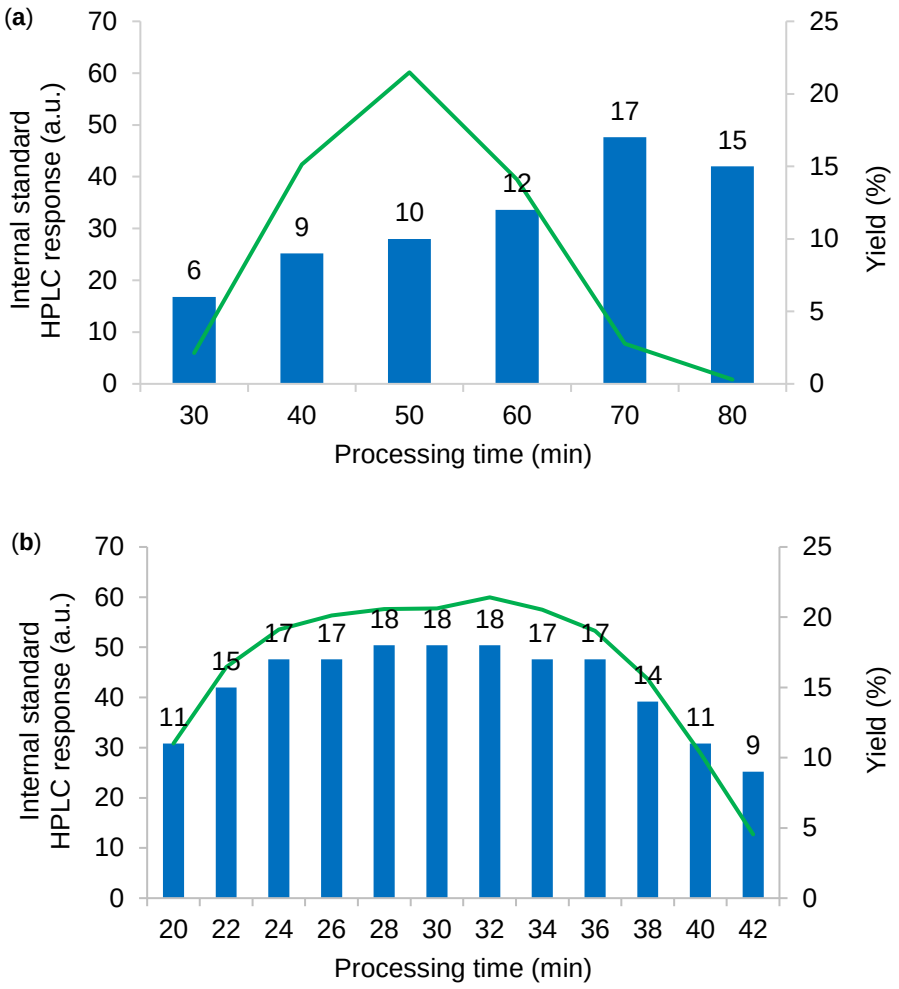

Figure 14. (**a**) HPLC response of internal standard, relative to concentration (green line) and yield (blue bars) profile over the collection time for reaction performed in the HANU™ reactor in the absence of photocatalyst **L** at 460 nm. (**b**) HPLC response profile for the reaction performed in the Corning Lab Photo reactor in the absence of photocatalyst **L** at 395 nm. Yields determined by HPLC using 4-ethylbiphenyl as the internal standard.

To ascertain that this is phenomenon is unrelated to issues in reaching steady state conditions, the reaction was carried out with a 50 mL stock solution (in place of 25 mL), in which case an identical trend in yield was observed (Figure 15, yellow bars and red line). Furthermore, no difference was seen when the reactor was filled with the reaction mixture prior to turning on the lamps, ensuring a constant concentration of reaction mixture at the beginning of the reaction (Figure 15, blue bars and green line). A similar observation (with opposite effect) has been made in a recent report on handling solids in a photo CSTR cascade, which was explained by a poor residence time distribution.[56]

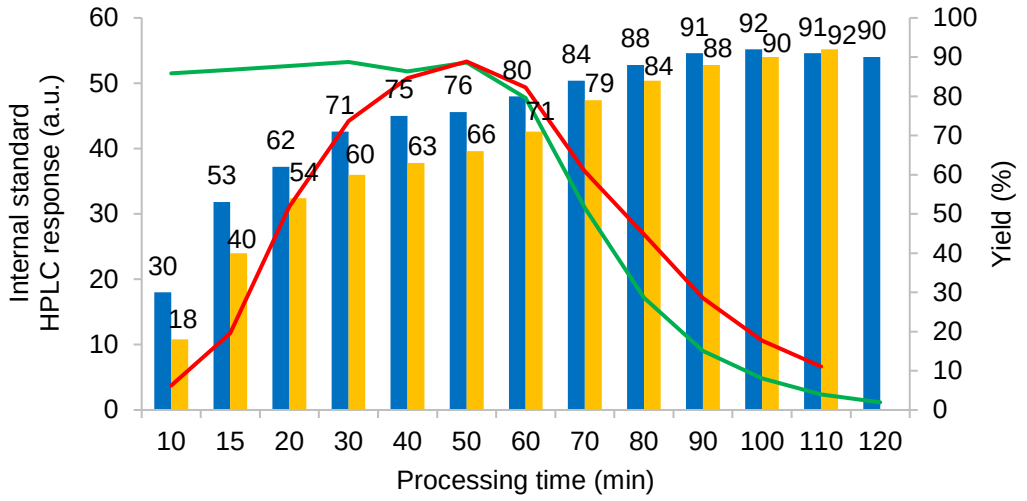

Figure 15. HPLC response of internal standard, relative to concentration (green line) and yield (blue bars) profile over the collection time for the experiment with the reactor was pre-filled with the reaction mixture. HPLC response of internal standard, relative to concentration (red line) and yield (yellow bars) profile over the collection time for the experiment with the larger stock solution, under the standard conditions. Yields determined by HPLC using 4-ethylbiphenyl as the internal standard.

Accordingly, further efforts were devoted to the characterization of the reactor, in order to understand and minimize this effect. To this aim, a series of residence time distribution (RTD) experiments were designed and carried out. Specifically, these focused on the two novel process parameters in this reactor setup: pulsation amplitude (mL displaced per pump stroke) and frequency (number of strokes per second, Hz). First, the correlation between the programmed pulsation amplitude and displaced volume was quantified, proving its linearity, with a maximum displaced volume of about 0.44 mL per stroke (see Section 5.5 for details). Subsequently, an array of RTD experiments were carried out at different pulsation amplitudes and frequencies by using a colored tracer pulse (rose Bengal in DMAc 10^{-4} M, injected *via* a Y-piece mixer between the metering pump and the pulsator, in a carrier stream of pure DMAc). An in-line UV/Vis flow cell was installed after the BPR and connected to a spectrometer, in order to record the distribution profiles. These graphical indications could be then quantified by low Bodenstein numbers (dimensionless number, Bo, which characterizes the extent of axial dispersion within the reactor, see Section 5.5 for details), calculated from the mathematical deconvolution of the tracer experiments. The Bodenstein value should be maximized, and values below 100 represent an appreciable level of axial dispersion (i.e., non-ideal plug flow behavior, Figure 16).[61,63]

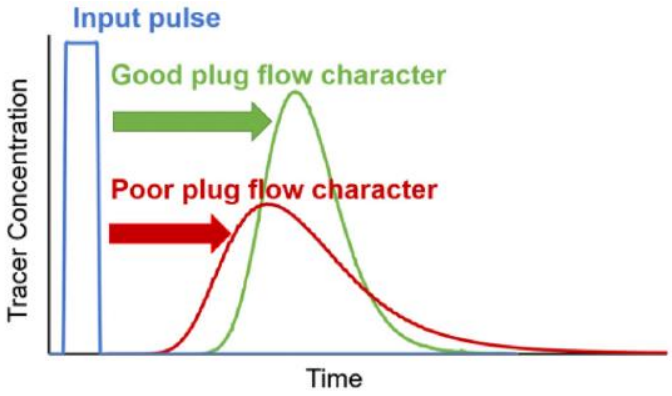

Figure 16. Simplified representation of a reactor's plug flow character estimated using tracer injection (blue line) experiments. Good plug flow character has low axial dispersion (green line) while poor plug flow character has significant axial dispersion (red line).[61]

As benchmark, a curve was plotted in the absence of pulsation, which resulted in a fairly wide distribution profile (Figure 17a, yellow line, Bo = 48). The distribution profiles proved to be even broader at high pulsation amplitudes (30-100% amplitude, Figure 17a, orange, brown and purple line; Bo = 16-10). Gratifyingly, the lowest pulsation amplitude of 0.04 mL per stroke (about 5% amplitude) actually provided a significantly narrower RTD curve compared to the benchmark case (without pulsation), implying a significant decrease in axial dispersion. The corresponding Bo values quantified this observation, providing a substantial increase from 48 to 128.

In parallel, the effect of pulsation frequency showed a trend of increasing Bo with decreased pulsation amplitude from 3 to 0.6 Hz (Figure 17b). A maximum Bo value of 184 could be achieved (0.04 mL per stroke, 0.6 Hz), demonstrating good plug flow behavior for the microstuctured flow photoreactor. These observations serve to reinforce the significant benefits of using an oscillatory flow regime in combination with flow reactors to enable the handling of solids in continuous flow.

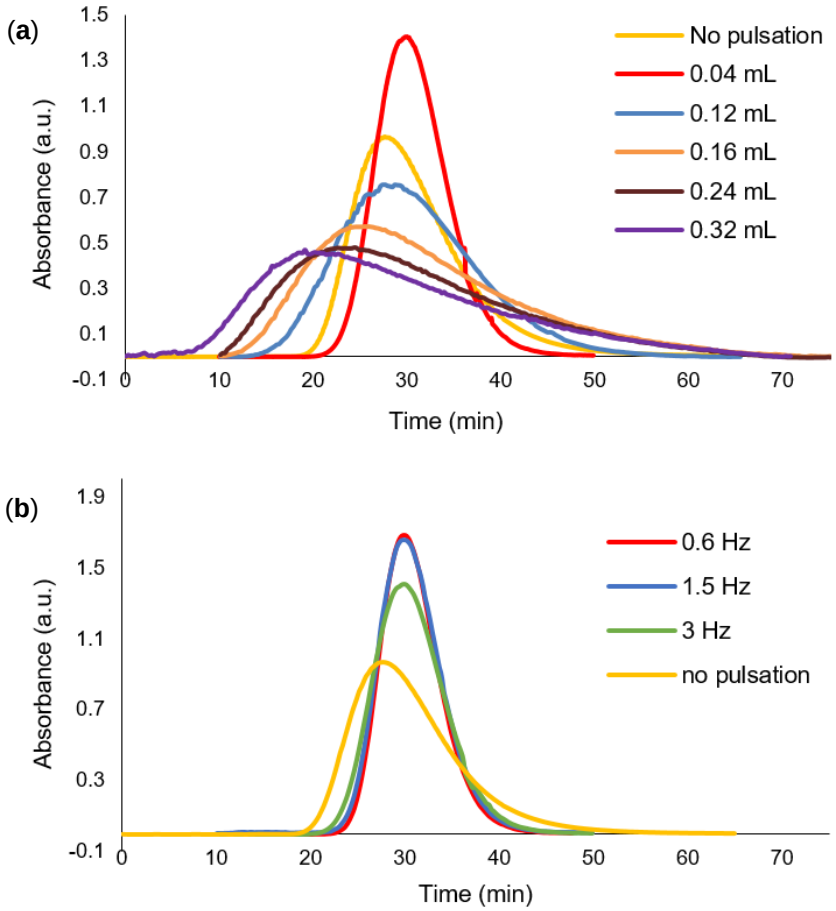

Figure 17. RTD profiles using pulses of rose Bengal dye in DMAc. Conditions: flow rate = 0.75 mL/min, back pressure = 3 bar, injected tracer volume = 1 mL. (**a**) Experiments performed at 3 Hz (100%) pulsation frequency and different pulsation amplitudes. (**b**) Experiments performed at 0.04 mL (about 5%) pulsation amplitude using different pulsation frequencies.

The numerical interpretation of the initial RTD trials therefore confirm the presence of a non-ideal plug flow behavior. This result is consistent with the observed chemical result (Figure 13), since the initial reactions were performed under conditions providing an extremely low Bo value (0.32 mL per stroke, 3 Hz, Bo = 10). Based on this correlation, setting suitable pulsation parameters is essential to ensure proper suspension of the solid photocatalyst, whilst maintaining plug flow behavior (minimizing backmixing).

In light of the preliminary results in the model aryl amination, further optimization experiments were performed minimizing the pulsation amplitude and frequency (Table 1). As anticipated, reducing the pulsation amplitude from 0.32 mL per stroke (70%) to 0.16 mL per stroke (30%) led to an increase in yield of product **20a** from 77% to 83% (entries 1-2, Table 1). In addition, lowering the amplitude to 0.12 mL per stroke (20%, the minimum value capable of keeping **L** suspended) and extending the residence time to 20 min, provided compound **20a** in 94% yield (entry 4, Table 1). Finally, decreasing the pulsation frequency to the minimum affordable value of 1.5 Hz (50%) resulted in a quantitative formation of **20a** (entry 5, Table 1). Remarkably, this demonstrates that finding the ideal compromise between sufficient solid suspension and reduced backmixing ensures excellent solid-handling and high yields of the amination product **20a**. Compared with the previously

reported procedure in batch, this flow procedure offers a significant improvement in terms of reaction time (20 minutes *vs* 8 hours).[50]

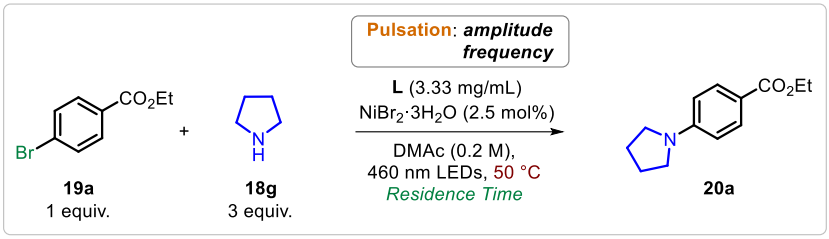

Entry	Residence time (min)	Pulsation amplitude (mL / percentage)	Pulsation frequency (Hz / percentage)	Yield[a]
1	15	0.32 / 70%	3 / 100%	77%
2	15	0.16 / 30%	3 / 100%	83%
3	15	0.12 / 20%	3 / 100%	86%
4	20	0.12 / 20%	3 / 100%	94%
5	20	0.12 / 20%	1.5 / 50%	99%

Table 1. Metallaphotoredox aryl amination optimization study. Reaction conditions: ethyl 4-bromobenzoate (**19a**, 5 mmol scale), pyrrolidine (**18g**, 3 equiv.), $NiBr_2 \cdot 3H_2O$ (2.5 mol%) and CN **L** (3.33 mg/mL) in DMAc (0.2 M) under blue light irradiation (460 nm). Reactions were performed using a 25 mL stock solution. [a] Yields were determined by HPLC assay at the time point where concentration was at a maximum, using 4-ethylbiphenyl as the internal standard.

Likely the most substantial benefit of using a heterogeneous photocatalyst is its ease of separation (i.e., filtration) and potential recyclability.[50,64,65] Therefore, we sought to determine whether CN **L** is recyclable in this setup under the optimized reaction conditions. Previous studies have shown that the deposition of nickel-black agglomerates, formed over time, on the heterogeneous material can affect its catalytic properties.[50] We envisage that, due to the far shorter irradiation time in flow, it may be possible to limit the nickel catalyst deactivation, allowing more effective recycling of the heterogeneous photocatalyst. **L** was recovered after each run by centrifugation, was washed, and used again in the next run by adding fresh nickel(II) bromide. Gratifyingly, no loss of activity was observed over six cycles. Thereafter, a minor reduction in the yield of **20a** was observed (from 99% to 95% yield in the tenth cycle), but this can be rationalized by the loss of small amounts of **L** (about 3 mg per experiment) during the manual recovery operations between experiments. Indeed, by using fresh **L** in the same quantity as the last cycle, a comparable result was obtained (94% yield) confirming our hypothesis (Figure 18). This outcome suggests that catalyst deactivation can be avoided by using intensified conditions to prevent deleterious off-cycle side reactions.

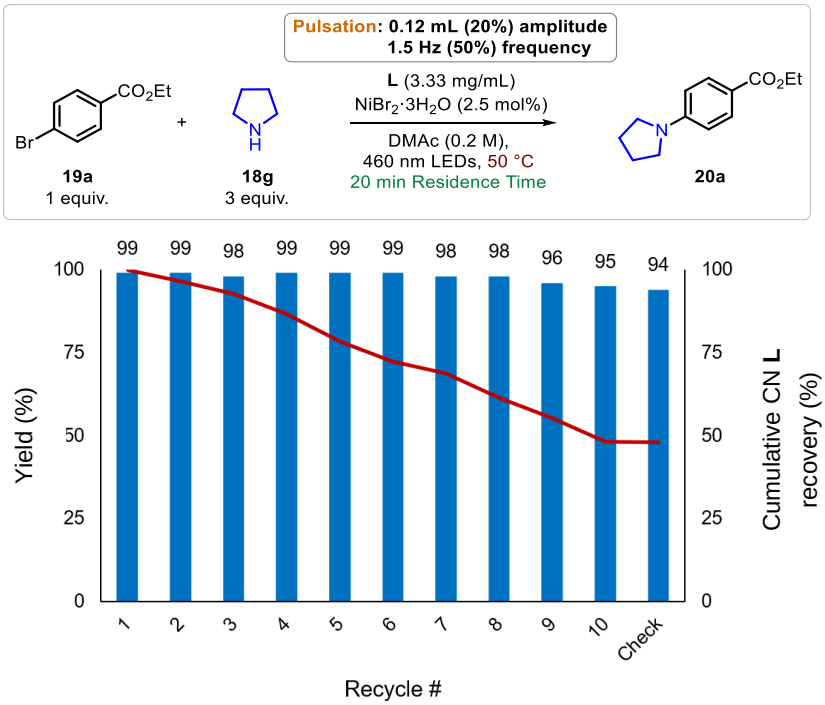

Figure 18. Catalytic performance of recovered CN **L** over ten cycles under the optimized reaction conditions. Yields of product **20a** (blue bars) were determined by HPLC assay using 4-ethylbiphenyl as the internal standard at the concentration maximum over the collection time. CN **L** recovery (red line) was determined by weighing the recovered material after centrifugation, washing and drying.

Thereafter, a scale-out experiment was performed in order to demonstrate the stability, robustness and scalability of our protocol. It should be noted that the preparation of the photocatalyst **L** by simple calcination,[50] results in particles that differ in size and aggregation tendency.[66] The material was observed to have two distinct median particle sizes (D_{50}), of about 5 µm and 20 µm (see Section 5.5 for details). The larger type of these particles led to a further complication in handling for long periods, due to settling in the outlet tube of the reactor, even at adequately high pulsation. Attempts to mill the particles to smaller sizes were unsuccessful.

In order to avoid this problem, the reaction setup was altered in a manner such that the reaction pathway was continually descending from the metering pump to the collection vessel (see Section 5.5). Moreover, a vibrating motor was installed on the pump inlet and every 15 minutes a small argon bubble was introduced into the system from the headspace of the starting mixture vessel. Using these modifications, the model reaction was carried out in a stable manner for over 5 hours, using the previously optimized conditions, but with a higher concentration to maximize the productivity (0.3 M instead of 0.2 M, without changing the loading of photocatalyst **L**).

HPLC analysis revealed a stable assay yield of >99% for the duration of the experiment (Figure 19). The output material was collected for 4.5 hours of steady state operation, resulting in 12 g (90% isolated yield) of the desired coupling product **20a**, without column chromatography. This corresponds to an exceptionally high productivity of 2.67 g h^{-1} (15 mmol h^{-1}), a value to our knowledge only surpassed by some homogeneous Ir- or Ru-based photoredox catalyzed C-N couplings.[67] It is noteworthy that the larger version of the HANU™ reactor (150 mL volume, 10 × scale up) maintains all of its process characteristics (e.g. channel dimensions, mass-, heat, and light transfer capacities, RTD), thus can allow for straightforward scale-up of such procedures.

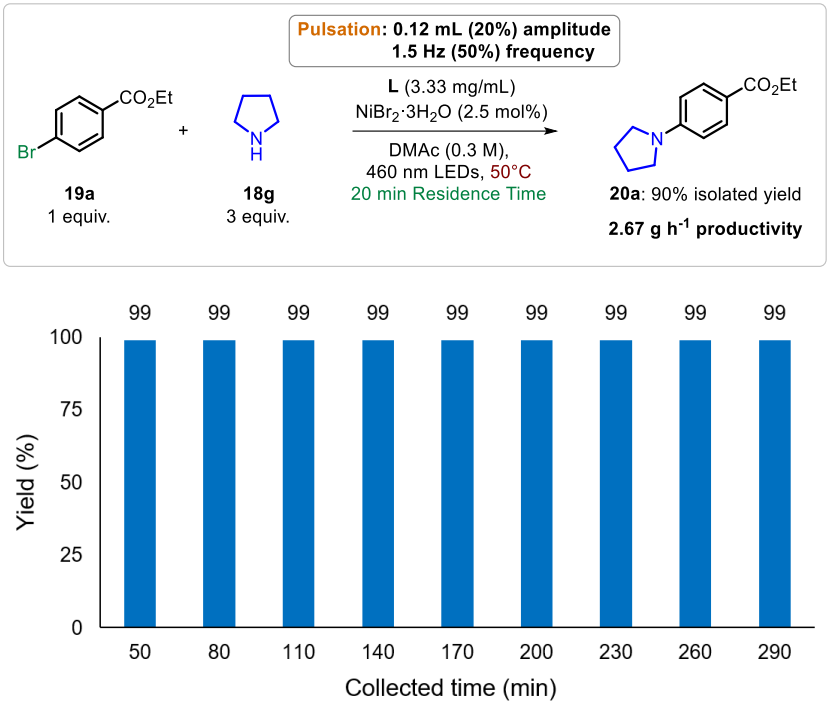

Figure 19. Scale-out experiment under the optimized conditions. Yields of product **20a** at 30-minute time increments throughout the scale out synthesis. These were determined by HPLC assay using 4-ethylbiphenyl as the internal standard.

Finally, we envisaged that this protocol could be used for the preparation of an active pharmaceutical ingredient (API) precursor. In particular, tetracaine,[68] a local anaesthetic selected by the World Health Organization (WHO) as an essential medicine,[69] contains a butylamino aryl core, which can be accessed from precursor **20b** by a coupling reaction between **19a** and butylamine **18h** (Figure 20). The final API can then be obtained from **20b** by simple transesterification with *N,N*-dimethylamino ethanol.[70]

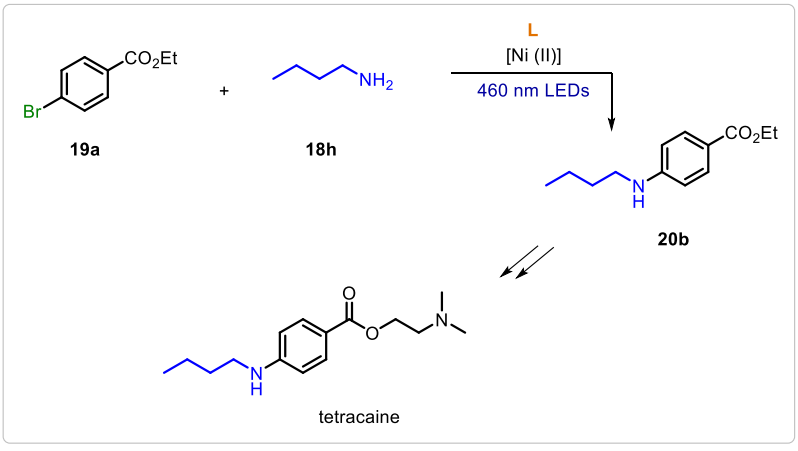

Figure 20. Reaction scheme for the preparation of tetracaine through a photochemical aryl amination.

Despite the use of reactive aryl bromide **19a**, the coupling reaction with primary aliphatic amines is challenging and requires harsher conditions. In fact, this difference in reactivity is so substantial that recent studies have been published with the specific aim to improve their reactivity.[26,28] A new optimization study was then performed starting from the previous conditions with optimized oscillation settings (Table 2). Using the previously optimized conditions, but with a slightly elevated

temperature of 60°C, product **20b** was observed in only 24% yield (entry 1, Table 2). Then, increasing the concentration to 0.4 M and the nickel loading to 5 mol%, without varying the photocatalyst amount, led to a reasonable increment in yield of **20b** to 38% (entry 2, Table 2). An extended residence time of 60 minutes subsequently resulted in 69% yield (entry 3, Table 2). Finally, further increasing the temperature to 80°C led to the formation of **20b** in almost quantitative yield (94%, entry 4, Table 2).

It is noteworthy that under these harsh reaction conditions, the formation of a small amount of nickel-black agglomerate was observed (see Section 5.5). Notwithstanding, the result obtained is of relevance for the preparation of the API precursor, since it can be produced in a significantly shorter reaction time, when compared with the state of the art.[26,71] Consequently, in order to isolate product **20b**, the amination reaction was carried out over a runtime of more than four hours employing the optimized conditions. The coupled product **20b** was collected in the steady state for 80 minutes (92% average HPLC assay yield), leading to an isolated yield of 1.5 g (84%), which corresponds to a productivity of 1.12 g h^{-1}.

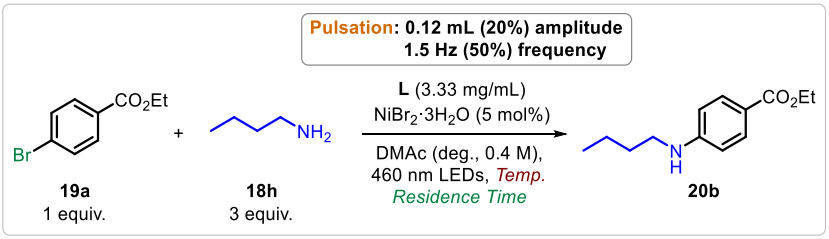

Entry	Residence time (min)	Temperature (°C)	Concentration (M)	$NiBr_2 \cdot 3H_2O$ (mol%)	Yield[a]
1	20	60	0.2	2.5	24%
2	20	60	0.4	5	38%
3	60	60	0.4	5	69%
4	60	80	0.4	5	94%

Table 2. Tetracaine precursor optimization study. Reaction conditions: ethyl 4-bromobenzoate (**19a**, 5 - 10 mmol scale), butylamine (**18h**, 3 equiv.), $NiBr_2 \cdot {}_3H2O$ (2.5 - 5 mol%) and **L** (3.33 mg/mL) in DMAc (0.2 - 0.4 M) under blue light irradiation (460 nm). Reactions were performed using a 25 mL stock solution and 20 or 60 min residence time (0.75 or 0.25 mL min^{-1}). [a]Yields were determined by HPLC using 4-ethylbiphenyl as the internal standard.

5.5 Conclusions

In conclusion, we demonstrated the utility of an oscillatory plug flow photoreactor, capable of handling solids in continuous flow, for an industrially relevant metallaphotoredox C-N coupling reaction. A detailed investigation of the system performance in terms of RTD led to finding the ideal match toward processability of solids and reactor performance. Following an optimization study, excellent yield was achieved in a model C-N coupling reaction on multi-gram scale, using a short residence time. A gram-scale operation of several hours runtime demonstrated the ability to successfully scale up heterogeneous photocatalysis processes by the implementation of oscillatory flow reactor technology. The intensified conditions achieved using the flow photoreactor allowed for facile recycling of the carbon nitride photocatalyst over ten cycles. Finally, a pharmaceutically relevant intermediate was synthesized using slightly modified conditions, showing its applicability for preparative scale production of medicinally relevant compounds.

5.6 Experimental Section

5.6.1 General Information

The NMR spectra were recorded on Bruker 300 MHz spectrometer (^{1}H: 300 MHz, ^{13}C: 75 MHz. Analytical HPLC (Shimadzu LC20) analysis were carried out on a C18 reversed phase (RP) analytical column (150 mm × 4.6 mm, particle size 5 µm) at 37 °C using mobile phases A (90:10 v/v water/acetonitrile + 0.1% TFA) and B (MeCN + 0.1% TFA) at a flow rate of 1.5 mL min^{-1}. The following gradient was applied: linear increase from 30% to 100% B over 10 min. UV-Vis spectra were recorded using a fiber-coupled Avantes Starline AvaSpec-2048 spectrometer, with an Avantes AvaLight-DHc lamp as the light source. These spectra were processed using Avasoft 8.7 software. Centrifugation was performed using an Eppendorf Centrifuge 5804. Laser diffraction (LD) analyses were carried out on a Sympatec Helos H2395 particle sizing instrument. Approximately 1 mg of solid was added to 50 mL of deionized water in a cuvette, followed by a small drop of tween 80 surfactant (to aid suspension). The sample in the cuvette was then sonicated for approximately 5 s and was stirred at 1000 rpm during measurements. Two separate 30 s measurements were taken, to cover a combined particle size range of 0.45-875 µm.

General Procedures

All photochemical reactions were conducted in a commercial continuous-flow reactor: Creaflow HANU^{TM} Reactor (Figure 21).

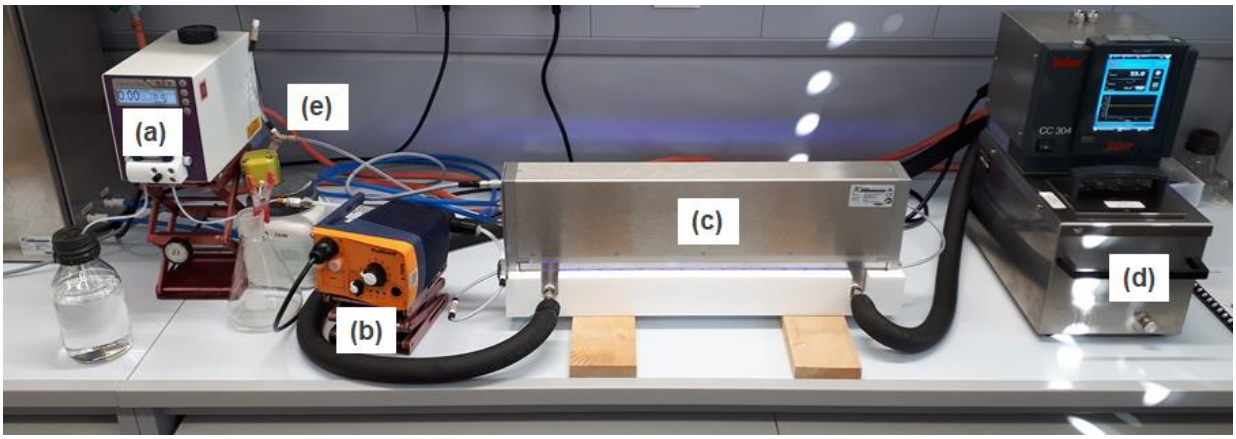

Figure 21. Photograph of commercial photoreactor setup: a) metering peristaltic pump (SF-10, Vapourtec); b) pulsator (Creaflow customized ProMinent (beta/4) pump with PTFE/carbon pump head); c) Reactor Module consisting of a HANUTM reactor and Peschl LED module; d) temperature control for reaction plate (Huber); e) backpressure regulator (BPR-10, Zaiput) with Creaflow pulsation dampener. Photograph of the LED control panel, containing the cooling system, has been omitted.

Reactor module (HANU^{TM} HX 15-C276-CUB reactor, Creaflow): A Hastelloy-based microstructured plug flow reactor (540 × 60 × 60 mm size; channel dimensions: 480 × 20 × 2 mm, 15 mL internal volume) held in a PTFE housing.

Light source: LED module ("novaLIGHT FLED75" water cooled high-performance LED array, Peschl Ultraviolet) was mounted on the top of the reactor plate (35 mm from the center of the reaction channel). The LED panel (460 nm) was equipped with 36 LEDs (3 strips of 12 LEDs).

Temperature control: Thermal regulation of the reactor was carried out using a Huber CC304 thermostat filled with silicon oil (temperature range –20 °C to 195 °C).

Metering pump: The feed mixture was conveyed through the reactor using a Vapourtec SF-10 peristaltic pump equipped with "blue" peristaltic tubing (0.02-10.00 mL/min) as metering pump.

Pulsator: Between the metering pump and the reactor, the feed mixture was pulsed using a Creaflow customized ProMinent Beta/4 pump (PTFE/carbon pump head). This had a tunable amplitude (<5-100%), which was experimentally found to constitute a range of approximately 0.04-0.44 mL per stroke (see Fig. S14). The frequency could be tuned from 10-100%, corresponding to a range of 0.3-3 Hz.

Pulsation dampener: The pulsation dampener was constituted by a piece of 1/4" PFA tubing, filled with air, closed on one side and connected in between the reactor output and the backpressure regulator through a PEEK Y-piece.

Back pressure regulator: A dome-type back pressure regulator (Zaiput Flow Technologies, BPR-10) was installed after the pulsation dampener with a set point of 3 bar.

General connections: Connection between the starting mixture flask and the metering pump was achieved using 1/8" o.d. (~1.6 mm i.d.) PTFE tubing with PEEK fittings. Connection between the metering pump and the pulsator was achieved using 1/8" o.d. (~1.6 mm i.d.) PTFE tubing with PEEK fittings and 1/4" o.d (3.2 mm i.d.) PFA tubing with stainless steel (Swagelok) fittings. Reactor plate input and output, as well as pulsation dampener were connected using 1/4" (3.2 mm i.d.) PFA tubing (Swagelok) with PEEK fittings. Backpressure regulator input and output was achieved using 1/8" o.d. (1.6 mm i.d.) PFA tubing with PEEK fittings. Fittings were lined with PTFE tape, to ensure a tight seal.

Chromatographic purification of products was accomplished using a Biotage Isolera automated flash chromatography system with cartridges packed with KP-SIL, 60 Å (32–63 µm particle size). For thin layer chromatography (TLC) analysis, Merck pre-coated TLC plates (silica gel 60 GF_{254}, 0.25 mm) were employed, using UV light as the visualizing agent (254 nm), basic aqueous potassium permanganate ($KMnO_4$) stain solution or iodine and heat as developing agents. Organic solutions were concentrated under reduced pressure on a Büchi rotatory evaporator.

Materials

Commercial reagents and solvents were purchased (Sigma-Aldrich, Fluka, Alfa Aesar, Fluorochem or VWR) and used as received, without further purification, unless otherwise stated. Ethyl 4-bromobenzoate (**19a**), pyrrolidine (**18g**), butylamine (**18h**), nickel(II) bromide trihydrate, and 4-ethylbiphenyl were all commercially available. Carbon nitride photocatalyst (**L**) was prepared by *Mr. Sebastian Gisbertz* within the Pieber group, according to the literature procedure.[50]

^{1}H NMR and ^{13}C traces and spectra are available in the published manuscript[1] and are not reported in the present thesis.

5.6.2 Correlation between Pulsation Amplitude and Displaced Volume

An array of experiments was carried out in order to determine the physical correlation between the pulsation amplitude generated by the pulsator and the corresponding displaced volume. For this purpose, a 50 cm length of PFA tubing (1/4" o.d., ~3.2 mm i.d.) was installed after the pulsator and attached to a ruler (Figure 22). The system was filled with toluene, then a solution of methylene blue in water was pumped through to provide a liquid/liquid biphasic mixture inside the aforementioned tubing. In absence of any net flow rate, the pulsator was switched on, allowing the colored slugs to move back and forth inside the tube. The overall motion was recorded using a camera set at high frame per seconds rate (240 FPS) giving the possibility to calculate the resulting displaced volume for the selected pulsation amplitude.

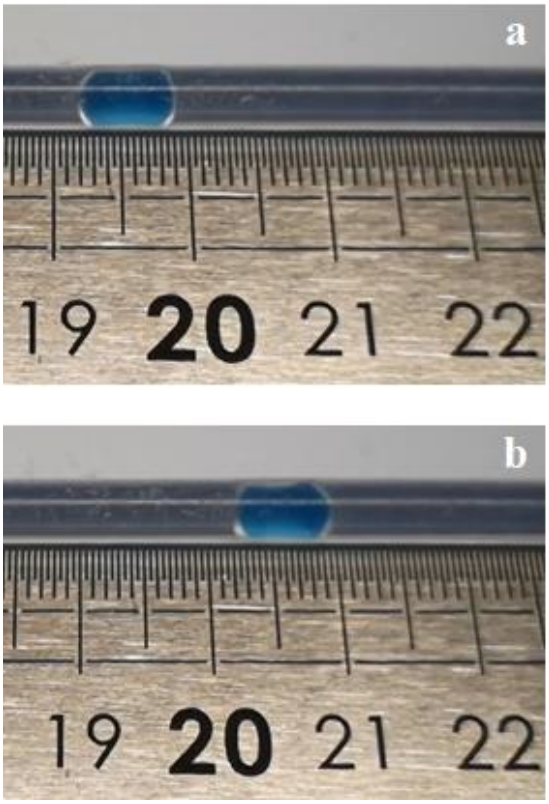

Figure 22. Tubing installed after the pulsator, attached to a ruler for the displaced volume determination. (**a**) Initial position of the considered tracer slug after the backward pulsation. (**b**) Final position of the considered tracer slug after the forward pulsation.

A linear relationship was observed between the pulsation amplitude and the displaced volume in absence of any net flow rate (Figure 23).

Entry	Pulsation amplitude	Displaced Volume (mL)
1	about 5%	0.036
2	10%	0.080
3	20%	0.120
4	30%	0.161
5	50%	0.265
6	70%	0.297
7	100%	0.442

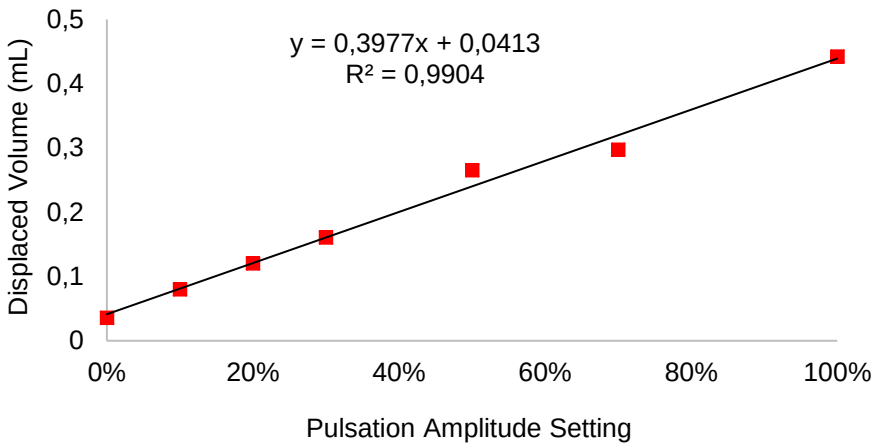

Figure 23. Correlation between pulsation amplitude and displaced volume.

5.6.3 Bodenstein Number (Bo) Determination

From each of these RTD profiles, the dimensionless Bodenstein (Bo) number was calculated, consisting of the mean residence time ($\bar{t}$) multiplied by two, divided by the variance (σ^2):

$$Bo = \frac{2 \cdot \bar{t}}{\sigma^2}$$

The variance can be calculated from a given RTD experiment using the following formula:

$$\sigma^2 = \frac{\sum t_i^2 \cdot C_i \cdot \Delta t}{\sum C_i \cdot \Delta t} - \bar{t}^2$$

A Bo value greater than 100 indicates that plug flow behavior is exhibited (Table 3).[63]

Entry	Flow rate (mL/min)	Pulsation Amplitude (mL/%)	Pulsation Frequency (Hz/%)	Bodenstein number
1	0.75	0 / 0	0/0	48
2	0.75	0.04 / about 5	3 / 100	128
3	0.75	0.12 / 20	3 / 100	35
4	0.75	0.16 / 30	3 / 100	16
5	0.75	0.24 / 50	3 / 100	13
6	0.75	0.32 / 70	3 / 100	10
7	0.75	0.04 / about 5	1.5 / 50	153
8	0.75	0.04 / about 5	0.6 / 20	184
9	0.75	0.12 / 20	1.5 / 50	32
10	0.25	0.12 / 20	1.5 / 50	23
11	0.5	0.12 / 20	1.5 / 50	25
12	1	0.12 / 20	1.5 / 50	76
13[a]	0.75	0.12 / 20	1.5 / 50	33

Table 3. RTD experiments performed under different pulsation and flow settings, with their corresponding Bodenstein (Bo) numbers, to characterize the extent of axial dispersion in each case. Higher Bo corresponds to a lesser extent of back mixing. [a] Experiment performed at 50°C.

5.6.4 General Procedure for the Model Aryl Amination (G1) and Characterization Data

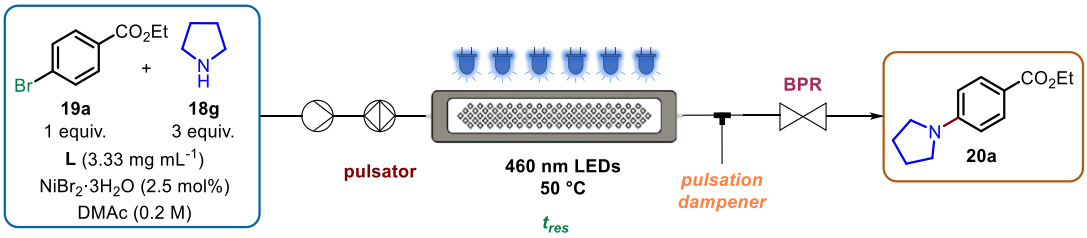

The LED array, equipped with 460 nm LEDs, was switched on and the reaction plate thermostat was set to 50 °C. A mixture of ethyl 4-bromobenzoate **19a** (5 mmol, 1 equiv.), pyrrolidine **18g** (15 mmol, 3 equiv.), **L** (3.33 mg mL^{-1} with respect to the solvent, 83.2 mg), nickel(II) bromide trihydrate (0.125 mmol, 2.5 mol%), 4-ethylbiphenyl (internal standard, 0.5 mmol, 0.1 equiv.) was made up in *N,N*-dimethylacetamide (25 mL total volume in a flask, $[\mathbf{19a}]_0 = 0.2$ M). Using the back pressure regulator, a pressure of 3 bar was set. The reaction mixture was degassed prior to use by sparging with an argon balloon for 15 minutes, then pumped through the reactor at 0.75 mL min^{-1} flow rate, corresponding to 20 min residence time. The pulsator was set to 20% (0.12 mL per stroke) pulsation

amplitude and 50% (1.5 Hz) pulsation frequency. Samples were collected over the time for analysis by HPLC, after filtration (0.45 µm syringe filter).

Scale-out Synthesis of 20a

For the scale-out experiment, the setup shown in Figure 24 was used. A mixture of ethyl 4-bromobenzoate **19a** (75 mmol, 1 equiv.), pyrrolidine **18g** (225 mmol, 3 equiv.), **L** (3.33 mg mL^{-1}, with respect to the solvent, 832 mg), nickel(II) bromide trihydrate (1.88 mmol, 2.5 mol%), 4-ethylbiphenyl (internal standard, 7.5 mmol, 0.1 equiv.) was made up in *N,N*-dimethylacetamide (250 mL total volume in a flask, $[\mathbf{19a}]_0$ = 0.3 M). Using the back pressure regulator, a pressure of 3 bar was set. The reaction mixture was degassed prior to use by sparging with an argon balloon for 30 minutes, then pumped through the reaction plate at 0.75 mL min^{-1} flow rate, corresponding to 20 min residence time, 20% (0.12 mL per stroke) pulsation amplitude and 50% (1.5 Hz) pulsation frequency. In order to avoid particle settling in the tubing, a vibrating motor (Figure 25) was installed on the peristaltic pump inlet and a small argon bubble was introduced to the system from the headspace of the starting mixture vessel every 15 minutes. Samples were collected over the time for analysis by HPLC, after filtration (0.45 µm syringe filter). The processed mixture, containing compound **20a**, was collected in the steady state over 270 min (4 hours and 30 min, from minute 50 to minute 320, providing a theoretical yield of 60.75 mmol, Figure 26). The crude reaction mixture was centrifuged at 6000 rpm for 5 minutes and the liquid phase was carefully separated before being diluted with water and extracted with ethyl acetate. The combined organic phases were washed with water, $NaHCO_3$ saturated solution and brine, dried over sodium sulfate and concentrated. The crude product was purified by trituration with petroleum ether and filtration to give the corresponding aryl amino compound **20a**.

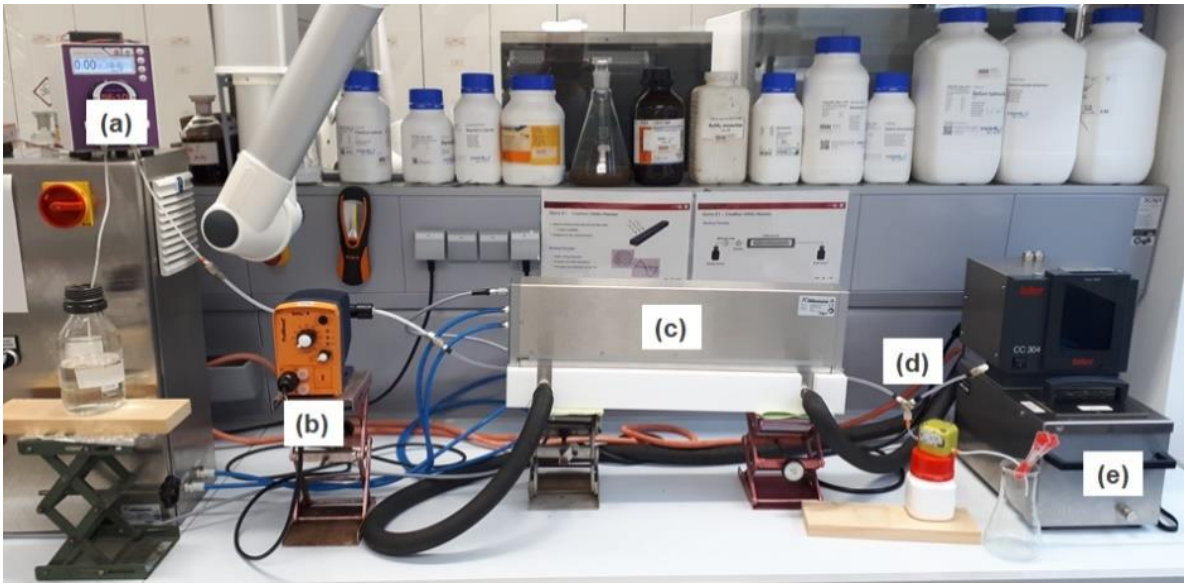

Figure 24. Photograph of commercial photoreactor setup for the scale-out experiment: a) metering peristaltic pump (Vapourtec); b) pulsator; c) reactor module housing, within the reaction plate and the LED module on the top; d) backpressure regulator with pulsation dampener; e) temperature control for the reactor (Huber).

Figure 25. Photograph of commercial vibrating motor and the battery power supply installed on the peristaltic pump inlet.[56]

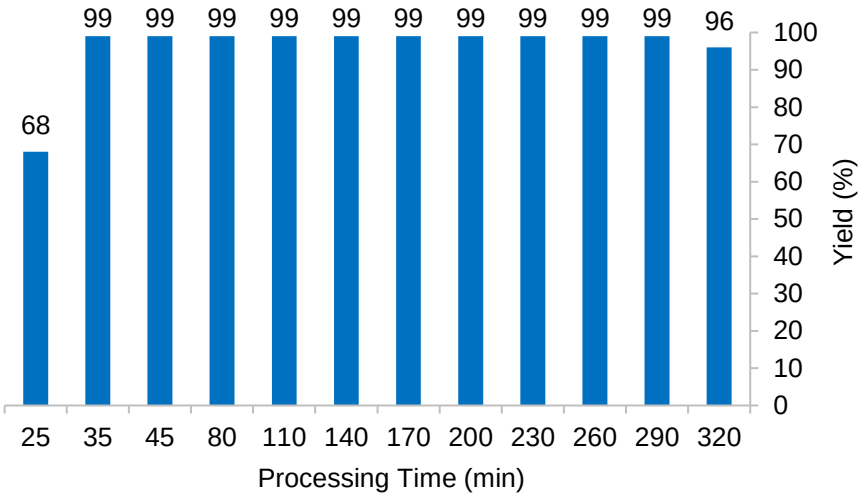

Figure 26. HPLC yield profile of the model reaction samples collected over the run time.

Characterization Data

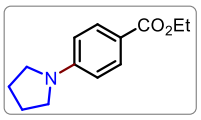

Ethyl 4-(pyrrolidin-1-yl)benzoate (20a). Prepared according to the scale-out procedure **G1**. The product **20a** was obtained as an off-white solid (12.05 g, 90% yield). The characterization of the compound matches the data reported in the literature.[49]

5.6.5 General Procedure for the Tetracaine Precursor Synthesis (G2) and Characterization Data

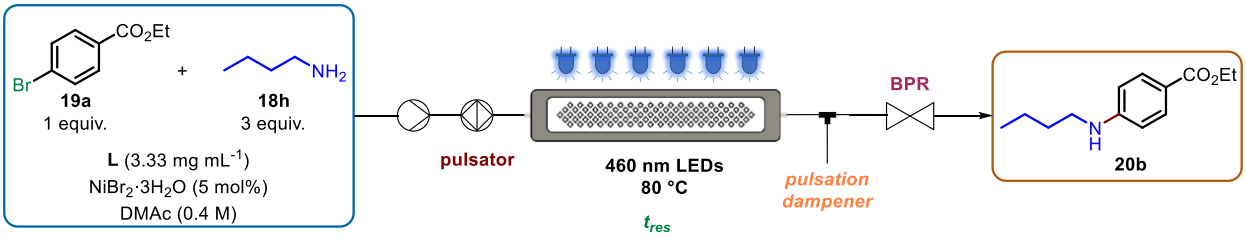

The LED array, equipped with 460 nm LEDs, was switched on and the reaction plate thermostat was set to 80 °C. A mixture of ethyl 4-bromobenzoate **19a** (10 mmol, 1 equiv.), butylamine **18h** (30 mmol, 3 equiv.), **L** (3.33 mg mL^{-1} with respect to the solvent, 83.2 mg), nickel(II) bromide trihydrate (0.5 mmol, 5 mol%), 4-ethylbiphenyl (internal standard, 1 mmol, 0.1 equiv.) was made up in *N,N*-dimethylacetamide (25 mL total volume in a flask, $[\mathbf{19a}]_0$ = 0.4 M). Using the back pressure regulator, a pressure of 3 bar was set. The reaction mixture was degassed prior to use by sparging with an argon balloon for 15 minutes, then pumped through the reactor at 0.25 mL/min flow rate, corresponding to 60 min residence time. Samples were collected over the time for analysis by HPLC, after filtration (0.45 µm syringe filter).

Isolation Run Experiment

For the isolation run experiment, setup shown in Figure 24 was used. A mixture of ethyl 4-bromobenzoate **19a** (30 mmol, 1 equiv.), butylamine **18h** (90 mmol, 3 equiv.), **L** (3.33 mg/mL with respect to the solvent, 250 mg), nickel(II) bromide trihydrate (1.5 mmol, 5 mol%), 4-ethylbiphenyl (internal standard, 3 mmol, 0.1 equiv.) was made up in *N,N*-dimethylacetamide (75 mL total volume in a flask, $[\mathbf{19a}]_0$ = 0.4 M). Using the back pressure regulator, a pressure of 3 bar was set. The reaction mixture was degassed prior to use by sparging with an argon balloon for 30 minutes, then pumped through the reactor at 0.25 mL min^{-1} flow rate, corresponding to 60 min residence time. In order to avoid particles settling in the tubing, a vibrating motor (Figure 25) was installed on the peristaltic pump inlet and a small argon bubble was let enter to the system from the headspace of the starting mixture vessel every 15 minutes. Samples were collected over the time for analysis by HPLC, after filtration (0.45 µm syringe filter). The processed mixture, containing compound **20b**, was collected in the steady state over 80 min (from minute 140 to minute 220, providing a theoretical yield of 8 mmol, Figure 27). The crude mixture was centrifuged at 6000 rpm for 5 minutes and the liquid phase was carefully separated before being evaporated under reduced pressure. The residue was purified by column chromatography (petroleum ether/ethyl acetate 80:20) to give the corresponding tetracaine precursor **20b**.

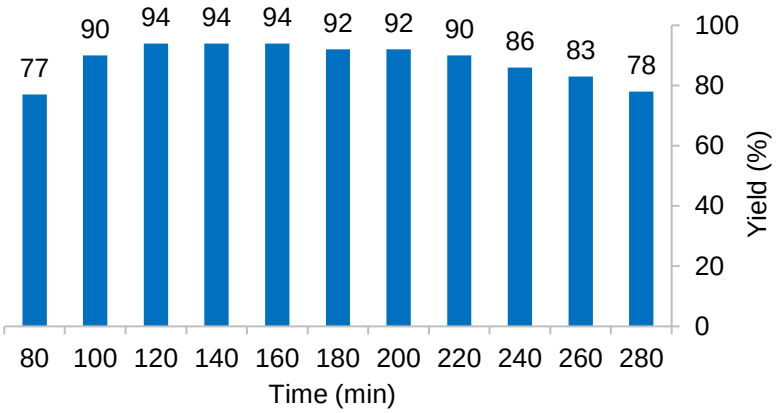

Figure 27. HPLC yield profile of the tetracaine precursor samples collected over the run time.

Characterization Data

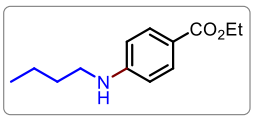

Ethyl 4-(butylamino)benzoate (20b). Prepared according to the isolation run procedure **G2**. The product **20b** was obtained as white solid (1.49 g, 84% yield). The characterization of the compound matches the data reported in the literature.[72]

5.6.6 Particle Size Distribution (PSD) of L

In order to determine the particle size distribution (PSD) of photocatalyst **L**, a series of Laser Diffraction (LD) measurements were carried out. Preliminarily, a mixture of **L** in DMAc (3.33 mg mL^{-1}) was pumped through the reaction system (screening experiments setup, Figure 21) at 0.75 mL min^{-1}, 20% pulsation amplitude and 50% pulsation frequency to simulate a reaction. Therefore, the particles that can pass through the apparatus can be separated from those which in the tubing after the reactor. The latter ones were finally removed by flushing the system at 10 mL min^{-1} flow rate and maximum pulsation. The two materials were individually collected, analyzed by LD using the parameters defined in Section 5.5.1 and compared with the unprocessed **L**. The resulting PSD profiles are shown in Figure 28.

The D10, D50 and D90 values for these particles were recorded:

D10 = Diameter at which 10% of particles are smaller.

D50 = Median particle diameter.

D90 = Diameter at which 90% of particles are smaller.

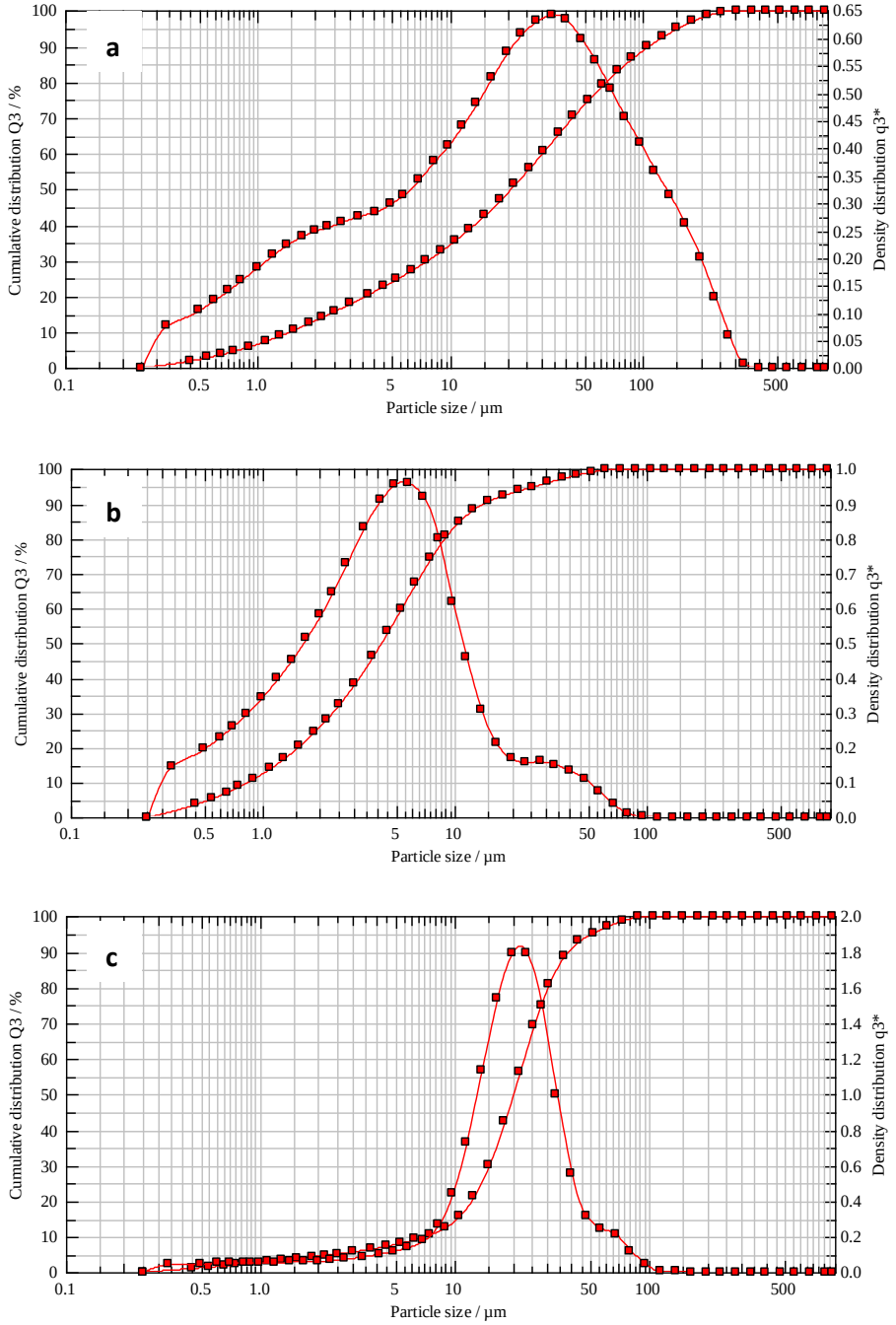

Figure 28. PSD profiles obtained from LD analysis. (**a**) unprocessed **L**; (**b**) particles passed through the reactor system; (**c**) particles which stuck in the tubing after the reactor.

The particles passed through the system have shown a PSD centered on ≈ 5 µm (D10 = 0.9 µm, D50 = 4.3 µm, D90 = 15 µm, Figure 28b). On the other hand, particles which stuck in the tubing have shown a PSD centered on ≈ 20 µm (D10 = 7 µm, D50= 20 µm, D90 = 40 µm, Figure 28c). Both the distributions are present in the unprocessed CN-OA-m PSD (Figure 28a).

Ball milling of the material was attempted (Retsch MM 400 mill) in efforts to reach a single size distribution, but this failed to show any change from the original PSD (Figure 28a).

5.7 References Chapter V

(1) Rosso, C.; Gisbertz, S.; Williams, J. D.; Gemoets, H. P. L.; Debrouwer, W.; Pieber, B.; Kappe, C. O. An Oscillatory Plug Flow Photoreactor Facilitates Semi-Heterogeneous Dual Nickel/Carbon Nitride Photocatalytic C-N Couplings. *React. Chem. Eng.* **2020**, *5*, 597–604.

(2) Bariwal, J.; Van Der Eycken, E. C-N Bond Forming Cross-Coupling Reactions: An Overview. *Chem. Soc. Rev.* **2013**, *42*, 9283–9303.

(3) Ullmann, F. Ueber Eine Neue Bildungsweise von Diphenylaminderivaten. *Ber. Dtsch. Chem. Ges.* **1903**, *36*, 2382–2384.

(4) Goldberg, I. Ueber Phenylirungen Bei Gegenwart von Kupfer Als Katalysator. *Ber. Dtsch. Chem. Ges.* **1906**, *39*, 1691–1692.

(5) Guram, A. S.; Rennels, R. A.; Buchwald, S. L. A Simple Catalytic Method for the Conversion of Aryl Bromides to Arylamines. *Angew. Chemie Int. Ed. English* **1995**, *34*, 1348–1350.

(6) Louie, J.; Hartwig, J. F. Palladium-Catalyzed Synthesis of Arylamines from Aryl Halides. Mechanistic Studies Lead to Coupling in the Absence of Tin Reagents. *Tetrahedron Lett.* **1995**, *36*, 3609–3612.

(7) Dorel, R.; Grugel, C. P.; Haydl, A. M. The Buchwald–Hartwig Amination After 25 Years. *Angew. Chem. Int. Ed.* **2019**, *58*, 17118–17129.

(8) Ruiz-Castillo, P.; Buchwald, S. L. Applications of Palladium-Catalyzed C-N Cross-Coupling Reactions. *Chem. Rev.* **2016**, *116*, 12564–12649.

(9) Magano, J.; Dunetz, J. R. Large-Scale Applications of Transition Metal-Catalyzed Couplings for the Synthesis of Pharmaceuticals. *Chem. Rev.* **2011**, *111*, 2177–2250.

(10) West, J. M.; Fyfe, J. W. B.; Vantourout, J. C.; Watson, A. J. B. Mechanistic Development and Recent Applications of the Chan−Lam Amination. *Chem. Rev.* **2019**, *119*, 12491−12523.

(11) Butters, M.; Catterick, D.; Craig, A.; Curzons, A.; Dale, D.; Gillmore, A.; Green, S. P.; Marziano, I.; Sherlock, J. P.; White, W. Critical Assessment of Pharmaceutical Processes - A Rationale for Changing the Synthetic Route. *Chem. Rev.* **2006**, *106*, 3002–3027.

(12) Wolfe, J. P.; Buchwald, S. L. Nickel-Catalyzed Amination of Aryl Chlorides. *J. Am. Chem. Soc.* **1997**, *119*, 6054–6058.

(13) Lavoie, C. M.; Stradiotto, M. Bisphosphines: A Prominent Ancillary Ligand Class for Application in Nickel-Catalyzed C-N Cross-Coupling. *ACS Catal.* **2018**, *8*, 7228–7250.

(14) Zhu, C.; Yue, H.; Jia, J.; Rueping, M. Recent Advances in Nickel-Catalyzed C-Heteroatom Cross-Coupling Reactions under Mild Conditions via Facilitated Reductive Elimination. *Angew. Chem. Int. Ed.* **2020**, DOI: 10.1002/anie.202013852.

(15) Wenger, O. S. Photoactive Nickel Complexes in Cross-Coupling Catalysis. *Chem. Eur. J.* **2020**, DOI: 10.1002/chem.202003974.

(16) Till, N. A.; Tian, L.; Dong, Z.; Scholes, G. D.; MacMillan, D. W. C. Mechanistic Analysis of Metallaphotoredox C-N Coupling: Photocatalysis Initiates and Perpetuates Ni(I)/Ni(III) Coupling Activity. *J. Am. Chem. Soc.* **2020**, *142*, 15830–15841.

(17) Qi, Z. H.; Ma, J. Dual Role of a Photocatalyst: Generation of Ni(0) Catalyst and Promotion of Catalytic C-N Bond Formation. *ACS Catal.* **2018**, *8*, 1456–1463.

(18) Koo, K.; Hillhouse, G. L. Carbon-Nitrogen Bond Formation by Reductive Elimination from

Nickel(II) Amido Alkyl Complexes. *Organometallics* **1995**, *14*, 4421–4423.

(19) Ilies, L.; Matsubara, T.; Nakamura, E. Nickel-Catalyzed Synthesis of Diarylamines via Oxidatively Induced C-N Bond Formation at Room Temperature. *Org. Lett.* **2012**, *14*, 5570–5573.

(20) Sun, R.; Qin, Y.; Nocera, D. G. General Paradigm in Photoredox Nickel-Catalyzed Cross-Coupling Allows for Light-Free Access to Reactivity. *Angew. Chem. Int. Ed.* **2020**, *59*, 9527–9533.

(21) Kingston, C.; Palkowitz, M. D.; Takahira, Y.; Vantourout, J. C.; Peters, B. K.; Kawamata, Y.; Baran, P. S. A Survival Guide for the "Electro-Curious." *Acc. Chem. Res.* **2020**, *53*, 72–83.

(22) Yan, M.; Kawamata, Y.; Baran, P. S. Synthetic Organic Electrochemical Methods since 2000: On the Verge of a Renaissance. *Chem. Rev.* **2017**, *117*, 13230–13319.

(23) Li, C.; Kawamata, Y.; Nakamura, H.; Vantourout, J. C.; Liu, Z.; Hou, Q.; Bao, D.; Starr, J. T.; Chen, J.; Yan, M.; Baran, P. S. Electrochemically Enabled, Nickel-Catalyzed Amination. *Angew. Chem. Int. Ed.* **2017**, *56*, 13088–13093.

(24) Kawamata, Y.; Vantourout, J. C.; Hickey, D. P.; Bai, P.; Chen, L.; Hou, Q.; Qiao, W.; Barman, K.; Edwards, M. A.; Garrido-Castro, A. F.; Degruyter, J. N.; Nakamura, H.; Knouse, K.; Qin, C.; Clay, K. J.; Bao, D.; Li, C.; Starr, J. T.; Garcia-Irizarry, C.; Sach, N.; White, H. S.; Neurock, M.; Minteer, S. D.; Baran, P. S. Electrochemically Driven, Ni-Catalyzed Aryl Amination: Scope, Mechanism, and Applications. *J. Am. Chem. Soc.* **2019**, *141*, 6392–6402.

(25) Glaser, F.; Kerzig, C.; Wenger, O. S. Multi-Photon Excitation in Photoredox Catalysis: Concepts, Applications, Methods. *Angew. Chem. Int. Ed.* **2020**, *59*, 10266–10284.

(26) Corcoran, E. B.; Pirnot, M. T.; Lin, S.; Dreher, S. D.; Dirocco, D. A.; Davies, I. W.; Buchwald, S. L.; Macmillan, D. W. C. Aryl Amination Using Ligand-Free Ni(II) Salts and Photoredox Catalysis. *Science* **2016**, *353*, 279–283.

(27) Du, Y.; Pearson, R. M.; Lim, C. H.; Sartor, S. M.; Ryan, M. D.; Yang, H.; Damrauer, N. H.; Miyake, G. M. Strongly Reducing, Visible-Light Organic Photoredox Catalysts as Sustainable Alternatives to Precious Metals. *Chem. Eur. J.* **2017**, *23*, 10962–10968.

(28) Kudisch, M.; Lim, C.-H.; Thordarson, P.; Miyake, G. M. Energy Transfer to Ni-Amine Complexes in Dual Catalytic, Light-Driven C–N Cross-Coupling Reactions. *J. Am. Chem. Soc.* **2019**, *141*, 19479–19486.

(29) Escobar, R. A.; Johannes, J. W. A Unified and Practical Method for Carbon–Heteroatom Cross-Coupling Using Nickel/Photo Dual Catalysis. *Chem. Eur. J.* **2020**, *26*, 5168–5173.

(30) Lim, C. H.; Kudisch, M.; Liu, B.; Miyake, G. M. C-N Cross-Coupling via Photoexcitation of Nickel-Amine Complexes. *J. Am. Chem. Soc.* **2018**, *140*, 7667–7673.

(31) Romero, N. A.; Nicewicz, D. A. Organic Photoredox Catalysis. *Chem. Rev.* **2016**, *116*, 10075–10166.

(32) Friedmann, D.; Hakki, A.; Kim, H.; Choi, W.; Bahnemann, D. Heterogeneous Photocatalytic Organic Synthesis: State-of-the-Art and Future Perspectives. *Green Chem.* **2016**, *18*, 5391–5411.

(33) Gisbertz, S.; Pieber, B. Heterogeneous Photocatalysis in Organic Synthesis. *ChemPhotoChem* **2020**, *4*, 1–21.

(34) Caputo, J. A.; Frenette, L. C.; Zhao, N.; Sowers, K. L.; Krauss, T. D.; Weix, D. J. General and

Efficient C-C Bond Forming Photoredox Catalysis with Semiconductor Quantum Dots. *J. Am. Chem. Soc.* **2017**, *139*, 4250–4253.

(35) Liu, Y. Y.; Liang, D.; Lu, L. Q.; Xiao, W. J. Practical Heterogeneous Photoredox/Nickel Dual Catalysis for C-N and C-O Coupling Reactions. *Chem. Commun.* **2019**, *55*, 4853–4856.

(36) Su, D. S.; Zhang, J.; Frank, B.; Thomas, A.; Wang, X.; Paraknowitsch, J.; Schlögl, R. Metal-Free Heterogeneous Catalysis for Sustainable Chemistry. *ChemSusChem* **2010**, *3*, 169–180.

(37) Monai, M.; Melchionna, M.; Fornasiero, P. From Metal to Metal-Free Catalysts: Routes to Sustainable Chemistry. In *Advances in Catalysis*; Academic Press, 2018; pp 1–73.

(38) Rosso, C.; Filippini, G.; Prato, M. Carbon Dots as Nano-Organocatalysts for Synthetic Applications. *ACS Catal.* **2020**, *10*, 8090–8105.

(39) Wang, Y.; Wang, X.; Antonietti, M. Polymeric Graphitic Carbon Nitride as a Heterogeneous Organocatalyst: From Photochemistry to Multipurpose Catalysis to Sustainable Chemistry. *Angew. Chem. Int. Ed.* **2012**, *51*, 68–89.

(40) Savateev, A.; Antonietti, M. Heterogeneous Organocatalysis for Photoredox Chemistry. *ACS Catal.* **2018**, *8*, 9790–9808.

(41) Mazzanti, S.; Savateev, A. Emerging Concepts in Carbon Nitride Organic Photocatalysis. *Chempluschem* **2020**, *85*, 2499–2517.

(42) Savateev, A.; Ghosh, I.; König, B.; Antonietti, M. Photoredox Catalytic Organic Transformations Using Heterogeneous Carbon Nitrides. *Angew. Chem. Int. Ed.* **2018**, *57*, 15936–15947.

(43) Markushyna, Y.; Smith, C. A.; Savateev, A. Organic Photocatalysis: Carbon Nitride Semiconductors vs. Molecular Catalysts. *Eur. J. Org. Chem.* **2019**, 1294–1309.

(44) Wang, X.; Blechert, S.; Antonietti, M. Polymeric Graphitic Carbon Nitride for Heterogeneous Photocatalysis. *ACS Catal.* **2012**, *2*, 1596–1606.

(45) Cao, S.; Low, J.; Yu, J.; Jaroniec, M. Polymeric Photocatalysts Based on Graphitic Carbon Nitride. *Adv. Mater.* **2015**, *27*, 2150–2176.

(46) Liu, G.; Zhen, C.; Kang, Y.; Wang, L.; Cheng, H. M. Unique Physicochemical Properties of Two-Dimensional Light Absorbers Facilitating Photocatalysis. *Chem. Soc. Rev.* **2018**, *47*, 6410–6444.

(47) Vinu, A.; Ariga, K.; Mori, T.; Nakanishi, T.; Hishita, S.; Golberg, D.; Bando, Y. Preparation and Characterization of Well-Ordered Hexagonal Mesoporous Carbon Nitride. *Adv. Mater.* **2005**, *17*, 1648–1652.

(48) Han, Q.; Wang, B.; Gao, J.; Cheng, Z.; Zhao, Y.; Zhang, Z.; Qu, L. Atomically Thin Mesoporous Nanomesh of Graphitic C3N4 for High-Efficiency Photocatalytic Hydrogen Evolution. *ACS Nano* **2016**, *10*, 2745–2751.

(49) Ghosh, I.; Khamrai, J.; Savateev, A.; Shlapakov, N.; Antonietti, M.; König, B. Organic Semiconductor Photocatalyst Can Bifunctionalize Arenes and Heteroarenes. *Science* **2019**, *365*, 360–366.

(50) Gisbertz, S.; Reischauer, S.; Pieber, B. Overcoming Limitations in Dual Photoredox/Nickel-Catalysed C–N Cross-Couplings Due to Catalyst Deactivation. *Nat. Catal.* **2020**, *3*, 611–620.

(51) Qin, Y.; Martindale, B. C. M.; Sun, R.; Rieth, A. J.; Nocera, D. G. Solar-Driven Tandem

Photoredox Nickel-Catalysed Cross-Coupling Using Modified Carbon Nitride. *Chem. Sci.* **2020**, *11*, 7456–7461.

(52) Hartman, R. L. Managing Solids in Microreactors for the Upstream Continuous Processing of Fine Chemicals. *Org. Process Res. Dev.* **2012**, *16*, 870–887.

(53) Filipponi, P.; Gioiello, A.; Baxendale, I. R. Controlled Flow Precipitation as a Valuable Tool for Synthesis. *Org. Process Res. Dev.* **2016**, *20*, 371–375.

(54) Liguori, L.; Bjørsvik, H. R. Multijet Oscillating Disc Millireactor: A Novel Approach for Continuous Flow Organic Synthesis. *Org. Process Res. Dev.* **2011**, *15*, 997–1009.

(55) Falß, S.; Tomaiuolo, G.; Perazzo, A.; Hodgson, P.; Yaseneva, P.; Zakrzewski, J.; Guido, S.; Lapkin, A.; Woodward, R.; Meadows, R. E. A Continuous Process for Buchwald-Hartwig Amination at Micro-, Lab-, and Mesoscale Using a Novel Reactor Concept. *Org. Process Res. Dev.* **2016**, *20*, 558–567.

(56) Pomberger, A.; Mo, Y.; Nandiwale, K. Y.; Schultz, V. L.; Duvadie, R.; Robinson, R. I.; Altinoglu, E. I.; Jensen, K. F. A Continuous Stirred-Tank Reactor (CSTR) Cascade for Handling Solid-Containing Photochemical Reactions. *Org. Process Res. Dev.* **2019**.

(57) Mo, Y.; Jensen, K. F. A Miniature CSTR Cascade for Continuous Flow of Reactions Containing Solids. *React. Chem. Eng.* **2016**, *1*, 501–507.

(58) Chapman, M. R.; Kwan, M. H. T.; King, G.; Jolley, K. E.; Hussain, M.; Hussain, S.; Salama, I. E.; González Nino, C.; Thompson, L. A.; Bayana, M. E.; Clayton, A. D.; Nguyen, B. N.; Turner, N. J.; Kapur, N.; Blacker, A. J. Simple and Versatile Laboratory Scale CSTR for Multiphasic Continuous-Flow Chemistry and Long Residence Times. *Org. Process Res. Dev.* **2017**, *21*, 1294–1301.

(59) McGlone, T.; Briggs, N. E. B.; Clark, C. A.; Brown, C. J.; Sefcik, J.; Florence, A. J. Oscillatory Flow Reactors (OFRs) for Continuous Manufacturing and Crystallization. *Org. Process Res. Dev.* **2015**, *19*, 1186–1202.

(60) Okafor, O.; Weilhard, A.; Fernandes, J. A.; Karjalainen, E.; Goodridge, R.; Sans, V. Advanced Reactor Engineering with 3D Printing for the Continuous-Flow Synthesis of Silver Nanoparticles. *React. Chem. Eng.* **2017**, *2*, 129–136.

(61) Bianchi, P.; Williams, J. D.; Kappe, C. O. Oscillatory Flow Reactors for Synthetic Chemistry Applications. *J. Flow Chem.* **2020**, *10*, 475–490.

(62) Plutschack, M. B.; Pieber, B.; Gilmore, K.; Seeberger, P. H. The Hitchhiker's Guide to Flow Chemistry. *Chem. Rev.* **2017**, *117*, 11796–11893.

(63) Levenspiel, O.; Bischoff, K. B. Backmixing in the Design of Chemical Reactors. *Ind. Eng. Chem.* **1959**, *51*, 1431–1434.

(64) Cavedon, C.; Madani, A.; Seeberger, P. H.; Pieber, B. Semiheterogeneous Dual Nickel/Photocatalytic (Thio)Etherification Using Carbon Nitrides. *Org. Lett.* **2019**, *21*, 5331–5334.

(65) Pieber, B.; Malik, J. A.; Cavedon, C.; Gisbertz, S.; Savateev, A.; Cruz, D.; Heil, T.; Zhang, G.; Seeberger, P. H. Semi-Heterogeneous Dual Nickel/Photocatalysis Using Carbon Nitrides: Esterification of Carboxylic Acids with Aryl Halides. *Angew. Chem. Int. Ed.* **2019**, *58*, 9575–9580.

(66) Zhang, G.; Li, G.; Lan, Z.; Lin, L.; Savateev, A.; Heil, T.; Zafeiratos, S.; Wang, X.; Antonietti, M.

Optimizing Optical Absorption, Exciton Dissociation, and Charge Transfer of a Polymeric Carbon Nitride with Ultrahigh Solar Hydrogen Production Activity. *Angew. Chem. Int. Ed.* **2017**, *56*, 13445–13449.

(67) Park, B. Y.; Pirnot, M. T.; Buchwald, S. L. Visible Light-Mediated (Hetero)Aryl Amination Using Ni (II) Salts and Photoredox Catalysis in Flow: A Synthesis of Tetracaine. *J. Org. Chem.* **2020**, *85*, 3234–3244.

(68) Gyorke, S.; Lukyanenko, V.; Gyorke, I. Dual Effects of Tetracaine on Spontaneous Calcium Release in Rat Ventricular Myocytes. *J. Physiol.* **1997**, *500*, 297–309.

(69) *World Health Organization Model List of Essential Medicines - 21st List*; 2019.

(70) Yuan, M. L.; Xie, J. H.; Zhou, Q. L. Boron Lewis Acid Promoted Ruthenium-Catalyzed Hydrogenation of Amides: An Efficient Approach to Secondary Amines. *ChemCatChem* **2016**, *8*, 3036–3040.

(71) Oderinde, M. S.; Jones, N. H.; Juneau, A.; Frenette, M.; Aquila, B.; Tentarelli, S.; Robbins, D. W.; Johannes, J. W. Highly Chemoselective Iridium Photoredox and Nickel Catalysis for the Cross-Coupling of Primary Aryl Amines with Aryl Halides. *Angew. Chem. Int. Ed.* **2016**, *55*, 13219–13223.

(72) Wahba, A. E.; Hamann, M. T. Reductive N -Alkylation of Nitroarenes: A Green Approach for the N-Alkylation of Natural Products. *J. Org. Chem.* **2012**, *77*, 4578–4585.